UNIVERSITÀ DEGLI STUDI DI PADOVA

Dipartimento di Fisica "G. Galilei", Via Marzolo, 8, PADOVA
Scuola di Dottorato di ricerca in FISICA
Ciclo XXIV

Charm production at the LHC via $\mathrm{D}^0 \to \mathrm{K}^-\pi^+$ reconstruction in ALICE: cross section in pp collisions and first flow measurement in Pb–Pb collisions

Direttore della Scuola: Ch.mo Prof. Andrea Vitturi

Supervisore: Dott. Marcello Lunardon

Co-supervisore: Dott. Andrea Dainese

Dottoranda: Chiara Bianchin

Contents

Introduction

ALICE (A Large Hadron Collider Experiment) is one of the CERN-LHC (Large Hadron Collider) experiments. The main goal of ALICE is investigating the properties of the state of matter formed in ultra-relativistic heavy-ion collisions, the strongly-interacting quark-gluon plasma (QGP). The extremely high-energy-density and high-temperature matter produced in Pb–Pb collisions at centre-of-mass-energy of 2.76 TeV at the LHC is similar to the state of the matter that constituted the Universe few microseconds after the Big Bang.

Nucleus-nucleus collisions have been carried out for the last 20 years by the Super Proton Synchrotron at CERN and by the Relativistic Heavy Ion Collider at Brookhaven to study this state of matter in a laboratory.

The experimental results confirm the production of a deconfined system that reaches a thermal equilibrium and behaves like an almost perfect fluid, following the equations of hydrodynamics, until it cools down and hadrons are produced again. The properties of such a medium can be studied via probes coming from the interaction itself, namely the final-state detected particles. Heavy quarks are particularly effective in probing the medium.

The charm quark is the subject of this thesis, which presents the measurement of the production of D^0 mesons, containing a charm quark, at the LHC. The D^0 meson production cross section measurement in pp collisions and the first measurement of the D^0 elliptic flow in Pb–Pb collisions will be described. The first result serves as a test for pQCD calculations at unprecedented high centre-of-mass energy, 7 TeV for pp and 2.76 TeV for Pb–Pb collisions, and as a reference for measurements made in a heavy-ion environment, like the measurement of the D^0 yield suppression due to energy loss in the medium. The second result is a starting point to investigate the degree of thermalization of the quark-gluon plasma.

The topics treated in each chapter of this thesis are outlined in the following.

In Chapter 1 a general introduction about the physics goals in heavy-ion and proton-proton collisions will be drawn. In the context of the Standard Model, the strong interaction will be introduced. Then, the evolution of a nucleus-nucleus collision will be described and the observables useful for probing the properties of the quark-gluon plasma will be presented. A large part of the chapter will be finally devoted to the physics of heavy quarks in pp and heavy-ion collisions.

Chapter 2 will present the ALICE detector, describing mainly the sub-detectors used for heavy-flavour analyses. The tools developed for simulation, reconstruction and analyses will be summarised as well. The performance achieved by the detectors involved in heavy-flavour analyses, both in pp and Pb–Pb collisions, during the first year of data taking will be presented.

The analysis tools implemented during this thesis will be described in Chapter 3.

Chapter 4 will be devoted to the description of the measurement of the D^0 meson cross section in pp collisions, in the decay channel $D^0 \to K^-\pi^+$. In particular, I participated in the study of the variables used for the selection of the signal and in the yield extraction through an invariant mass analysis. The displaced decay vertices ($c\tau(D^0) = 122.9$ μm) are reconstructed, then pairs of unlike-sign tracks are combined and their species identified. Finally the topological selections are applied and a fit to the invariant mass spectrum is performed to determine the D^0 yield. To compute the final cross section, the extracted yield must be corrected and properly normalized. The measured D^0 production cross section [1] extends to the region of transverse momentum

from 1 to 16 GeV/c and was compared to pQCD calculations, which are found to be in agreement with data.

Chapter 5 will present the first measurement of the D^0 meson elliptic flow in the transverse momentum region from 2 to 12 GeV/c. A sample of 3 million events from 2010 data, in the centrality class 30-50% was used and several equivalent methods were applied, giving compatible results. I was responsible for the tuning of the selection of the D^0 candidates, for the signal extraction and for the determination of the elliptic flow with the event plane method, which consists in extracting the signal in two intervals of angle between the D^0 and the event plane azimuths. The preliminary result was approved by the ALICE Collaboration and I presented it for the first time in an International conference.

Finally, Chapter 6 will contain a summary of the motivation for the work carried out during this thesis and the conclusions that can be drawn from the results.

Introduzione

ALICE (A Large Hadron Collider Experiment) è uno degli esperimenti di LHC (Large Hadron Collider) al CERN. Lo scopo principale di ALICE è lo studio delle proprietà dello stato di materia formato in collisioni ultra-relativistiche di ioni pesanti, il plasma di quark e gluoni (QGP), dominato dalle interazioni forti tra i suoi componenti elementari. Lo stato di materia formato in collisioni Pb–Pb prodotte a LHC, con un'energia nel centro di massa di 2.76 TeV, è caratterizzato da una densità di energia e una temperatura estreme, condizioni simili a quelle della materia di cui era formato l'Universo qualche microsecondo dopo il Big Bang.

La storia dei collider adronici è iniziata circa 20 anni fa con il Super Proton Synchrotron al CERN e, successivamente, il Relativistic Heavy Ion Collider a Brookhaven. Grazie a questi acceleratori si possono effettuare collisioni tra nuclei e studiare l'origine dell'Universo riproducendo la materia primordiale in laboratorio.

I risultati sperimentali confermano la produzione di una sistema deconfinato, in cui quark e gluoni sono liberi di muoversi. Questo stato di materia può essere descritto tramite le leggi della fluidodinamica, che regolano un fluido in equilibrio termico. Successivamente, espandendosi, la materia si raffredda e la formazione degli adroni è di nuovo possibile. Le proprietà di tale mezzo possono essere studiate utilizzando sonde che provengono direttamente al suo interno, attraverso le particelle finali rilevate dall'esperimento. Gli heavy quarks, quali il charm, sono particolarmente efficaci come sonde, in quanto vengono prodotti nelle interazioni iniziali tra partoni.

Questa tesi è dedicata in particolare allo studio del charm, attraverso l'analisi dei mesoni D^0, che contengono appunto un quark charm. Si descriverà la misura della sezione d'urto di produzione del mesone D^0 a LHC, importante come test delle predizioni di QCD perturbativa (pQCD) ad un'energia nel centro di massa di 7 TeV, raggiunta sperimentalmente per la prima volta a LHC. La produzione di mesoni D^0 in collisioni protone-protone è inoltre fondamentale come riferimento per le misure compiute in collisioni tra ioni, ad esempio la soppressione nella produzione di mesoni D^0, dovuta alla perdita di energia nel mezzo. Successivamente si descriverà la prima misura di flow ellittico della D^0, importante per la comprensione del grado si equilibrio termico raggiunto dal QGP.

Gli argomenti trattati in ogni capitolo sono elencati di seguito.

Nel Capitolo 1 verrà delineata un'introduzione generale sugli obiettivi di fisica in collisioni pp e Pb–Pb. In particolare si introdurranno il Modello Standard e le interazioni forti. Descrivendo l'evoluzione di una collisione nucleo-nucleo, si elencheranno le osservabili importanti per lo studio delle proprietà del quark-gluon plasma. Inoltre, una parte del capitolo verrà dedicata all'approfondimento del tema degli heavy flavour.

Nel Capitolo 2 si descriverà il rivelatore ALICE, attraverso i vari sotto-rivelatori di cui è composto, dando particolare risalto a quelli utilizzati per le analisi sugli heavy flavour e alle loro performance. Verranno riassunti inoltre gli strumenti di simulazione, ricostruzione e analisi utilizzati all'interno dell'esperimento.

Il Capitolo 3 tratterà dei temi più tecnici descrivendo alcuni degli strumenti di analisi sviluppati durante il lavoro di tesi.

Il Capitolo 4 è dedicato alla descrizione dell'analisi per la misura della sezione d'urto di produzione del mesone D^0 nel canale di decadimento $D^0 \to K^-\pi^+$ in collisioni pp [1]. In particolare mi sono occupata direttamente della procedura di estrazione del segnale. Ho messo a punto dei metodi di selezione utilizzando variabili adatte a riconoscere la topologia di decadimento del mesone D^0 in modo da aumentare il rapporto segnale su

fondo e la procedura di fit per l'estrazione del segnale attraverso un'analisi di massa invariante. L'analisi parte dalla ricostruzione dei vertici secondari (il $c\tau$ del mesone D^0 è infatti 122.9 μm), procedendo con l'accopiamento di tracce di segno opposto che vengono poi sfoltite a seconda della natura delle particelle coinvolte e dell'accordo con le selezioni topologiche. Il segnale estratto viene quindi corretto e normalizzato per ottenere la sezione d'urto finale. La misura della sezione d'urto è stata effettuata nella regione di impulso trasverso tra 1 e 12 GeV/c ed è stata confrontata con delle predizioni di pQCD, che risultano compatibili con i dati.

Il Capitolo 5 è dedicato alla misura del flow ellittico del mesone D^0, ricavato nella regione di momento trasverso tra 2 e 12 GeV/c con 3 milioni di eventi registrati nel 2010 nella regione di centralità tra 30 e 50%. Sono stati utilizzati più metodi equivalenti per testare la robustezza della misura e sono stati ottenuti dei risultati compatibili. Mi sono occupata nuovamente della selezione del segnale con un'analisi di massa invariante e della determinazione del flow ellittico con un metodo che estrae il segnale in diversi intervalli dell'angolo azimutale compreso tra l'impulso del mesone D^0 e la direzione del piano di reazione.

Infine, nel Capitolo 6 verrano fornite delle considerazioni riassuntive sugli scopi delle misure effettuate durante il lavoro di tesi e sulle conclusioni che si possono trarre dalle quantità misurate.

Chapter 1

Studying the quark-gluon plasma at the LHC with heavy-ion collisions

1.1 Physics at the LHC

The Large Hadron Collider (LHC) is the largest machine ever built with the highest centre of mass energy, accelerating protons and fully stripped lead ions $^{208}Pb^{82+}$. Designed for $\sqrt{s} = 14$ TeV in pp collisions, it is temporarily limited to $\sqrt{s} = 7$ TeV. The nominal peak luminosity is 1×10^{34} [1] and 1×10^{27} cm^{-2} s^{-1} for pp and Pb–Pb, respectively. This outstanding performance is required for the study of "new physics", which is the main goal of the LHC. Rare signals, such as the Higgs boson, supersymmetry, and CP violation, need in fact very high integrated luminosity together with very efficient trigger capabilities. Those are the physics goals being fulfilled by the two large multi-purpose experiments, ATLAS and CMS, and by LHCb which is dedicated to B-physics. Heavy-ion physics is, instead, the main focus of ALICE (A Large Ion Collider Experiment), designed to work in the high charged particle multiplicity environment of Pb–Pb collisions. ALICE has complementary capabilities with respect to ATLAS and CMS, both in pp and in Pb–Pb, for example the low-p_t reach. The LHC experiments as a whole can access a wide range of measurements thanks to their complementarity. At the same time their results can be compared and combined to achieve better precision.

The main goals of the ALICE experiment are discussed in this chapter. Section 1.2gives an overview of the Standard Model and of the heavy-ion physics. Section 1.3 focus on heavy-flavour physics, both in proton-proton and heavy-ion collisions. The relevant results from RHIC and SPS are described as well. Finally, Section 1.4 presents an overview of the main results from ALICE with the first year data.

1.2 Quark Gluon Plasma in heavy-ion collisions

1.2.1 The Standard Model and the strong interaction

The Standard Model describes the fundamental forces and the composition of matter. It is a gauge theory including strong, weak, and electromagnetic forces and the related interactions (excluding gravity). Matter is constituted out of point-like particles which have a spin of 1/2 and are grouped into three families, each containing two *quarks* and two *leptons*, as depicted in Fig. 1.1, left panel. Leptons are affected by the weak force and the charged ones also by the electromagnetic force. Quarks exhibit six different

[1] In ATLAS and CMS interaction points.

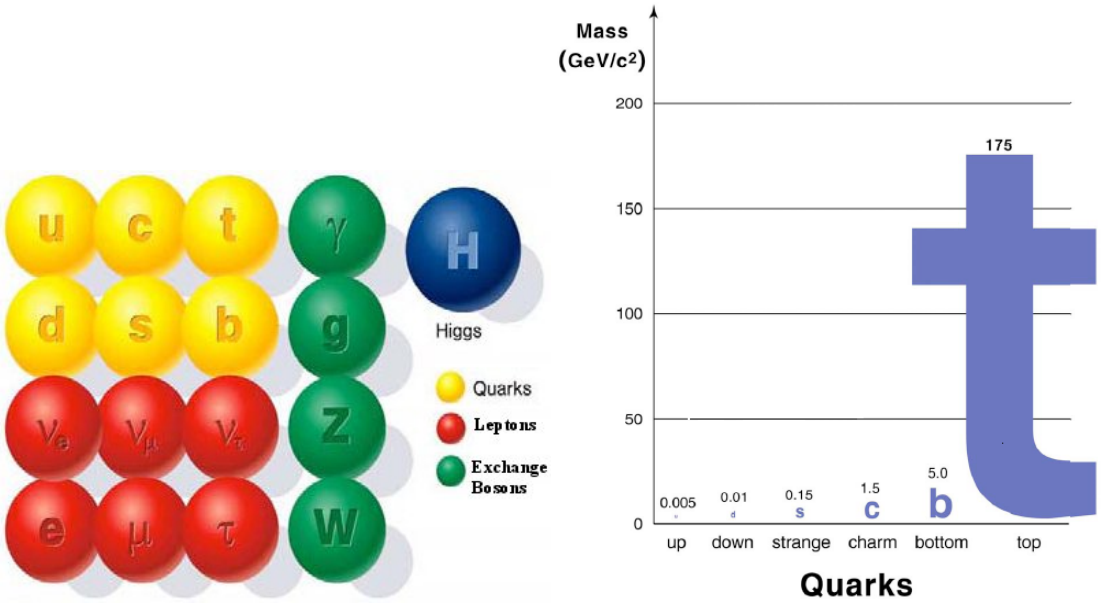

Figure 1.1: Left panel: Standard Model families of leptons and quarks and the gauge bosons. Out of the schema, the Higgs boson, expected to be responsible for particle masses. Right panel: Masses of the different quark flavours.

so-called *flavours*: from lighter to heavier *up*, *down*, *strange*, *charm*, *beauty/bottom*, and *top*. Their masses are not predicted by the theory and they range between 5 MeV/c^2 and 175 GeV/c^2 (right panel of Fig. 1.1). Quarks have a property called *colour* playing the role of charge in the strong force. The colour can take one out of three possible values (conventionally *red*, *green*, and *blue*) which never appear freely but are hidden in the colourless hadrons. Hadrons are grouped into *baryons* and *mesons*. Baryons consist of three quarks, qqq (e.g. the proton: uud), mesons consist of two quarks, $q\bar{q}$ (e.g. the π: $u\bar{d}$). Quarks are affected by the strong, weak, and electromagnetic forces. These forces are mediated by the exchange of gauge bosons: γ, $W^{\pm}$, and Z^0 for the electroweak force and *gluons* for the strong force. The Quantum Electro-Dynamics (QED) is the theory of electromagnetic interactions, while the strong force is described by the Quantum Chromo-Dynamics (QCD). The main characteristic of the strong force is that gluons interact among each other, differently from photons. The QCD potential is given by a Coulombian term and a confining term, arising because of the self-interaction property of the colour field, as:

$$V(r) \propto \frac{1}{r} + r. \tag{1.1}$$

At low energy the confinement dominates, giving that the quarks can only be seen within hadrons. The energy required to produce a separation far exceeds the pair production energy of a quark-anti-quark pair, so instead of pulling out an isolated quark, a meson is produced, as the produced quark-anti-quark pairs combine (see Fig. 1.2).

At high energy the interaction weaken giving an asymptotic freedom. Quarks and gluon are quasi-free and the state of matter formed is a *quark-gluon plasma (QGP)*.

1.2.2 Confinement and phase diagram

At "low" temperature, quark-based matter appears as confined hadrons in the form of baryons and mesons. These quarks cannot be isolated by pulling them apart, since the

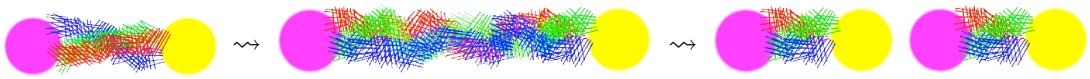

Figure 1.2: Sketch of the confinement. Two quarks pulled apart from each other (left). The coloured string represents the strong force interaction, which is like an elastic stretching when the quarks get further (centre). When the energy between the two quarks becomes to high (the elastic is at the maximum length it can afford), higher than that needed to create a pair of quark-anti-quark, the colour string breaks up into two quark-anti-quark-pairs.

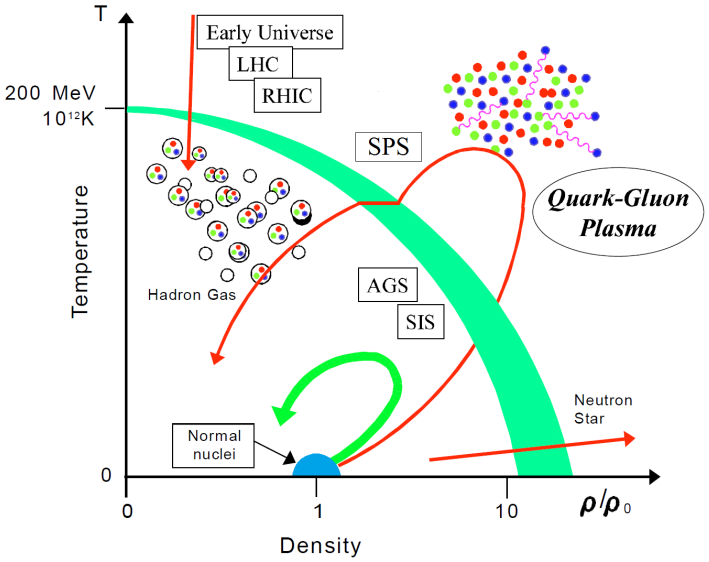

Figure 1.3: Phase diagram of hadronic matter.

potential energy between them increases with the distance. When the temperature or the baryon density become very high, the force between quarks and gluons weaken and a phase transition to a deconfined state is predicted. The order of the phase transition depends on the hypothesis on the quark masses. In Fig. 1.3, the phase transition is represented in the plane of temperature as a function of the relative nuclear density. In the figure, the region above the deconfinement band is the quark-gluon plasma. According to the Big Bang theory [2], the state of the Universe a few tenths of μs after the the Big Bang was actually a quark-gluon plasma (high temperature and low density in the diagram). The same state of matter is now probably present in the very dense core of neutron stars [3], which can be situated in the bottom right region of the phase diagram.

The goal of ultra-relativistic heavy-ion collisions is to create the quark-gluon plasma in the laboratory moving to high temperature and vanishing baryon density in the phase diagram. The energy density and the temperature reached in the interaction region (*fireball*) right after the collision are high enough to allow for a phase transition to the QGP. The size of the QGP is expected to be of the order of a few fm and the life-time of the order of a few fm/c. Since 20 years physicists have been building more and more powerful accelerators aimed at reproducing the QGP: AGS, SPS, RHIC, and LHC.

Developing a quantitative understanding of the phase transition has proven to be a challenging task. QCD calculations are possible only in the perturbative regime (pQCD), when the energy exchange is high and the coupling constant is small. Going to softer

interactions and larger distance, a description via pQCD is not possible. Simple phenomenological models based on QCD are able to describe some aspects. For instance the "M.I.T. Bag Model" [4] is a simple model considering an external pressure that keeps the quarks confined in the hadron and allow them to be free inside the *bag*. Numerical calculations in a discrete grid of space-time coordinates (*lattice*) allow to reproduce pQCD calculation and some non-perturbative processes. The limitation of the so-called *lattice QCD* is the computational power needed and the finite step of the lattice. So far most calculations do not include a finite baryo-chemical potential, i.e. assume baryonic density equal zero.

At RHIC, the energy density of the QGP was measured according to the Bjorken formula [5]:

$$\epsilon_{\mathrm{Bj}} = \frac{\mathrm{d}E_{\perp}}{\mathrm{d}y}\frac{1}{S_{\perp}\tau}, \tag{1.2}$$

where $E_{\perp}$ is the total energy in the plane perpendicular to the beam direction (transverse energy), y is the rapidity, defined as $\frac{1}{2}\ln\left(\frac{E+p_z}{E-p_z}\right)$, where E is the energy and p_z the momentum in the beam direction, $S_{\perp}$ is the transverse overlap area of the colliding nuclei and τ the formation time of the QGP. The transverse energy is approximated by the charged-particle rapidity distribution and the transverse overlap area is extracted from the measured multiplicity using the Glauber model [6], a semi-classical model of the collision geometry which parametrizes the nucleus-nucleus interaction via incoherent superposition of the nucleons belonging to the colliding nuclei. Through the Glauber model it is possible to calculate the probability of interaction, the number of elementary nucleon-nucleon collisions (N_{coll}), the number of nucleons participating in the collision (N_{part}), the number of spectator nucleons, the overlap area.... The sketch in the left panel of Fig. 1.4 shows the geometry of a peripheral (left) and of a central (right) collision, where the participants and the spectator nucleons are visible and the impact parameter, which is the distance between the centre of the colliding nuclei in the transverse plane, is indicated by the b. In Fig. 1.4, right panel, the dependence of $\epsilon_{\mathrm{Bj}} \times \tau$, measured by STAR, versus the number of participant N_{part} (also estimated via the Glauber model) is shown for two centre of mass energies. Assuming a formation time $\tau < 1$ fm/c the energy densities reached exceed the phase transition energy density of 1 GeV/fm^3 predicted by lattice QCD [7, 8]. The actual value of τ at RHIC, however, is still under debate.

In Fig. 1.5, the lattice QCD calculation of ϵ/T^4 for 2- and 3- flavours QCD with light quarks and for 2 light plus 1 heavier (strange) quark (indicated by the central line) as a function of temperature is reported. The latter case is likely to be the closest to the physically realized quark mass spectrum. The number of flavours and the masses of the quarks constitute the main uncertainties in the determination of the critical temperature and critical energy density. The critical temperature is estimated to be $T_{\mathrm{c}} = (175 \pm 15)$ MeV and the critical energy density $\epsilon_{\mathrm{c}} \simeq (6 \pm 2)T_{\mathrm{c}}^4 \simeq (0.3$ - $1.3)$ GeV/fm^3. Most of the uncertainty on ϵ_{c} arises from the 10% uncertainty on T_{c}. Although the transition is not a first order one (which would be characterized by a discontinuity of ϵ at $T = T_{\mathrm{c}}$), a large 'jump' of $\Delta\epsilon/T_{\mathrm{c}}^4 \simeq 8$ in the energy density is observed in a temperature interval of only about 40 MeV (for the 2-flavours calculation). Considering that the energy density of an equilibrated ideal gas of particles with n_{dof} degrees of freedom is

$$\epsilon = n_{\mathrm{dof}}\frac{\pi^2}{30}T^4 \tag{1.3}$$

the dramatic increase of $\epsilon/T_{\mathrm{c}}^4$ can be interpreted as due to the change of n_{dof} from 3 in

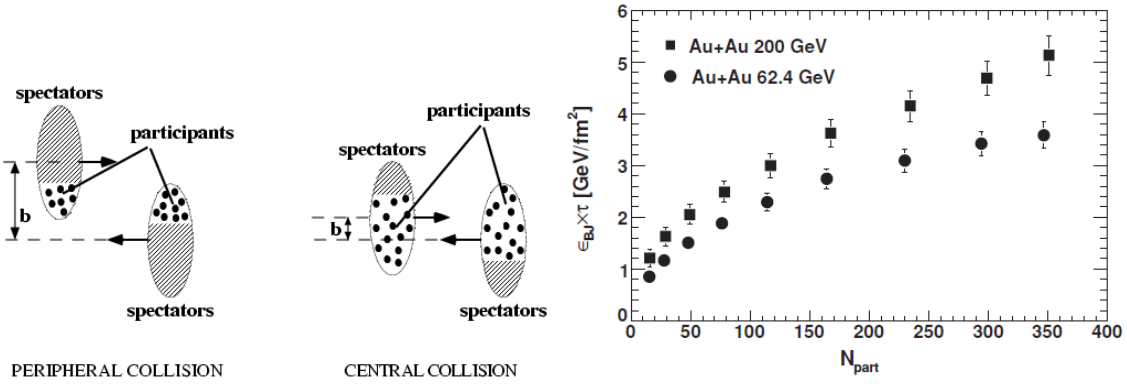

Figure 1.4: Left panel: Sketch of a nucleus-nucleus collision in the transverse plane. The participants (dots) and the spectators (shadow) are shown in central (right) and peripheral (left) collisions. Right panel: $\epsilon_{\rm Bj} \times \tau$ as a function of collision centrality ($N_{\rm part}$) by STAR and for $\sqrt{s} = 200$ (square) and 62.4 (circle) GeV. Figure taken from [9].

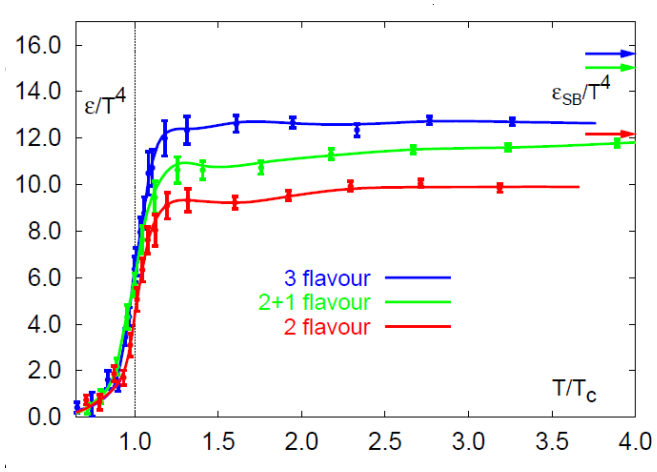

Figure 1.5: Energy density in lattice QCD with 2 (red line below) and 3 (blue line above) light quarks and with 2 light plus one heavier (green line in between) quarks. The calculation uses baryo-chemical potential $\mu_{\rm B} = 0$. From [8].

the pion gas phase to 37 (with 2 flavours) in the deconfined phase, where the additional colour and quark flavour degrees of freedom are available[2].

1.2.3 Evolution of heavy-ion collisions

The evolution of the collision is pictorially represented in Fig. 1.6: the system expands under pressure gradients and cools down. At first the most energetic interaction take place, the heavy- and high-momentum quarks are produced. The system reaches the QGP state after a pre-equilibrium phase when the medium is not yet in thermal equilibrium (*"thermalized"*). As it will be shown below, the QGP reaches the thermalization and the particles interact until the temperature is low enough to allow for the *hadronization* processes. The latter end when the *chemical freeze-out* occurs, establishing the particle

[2]In a pion gas the degrees of freedom are only the 3 values of the isospin for π^+, π^0, π^-. In a QGP with 2 quark flavours the degrees of freedom are $n_g + 7/8(n_q + n_{\bar{q}}) = N_g(8)N_{\rm pol}(2) + 7/8 \times 2 \times N_{\rm flav}(2)N_{\rm col}(3)N_{\rm spin}(2) = 37$. The factor 7/8 accounts for the difference between Bose-Einstein (gluons) and Fermi-Dirac (quarks) statistics.

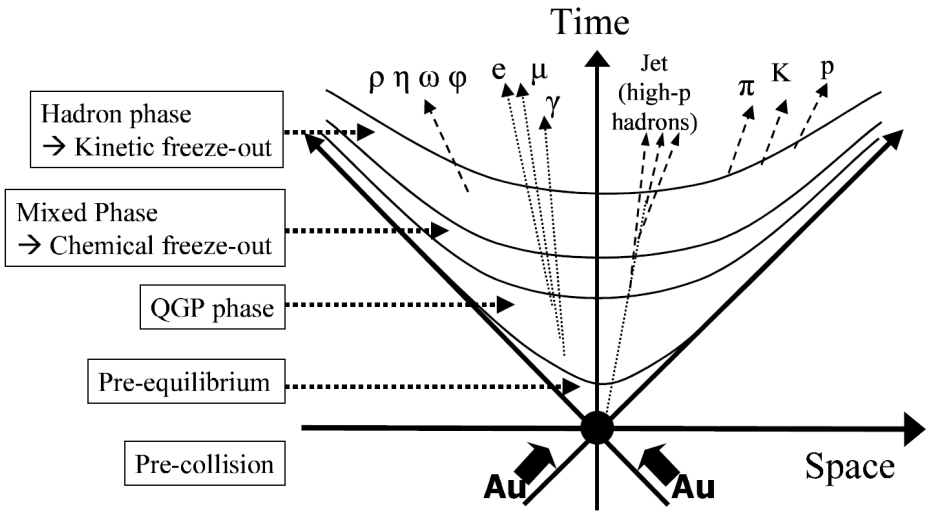

Figure 1.6: Sketch of a heavy-ion collision evolution.

abundances. The temperature of the chemical freeze-out is observed to be about 160 MeV, independent of the energy of the collision, of the centrality and of the initial QGP temperature (see left panel of Fig. 1.7). The measured value is also similar to lattice QCD calculations of the cross-over temperature between the deconfined phase and the hadronic phase. This observation can be understood considering that the freeze-out temperature is not related to kinetic processes and hadronization should be universal. The chemical freeze-out properties are measured using the particle ratios in the context of the thermal equilibrium model (see Refs. [120-123] of [9]).

After being formed, the hadrons continue to re-scatter until the elastic interactions vanish and, with the *thermal* (or *kinetic*) *freeze-out*, the momentum spectra are also essentially fixed. The particle yields are well described by the hydrodynamic-motivated blast-wave model (Refs. [120-123] of [9]). The blast-wave model makes the assumption that particles are locally thermalized at a kinetic freeze-out temperature and are moving with a common collective transverse radial flow velocity field originating from the expantion of the system. The common flow velocity results in a larger transverse momentum of heavier particles. The simultaneous fit of six particle spectra ($\pi^{\pm}$, $K^{\pm}$, p and $\bar{p}$) allows to determine, among others, the kinetic freeze-out temperature and the average transverse velocity $\langle\beta\rangle$. Both the freeze-out temperatures (chemical and kinetic), measured by STAR, are shown in Fig. 1.7, left panel, as a function of the charged particle multiplicity per unit of rapidity [9]. In the right panel, the average radial flow velocity $\langle\beta\rangle$ is also shown. Note that the average thermal freeze-out temperature is very similar to the chemical freeze-out temperature and it decreases going to central Au-Au collision. The corresponding $\langle\beta\rangle$ increases starting from the same centrality, suggesting that a higher initial energy density results in a larger expansion rate and longer expansion time, yielding larger flow velocity and lower kinetic freeze-out temperature.

Finally the unstable particles decay and their products are measured by the detectors.

In Section 1.2.4 the treatment of the QGP via hydrodynamical models, possible if it thermalizes, will be discussed. In Section 1.2.5 some particular observables which can help in decoding the information about the QGP phase brought by the final state particles will be discussed.

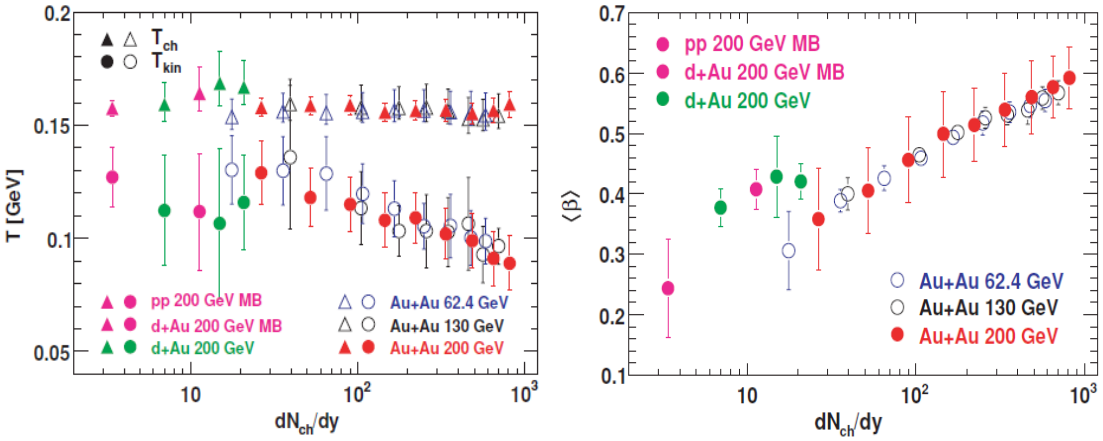

Figure 1.7: Left panel: chemical (triangle) and kinetic (circle) freeze-out temperature measured by STAR at different energies as a function of charged multiplicity. Right panel: Radial flow velocity for different systems and energies as a function of the charged-hadron multiplicity, measured by STAR. Figures from [9].

1.2.4 Hydrodynamical treatment of the QGP

The treatment of the QGP via hydrodynamic equations is possible under the assumption that the particles formed in the primary collisions would re-scatter often enough to reach local thermal equilibrium and behave as a fluid, not as independent particles. If such a state is reached, the particles observed in the final state should show a collective behaviour such as *flow*. The applicability of the hydrodynamics was far from being certain until the measurement of flow performed at RHIC, described in detail in Section 1.2.5, showed that, at least for low transverse momentum ($p_t \leq 1.5$ GeV/c) and collisions with impact parameter below 7 fm, hydrodynamics reproduces the data properly.

If local thermal equilibrium is reached, the system can be characterised by the fields of temperature ($T(x)$), chemical potentials associated with conserved charges ($\mu_i(x)$), and flow velocity ($u^\mu(x)$). The evolution of these fields is then determined by the hydrodynamical equations of motion until the system is so dilute that the assumption of local thermal equilibrium breaks down and the particles begin to behave as free. Hydrodynamical models have the advantage of being relatively simple and essentially do not need any other information other than the equilibrium equation of state to solve the equations of motion. Once the equation of state and the initial conditions are defined, the expansion dynamics is determined and there is no need to know the details of the interaction at the microscopic level. This is especially practical when studying the transition from hadronic to partonic degrees of freedom, which is largely unknown. On the other hand, the disadvantages are the assumptions to be fulfilled, that is a local kinetic and chemical equilibrium and the lack of dissipative phenomena, like viscosity.

There is no proper proof of thermalization in heavy ion collisions. The reach of thermal equilibrium can be deduced by comparing the collision rate σ of secondary particles (from pQCD for instance) with the lifetime of the system (estimated from hydrodynamics). If the mean free path, $\lambda = 1/(n\sigma)$, where n is the parton density, is much smaller than the system size, the system has a chance to thermalize. Another way to argue for thermalization is to refer to the measurements of particle azimuthal anisotropies (like the *elliptic flow*, defined in Section 1.2.5) which can be reproduced by a hydrodynamical model. The lack of dissipation, hence the assumption of "perfect fluid"

may be valid or not, but the viscosity, if present, is anyway very small. Recent works introduce a non-zero shear viscosity to the hydrodynamic models [10].

The equations of motion of relativistic fluid dynamics are obtained from local conservation of the energy-momentum tensor $T^{\mu\nu}$ and of currents, j_i^μ, $i = 1, \ldots, n$, corresponding to conserved charges:

$$\partial_\mu T^{\mu\nu} = 0 \qquad \text{and} \qquad \partial_\mu j_i^\mu = 0. \tag{1.4}$$

Without any additional constraints these $4 + n$ equations contain $10 + 4n$ unknown variables, where n is the number of conserved charges. The simplest and most commonly used approach is the *ideal fluid approximation*, which reduces the number of unknown variables to $5 + n$. In this approximation the energy-momentum tensor and the currents have the forms:

$$T^{\mu\nu} = (\epsilon + p)u^\mu u^\nu - pg^{\mu\nu} \tag{1.5}$$

$$j_i^\mu = n_i u^\mu, \tag{1.6}$$

where ϵ, p, and n_i are energy density, pressure, and number density of the charge i in the local rest frame of the fluid, and u^μ is the flow four-velocity of the fluid. The equation needed to close the system is the equilibrium equation of state (EoS) of the matter, which connects the pressure and the densities: $P = P(\epsilon, n_1, \ldots, n_n)$.

Another possible approximation is the *Bjorken model* where the longitudinal flow is assumed to scale like $v_z = z/t$, where z is the longitudinal coordinate, at all times t. This requirement leads to boost invariance of the system. The drawback of this approximation is that the results are independent on rapidity and can be discussed only in the transverse plane.

Hydrodynamical models do not apply to the very beginning of the heavy-ion collision when the equilibrium in not yet reached. The density distributions and flow velocities at the time τ_0 when the hydrodynamical description becomes applicable must be given as external input. The initial time τ_0 itself cannot be calculated, it is a free parameter measured from a fit to the data, or it can be argued from, e.g. the saturation scale in pQCD calculations. As a consequence, its value can vary in a quite large range.

The simplest method to determine the initial state was proposed by Hwa and Kajantie [11]. Since ideal fluid expansion is isentropic and entropy is directly related to the multiplicity, the final multiplicity gives also the initial entropy of the system. This approach does not tell anything about the initial density distributions and more constraints are needed to study flow.

In order to determine the initial density, different approaches are possible. One of those exploits the proportionality between the density in the transverse plane and the number of participants per unit area in the transverse plane (n_{WN}, WN stands for wounded nucleons, that is equivalent to participant nucleons). It is natural to assume that also the initial entropy density scales with the number of participants and the corresponding parametrization is called s_{WN}. If the initial energy density instead of the entropy density is the quantity that scales with the number of participants, another initialization, e_{WN}, is obtained. Going to higher collision energies, the hard collisions between incoming partons dominate particle production. In the limit each nucleus-nucleus collision contributes equally to the particle and energy production, then the number of produced particles scales with the number of binary collisions (n_{BC}). The density of produced particles defines the initial entropy density at the beginning of the hydrodynamical expansion, thus the entropy density should be proportional to the number of

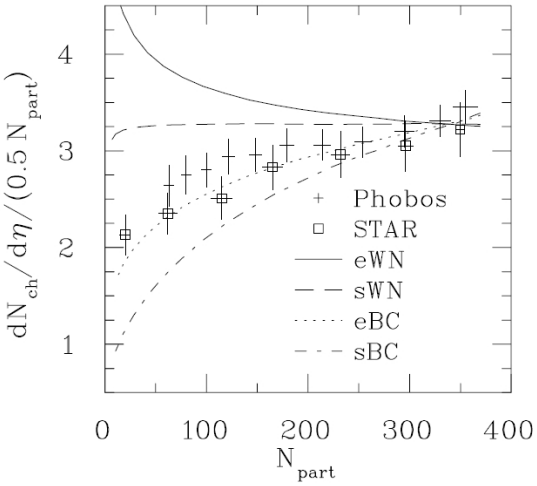

Figure 1.8: Charged particle yield per participating nucleon pair at mid-rapidity as a function of the number of participants for different initialization models discussed in the text. All curves were normalized to $\mathrm{d}N_{\mathrm{ch}}/\mathrm{d}\eta = 550$ for 5% of the most central collisions ($b = 2.3$ fm). The data are from Refs. [12, 13], the figure from [14].

binary collisions, giving the s_{BC} parametrization for initialization. If each binary collision equally contributes to the energy carried by the particles, the energy density is then proportional to the number of binary collisions and lead to the e_{BC} parametrization. The comparison with data favours the e_{BC} parametrization, but the linear behaviour of s_{WN} is also close to the data as it is shown in Fig. 1.8. An alternative approach to determine the initial state is to use some other model to calculate it, e.g. event generators or pQCD calculations.

Most of the hydrodynamical models developed for RHIC foresees a hadronic phase which is constructed as a gas of free hadrons and resonances, a plasma phase of ideal massless partons with a bag constant, and a first order phase transition between the two phases. The major difference to the equation of state obtained comes from whether the hadron phase is assumed to be in chemical equilibrium or not. As it was described before, from the chemical and kinetic freeze-out temperatures measured at RHIC, the inelastic collisions cease first and chemical freeze-out occurs at a higher temperature than kinetic freeze-out. Chemical non-equilibrium can be included in the hydrodynamical description. In this case the temperature decreases faster as the energy density decreases, hence the kinetic freeze-out temperature is reached faster.

The hydrodynamic behaviour is conventionally chosen to be applicable inside a hypersurface where the temperature (or energy density) has a fixed freeze-out value of the order of the mass of the pion, obtained from a fit to the data. Alternatively the transition between hydrodynamical description and microscopic transport model can intervene well within the region where hydrodynamics is supposed to be applicable [15, 16]. Besides giving a better description of freeze-out, such models include the separate chemical and kinetic freeze-outs. Also in this case, as with the hypersurface in the previous approach, the correct region where to perform the switch is very uncertain: usually it is chosen to happen immediately after hadronization.

The output of the hydrodynamic description must be translated into particle spectra. This is usually done via the Cooper-Frye prescription [17].

In the hydrodynamical environment, the concept of radial flow refers to the expansion with transverse velocity v_r induced by the pressure gradients between the dense centre

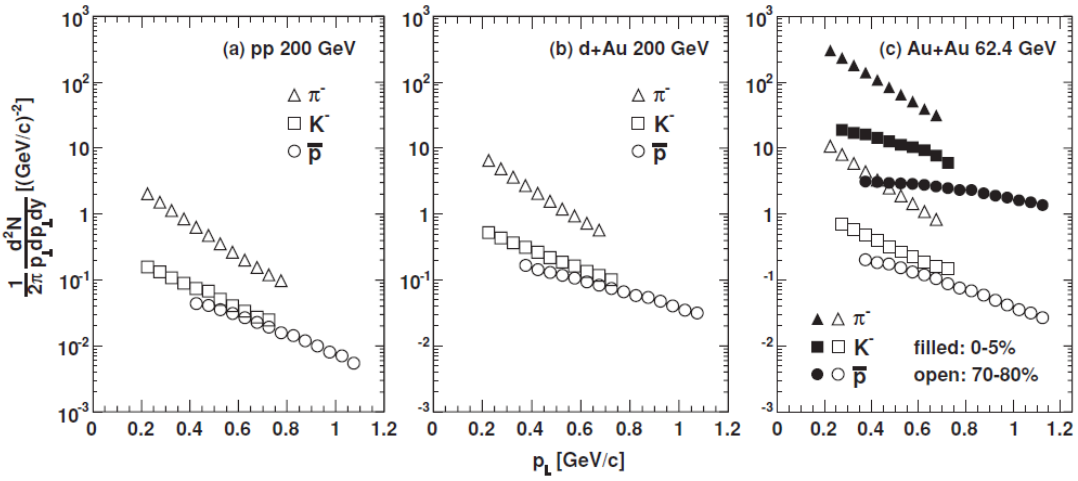

Figure 1.9: Comparison of particle spectra for pions (triangle), kaons (rectangle) and anti-protons (circle) in p+p (left), d+Au (middle) and Au+Au (right) collisions, measured by STAR. In the right figure filled symbols are for central collisions and open for peripheral. From [9].

of the system and the ambient vacuum. The equation of state is closely related to the build up of flow: the *stiffer* the EoS, the larger the flow. On the other hand, many other factors, such as the initial density and the freeze-out temperature, affect flow, therefore the p_{t} spectra constrain the EoS only weakly. According to the initial shape of the system, the transverse flow can present an azimuthal anisotropy resulting in a momentum anisotropy. A large anisotropy can be a sign of frequent re-scattering, hence of thermalization of the system. Since hydrodynamics assumes zero mean free path, thus infinite re-scattering, it also gives the upper limit to the elliptic anisotropy.

1.2.5 Observables sensitive to the QGP

Bulk particle production

If the QGP can be treated as a fluid, it can be characterised by quantities like temperature, pressure, viscosity, EoS, etc. For these observable to be meaningful, the mean free path of the particles must be much smaller than the system size.
The description in terms of hydrodynamic equations hold if the QGP thermalizes in a early time. It was already highlighted that the identified particle spectra ($\pi^{\pm}$, $\mathrm{K}^{\pm}$, p and $\bar{\mathrm{p}}$) provide many pieces of information about the evolution of the collisions and its specific properties, for instance freeze-out temperatures and collective radial flow velocity. A more extensive review is given in [9].

In Fig. 1.9 the invariant yields of $\pi^{\pm}$, $\mathrm{K}^{\pm}$, p and $\bar{\mathrm{p}}$, measured by STAR at RHIC, are shown as a function of p_{t}, for different systems. The π slope does not change with system and collision centrality, while the slope of more massive particles flattens when going to central Au-Au collisions. Hardening of the spectra is more pronounced by increasing centrality and particle mass.

Azimuthal anisotropy in particle production

The measurement of the particle production in the transverse plane can be more informative about possible asymmetry in the collective motions (*flow*) [18]. The azimuthal distribution of particles is isotropic when the mean free path is larger than the size of

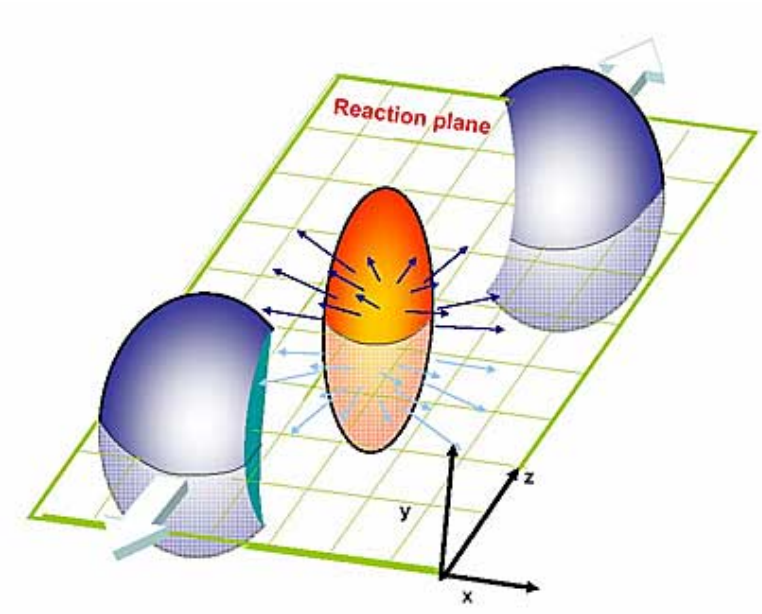

Figure 1.10: Reaction plane in nucleus-nucleus collision.

the system, otherwise the emission pattern is affected by the shape of the system. In non-central collisions, when the impact parameter is different from zero, the overlap zone is anisotropic, featuring an almond shape (see Fig. 1.10). The spatial anisotropy determines larger pressure gradients along the short axis of the "almond" with respect to the long one. This is reflected to the space of momenta leading to a preferential direction in the particle emission. The effect is self-quenching: in a short time-scale, indeed, the pressure gradients are equilibrated, but the effect on the momenta is visible in the final state azimuthal distributions. The measured anisotropy points directly to the initial QGP state, giving information about its equation of state and the sound velocity [18]. From a measurement of anisotropy it is possible to deduce whether flow originates from partonic or hadronic matter or from the hadronization processes. In particular, the observation of particles with heavy quarks genuinely probes the very first stage after the collision, when the heavy quark production takes place via partonic hard scatterings. The heavy quarks then coexist with the surrounding medium providing essential information on its properties.

A convenient way of characterizing the pattern of anisotropic flow is to use a Fourier expansion of the triple differential invariant distribution [19]:

$$E\frac{\mathrm{d}^3N}{\mathrm{d}^3p} = \frac{1}{2\pi}\frac{\mathrm{d}^2N}{p_\mathrm{t}\mathrm{d}p_\mathrm{t}\mathrm{d}y}\left(1+\sum_{n=1}^{\infty}2v_n\cos\left[n(\phi-\Psi_\mathrm{RP})\right]\right), \tag{1.7}$$

where ϕ and Ψ_RP are the particle and reaction-plane azimuths, respectively, in the laboratory frame. The reaction plane (Fig. 1.10) is defined by the beam direction and the impact parameter. The sine terms in eq. (1.7) vanish due to reflection symmetry with respect to the reaction plane. The Fourier coefficients are given by

$$v_n(p_\mathrm{t},y) = \langle\cos\left[n(\phi-\Psi_\mathrm{RP})\right]\rangle, \tag{1.8}$$

where the brackets denote an average over the particles, summed over all events, in the (p_t, y) region under study. The first two coefficients, v_1 and v_2 are known as *direct* and

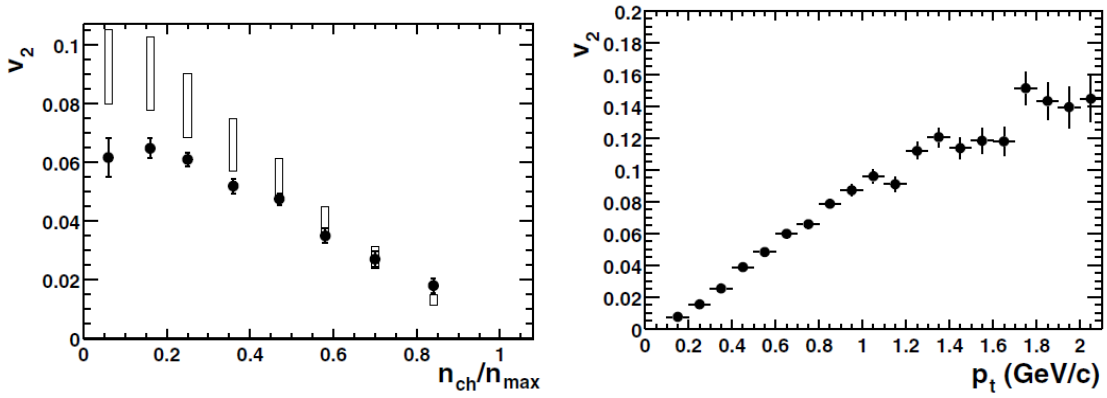

Figure 1.11: Left panel: Elliptic flow (circle) as a function of centrality expressed as $n_{\rm ch}/n_{\rm max}$, the number of tracks normalized by the maximum observed number of tracks. The open rectangles show a range of values expected for v_2 in the hydrodynamic limit, scaled from ϵ, the initial space eccentricity of the overlap region. The lower edges correspond to ϵ multiplied by 0.19 and the upper edges to ϵ multiplied by 0.25. Right panel: Elliptic flow as a function of transverse momentum for minimum bias events. Both measurements are from STAR [20].

elliptic flow, respectively. Elliptic flow has its origin in the amount of re-scattering and in the spatial eccentricity of the collision zone (Fig. 1.10). The amount of re-scattering is expected to increase with centrality, while the spatial eccentricity decreases. The spatial eccentricity is defined by

$$\epsilon = \frac{\langle y^2 - x^2 \rangle}{\langle y^2 + x^2 \rangle}, \tag{1.9}$$

where x and y are the spatial coordinates in the transverse plane and the brackets denote an average weighted with the initial density.

Fig. 1.11 shows the elliptic flow of charged tracks measured by STAR as a function of centrality (left), expressed as the number of tracks normalized by the maximum observed number of tracks, and as a function of $p_{\rm t}$ (right) [20]. In the left panel, the open rectangles show, for a range of possible values of the velocity of sound, the expected v_2 values from ideal hydrodynamics. For $n_{\rm ch}/n_{\rm max} \geq 0.5$ (corresponding to impact parameters ≤ 7 fm) data is well described by ideal hydrodynamics.

The observed large amount of collective flow is one of the main discoveries at RHIC and the main evidence suggesting nearly perfect fluid properties of the created matter. Consequence of the perfect fluid hydrodynamics behaviour of the QGP is that some scaling laws are expected to hold: (a) v_2 scaling should hold for a broad range of impact parameters for which the eccentricity varies, i.e. v_2/ϵ should be independent of centrality; (b) $v_2(p_{\rm t})$ should be independent of colliding system size for a given eccentricity; and (c) for different particle species, $v_2(KE_{\rm T})$ at mid-rapidity should scale with the transverse kinetic energy $KE_{\rm T} = m_{\rm T} - m$, where $m_{\rm T} = \sqrt{p_{\rm t}^2 + m^2}$ is the transverse mass of the particle.

Figure 1.12, left panel, shows the differential $v_2(p_{\rm t})$ for charged hadrons obtained in Au-Au (top) and Cu-Cu (central) collisions [21]. As expected, the resulting v_2 increases as collisions become more peripheral and the $p_{\rm t}$ increases. To test the eccentricity scaling, the v_2 results are divided by the v_2 integrated over the $p_{\rm t}$ range 0.3-2.5 GeV/c, for each centrality (bottom). The hydrodynamic model predicts that this ratio is constant with centrality and independent of colliding system because ϵ is proportional to the $p_{\rm t}$-integrated v_2 values (i.e. $\epsilon = k \times v_2$). A Glauber model estimate of ϵ (Ref. [35] of [21])

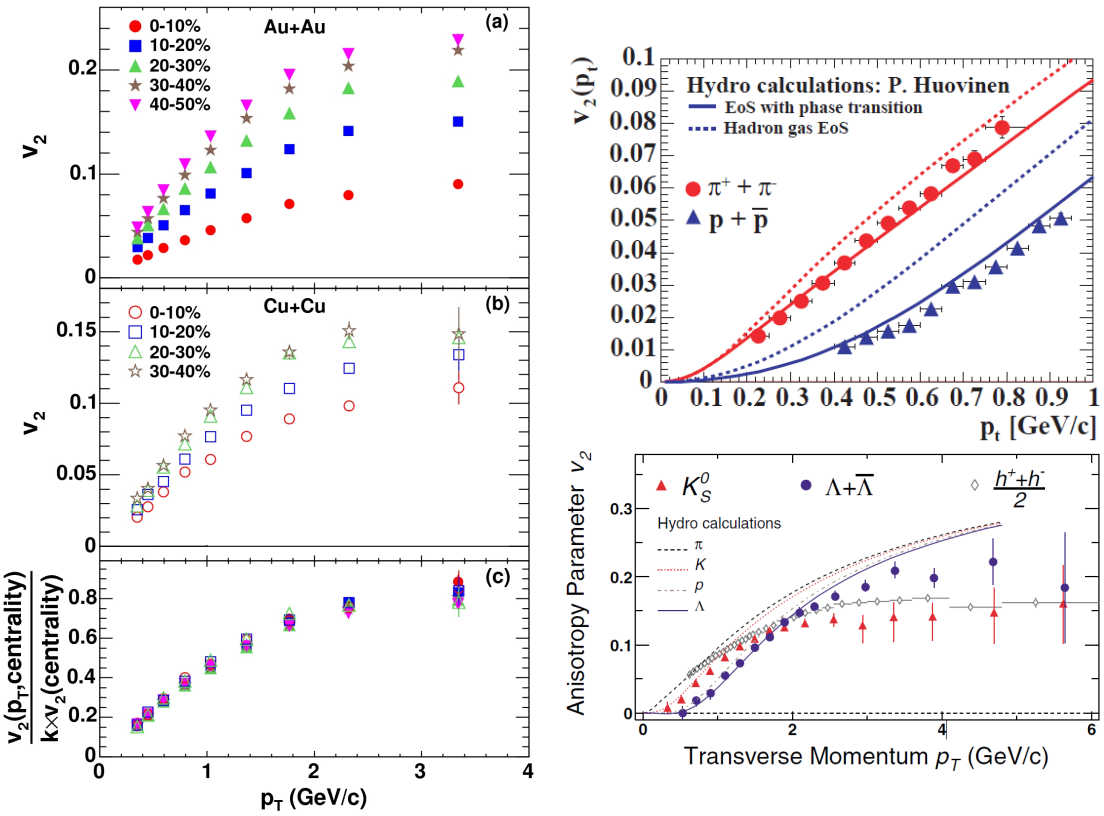

Figure 1.12: Left panel: v_2 vs. p_t for charged hadrons obtained in (a) Au+Au and (b) Cu+Cu collisions for the centralities indicated. (c) v_2(centrality, p_t) divided by $k = 3.1$ (the factor which correlate ϵ to the integrated v_2) times the p_t-integrated value v_2(centrality) for Au+Au and Cu+Cu collisions [21]. Top right panel: Elliptic flow of pions and protons as function of transverse momentum [22]. The lines are hydrodynamical model calculations using two different EoS: the dashed lines represent calculations done with a hadron gas EoS while the solid curves are calculation with an EoS which incorporates the QCD phase transition. From [23]. Bottom right panel: The minimum-bias (0-80% of the collision cross section) $v_2(p_t)$ for K^0_S, $\Lambda + \bar{\Lambda}$ and $h^{\pm}$. Hydrodynamical calculations of v_2 for pions, kaons, protons and lambdas are also drawn [24]. Results from STAR [25].

gives $k = 3.1 \pm 0.2$. These scaled values are indeed essentially independent on the system size and show perfect scaling for the full range of centralities (or ϵ) presented. The magnitude of v_2/ϵ depends on the sound speed c_s. Under reasonable approximations, for $b = 8$ fm and a constant speed of sound, it results that $c_s \sim 0.35 \pm 0.05$ (cf. [21] and references therein). This value suggests an effective EoS which is softer than that for the high temperature QGP but does not reflect a strong first order phase transition in which $c_s = 0$ during an extended hadronization period.

Fig. 1.12, right panel, shows v_2 for identified particles as a function of transverse momentum. At low p_t (top panel) the elliptic flow depends on the mass of the particle with v_2 at fixed p_t decreasing with increasing mass. This dependence is expected in a scenario where all particles have a common radial flow velocity as shown from the curves for ideal hydrodynamics. The difference between the dashed and solid curves is the EoS: the dashed correspond to calculations done with hadron resonance gas EoS, while the solid curves are hydro calculations incorporating the QCD phase. It is clear that the latter describe better the observed mass splitting.

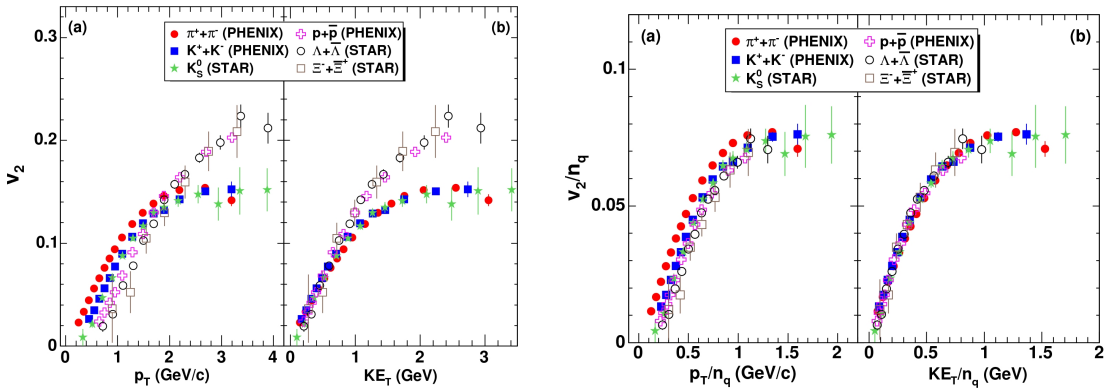

Figure 1.13: Left panel: (a) v_2 vs $p_{\rm t}$ and (b) v_2 vs $KE_{\rm T}$ for identified particle species obtained in minimum bias Au+Au collisions. Right panel: (a) v_2/n_q vs $p_{\rm t}/n_q$ and (b) v_2/n_q vs $KE_{\rm T}/n_q$ for identified particle species obtained in minimum bias Au+Au collisions. Figures taken from [21] and Refs. therein.

At high $p_{\rm t}$ the measured v_2 starts to deviate significantly from hydrodynamics for all particle species, as shown in Fig. 1.12, bottom right panel. The heavier baryon v_2 is larger than the lighter meson v_2, contrary to the mass ordering at low $p_{\rm t}$ and to the hydrodynamic behaviour in the whole $p_{\rm t}$ range. This effect can be explained by the coalescence picture [26, 27]. Before investigating further the mass ordering breaking, it is worth to note that if the v_2 scaling at low-$p_{\rm t}$ is driven by a hydrodynamic pressure gradient, the prediction is that the differential v_2 values observed for each particle species should scale with $KE_{\rm T}$. In Fig. 1.13, left panel, v_2 is shown as a function of both $p_{\rm t}$ (a) and $KE_{\rm T}$ (b). At $p_{\rm t} \lesssim 2$ GeV/c, a mass ordering is clear as a function of $p_{\rm t}$, while all the particle species scale to a common elliptic flow as a function of $KE_{\rm T}$, for $KE_{\rm T} \lesssim 1$ GeV. The pressure gradient that drives elliptic flow is directly linked to the collective kinetic energy of the emitted particles. For higher values of $p_{\rm t}$ ($p_{\rm t} \sim 2$ - 4 GeV/c), mass ordering is broken and v_2 is more strongly dependent on the quark composition of the particles than on their mass. Indeed, for $KE_{\rm T} \gtrsim 1$ GeV, a clear splitting into a meson branch (lower v_2) and a baryon branch (higher v_2) rises, as a function of $KE_{\rm T}$. Fig. 1.13, right panel shows the results obtained after quark number scaling of the v_2 values shown in the left panel, that is, v_2, $p_{\rm t}$, and $KE_{\rm T}$ are divided by the number of the constituent quarks ($n_q = 2$ for mesons and $n_q = 3$ for baryons). This can be interpreted as an indication of the quark-like degrees of freedom in the flowing matter. These degrees of freedom are gradually revealed as $KE_{\rm T}$ increases above ~ 1 GeV and are apparently hidden by the strong hydrodynamic mass scaling, which predominates at low $KE_{\rm T}$. The fact that v_2/n_q shows such good scaling over the entire range of $KE_{\rm T}/n_q$ and does not for $p_{\rm t}/n_q$, serves to highlight the fact that hydrodynamic mass scaling is preserved over the domain of the linear increase in $KE_{\rm T}$. Fig. 1.13, right panel (b) should serve to distinguish between different quark coalescence models.

Using the models that successfully describe RHIC data, predictions for LHC were made. In Fig. 1.14 different predictions for v_2/ϵ as a function of $\sqrt{s}$ assuming a Color Glass Condensate (CGC) estimate for the initial condition, are shown. In squared markers the calculation evolves with hydro behaviour of flow up to a kinetic freeze-out temperature of 100 MeV. More realistic estimates are obtained by assuming hydrodynamics up to the chemical freeze-out temperature of 169 MeV followed by hadron cascade description of the final phase (circle). The contribution from the QGP phase is shown by trian-

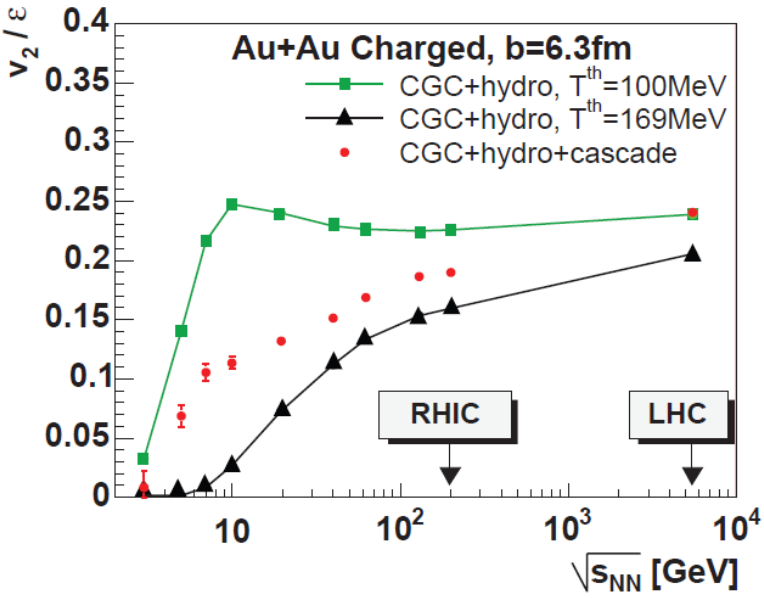

Figure 1.14: Theoretical predictions of v_2/ϵ versus collision energy using color glass condensate estimates for the initial conditions. Ideal hydrodynamic expansion up to kinetic freeze-out (squares) or up to chemical freeze-out (triangles) is assumed. The full circles are results using a hadronic cascade model to describe the final phase after chemical freeze-out. Figure from [23].

gles in the figure, leading to a much larger contribution at LHC with respect to RHIC. Theoretical calculation as that shown in Fig. 1.14 or [28], as well as straight-forward extrapolations from lower energies based on particle multiplicities, predict maximum flow values of about 5-10% at the LHC.

The previous hydro estimates assume zero shear viscosity during the QGP phase. Even a small shear viscosity has a large effect on v_2 [29], hence viscous correction have been implemented into hydro models [30].
Another strategy used in order to understand the deviation from the ideal hydrodynamics, is to describe the evolution of the system in its different phases. For instance a hybrid model [31] consisting in: an early QGP stage, including its hadronization, described by full three-dimensional ideal hydrodynamics [32] followed (at $T \sim 169$ MeV) by a dilute hadronic re-scattering stage, described by a cascade model (JAM [33]). A large fraction of the deviation from ideal hydrodynamics is due to late viscosity caused by dissipative effects.

The measurement of the particle azimuthal distributions will be treated again later, being a topic of this thesis.

Other observables probing the QGP properties include the predicted enhancement of multi-strange particles, the J/ψ suppression and regeneration, the softening of high-p_t particle spectrum, and the jet quenching.

Strangeness enhancement

The mass of the hadrons is only partly due to the mass of the constituent valence quarks. Näively speaking, the quarks "dress up" due to the strong interaction that keeps them confined. Once they are free, as in a QGP, the quarks recover their bare masses. It was predicted that, if the QGP is formed, an enhancement of the strange quarks should occur [34], because the production of $s\bar{s}$ pairs becomes easier due to the lower energy

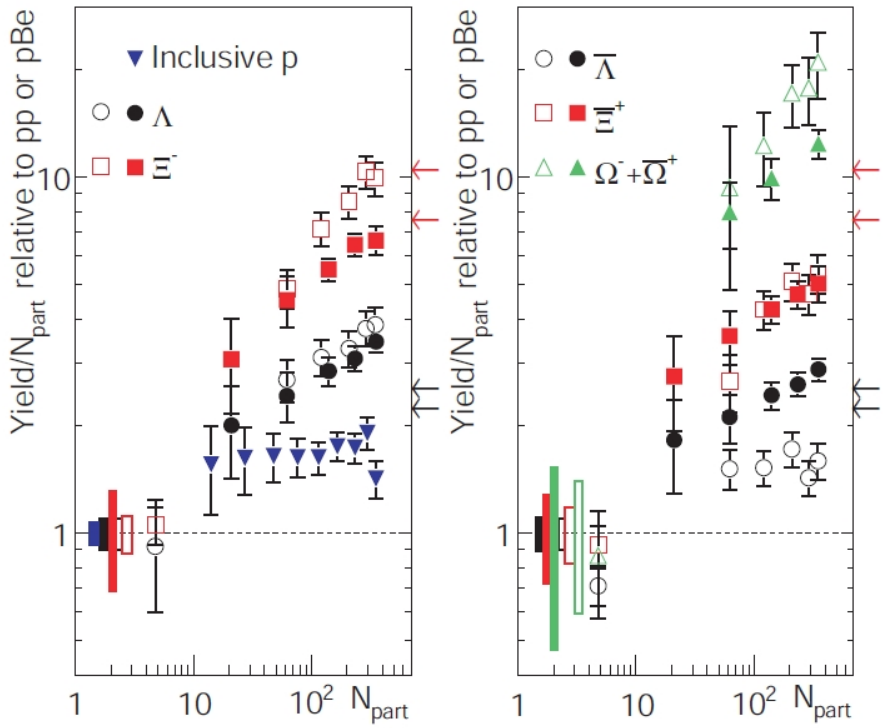

Figure 1.15: Observed multi-strange baryon (for Λ, $\bar{\Lambda}$ $|y| < 1$, Ξ^-, $\bar{\Xi}^+$, Ω^-, $\bar{\Omega}^+$ $|y| < 0.75$) yields per participant nucleon, normalized to the ratio measured in p-p or p-Be collision as a function of the number of participants. The inclusive proton data ($|y| < 0.5$) illustrate the effects for non-strange baryons. The arrows are the expected yields for Λ and Ξ. Data are from NA57 experiment at SPS [36] (open) and STAR experiment at RHIC [37] (closed).

needed. When the QGP cools down, eventually these strange quarks recombine into hadrons favouring also an enhancement of strange hadrons. This effect is larger for hadrons with higher strangeness, with the following scaling for the number N of each type: $N(\Omega^-) > N(\Xi^-) > N(\Lambda)$ [35]. A certain enhancement of strange hadrons can occur also in a hadron gas system, but the processes of hadronization in this case are relatively easy for K and Λ and progressively harder for hadrons with higher strangeness content, hence the relation would be in the opposite direction: $N(\Omega^-) < N(\Xi^-) < N(\Lambda)$. The production of multi-strange hadrons with respect to pp-like collisions is a signature of the QGP and it was observed at SPS and RHIC (Fig. 1.15).

Charmonium production in the medium

In 1986, Matsui and Satz [38] predicted that in a colourful medium the $c\bar{c}$ and $b\bar{b}$ bound states, known as quarkonia, should be suppressed with respect to the production in the vacuum. This because the colour field in the QGP behaves like a screen for the colour-charged quarks. At a critical distance, the strength of the interaction becomes too weak to create a bound state. This effect was already known in the case of electromagnetic interaction under the name of Debye screening. The critical distance is called Debye radius. The different charmonium states, i.e. J/ψ, $\psi(2S)$, χ_c, etc., have a characteristic radius, the J/ψ being the most bound and the χ_c the least (see Fig. 1.16, top left panel). The measurement of the in-medium dissociation probability of the different quarkonia states is expected to provide an estimate of the initial temperature of the system: the hotter the medium the fewer the quarkonia states that can survive. At the SPS, the

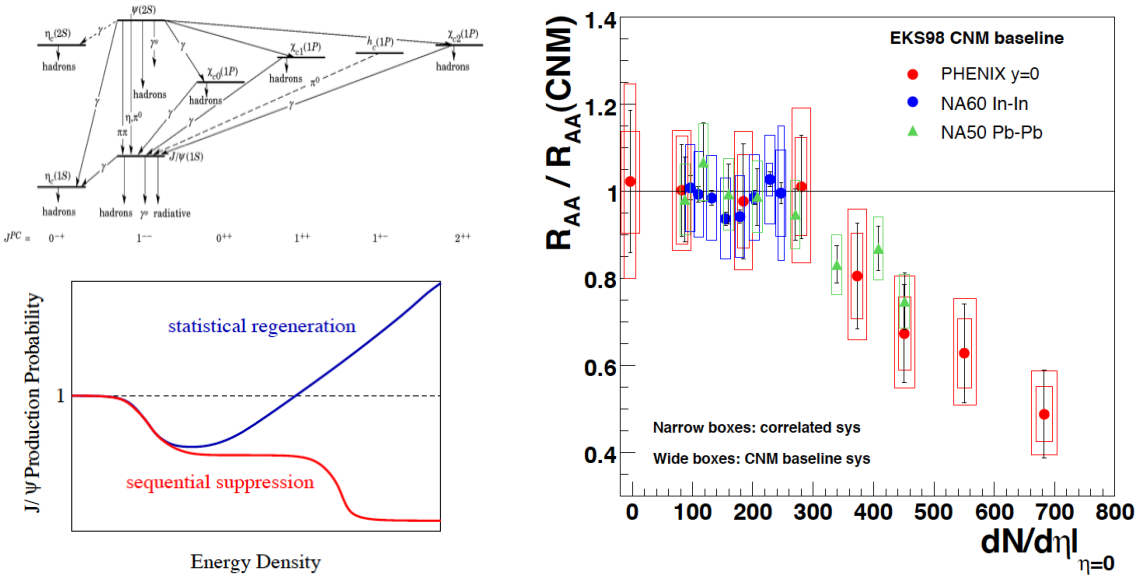

Figure 1.16: Top left: J/ψ feed-down schema. Bottom left: possible behaviour in the scenarios of statistical regeneration (blue) and sequential suppression of the charmonia states (red) as a function of the energy density. Right: J/ψ suppression as a function of centrality measured by SPS and RHIC experiments [39, 40]. The Cold Nuclear Matter (CNM) effects are subtracted. The $R_{\rm AA}$ is defined in Eq. (1.10).

number of J/ψ measured at forward rapidity was suppressed more than as expected from nuclear absorption. At RHIC, the näive extrapolation was that, given the higher energy and the hottest and longer-lived QGP, no surviving J/ψ were expected. The measurement did not confirm this hypothesis: the suppression at mid-rapidity was found to be at the same level as at SPS, as it is shown in Fig. 1.16, right panel, while a larger suppression was observed at forward rapidity.

The dissociation of the higher resonances only, like χ_c and $\psi(2S)$, is one possible interpretation of the observed suppression. RHIC data allow for a partial thermal recombination of primordially produced c and $\bar{c}$ quarks at the hadronization transition [41] competing with the dissociation in the QGP. The role of LHC is crucial to disentangle between the two hypotheses, which are qualitatively visualized in Fig. 1.16, bottom left panel. At the LHC, ten times more charm pairs are produced with respect to RHIC and the temperature of the QGP should be high enough to melt primary J/ψ. If recombination is the dominant effect, an enhancement of J/ψ should be observed, in the other case the suppression should exceed both SPS and RHIC measurements.

Energy loss

High $p_{\rm t}$ hadrons are sensitive probes of the QGP, since they are produced by hard scattering at the very beginning of the collision and, in their travel all along the matter, they strongly interact with the partons, losing energy (Section 1.3.3). The global effect is a softening of the hadron $p_{\rm t}$ spectrum. The *nuclear modification factor* ($R_{\rm AA}$) is the observable that quantifies the suppression versus $p_{\rm t}$, y, or centrality:

$$R_{\rm AA} = \frac{{\rm d}^2N^{\rm AA}/{\rm d}p_{\rm t}{\rm d}\eta}{\langle N_{\rm coll}\rangle\, {\rm d}^2N^{\rm pp}/{\rm d}p_{\rm t}{\rm d}\eta} \tag{1.10}$$

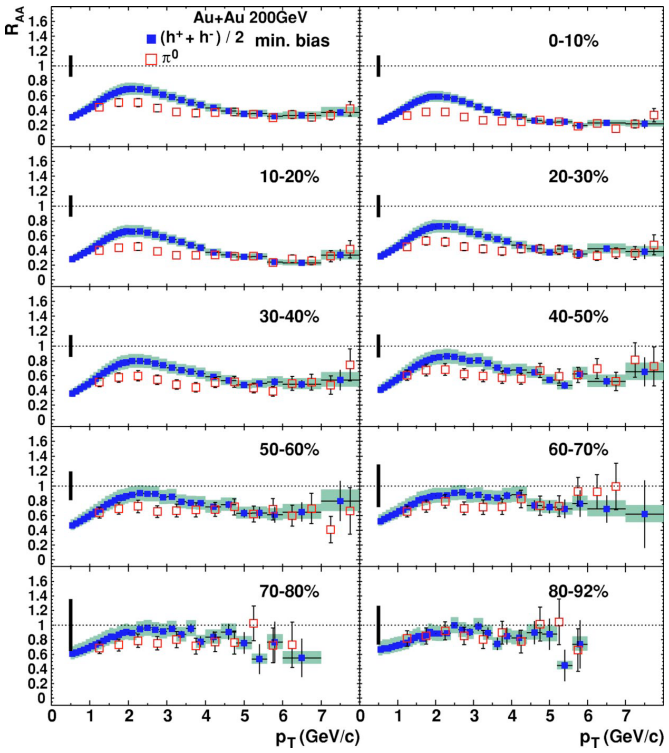

Figure 1.17: Nuclear modification factor for charged hadrons ($\frac{h^+ + h^-}{2}$) and π^0 as a function of $p_{\rm t}$ measured by PHENIX. From top left to bottom right: minimum bias and bins of 10% centrality, apart from the last one (80-92%). From [42].

$R_{\rm AA}$ is defined as the differential spectrum (with respect to $p_{\rm t}$ and rapidity) in nucleus-nucleus (A-A) collisions divided by the differential spectrum in pp collisions normalized by the number of binary collisions ($\langle N_{\rm coll} \rangle$) expected to happen between colliding nucleons. If there is no effect with respect to a superposition of p-p collisions (binary scaling), $R_{\rm AA} = 1$. Any deviation from unity spots a specific behaviour of A-A collisions either due to the QGP or to the presence of the nuclei themselves (cold nuclear matter effects). The latter can be assessed using p-A collisions. At RHIC, $R_{\rm AA}$ for different particle species was measured. A suppression of a factor 5 is observed for charged particles at $p_{\rm t} > 5$ GeV/c in 0-10% central collisions, as shown in Fig. 1.17. The nuclear modification factor of identified hadrons can spot effects related to the mass of the quarks involved. In Section 1.3.5 the case of the charm quark will be treated in detail, because related to the measurement of heavy-flavour flow.

Another interesting observable carrying information on the energy loss in the medium is the jet quenching (see Fig. 1.18, left panel): the hadronization of a pair of high-$p_{\rm t}$ quarks located in the peripheral region of the fireball produces a pair of nearly back-to-back jets of particles. One of the jets escapes the medium without suffering any energy loss. The another has a long path through the medium, where it suffers a conspicuous energy loss. By triggering on a high-$p_{\rm t}$ hadron its partner is expected in a region of $\phi \sim \pi$ radians away. Due to the energy loss experienced within the medium, the away side distribution is expected to be suppressed with respect to pp and p-A collisions. This was observed at RHIC [43] and it is shown in Fig. 1.18, right panel.

1.2.6 pp and p-A references

From the previous discussion, it emerges that a reference for the measurements in A-A collisions is fundamental. The reference, in fact, represents the "normal" behaviour when no QGP is expected, but should also take into account those effects which have the same

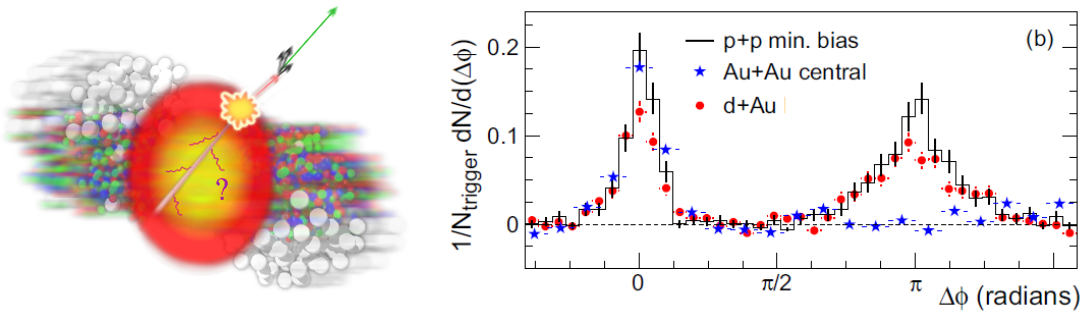

Figure 1.18: Left panel: sketch of a pair of quarks produced at the border of the fireball in heavy-ion collisions. The high-p_t hadrons produced towards the outside travel freely, while the opposite side hadrons are absorbed in the medium. Right panel: Distribution of the difference of the azimuthal angle of a trigger high-p_t particle and of the corresponding particle in the away side for pp (solid black), d+Au (red circle) and Au+Au (blue star) collisions. Measured by STAR [43].

signature as the QGP, but are actually due to other sources and must be subtracted. For RHIC and LHC the comparison with p-A collisions is the most recommendable since it allows to take into account the cold nuclear matter effects. For the $J/\psi \to \mu^+\mu^-$ measurement at SPS, the Drell-Yan yield was taken as the denominator of the $R_{\rm AA}$. At RHIC d-Au collisions were used, with deuteron instead of proton for technical reasons only and with no impact on the result. At LHC, p-Pb collisions are planned for 2012. The measurements which require to estimate the CNM effects, e.g. J/ψ suppression and $R_{\rm AA}$, cannot yet be compared to pA data. This implies that the interpretation of the results must be more careful and in certain situations is not conclusive.

1.3 Role of heavy flavours in proton and heavy ion collisions

This section is devoted to heavy-flavour physics and it is meant as an introduction to the physics involved in the measurements that will be described in Chapters 4 and 5.

As already mentioned, heavy-quarks are produced during the hard scatterings happening at the very beginning of the collision. Due to their large mass, it is very unlikely that they can be produced later, when the momentum exchange in the interactions is small. Heavy-quarks are "spectators" of all the evolution of the collision: they interact with the partons in the quark-gluon plasma and finally hadronize. The measurement of mesons and baryons with heavy-flavour content brings precious pieces of information on the primordial state of matter.

A detailed treatment of the physics of hadron and jet production at high p_t and their interaction in a hot QCD matter can be found e.g. in [44] and references therein. Some highlights useful for the scope of this thesis are reported here.

1.3.1 Production cross section calculation: factorization theorem

Because of asymptotic freedom, the QCD coupling constant α_s is small for high-energy (short distance) parton interactions. The inclusive production of a high-p_t parton c, in a *parton-parton* collision $a + b \to c + X$ can be calculated using perturbative theory techniques. In high-energy *hadron-hadron* collisions the production of high-p_t particles can be computed from the underlying *parton-parton* processes using the QCD "factorization

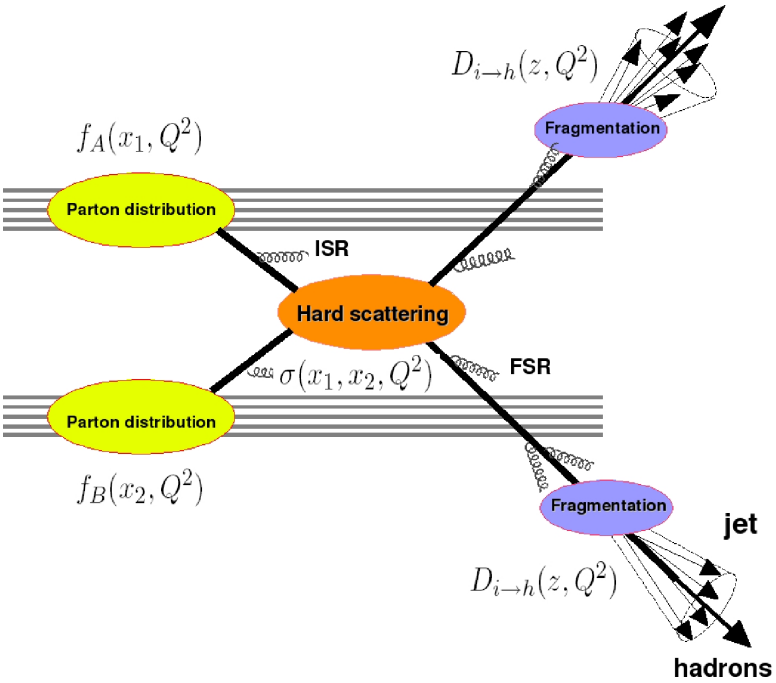

Figure 1.19: Sketch of dijet production and pQCD collinear factorization in hadronic collisions: ISR (FSR) represents the initial(final)-state radiation. Refer to Eq. (1.11) and to the text for the different terms. Picture from [44].

theorem" (see Fig. 1.19). Let be $a, b = q, \bar{q}, g$, the hadron-hadron cross section is:

$$\mathrm{d}\sigma^{\mathrm{hard}}_{AB\to h} = \sum_{a,b} f_{a/A}(x_1,Q^2) \otimes f_{b/B}(x_2,Q^2) \otimes \mathrm{d}\hat{\sigma}^{\mathrm{hard}}_{ab\to c}(x_1,x_2,Q^2) \otimes D_{c\to h}(z,Q^2) \quad (1.11)$$

where $\mathrm{d}\hat{\sigma}^{\mathrm{hard}}_{ab\to c}(x_1,x_2,Q^2)$ is the perturbative partonic cross section computable up to a given order in α_{s} and the two non-perturbative terms $f_{a/A}(x_1,Q^2)$ and $D_{c\to h}(z,Q^2)$ are universal, i.e. can be determined experimentally for instance in deep inelastic scattering $e^{\pm}$-nucleus and e^+e^- collisions, respectively and used in hadron collisions. They are:

- $f_{a/A}(x_1,Q^2)$: the parton distribution functions (PDFs), encoding the probability of finding a parton of species a and momentum fraction $x = p_{\mathrm{parton}}/p_{\mathrm{nucleon}}$ inside the hadron A;
- $D_{c\to h}(z,Q^2)$: the fragmentation function (FF), describing the probability that the outgoing parton c fragments into a final hadron h with fractional momentum $z = p_{\mathrm{hadron}}/p_{\mathrm{parton}}$.

The assumption underlying factorization is that the characteristic time of the parton-parton interaction is much shorter than any long-distance interaction occurring before (among partons belonging to the same PDF) or after (during the evolution of the struck partons into their hadronic final state). An incoherent sum of scatterings occurs among partons, hence the nucleus can be treated as a collection of free partons. Under this assumption $f_{a/A}(x_1,Q^2) \approx A \cdot f_{a/p}(x_1,Q^2)$. Thus:

$$\mathrm{d}\sigma^{\mathrm{hard}}_{AB\to h} \approx A \cdot B \cdot \sum_{a,b} f_{a/p}(x_1,Q^2) \otimes f_{b/p}(x_2,Q^2) \otimes \mathrm{d}\hat{\sigma}^{\mathrm{hard}}_{ab\to c}(x_1,x_2,Q^2) \otimes D_{c\to h}(z,Q^2). \quad (1.12)$$

In reality the PDFs are modified compared to proton PDFs by initial state (anti-)shadowing effects. Eq. (1.11) implies that the hard inclusive cross sections in a $A \leftrightarrow B$ reaction scale simply as $A \cdot B$ times the corresponding pp cross sections:

$$\mathrm{d}\sigma_{AB}^{\mathrm{hard}} = A \cdot B \mathrm{d}\sigma_{\mathrm{pp}}^{\mathrm{hard}}. \tag{1.13}$$

In terms of yields, eq. (1.13) becomes:

$$\mathrm{d}N_{AB}^{\mathrm{hard}}(b) = \langle T_{AB}(b) \rangle \cdot \mathrm{d}\sigma_{\mathrm{pp}}^{\mathrm{hard}} \tag{1.14}$$

$$\text{or} \quad N_{AB}^{\mathrm{hard}}(b) = \langle N_{\mathrm{coll}}(b) \rangle \cdot \mathrm{d}N_{\mathrm{pp}}^{\mathrm{hard}} \text{ using } N_{\mathrm{coll}} = T_{AB}(b) \cdot \sigma_{\mathrm{NN}}^{\mathrm{inel}}, \tag{1.15}$$

This scaling is often known as "binary collision scaling". $T_{AB}(b)$ is the nuclear overlap function at the impact parameter b. It is determined within a geometric Glauber model from the measured Wood-Saxon distribution for the interacting nuclei. Intuitively, it is a function that characterise the surface profile of two "beams" of nucleons colliding with an impact parameter b. The units of $[\mathrm{area}]^{-1}$ indicate that it represents somehow the effective "parton integrated luminosity".

The standard method to quantify the effects of the medium on the yield of an hard probe in AA reactions is given by the already mentioned (eq. (1.10)) *nuclear modification factor*, that can be written also with an equivalent definition using the pp cross section and the nuclear overlap function:

$$R_{\mathrm{AA}}(p_{\mathrm{t}}, y; b) = \frac{\mathrm{d}^2 N^{\mathrm{AA}}/\mathrm{d}y\mathrm{d}p_{\mathrm{t}}}{\langle T_{\mathrm{AA}}(b) \rangle \times \mathrm{d}^2\sigma^{\mathrm{pp}}/\mathrm{d}y\mathrm{d}p_{\mathrm{t}}}. \tag{1.16}$$

This factor measures the deviation of AA collisions at impact parameter b from an incoherent superposition of nucleus-nucleus collisions (identified by $R_{\mathrm{AA}} = 1$).

1.3.2 Heavy flavour cross section calculations

The charm and beauty cross section can be calculated in pQCD by summing Feynman diagrams at the Fixed Order Next to Leading Log (FONLL [45]) level. These calculations exploit the fact that the mass of the heavy quark acts as an infrared cutoff on collinear singularities, and thus the cross section has a power expansion in the strong coupling constant, evaluated at a renormalization scale (μ_{R}) near the heavy-quark mass m. This approach is appropriate when the heavy-quark mass is the only relevant mass scale of the problem and it is bound to fail when the transverse momentum (p_{t}) of the heavy quark is much larger than its mass. In fact, in this case, one cannot pinpoint a single characteristic scale in the problem, since all momenta between m and p_{t} are equally involved. It turns out that large logarithms of the ratio p_{t}/m arise to all orders in the perturbative expansion, and spoil its convergence. In the FONLL calculation this logarithms are resummed at next-to-leading order.

In Fig. 1.20 the cross section for primary and secondary D^0 from B decay calculated with FONLL is shown. Systematic uncertainty limits are calculated by taking a range of possible values of the charm (beauty) quark mass. The factorization and renormalization scales, μ_F and μ_{R}, are varied independently in the ranges $0.5 < \mu_{\mathrm{F}}/m_{\mathrm{T}} < 2$, $0.5 < \mu_R/m_{\mathrm{T}} < 2$, with the constraint $0.5 < \mu_{\mathrm{F}}/\mu_{\mathrm{R}} < 2$, where $m_{\mathrm{T}} = \sqrt{p_{\mathrm{t}}^2 + m_c^2}$. The charm quark mass is varied in FONLL within $1.3 < m_c < 1.7$ GeV/c^2.

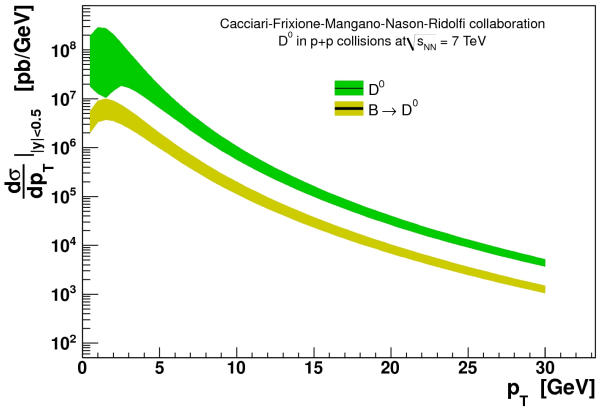

Figure 1.20: FONLL calculation of the primary and secondary D^0 cross-sections in pp collisions at 7 TeV for $|y| < 0.5$.

1.3.3 Parton energy loss in a medium

The energy lost by a particle in a medium, ΔE, provides fundamental information on the medium properties. In a general way ΔE depends both on the properties of the plasma (temperature T, particle-medium interaction coupling α, and thickness L) and on the characteristics of the particle traversing it (energy E, mass m, and charge). The following variables are extremely useful to characterise the interaction of a particle inside a medium:

- the *mean free path* $\lambda = 1/(\rho\sigma)$, where ρ is the medium density ($\rho \propto T^3$ for an ideal gas) and σ the integrated cross section of the particle-medium interaction;
- the *opacity* $N = L/\lambda$, or the average number of scatterings experienced by the particle in a medium of thickness L;
- the *Debye mass* $m_{\mathrm{D}}(T) \sim gT$ (where g is the coupling parameter) is the inverse of the screening length of the field in the plasma. m_{D} characterises the typical momentum exchange with the medium;
- the *transport coefficient* $\hat{q} \equiv m_{\mathrm{D}}^2/\lambda = m_{\mathrm{D}}^2\rho\sigma$ encodes the "scattering power" of the medium.

Before hadronizing, the partons lose energy via two main processes: gluon radiation and elastic re-scattering with the medium gluons. In Fig. 1.21, top left panel, the diagrams of these two types of interactions are sketched. The "gluon bremsstrahlung" contribution is expected to be larger than the collisional energy loss.

- *Collisional energy loss* dominates at low particle momentum. The average energy loss in one scattering (with cross section $\mathrm{d}\sigma/\mathrm{d}t$, where $t = Q^2$ is the squared transferred momentum) in a medium of temperature T is:

$$\left\langle \Delta E_{\mathrm{coll}}^{\mathrm{onescat}} \right\rangle \approx \frac{1}{\sigma T} \int_{m_{\mathrm{D}}^2}^{t_{\max}} t \frac{\mathrm{d}\sigma}{\mathrm{d}t} \mathrm{d}t. \tag{1.17}$$

- *Radiative energy loss* dominates at high momenta. It can be determined from the single- or double-differential gluon (or photon) bremsstrhalung spectra. Let be ω

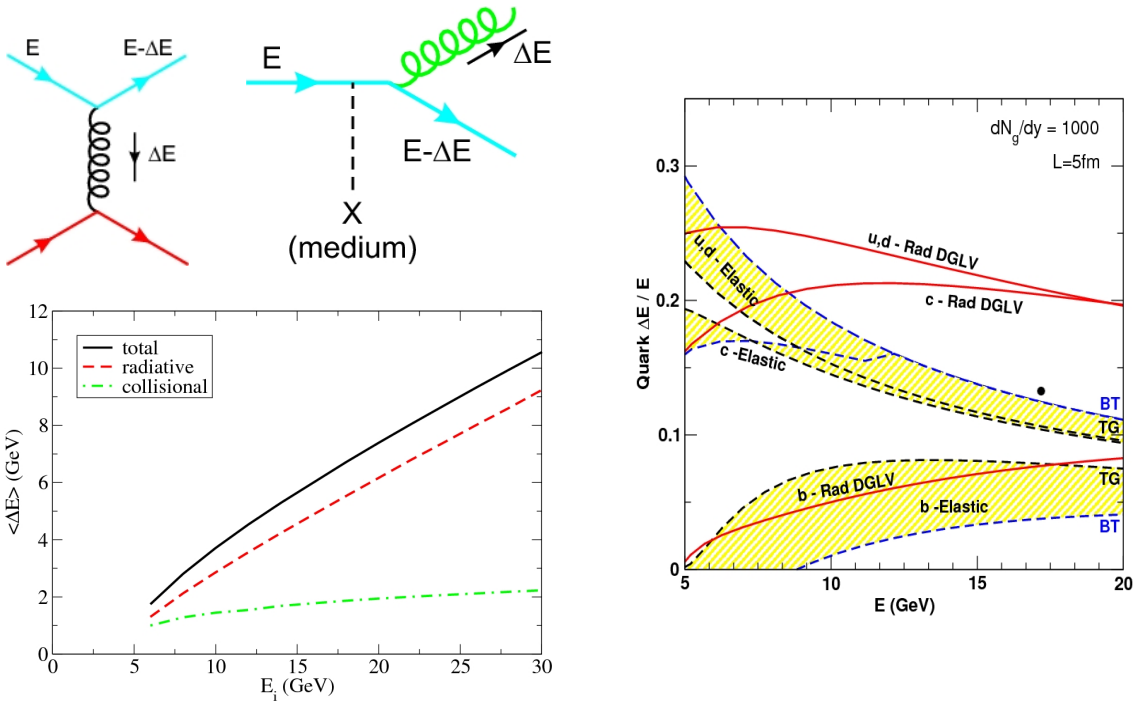

Figure 1.21: Top left panel: Diagrams for collisional (left) and radiative (right) energy loss. Bottom left panel: Comparison of the average radiative (red dashed) and elastic (green dot-dashed) energy loss for light quarks. The solid black line is the total. Right panel: Relative energy loss for light- and heavy-quarks passing through the medium produced in central Au+Au collisions at RHIC energies as obtained by the AMY and DGLV models. From [44].

the energy and $k_\perp$ the transverse momentum of the radiated gluon, the two spectra are $\omega\frac{\mathrm{d}I_{\mathrm{rad}}}{\mathrm{d}\omega}$ and $\omega\frac{\mathrm{d}^2 I_{\mathrm{rad}}}{\mathrm{d}\omega \mathrm{d}k_\perp}$, respectively, and the energy lost in one interaction can be written as:

$$\left\langle \Delta E_{\mathrm{rad}}^{\mathrm{onescat}} \right\rangle = \int^E \omega \frac{\mathrm{d}I_{\mathrm{rad}}}{\mathrm{d}\omega}\mathrm{d}\omega \tag{1.18}$$

$$\left\langle \Delta E_{\mathrm{rad}}^{\mathrm{onescat}} \right\rangle = \int^E \int^{k_{\perp,\max}} \omega \frac{\mathrm{d}^2 I_{\mathrm{rad}}}{\mathrm{d}\omega \mathrm{d}k_\perp^2}\mathrm{d}\omega \mathrm{d}k_\perp^2 . \tag{1.19}$$

For incoherent scatterings the total energy loss is given by $\Delta E^{\mathrm{tot}} = N \cdot \Delta E^{\mathrm{onescat}}$, where $N = L/\lambda$ is the medium opacity, and the energy loss per unit length (or *stopping power*) by:

$$-\frac{\mathrm{d}E}{\mathrm{d}l} = \frac{\left\langle \Delta E^{\mathrm{tot}} \right\rangle}{L} \tag{1.20}$$

Energy loss in a QCD medium

To obtain the actual expressions of the two types of energy loss in a QCD medium, the coupling of quarks and gluons with the medium and the probability for a gluon (quark) to radiate a gluon must be taken into account.

Plugging into eq. (1.17) the dominant contribution to the parton-parton t-differential elastic cross section:

$$\frac{\mathrm{d}\sigma}{\mathrm{d}t} \approx C_i \frac{4\pi\alpha_{\mathrm{s}}^2(t)}{t^2}, \text{ with } \alpha_{\mathrm{s}}(t) = \frac{12\pi}{(33 - n_{\mathrm{f}})\ln(t/\Lambda_{\mathrm{QCD}}^2)}, \tag{1.21}$$

where $C_i = 9/4,\ 1,\ 4/9$ are the colour factors for gg, gq, and qq scattering respectively, the collisional energy loss per unit length is:

$$-\left.\frac{\mathrm{d}E_{\mathrm{coll}}}{\mathrm{d}l}\right|_{q,g} = \frac{1}{4}C_{\mathrm{R}}\alpha_{\mathrm{s}}(ET)m_{\mathrm{D}}^2\ln\left(\frac{ET}{m_{\mathrm{D}}^2}\right) \text{ for light-quark and gluon} \tag{1.22}$$

$$-\left.\frac{\mathrm{d}E_{\mathrm{coll}}}{\mathrm{d}l}\right|_{Q} = -\left.\frac{\mathrm{d}E_{\mathrm{coll}}}{\mathrm{d}l}\right|_{q} - \frac{2}{9}C_{\mathrm{R}}\pi T^2\left[\alpha_{\mathrm{s}}(M^2)\alpha_{\mathrm{s}}(ET)\ln\left(\frac{ET}{M^2}\right)\right] \text{ for heavy-quark} \tag{1.23}$$

with $C_{\mathrm{R}} = 4/3$ (3) for quark (gluon) colour charge. As a numerical example, taking $E = 20$ GeV and a medium with $T = 0.4$ GeV, the elastic energy losses per unit length are $-\mathrm{d}E_{\mathrm{coll}}/\mathrm{d}l|_q = 2.3$ GeV/fm ($m_{\mathrm{D}} = 1$ GeV/c^2) and $-\mathrm{d}E_{\mathrm{coll}}/\mathrm{d}l|_Q = 2.6$ GeV/fm ($M = 1.3$ GeV/c^2, $Q =$ charm quark), for light- and heavy- quarks respectively.

The dominant mechanism of energy loss of a fast parton in a QCD environment is by multiple radiation of gluons. The starting point to determine the radiation probabilities in the QGP are the DGLAP splitting functions in the vacuum (Ref. [5] in [44]), modified to take into account the enhanced medium induced radiation. The resulting radiated spectrum is proportional to the probability of a quark or gluon to emit a gluon. This can be computed assuming different phenomenologies that can be encoded in the transport coefficient parameter, $\hat{q}$. The radiative loss depends on the thickness of the medium. For a thin medium ($L \ll \lambda$) the particle suffers at most one scattering and the radiation spectrum is given by the Bethe-Heitler (BH) bremmstrhalung expression [46]. In a thick medium ($L \gg \lambda$) there are N scatterings, but a coherence effect (the Landau-Pomeranchuk-Migdal - LPM [47]) reduces the amount of radiation compared to N times BH. This is due to the fact that a finite time is needed to emit a gluon, hence neighbouring medium particles interfere coherently and act as one effective scattering centre. Making use of eq. (1.18) and (1.19), the basic QCD radiative energy loss formulas are:

- BH regime ($L \ll \lambda$)

$$\omega\frac{\mathrm{d}I_{\mathrm{rad}}}{\mathrm{d}\omega} \approx \alpha_{\mathrm{s}}\hat{q}L^2/\omega \Longrightarrow \Delta E_{\mathrm{rad}}^{\mathrm{BH}} \approx \alpha_{\mathrm{s}}\hat{q}L^2\ln(E/(m_{\mathrm{D}}^2 L)) \tag{1.24}$$

- LPM regime ($L \gg \lambda$)

$$\omega\frac{\mathrm{d}I_{\mathrm{rad}}}{\mathrm{d}\omega} \approx \alpha_{\mathrm{s}}\begin{cases}\sqrt{\hat{q}L^2/\omega}\\ \hat{q}L^2/\omega\end{cases} \Longrightarrow \Delta E_{\mathrm{rad}}^{\mathrm{LPM}} \approx \alpha_{\mathrm{s}}\begin{cases}\hat{q}L^2 & (\omega < \omega_{\mathrm{c}})\\ \hat{q}L^2\ln(E/(\hat{q}L)) & (\omega > \omega_{\mathrm{c}})\end{cases} \tag{1.25}$$

  where $\omega_{\mathrm{c}} = \frac{1}{2}\hat{q}L^2$ is the characteristic energy radiated gluons.

The LPM spectrum is suppressed in the infrared region (i.e. small ω) compared to the independent BH gluon spectrum. Due to the steeply falling spectrum of the radiated gluons, the integrated LPM spectrum is dominated by the region $\omega \lesssim \omega_{\mathrm{c}}$. The energy loss depends on L^2 and logarithmically on the energy of the traversing particle.

For a gluon with $E = 20$ GeV in a medium with $\hat{q} = 2$ GeV^2/fm and $L = 6$ fm, $\mathrm{d}E_{\mathrm{rad}}/\mathrm{d}l$ is $O(10$ GeV/fm), to be compared with the collisional energy loss of $O(2$ GeV/fm) estimated before. As shown in Fig. 1.21, bottom left panel, ΔE_{coll} is in general a small correction compared to ΔE_{rad} for light quarks and gluons, but it can be an important contribution for slower heavy-quarks (note the beauty case in the right panel figure).

Indeed, the gluon bremsstrahlung differs between heavy and massless quarks already in the vacuum. Due to kinematic constraints, the radiation is suppressed at angles smaller than the ratio of the quark mass (M) to its energy (E):

$$\theta < \theta_0 \equiv \frac{M}{E} = \frac{1}{\gamma}. \tag{1.26}$$

This effect, known as "*dead cone*" [48], results in a reduction of the total gluon radiation emitted by heavy quarks. The energy loss is hence expected to decrease with increasing mass of the quark. In the medium, the total amount of reduction depends in a non-trivial way on the various scales (E, M, L). The reduction for a charm (bottom) quark of mass 1.5 (4.5) GeV/c^2 is of the order of $\sim 25\%$ ($\sim 75\%$).

The use of hard partons as probes of hot and dense QCD matter in heavy-ion collisions relies on the possibility to compute theoretically both their perturbative cross section and their modifications suffered while propagating through a strongly-interacting medium. For an extensive treatment of the different models of energy loss refer to [44].

1.3.4 Heavy-flavour production measurements in proton-proton collisions

The interest of heavy-flavour measurement in pp collisions is twofold. On one hand, as already stated, it is fundamental as reference for Pb–Pb measurements. On the other hand, the LHC opens a completely unexplored range of energies where the perturbative QCD calculations have never been tested so far. Of particular interest is the measurement of the charm cross section: from previous measurements, that will be described below, the data lie on the upper edge of the theoretical curves.

The cross sections of $\mathrm{D}^0 \to \mathrm{K}^-\pi^+$, $\mathrm{D}^{*+} \to \mathrm{D}^0\pi^+$, and $\mathrm{D}^+ \to \mathrm{K}^-\pi^+\pi^+$ (and $\mathrm{D}_s^+ \to \phi\pi^+$, not shown) were measured by CDF at Tevatron in $p\bar{p}$ collisions at $\sqrt{s} = 1.96$ TeV [49]. CDF reconstructs the D meson candidates using a trigger that select tracks displaced from the beam line originated from decay of long-lived hadrons. No particle identification is applied. The yields are extracted via a fit of the invariant mass distributions of the selected candidates. The secondary D mesons, from B decay, are subtracted using the impact parameter of the net momentum vector of the charm candidate to the beam line. This points to the beam line for prompt charm [50]. The yield is then corrected for the efficiency to obtain the final cross sections shown in Fig. 1.22, compared to theoretical calculations. The solid curves are the theoretical predictions from Cacciari and Nason [51], with the uncertainties indicated by the shaded bands. The dashed curve shown with the D^{*+} cross section is the theoretical prediction from Kniehl [52], the dotted lines indicate the uncertainty. The uncertainties on the calculated cross section are evaluated by varying independently the renormalization and the factorization scales between 0.5 and 2 times the default value. The measured differential cross sections are higher than the theoretical predictions by about 100% at low p_{t} and 50% at high p_{t}, however they are compatible within uncertainties.

The inclusive charm+beauty cross section was measured later by PHENIX at RHIC in Au-Au collisions at $\sqrt{s} = 200$ GeV through the semi-electronic decay of the heavy-flavours [53]. The analysis exploits the electron identification capabilities of the Time Projection Chamber, the ElectroMagnetic Calorimeter, and the Čherenkov detector. The subtraction of the background uses two different techniques. One subtracts the background via a Monte Carlo cocktail tuned with measured π spectra and m_{T} scaled light hadrons (η, η', ρ^0, ω, ϕ) and simulated non-photonic background (semi-leptonic

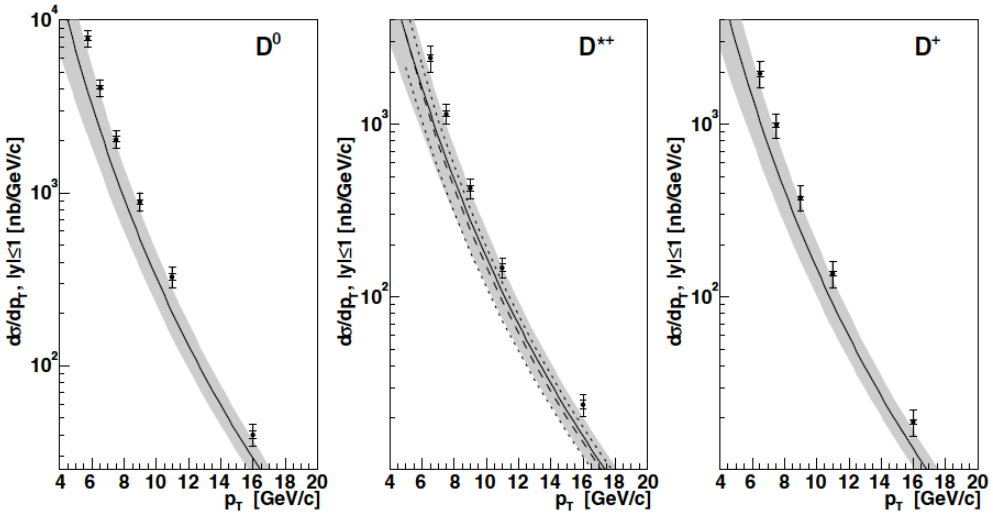

Figure 1.22: From left to right D^0, D^{*+}, and D^+ $d\sigma/dp_t$ versus p_t for $|y| \leq 1$ from CDF at Tevatron. See text for detail on the predictions. From [49].

decays of kaons $K \to e\pi\nu$, K_{e3}), which is a smaller contribution. On the other hand, the converter subtraction method is used on a special set of data, taken during the 2005 run, with an additional photon converter around the beam-pipe. The electrons from photon conversion can be precisely measured and subtracted from the inclusive electron spectrum, obtaining a precise estimation of non-photonic electrons. Small remaining non-photonic background is calculated and subtracted. The spectra obtained with the two analyses are be combined to get the final non-photonic electron spectrum. The non-photonic electron p_t-differential cross section was measured in the range from 0.3 to 9 GeV/c and compared with fixed-order-plus-next-to-leading-log (FONLL) pQCD calculation (see references [13] and [14] in [53]), as shown in Fig. 1.23, top panel. The contributions to FONLL from charm and beauty are also shown separately. As already observed commenting CDF results, the calculation is at the edge of the experimental data, but compatible within uncertainties.

Recently, STAR published the exclusive cross sections for charm and beauty separately [54], as shown in Fig. 1.23, bottom panel. The results were obtained from PHENIX inclusive electron spectrum exploiting the measured fraction of electrons from beauty with respect to the total non-photonic electrons from STAR [55]. The azimuthal correlation between non-photonic electrons and a charged hadron is used to spot the different origin of the electron. In addition, in this measurement, the contribution from heavy vector mesons (J/ψ and Υ) is also subtracted. The comparison with FONLL corresponding predictions are also shown in Fig. 1.23, bottom panel. The measured bottom electron cross section is consistent with the central value of FONLL calculation, while the charm electron cross section is between the central value and upper limit of the FONLL calculation.

ALICE can measure heavy flavour production both through D mesons and semi-electronic decays. The D meson production cross section measurement in pp collisions is one of the topics of this thesis and will be explained in detail in Chapter 4 for the D^0 case. It is intriguing to verify whether the theoretical expectations are in agreement with data also at the LHC energies and whether the charm cross section is reproduced by the calculations.

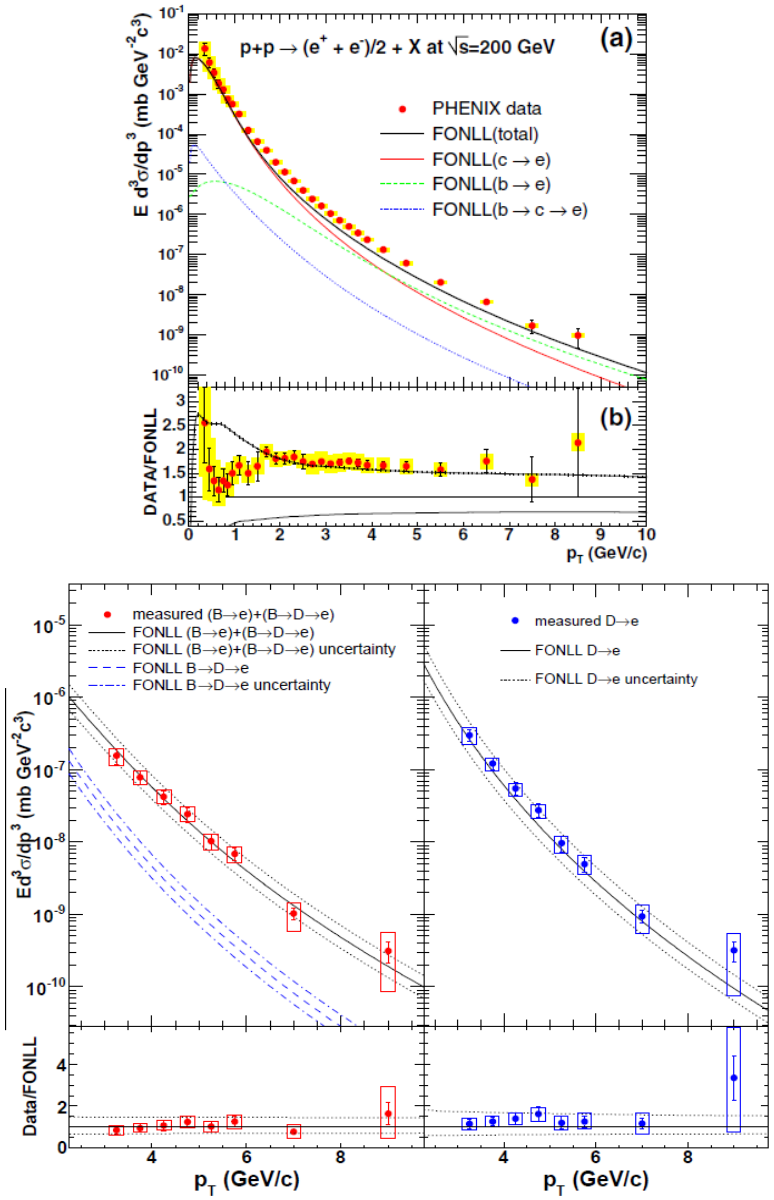

Figure 1.23: Top panel: (a) Invariant differential cross-section from heavy-flavour decays by PHENIX. The curves are the FONLL calculations for charm, beauty, feed-down (dotted lines), and total (solid) cross sections. (b) Ratio of the data to the FONLL c+b $\rightarrow$ e cross section calculation. The upper (lower) curve shows the theoretical upper (lower) limit of the FONLL calculation. In both (a) and (b) a 10% normalization uncertainty is not shown. From [53]. Bottom panel: Invariant cross-section of electrons from bottom (upper-left) and charm meson (upper-right) decay measured by STAR. In the lower panels the ratios to the FONLL predictions for bottom and charm electrons are reported. From [54].

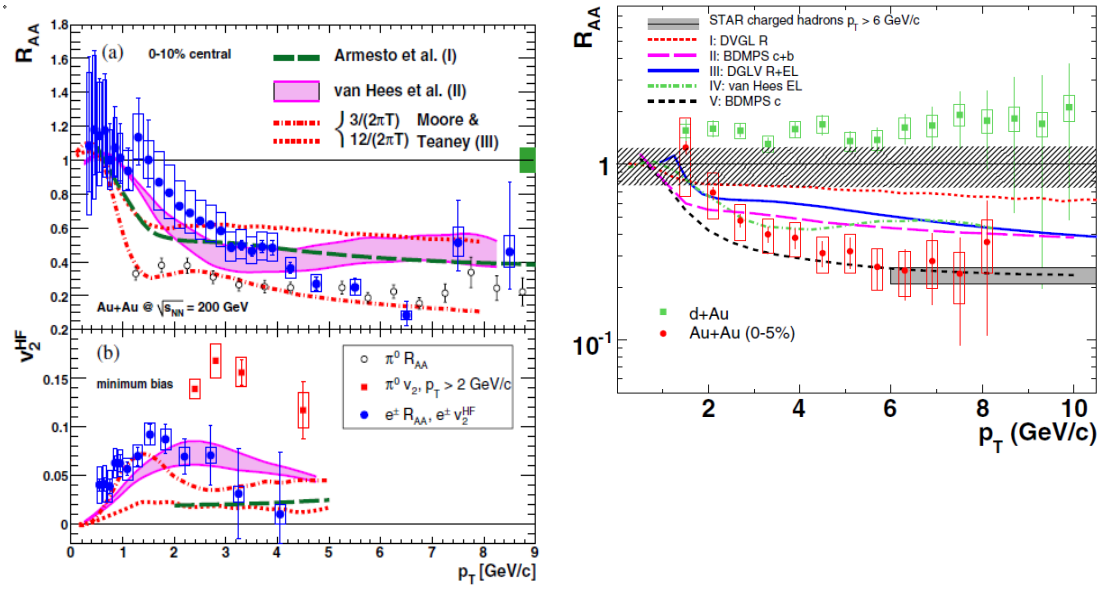

Figure 1.24: Left panel: $R_{\rm AA}$ as a function of $p_{\rm t}$ for heavy-flavour decay electrons (full circle) and π^0 (empty circle), measured by PHENIX. Some models are also superimposed: see Refs. [58], [59], and [60] for curve I, II, and III, respectively. In the bottom panel the v_2 of non-photonic electrons (circle) and π^0 (square) are shown. From [61]. Right panel: Nuclear modification factor of non-photonic electrons, $R_{\rm AA}$, for d-Au and Au-Au collisions at $\sqrt{s_{\rm NN}} = 200$ GeV. Error bars show the statistical uncertainties, boxes show uncorrelated systematic uncertainties, and the filled band at unity is the overall normalization uncertainty.

1.3.5 Heavy-flavour production measurements in Pb–Pb collisions

Heavy quarks are interesting probes of the QGP, because they are produced in the first partonic hard-scatterings, they coexist with the medium and are affected by the strong force interactions with the partons in the QGP.

As discussed before, energy loss can be studied with the nuclear modification factor and the dependence of the energy loss on the parton nature (quark/gluon) and mass can be investigated. The expected ordering is $R_{\rm AA}^{\pi} \lesssim R_{\rm AA}^{\rm D} \lesssim R_{\rm AA}^{\rm B}$ [56]. The RHIC experiments, before the upgrade with vertex detectors, have limited possibility of measuring exclusive charm and beauty $R_{\rm AA}$, but an inclusive measurement through non-photonic electrons was performed.

Figure 1.24 shows the non-photonic electron $R_{\rm AA}$ vs $p_{\rm t}$, measured by PHENIX (left) and STAR (right) at $\sqrt{s_{\rm NN}} = 200$ GeV. Both measurements show a suppression of the heavy-flavour yield almost at the same level as π^0 [42] (left) and charged hadrons [57] (right) at high-$p_{\rm t}$, where a large fraction of electrons is expected to come from beauty. PHENIX also measured v_2 of non-photonic electrons, as shown in Fig. 1.24, bottom left panel. STAR measured $R_{\rm AA}$ for d-Au (Fig. 1.24, right panel) which is consistent with a moderate Cronin enhancement.

Some predictions are also reported: Curve I in the left figure is a BDMPS pQCD calculation with radiative energy loss via multiple soft collisions [58] which describes the measured $R_{\rm AA}$ reasonably well using a large transport coefficient $\hat{q} = 14$ GeV^2/fm, which also provides a consistent description of light hadron suppression. This value of $\hat{q}$ would imply a strongly coupled medium. In this model the azimuthal anisotropy is only due to the path length dependence of energy loss, and the data clearly favour larger $v_2^{\rm HF}$ than

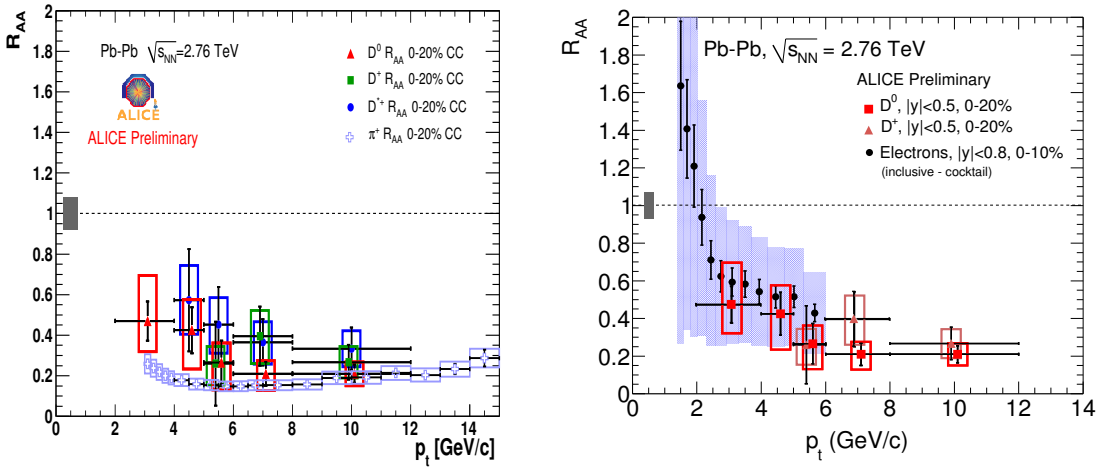

Figure 1.25: Left panel: $R_{\rm AA}$ of $\rm D^0$ (red triangle), $\rm D^+$ (green square), $\rm D^{*+}$ (blue circle), and π^+ (empty cross) as a function of $p_{\rm t}$ for 0-20% [64]. Right panel: $R_{\rm AA}$ of electrons from heavy-flavour (circle), in 0-10% central events, and electrons from charm obtained from $\rm D^0$ (square) and $\rm D^+$ (triangle), as a function of $p_{\rm t}$.

predicted from this effect alone. The same calculation [58] is compared to STAR results (Curve II right figure). At high-$p_{\rm t}$, it under-predicts the suppression: this discrepancy may indicate significant collisional (elastic) energy loss for heavy quarks. Dead cone reduction of energy loss is expected to be more significant for bottom than charm quarks in the reported $p_{\rm t}$ range. Curve V (right panel), which is the same calculation as Curve II but for D-meson decays only, agrees better with the data. A direct measurement of D mesons at high-$p_{\rm t}$ is required to understand energy loss of heavy quarks in detail.

The large $v_2^{\rm HF}$, measured by PHENIX, is better reproduced in Langevin-based heavy quark transport calculations [59, 60]. The heavy-quark energy loss is due to elastic scattering mediated by resonance excitations (D and B) and leading-order t-channel gluon exchange [59]. This calculation is in good agreement with both the measured $R_{\rm AA}$ and v_2 (Curve II, left panel) but compared to high-$p_{\rm t}$ STAR data the agreement is less satisfactory.

Energy loss and flow are also calculated in [60] (Curve III, left panel): while this model fails to simultaneously describe the measured $R_{\rm AA}$ and v_2 with one set of parameters, the range for parameters leading to reasonable agreement with $R_{\rm AA}$ and v_2 is similar to that from [59].

Curve I in Fig. 1.24 right panel uses DGLV radiative energy loss via few hard scatterings [62] with initial gluon density $\mathrm{d}N_g/\mathrm{d}y = 1000$, consistent with light quark suppression. Curve III is a DGLV-based calculation as well, including both radiative and collisional energy loss, together with path length fluctuations [63]. The calculated suppression is also markedly less than that observed.

As it will be shown in Section 4.3, ALICE is capable of measuring the production of D mesons and electrons from decays of heavy-flavour. The preliminary results on D mesons and heavy-flavour electron $R_{\rm AA}$ confirm the suppression of charm and beauty, as shown in Fig. 1.25 [64]. The uncertainties on the D meson measurements are still large and do not allow for a conclusive statement about the comparison with pions. Yet, at high $p_{\rm t}$ the D mesons and the pions seem superimposing.

Since heavy quarks suffer almost as much energy loss as pions at high $p_{\rm t}$, it is very

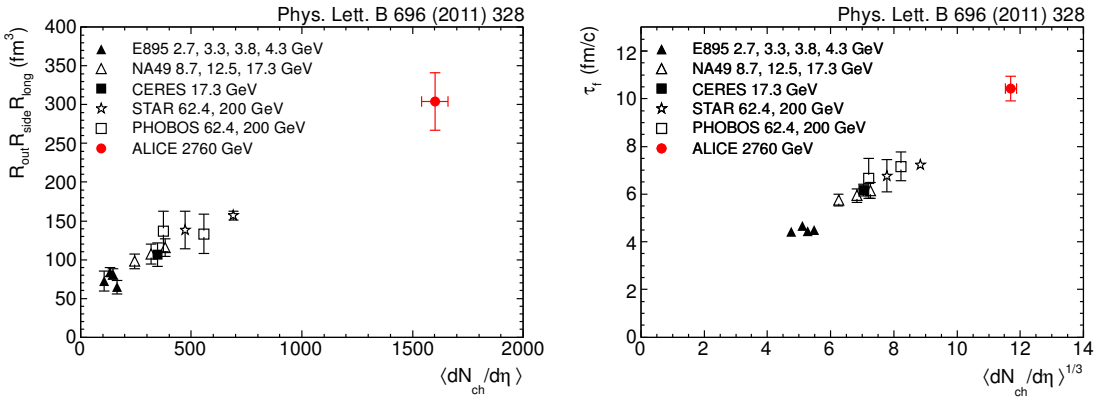

Figure 1.26: Left panel: Product of the three pion HBT radii at $k_{\mathrm{T}} = 0.3$ GeV/c compared to those obtained at lower energies. Right panel: Decoupling time extracted from R_{long}, one of the HBT radii, as a function of $\left\langle \frac{\mathrm{d}N}{\mathrm{d}\eta} \right\rangle^{1/3}$. From [67].

interesting to measure the heavy-flavour v_2 and investigate the heavy-quark thermalization, as it was done by PHENIX [61]. From the v_2 of non-photonic electrons shown in Fig. 1.24, bottom left panel, heavy-flavour decay electrons feature a non-zero flow at $p_{\mathrm{t}} \lesssim 2.5$ GeV/c. From the theoretical point of view, the simultaneous description of the observed R_{AA} and v_2 required an important effort by the authors of the calculations to tune their models. Performing the same measurement at LHC is crucial in having a clearer picture. Chapter 5 will be devoted to the measurement of elliptic flow of D^0 mesons in ALICE.

1.4 First year's results from ALICE at the LHC

From November 2009, the first collisions were carried out at $\sqrt{s} = 900$ GeV, then the energy was increased to 2.36 TeV and to 7 TeV. In November 2010 the first Pb–Pb collisions at $\sqrt{s_{\mathrm{NN}}} = 2.76$ TeV were delivered. A short pp run at $\sqrt{s} = 2.76$ TeV was also performed at the beginning of 2011, to provide a pp reference at the same energy as Pb–Pb collisions.

In this section, a selection of the main physics results from the ALICE experiment is collected.

In Pb–Pb collisions it is important to characterise the size of the system created, both in space and time. This was carried out by using the Hambury Brown-Twiss analysis (HBT) [65, 66] in the most central Pb–Pb collisions [67]. HBT is a technique which exploits the Bose-Einstein enhancement of identical bosons emitted close by in phase-space, giving access to the expansion rate and the spatial extent at decoupling. In Fig. 1.26 a volume in the coordinate system defined by the beam axis (R_{long}), the direction along the pair transverse momentum (R_{out}), and the perpendicular to the particle pair total p_{t} (R_{side}) is shown as a function of the charged particle density. This quantity is related to the region that contributes to the pion spectrum at a particular three-momentum, hence it is related to the size of the system. In the right panel the decoupling time as a function of the charged particle density to the power 1/3 is shown. The ALICE results are compared to those at lower energies. An increment of a factor two in the volume is observed with respect to RHIC. The decoupling time exceeds 10 fm/c, which is 40% larger than the estimated value at RHIC.

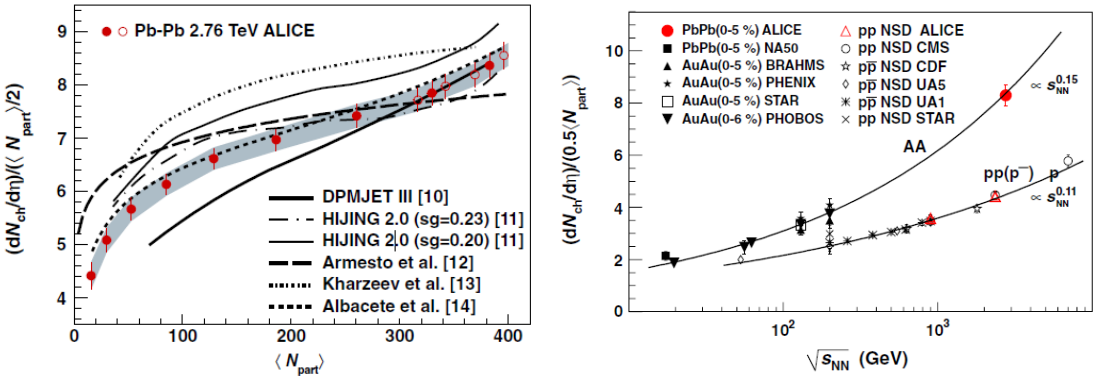

Figure 1.27: Left panel: Comparison of $\frac{\mathrm{d}N^{\mathrm{ch}}}{\mathrm{d}\eta}/\frac{\langle N_{\mathrm{part}}\rangle}{2}$ for Pb–Pb at $\sqrt{s_{\mathrm{NN}}} = 2.76$ TeV from ALICE with model calculations. The open circles are obtained with tinier centrality classes. From [70]. Right panel: Charged-particle pseudorapidity density per participant pair for central nucleus-nucleus and non-single-diffractive pp ($p\bar{p}$) collisions, as a function of $\sqrt{s_{\mathrm{NN}}}$. The solid lines $\propto s_{\mathrm{NN}}^{0.15}$ and $\propto s_{\mathrm{NN}}^{0.11}$ are superimposed on the heavy-ion and pp ($p\bar{p}$) data, respectively. From [68].

The total charged particle multiplicity in the 5% most central collisions at mid-rapidity was measured to be 1548±4(stat)±76(syst) [68]. The multiplicity as a function of centrality is shown in Fig. 1.27, left panel, compared to various of models. The centrality dependence is well reproduced by Albacete et al. saturation model [69] (for more details on the measurement and the models refer to [70]). A steep increase of the multiplicity per participating nucleon pair is observed, as show in Fig. 1.27, right panel with respect to lower energies. The ALICE point is at 8.3±0.4(syst).

Some of the probes sensitive to the QGP phase were analysed. The multi-strange baryon production was measured. The ratio of the spectra of Ξ and Ω with respect to pp normalized to $\langle N_{\mathrm{part}}\rangle$ is shown in Fig. 1.28. The results from lower energies are also reported for comparison. The strangeness enhancement is present but it is less pronounced at LHC than at RHIC and at SPS. Theoretical predictions using the Grand Canonical ensemble approach predict a significant decrease in all the (anti)baryon enhancements with collision energy [71].

Another important piece to be added to the mosaic is the measurement of the J/ψ yield in Pb–Pb collision which is about to be published by ALICE. The preliminary $R_{\mathrm{AA}} = \dfrac{Y_{J/\psi}^{\mathrm{Pb-Pb}}}{\langle T_{\mathrm{AA}}\rangle \times \sigma_{J/\psi}^{\mathrm{pp}}}$ is reported in Fig. 1.29 as a function of $\langle N_{\mathrm{part}}\rangle$. The number of participating nucleons, $\langle N_{\mathrm{part}}\rangle$, is scaled by the number of binary collisions $\langle N_{\mathrm{coll}}\rangle$ to wash out the bias coming from having wide centrality bins. Both $\langle N_{\mathrm{part}}\rangle$ and $\langle N_{\mathrm{coll}}\rangle$ are obtained via a Glauber model calculation [6]. The ALICE J/ψ R_{AA} do not exhibit a significant centrality dependence, differently from the results by PHENIX, superimposed to the figure.

The cold nuclear matter effects will be evaluated once the p-Pb data will be available. For the moment no strong conclusion can be drawn, but data seem to favour the regeneration hypothesis.

Another fundamental observable is the suppression of high-p_{t} particles in Pb–Pb collisions. The measurement of the nuclear modification factor of charged hadrons was performed with respect to the available pp data. The differential yields $\dfrac{\mathrm{d}^2N^{\mathrm{pp}}}{\mathrm{d}\eta\mathrm{d}p_{\mathrm{t}}}$ of charged

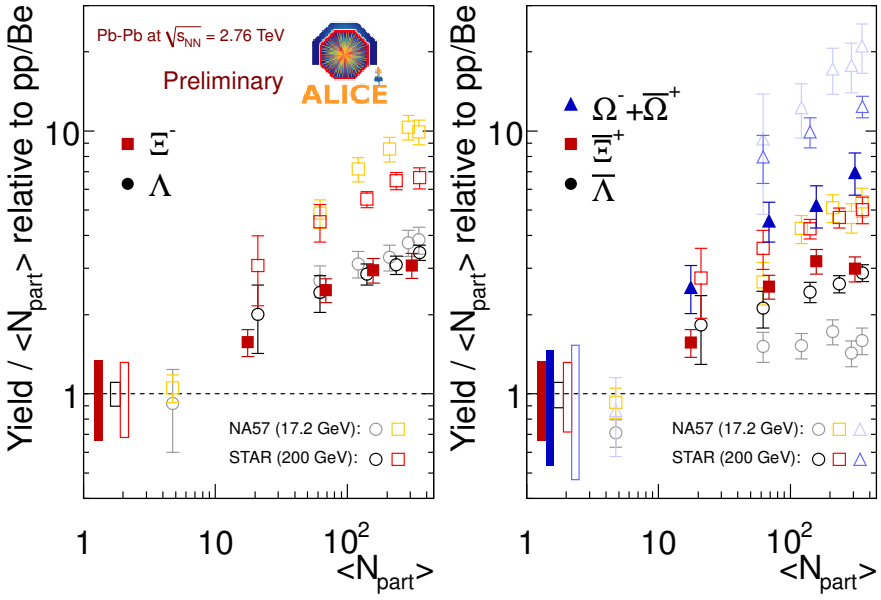

Figure 1.28: The observed baryon yields per participant nucleon, normalized to the ratio measured in pp or p-Be collision (depending on the experiment) as a function of the number of participants. Lower energy measurements by NA57 [36] and STAR [37].

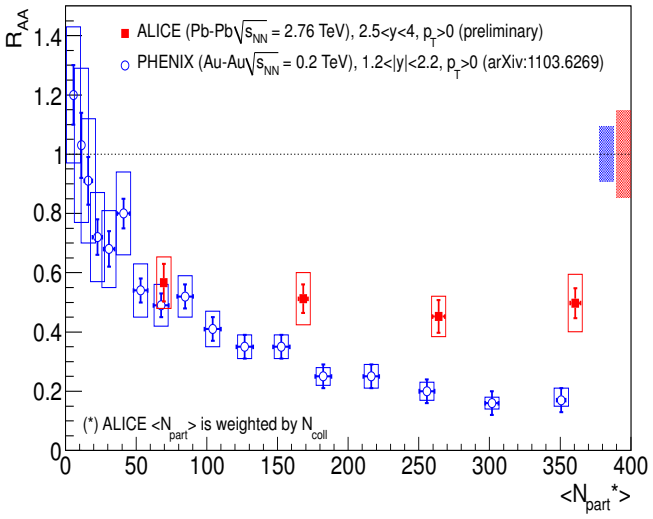

Figure 1.29: Left panel: Preliminary R_{AA} of $J/\psi \to \mu^+\mu^-$ as a function of $\langle N_{\mathrm{part}} \rangle$ by ALICE, in $-4 < y < -2.5$, Pb–Pb at $\sqrt{s_{\mathrm{NN}}} = 2.76$ TeV compared to that measured by PHENIX in $1.2 < y < 2.2$, Au-Au at $\sqrt{s_{\mathrm{NN}}} = 0.2$ TeV [72]. To ease the comparison with PHENIX the $\langle N_{\mathrm{part}} \rangle$ values for ALICE have been weighted by N_{coll}: $\langle N^*_{\mathrm{part}} \rangle = \langle N_{\mathrm{coll}} \times N_{\mathrm{part}} \rangle / \langle N_{\mathrm{coll}} \rangle$.

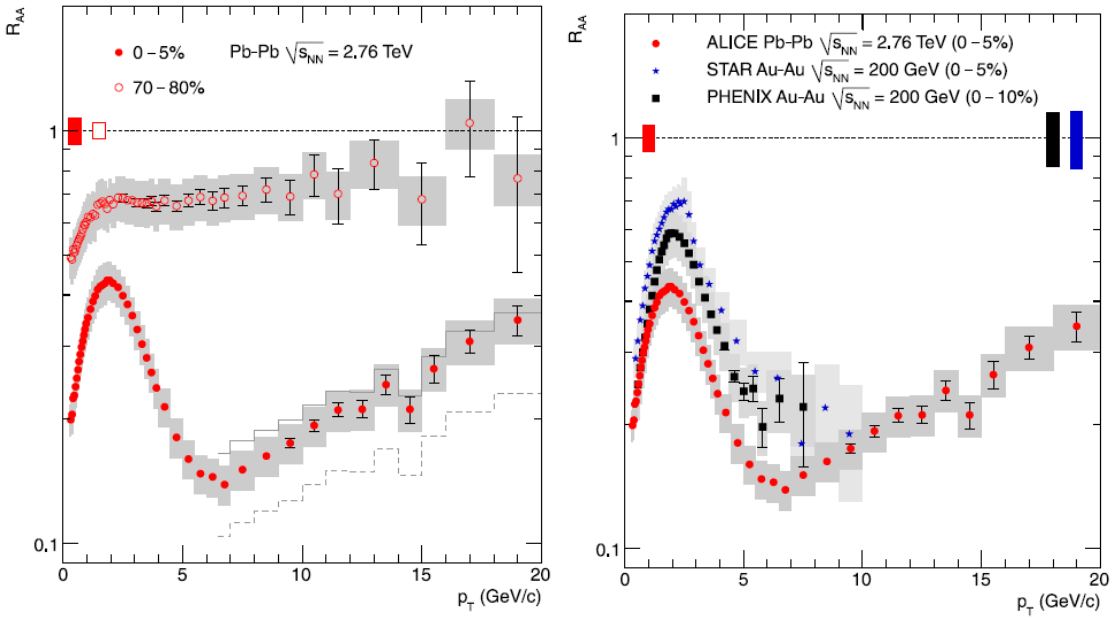

Figure 1.30: Left panel: $R_{\rm AA}$ of charged tracks from ALICE in central (0-5%) and peripheral (70-80%) collisions at $\sqrt{s_{\rm NN}} = 2.76$ TeV. The histograms indicate the result using alternative pp references obtained by the use of $p\bar{p}$ measurement at $\sqrt{s_{\rm NN}} = 1.96$ TeV (solid) and by applying a NLO scaling to the pp data at 0.9 TeV (dashed). Right panel: Comparison of the $R_{\rm AA}$ in the 0-5% centrality class from ALICE with 0-5% from STAR [57] and 0-10% from PHENIX [42]. Figures from [79].

particles measured by ALICE in inelastic pp collisions at $\sqrt{s} = 900$ GeV and 7 TeV are interpolated. The interpolation is performed in bins of $p_{\rm t}$, based on the assumption that the increase of the yield with $\sqrt{s}$ follows a power law. Above $p_{\rm t} = 2$ GeV/c, the measured spectra at the two energies are parametrized by a modified Hagedorn function [73] and a power law to reduce bin-by-bin fluctuations. The interpolation procedure was verified using PHOJET [74] and PYTHIA [75] (tunes D6T [76] and Perugia0 [77]) at 0.9, 2.76 and 7 TeV. The generated and interpolated spectra at 2.76 TeV agree within the quoted uncertainties.

Finally, the scaled pp yield in a given centrality class is obtained by multiplication of the pp reference spectrum with $\langle N_{\rm coll} \rangle$. In Fig. 1.30, left panel the ALICE $R_{\rm AA}$ vs $p_{\rm t}$ in 70-80% and 0-5% centrality classes is reported. The $R_{\rm AA}$ is below unity both for the peripheral and the central classes. At high $p_{\rm t}$, where the production from hard processes is expected to dominate, there is a marked difference between peripheral and central events. In peripheral collisions the nuclear modification factor reaches 0.7 and shows weak $p_{\rm t}$-dependence for $p_{\rm t} > 2$ GeV/c. In central collisions a strong $p_{\rm t}$-dependence is observed with a minimum of 0.14 at $p_{\rm t} = 6$-7 GeV/c and a maximum at $p_{\rm t} = 2$ GeV/c. A significant rise of a factor two is observed at $7 < p_{\rm t} < 20$ GeV/c. In the right panel of Fig. 1.30 the nuclear modification factor in central collisions is compared to STAR and PHENIX results [42, 57]. A rise towards high $p_{\rm t}$, is suggested also by the highest $p_{\rm t}$ points from RHIC, although the large uncertainties do not give a clear trend. Preliminary results using the measured pp reference at 2.76 TeV are shown in [78].

Azimuthal anisotropy of charged particles was measured with the very first data by ALICE [80]. The elliptic flow v_2, measured using the 4-particle correlation method (see Appendix A), averaged over transverse momentum and pseudorapidity is 0.087±

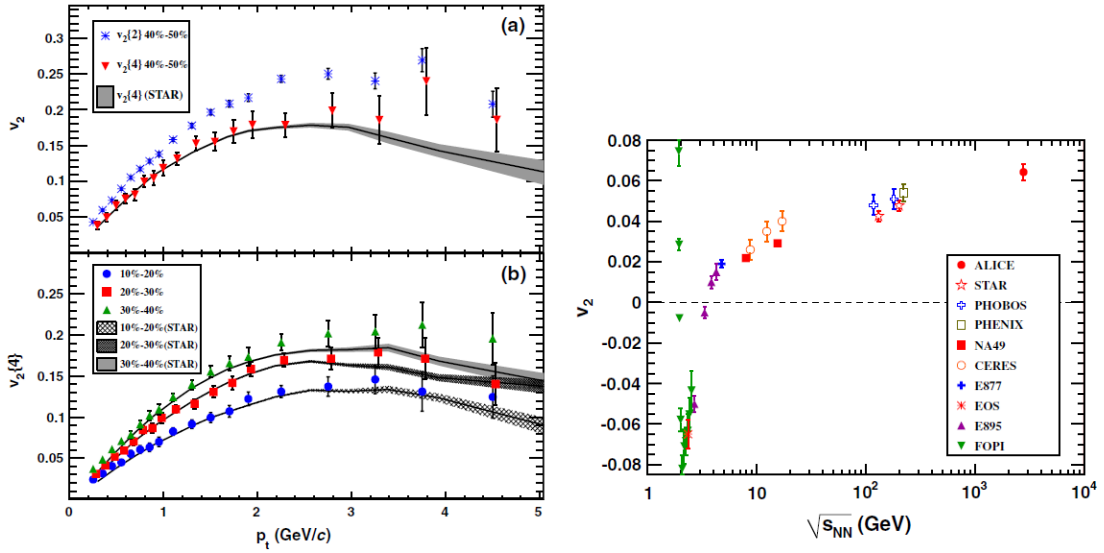

Figure 1.31: Left panel: v_2 measured with 2- and 4-particle correlation methods in various centrality classes. The markers are ALICE results, while the bands are STAR results. Right panel: Integrated elliptic flow at 2.76 TeV in Pb-Pb 20%-30% centrality class compared with results from lower energies taken at similar centralities (see Refs. [40, 43] from [80]). Figures from [80].

$0.002(\text{stat}) \pm 0.003(\text{syst})$ in the centrality class 40-50%. The differential elliptic flow $v_2(p_\text{t})$, shown in Fig. 1.24, left panel, reaches a maximum of 0.2 near $p_\text{t} = 3$ GeV/c. The p_t dependence does not change, within uncertainties, from $\sqrt{s_\text{NN}} = 200$ GeV to 2.76 TeV. Compared to RHIC Au-Au collisions at $\sqrt{s_\text{NN}} = 200$ GeV, the integrated elliptic flow in 20%-30% centrality class increases by about 30% (Fig. 1.31, right panel). The increase is not due to a larger differential flow, but to the larger average p_t at LHC. This increase is larger than in current ideal hydrodynamic calculations at LHC multiplicities, but some hydrodynamic model predictions which include viscous corrections are in agreement with the observed increase. The matching between the differential v_2 at RHIC and LHC could be accidental, given by a compensation between the pion v_2 and heavier hadrons v_2 which are predicted to have a different behaviour at LHC with respect to RHIC, as argued in [10], using a pure hydrodynamical model including non-zero specific shear viscosity.

Since the success of the ideal hydrodynamic description of the elliptic flow for the central Au-Au collisions at RHIC (see Section 1.2.5), hydrodynamics is considered as the most appropriate theory to describe a thermalized phase in the time evolution of the system created in a heavy-ion collision. An important test of the hydrodynamic description at the LHC is the interplay between radial (azimuthally symmetric radial expansion) and anisotropic flow which result in the mass splitting of the elliptic flow at small transverse momenta. Fig. 1.32, left panel, shows the elliptic flow of pions, kaons, and anti-protons vs p_t, measured with the scalar product (SP) [81] method. The mass dependence of v_2 at low transverse momenta, $p_\text{t} < 2.5$ GeV/c, is well reproduced by viscous hydrodynamic model calculations [10] with a color glass condensate initial condition (solid lines). Agreement with data, especially for protons, is improved when adding a hadronic cascade phase into the model calculations (dashed lines). Fig. 1.32, right panel, shows elliptic flow of pions, kaons, and anti-protons scaled with the number of constituent quarks, n_q ($n_q = 2$ for mesons, and $n_q = 3$ for baryons), vs transverse kinetic energy per quark, $(m_\text{T} - m_0)/n_q$. The observed approximate scaling of v_2 with

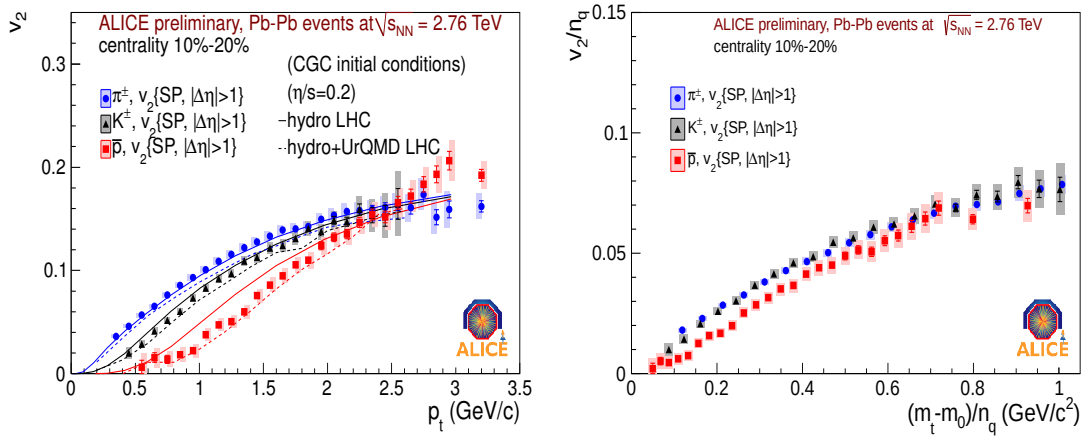

Figure 1.32: Left panel: v_2 as a function of transverse momentum for pions, kaons, and anti-protons. Right panel: Elliptic flow v_2 scaled with the constituent number of quarks as a function of the transverse kinetic energy per quark. In both panels v_2 is measured with the scalar product (SP) method by ALICE in Pb–Pb collisions at $\sqrt{s_{\rm NN}} = 2.76$ TeV.

the number of quarks in the range of $p_{\rm t} \sim$ 2-3 GeV/c ($m_{\rm T} \sim$ 0.6-1.0 GeV/c^2) reflects collectivity at the quark level and suggest that the system evolved through the phase of deconfined quarks and gluons.

Chapter 2

A Large Ion Collider Experiment at the LHC

2.1 Overview of the Large Hadron Collider (LHC) and its experiments

2.1.1 The challenge

The LHC is the largest and highest energy accelerator ever built. The first studies for the LHC project were performed in 1982 and the final decision of starting the construction was taken in 1996, two years after the approval from the CERN Council. In 2003 the LHC construction inside the LEP tunnel started and finally the beam commissioning took place in 2007-2008.

The main goal of LHC is the search for the Higgs boson. The upgrades with respect to previous machines (e^+e^- collisions with peak centre-of-mass energy of 209 GeV reached at CERN-LEP and of 1.96 TeV at BNL-Tevatron with $p\bar{p}$ collisions) concern the centre of mass energy, sufficient to produce the Higgs boson, if it exists, and the extremely high luminosity which allows to collect a high statistics in a very short time.

The extremely high luminosity is a challenge both for the machine and the experiments, which have to deal with 10^9 interactions per second.

From the accelerator point of view, the high luminosity is achieved combining high beam current, high number of bunches, and small beam size. The nominal parameters are 10^{11} particles per bunch 2800 bunches, with a time interval of 25 ns, and a spot-size of $\approx 16\mu$m.

The other big challenge is the nominal energy to be achieved: 7 TeV per beam. It can be reached only with a magnetic field of 8.3 T, almost twice the magnetic field of Tevatron, that can be obtained only with superconductor magnets.

2.1.2 CERN's accelerator complex

The final energy and luminosity of the LHC are achieved by a succession of acceleration steps in different machines, where the energy of the beams is gradually increased. In Fig. 2.1 the layout of the acceleration steps is reported. Each accelerator boosts the speed of a beam of particles, before injecting it into the next one in the sequence.

Protons and ions follow a different path in the first steps of the acceleration. Protons are obtained by removing electrons from hydrogen atoms. They are injected from the linear accelerator (LINAC-2) into the PS Booster, then the Proton Synchrotron (PS), followed by the Super Proton Synchrotron (SPS), before finally reaching the Large

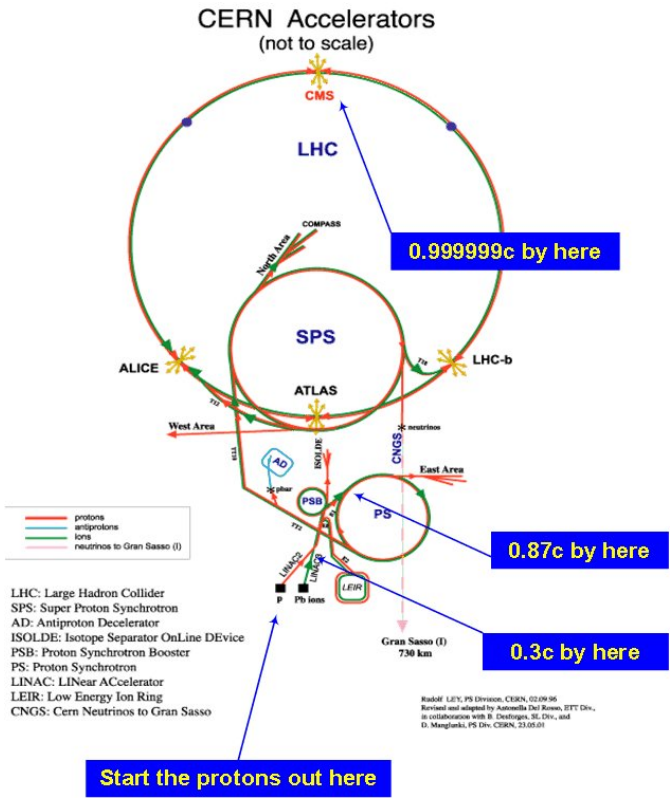

Figure 2.1: Chain of acceleration before the injection to LHC. LINAC2, Booster, PS, SPS, LHC are CERN accelerators produced in more than 50 years of history and still alive to feed the LHC.

Hadron Collider (LHC). Protons circulate in the LHC for 20 minutes before reaching the maximum speed and energy.

The present Linac-2 is an Alvarez Proton Linac, first run in 1978. It provides pulsed (1 Hz) beams of up to 175 mA at 50 MeV. At the PS Booster (PSB) entrance, the pulse lengths varies between 20 and 150 μs depending on the number of protons required by the eventual user.

The PS Booster is a synchrotron with four vertically stacked rings which accelerates the beam from 50 MeV to 1.4 GeV with a cycling time of 1.2 s.

With a circumference of 628 m, the PS has 277 conventional (room temperature) electromagnets, including 100 dipoles to bend the beams round the ring, and it operates at up to 26 GeV with a cycling time of 3.6 s. It has the role to create the 25 ns bunch train for LHC.

The SPS is the second largest machine in CERN's accelerator complex. Measuring nearly 7 km in circumference, it takes particles from the PS. The SPS has 1317 conventional (room temperature) electromagnets, including 744 dipoles to bend the beams round the ring, and it operates at up to 450 GeV.

Finally, the accelerated hadron are injected into the LHC, consisting of a 27-kilometre ring of superconducting magnets with a number of accelerating structures to boost the energy of the particles along the way. The beams travel in opposite directions in separate beam pipes, two tubes kept at ultra-high vacuum. They are guided around the accelerator ring by a strong magnetic field, achieved using superconducting electromagnets. These are built from coils of special electric cable that operates in a superconducting

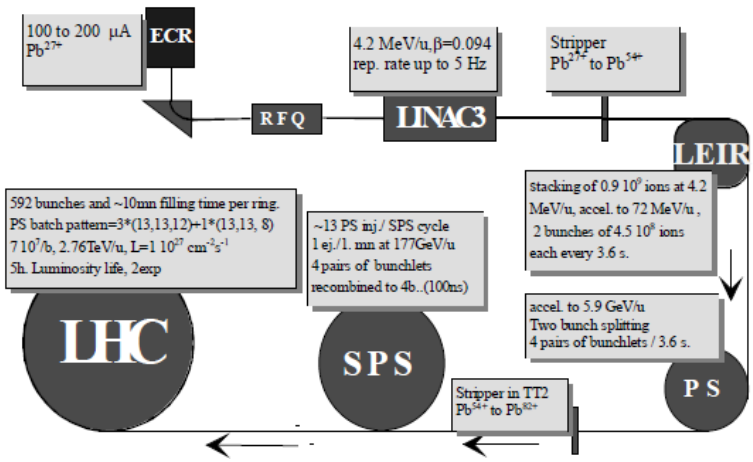

Figure 2.2: General layout of the production of lead ions beams for LHC. From [82]

state, efficiently conducting electricity without resistance or loss of energy. This requires chilling the magnets to about −271°C. For this reason, much of the accelerator is connected to a distribution system of liquid helium, which cools the magnets, as well as to other supply services. Thousands of magnets of different varieties and sizes are used to direct the beams around the accelerator. These include 1232 dipole magnets of 15 m length which are used to bend the beams, and 392 quadrupole magnets, each 5-7 m long, to focus the beams. Just prior to collision, another special quadrupole configuration is used to "squeeze" the particles closer together to increase the luminosity.

As far as the lead ions are concerned, their source is a 14.5 GHz electron cyclotron resonance (ECR) producing Pb 27+ ions at 2.5 keV/u[1]. After the source, the LINAC-3, an Heavy Ion Linac, commissioned in summer 1994, carries the beam to 4.2 MeV/u.

The ions are stripped to 54+ before entering LEIR, where they are accumulated and then accelerated to reach 72 MeV/u.

In the PS the ions are then accelerated to reach 5.9 GeV/u. An additional stripping produces Pb^{82+} ions injected in the SPS.

The SPS provides 177 GeV/u of energy and finally the ions are ready for LHC where they can reach a nominal energy of 5.5 TeV/u with a luminosity of 10^{27} cm^{-2}s^{-1}. The production of the lead ion beams for LHC is layout in Fig. 2.2.

The nominal beam contains 592 bunches spaced of 100 ns with 7×10^7 Pb ions each. The transverse beam-size is about 16 μm and the bunch length about 7.6 cm, similar to the proton beams.

For the moment, the energy per beam is limited to 3.5 TeV for protons and 1.353 TeV/u for Pb ions.

2.1.3 The LHC and its experiments

As shown in Fig. 2.3, the 27-kilometres ring has three regions (IR4, IR3, and IR7) where the beams are monitored and "cleaned", i.e. collimated to eliminate the beam losses and recover the nominal size needed to maintain the quality of the beam. One region is equipped with a septum magnet to extract the beam for the beam dump, painting it on a block of concrete and graphite about 700 m away from the extraction. Other four interaction regions are dedicated to the six experiments.

[1] An atomic mass unit (u) corresponds to $1.660538921(73) \times 10^{-27}$ kg.

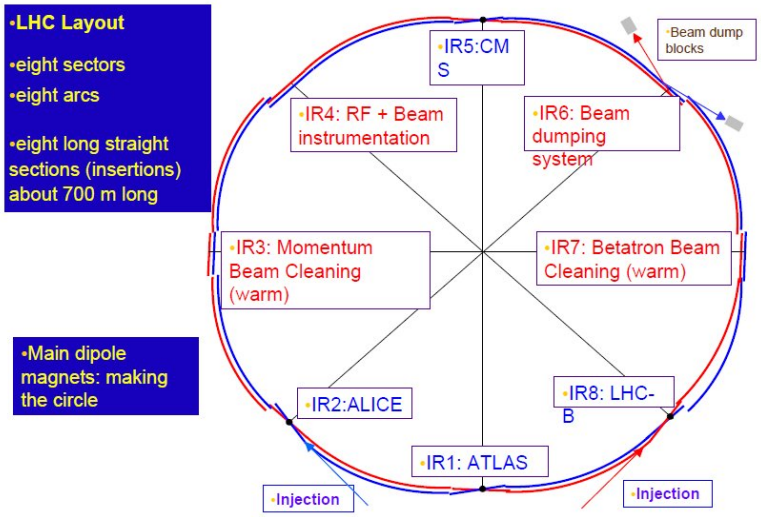

Figure 2.3: The LHC ring with the injection lines, the 4 interaction points where ATLAS (IR 1), ALICE (IR 2), CMS (IR 5), and LHCb (IR 8) seat, the beam dump blocks, and the accelerator instrumentation list in the other experimental areas (IR 3, 4, 6, 7).

ATLAS [83] (at IR1) and CMS [84] (at IR5) are general-purpose detectors that aim at investigating the largest possible range of physics. Their main goal is the discovery or the exclusion of the presence of the Higgs boson, predicted by the Standard Model (SM). At the same time they are looking for signal of new physics, beyond the SM predictions.

In the same caverns where ATLAS and CMS are located, other two little experiments found place, LHCf [85] and TOTEM [86], respectively. They are specialized in "forward physics", both in proton and heavy-ion collisions. They are detecting those phenomena happening between particle that just brush past each other as the beams collide, rather than meeting head-on. In particular, TOTEM goal is to measure the size of the proton and to monitor accurately the LHC luminosity. LHCf, instead, uses forward particles created inside the LHC as a source to simulate cosmic rays in laboratory conditions studying how collisions inside the LHC cause similar cascades of particles as cosmic rays helping scientists to interpret and calibrate large-scale cosmic-ray experiments that can cover thousands of kilometres.

By studying the beauty quark, LHCb, located at the IR8, investigates the slight differences between matter and antimatter which cause the Universe of being compound by matter.

The ALICE experiment, is located at the IR2. Its physics goals were already discussed in detail in Chapter 1. In Section 2.2 a brief summary of the physics purpose and of the composition of the detector is given. Section 2.3 will go deeper into the ALICE detector sub-systems, concentrating mainly on those sub-detectors used for the analyses described in this thesis.

In Section 2.4 the offline framework developed to deal with simulation, reconstruction, and analysis will be described. In Section 2.4.3 and 2.4.5 the performance concerning tracking and particle identification will be discussed.

In Section 2.5 the determination of the collision centrality in Pb–Pb collisions will be treated. Finally, in Section 2.6 the data taking conditions for the ALICE experiment, also comparing, to some extent, to the other main experiments, will be described. In addition, the statistics collected during the 2010 runs and analysed in Chapters 4 and 5 will be presented.

2.2 ALICE

ALICE, A Large Ion Collider Experiment, is a general-purpose, heavy-ion detector at the CERN LHC which focuses on QCD, the strong-interaction sector of the Standard Model. It is designed to address the physics of strongly interacting matter and the quark-gluon plasma at extreme values of energy density and temperature in nucleus-nucleus collisions. Besides running with Pb ions, the ALICE physics programme includes proton physics at unprecedented energy, collisions with lighter ions, lower energy running, and dedicated proton-nucleus runs. The aim of pp collisions for ALICE is to collect reference data for the heavy-ion programme and to address several QCD topics for which ALICE is complementary to the other LHC detectors.

The most stringent design constraint is to cope with the extreme particle multiplicity anticipated in central Pb–Pb collisions. The different subsystems were optimized to provide high-momentum resolution as well as excellent Particle Identification (PID) over a broad range in momentum, up to the highest multiplicities predicted for LHC. ALICE detector's overall dimensions are $16 \times 16 \times 26$ m^3 with a total weight of approximately 10000 t and 18 different detector systems. As the single dedicated heavy-ion experiment at the LHC, ALICE is a general-purpose detector addressing a broad range of observables which were typically covered at previous accelerators (AGS, SPS, RHIC) by a suite of more specialized experiments.

ALICE consists of a central barrel part, which measures hadrons, electrons, and photons, and a forward muon spectrometer. The central part covers polar angles from 45° to 135° and is embedded in a large solenoid magnet reused from the L3 experiment at LEP. From the inside out, the barrel contains an Inner Tracking System (ITS) made up of six layers of high-resolution silicon pixel (SPD), drift (SDD), and strip (SSD) detectors, a cylindrical Time-Projection Chamber (TPC), three particle identification arrays of Time-of-Flight (TOF), Ring Imaging Cherenkov (HMPID) and Transition Radiation (TRD) detectors, and two electromagnetic calorimeters (PHOS and EMCal). All detectors except HMPID, PHOS, and EMCal cover the full azimuth. The forward muon arm (2° - 9°) consists of a complex arrangement of absorbers, a large dipole magnet, and fourteen planes of tracking and triggering chambers. Several smaller detectors (ZDC, PMD, FMD, T0, V0) for global event characterization and triggering are located at small angles. An array of scintillators (ACORDE) on top of the L3 magnet is used to trigger on cosmic rays.

In Fig. 2.4 the longitudinal and transverse section of the ALICE detector are reported. The coordinate frame is defined as follow: the x-axis is perpendicular to the mean beam direction, aligned with the local horizontal and pointing to the accelerator centre; the y-axis is perpendicular to the x-axis and to the mean beam direction, pointing upward; the z-axis is parallel to the mean beam direction and pointing opposite to the muon spectrometer.

The design of ALICE was optimized for a value of about $\mathrm{d}N_{\mathrm{ch}}/\mathrm{d}\eta = 4000$, but tested with simulations up to twice that amount. The tracking was made particularly safe and robust by using mostly three-dimensional hit information with many points (up to 160) in a moderate field of 0.5 T. A large dynamic range is required for momentum measurement, spanning more than three orders of magnitude from tens of MeV/c (collective effects at large length scales, good acceptance for resonance decays) to well over 100 GeV/c (jet physics). This is achieved with a combination of very low material thickness to reduce multiple scattering at low p_{t} (13% X_0 up to the end of the TPC) and a large tracking lever arm of up to 3.5 m to guarantee a good resolution at high p_{t}. PID

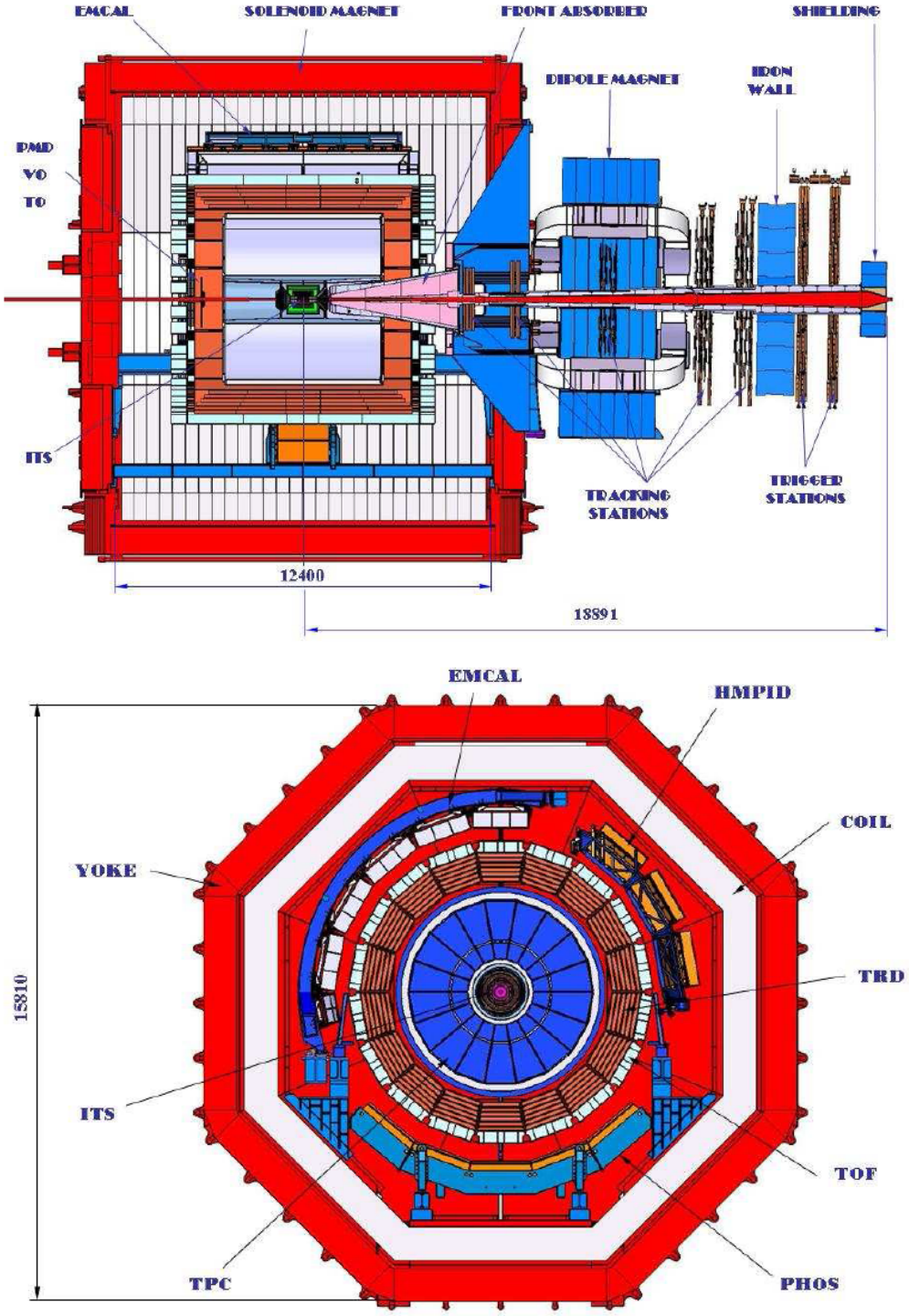

Figure 2.4: ALICE 2D cut along the yz direction (top) and along the xy direction (bottom). See text for the definition of the coordinate system.

over most of this momentum range is essential, as many observables are either mass or flavour dependent. ALICE employs specific ionization energy loss $\mathrm{d}E/\mathrm{d}x$, time-of-flight, transition and Cherenkov radiation, electromagnetic calorimetry, muon filters, and topological decay reconstruction. The instrumented part is concentrated over 2 units in rapidity around mid-rapidity for the barrel detectors and covers 1.5 units in rapidity at small angles for the muon measurement. The interaction rate with nuclear beams at LHC is low (10 kHz for Pb–Pb) and radiation doses are moderate (< 3000 Gy), allowing for the use of slow but high-granularity drift detectors like TPC and SDD. Rare signals are enriched with selective triggers operating at several levels wherever possible.

2.3 Detector overview

An full description of the ALICE experiment can be found in [87]. The detectors used for the analyses presented in this thesis are the ITS, the TPC, the TOF, the T0 and the V0. They will be described in Section 2.3.1, while the main characteristics of the other detectors will be summarized in Section 2.3.2.

2.3.1 Detectors used for heavy-flavour analyses

ITS

The main tasks of the Inner Tracking System, ITS, are the location of the primary vertex with a resolution better than 100 μm, the reconstruction of the secondary vertices from weak decays, the tracking and identification of particles with momentum below 200 MeV/c, and the improvement of momentum and angle resolution for tracks reconstructed by the TPC.

The ITS surrounds the beam pipe, for which it provides the mechanical support so that no relative movement takes place during operation. The beam pipe is a 800 μm-thick beryllium cylinder of 6 cm outer diameter, coaxial with the ITS detector layers. As shown schematically in Fig. 2.5, the ITS consists of six cylindrical layers of silicon detectors, located at radii between 4 and 43 cm. It covers the rapidity range of $|\eta| < 0.9$ for all vertices located within the length of the interaction diamond ($\pm 1\sigma$, i.e. ± 5.3 cm along the beam direction). The number, position and segmentation of the layers were optimized for efficient track finding and high impact-parameter resolution. In particular, the outer radius is determined by the necessity to match tracks with those from the TPC and the inner radius is the minimum allowed by the radius of the beam pipe. The first layer has a more extended pseudo-rapidity coverage ($|\eta| < 1.98$) to provide, together with the Forward Multiplicity Detectors (FMD), continuous coverage for the measurement of charged particles multiplicity. The detectors and on-board electronics are held by lightweight carbon-fibre structures.

The geometrical dimensions and the technology used in the various layers of the ITS are summarized in Table 2.1.

Because of the high particle density expected in heavy-ion collisions (as many as 50 particles per cm^2 have been predicted for the inner layer), in order to achieve the required impact parameter resolution, Silicon Pixel Detectors (SPD) have been chosen for the innermost two layers and Silicon Drift Detectors (SDD) for the following two layers. The two outer layers, where the track density is expected to be below one particle per cm^2, are equipped with double-sided Silicon micro-Strip Detectors (SSD). The four outer layers have analogue readout and therefore can be used for particle identification

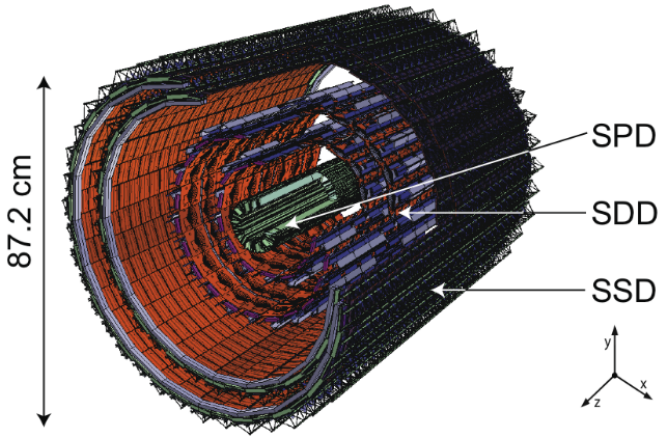

Figure 2.5: ITS layout.

Table 2.1: Dimensions of the ITS detectors (active areas).

Layer	Type	r (cm)	$\pm z$ (cm)	Area (cm^2)	Channels
1	pixel	3.9	14.4	0.07	3 276 800
2	pixel	7.6	14.1	0.14	6 553 600
3	drift	15.0	22.2	0.42	43 008
4	drift	23.9	29.7	0.89	90 112
5	strip	38.0	43.1	2.20	1 148 928
6	strip	43.0	48.9	2.8	1 459 200

via $\mathrm{d}E/\mathrm{d}x$ measurement in the non-relativistic $(1/\beta^2)$ region. The ITS has standalone capability as a low-p_{t} particle spectrometer.

The characteristics related to the spatial resolution of each of the three detectors are summarized in Table 2.2. The relative momentum resolution achievable with the ITS is better than 2% for pions with transverse momentum between 100 MeV/c and 3 GeV/c. The resolution on the impact parameter is better than 60 μm at 1 GeV/c, adequate for heavy-flavoured particles.

The momentum and impact parameter resolution for low-momentum particles are dominated by multiple scattering effects in the material of the detector; therefore the amount of material in the active volume has been kept to a minimum. The silicon detectors used to measure ionisation densities (drift and strips) have a minimum thickness of approximately 300 μm to provide acceptable signal-to-noise ratio. In addition, de-

Table 2.2: Resolution of the different ITS detectors.

	SPD	SDD	SSD
Spatial precision $r\phi$ (μm)	12	35	20
Spatial precision z (μm)	100	25	820
Two tracks resolution $r\phi$ (μm)	100	200	300
Two tracks resolution z (μm)	850	600	2400

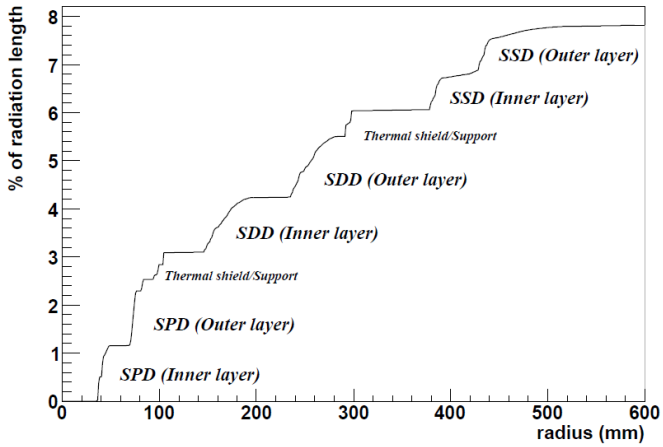

Figure 2.6: Integral of material thickness traversed by a perpendicular track originating at the primary vertex versus radius.

tectors must overlap to cover the solid angle entirely. The detectors effective thickness amounts to 0.4% of X_0. The additional material in the active volume, i.e. electronics, cabling, support structure, and cooling system, has been kept at a comparable effective thickness. Fig. 2.6 shows the integral of the material traversed by a particle crossing perpendicularly the ITS as a function of radius.

The Silicon Pixel Detector (SPD) constitutes the two innermost layers of the ITS. The SPD will operate in a region where the track density could be as high as 50 tracks/cm^2. It is a fundamental element for the determination of the position of the primary vertex as well as for the measurement of the impact parameter of secondary tracks originating from the weak decays of strange, charm, and beauty particles [88]. The SPD is based on hybrid silicon pixels, consisting of a two-dimensional matrix (sensor ladder) of reverse-biased silicon detector diodes bump-bonded to readout chips. Each diode is connected through a conductive solder bump to a contact on the readout chip corresponding to the input of an electronics readout cell. The readout is binary: in each cell, a threshold is applied to the pre-amplified and shaped signal and the digital output level changes when the signal is above a set threshold.

Each pixel chip provides a *Fast-OR* digital pulse when one or more of the pixels in the matrix are fired. The Fast-OR allows for the implementation of a unique prompt trigger capability. The pre-processed Fast-OR data can be used to contribute to the *Level 0* trigger decision in the ALICE Central Trigger Processor (CTP). This feature is very useful in particular in the case of events with very low multiplicities in pp runs. In the ALICE trigger system, the bunch-crossing ambiguity can be resolved by considering the coincidence between the pixel trigger signal and the V0 detector signal.

The Silicon Drift Detectors (SDD) equip the two intermediate layers of the ITS, where the track density is expected to reach up to 7 tracks per cm^{-2}. They have very good multitrack capability and provide two out of the four dE/dx samples needed for the ITS particle identification. The SDDs were produced from very homogeneous high-resistivity (3 kWcm) 300 μm thick Neutron Transmutation Doped (NTD) silicon [89]. The sensitive area is split into two drift regions by the central cathode strip to which a HV bias of -2.4 kV is applied. In each drift region, and on both detector surfaces, 291 p$^+$ cathode strips, with 120 μm pitch, fully deplete the detector volume and generate a drift field parallel to the wafer surface. The space precision along the drift direction ($r\phi$), as obtained during beam tests of full-size prototypes, is better than 38 μm over the

whole detector surface. The precision along the anode axis (z) is better than 30 μm over 94% of the detector surface and reaches 60 μm close to the anodes, where a fraction of clusters affects only one anode. The average values are 35 μm and 25 μm respectively. The detection efficiency is larger than 99.5% for amplitude thresholds as high as 10 times the electronic noise.

The outer layers of the ITS are crucial for the matching of tracks from the TPC to the ITS. Both outer layers use double sided Silicon Strip Detectors (SSD). They provide a two dimensional measurement of the track position. In addition they provide $\mathrm{d}E/\mathrm{d}x$ information to assist particle identification for low-momentum particles. The system is optimized for low mass in order to minimise multiple scattering. The spatial resolution of the SSD system is determined by the 95 μm pitch of the sensor readout strips and the charge-sharing between those strips. Without making use of the analogue information, the r.m.s spatial resolution is 27 μm. Beam tests have shown that a spatial resolution of better than 20 μm in the $r\phi$ direction can be obtained by analysing the charge distribution within each cluster. In the direction along the beam the spatial resolution is 820 μm.

TPC

The Time-Projection Chamber (TPC) [90] is the main tracking detector of the central barrel and is optimised to provide, together with the other central barrel detectors, charged-particle momentum measurements with good two-track separation, particle identification, and vertex determination. In addition, data from the central barrel detectors are used to generate a fast on-line High-Level Trigger (HLT) for the selection of low cross section signals. The phase space covered by the TPC in pseudo-rapidity is $|\eta| < 0.9$ for tracks with full radial track length (matches in ITS, TRD, and TOF detectors); for reduced track length (at reduced momentum resolution), an acceptance up to about $|\eta| < 1.5$ is accessible. The TPC covers the full azimuth (with the exception of the dead zones). A large p_{t} range, from low p_{t} of about 0.1 GeV/c up to 100 GeV/c, is accessible with good momentum resolution.

For pp runs, the memory time of the TPC is the limiting factor for the luminosity due to its ~ 90 μs drift time. In pp collisions with a luminosity of about 5×10^{30} cm^{-2}s^{-1} (interaction rate of about 350 kHz) "past" and "future" tracks from an average of 60 pp interactions are detected together with the triggered event; the detected multiplicity corresponds to about 30 minimum-bias pp events. The total occupancy, however, is lower by more than an order of magnitude than in Pb–Pb collisions, since the average pp multiplicity was estimated to be about a factor 10^3 lower than the Pb–Pb multiplicity for central collisions. Tracks from pile-up events can be eliminated because they point to the wrong vertex.

The TPC design is "conventional" in overall structure but innovative in many aspects. The TPC is cylindrical in shape; the active volume has an inner radius of about 85 cm, an outer radius of about 250 cm, and an overall length along the beam direction of 500 cm. The detector is made of a large cylindrical field cage, filled with 90 m^3 of $\mathrm{Ne/CO_2/N_2}$ (85.7%/9.5%/4.9%)[2], in which the primary electrons are transported over a distance of up to 2.5 m on either side of the central electrode to the end plates. Multiwire proportional chambers with cathode pad readout are mounted into 18 trapezoidal sectors at each end plate. The overall active area measures 32.5 m^2. Because of the

[2]From 2010 the N_2 is not used, so the proportion Ne/CO_2 end up to be 90%/10%, but the N_2 will possibly be restored in 2012.

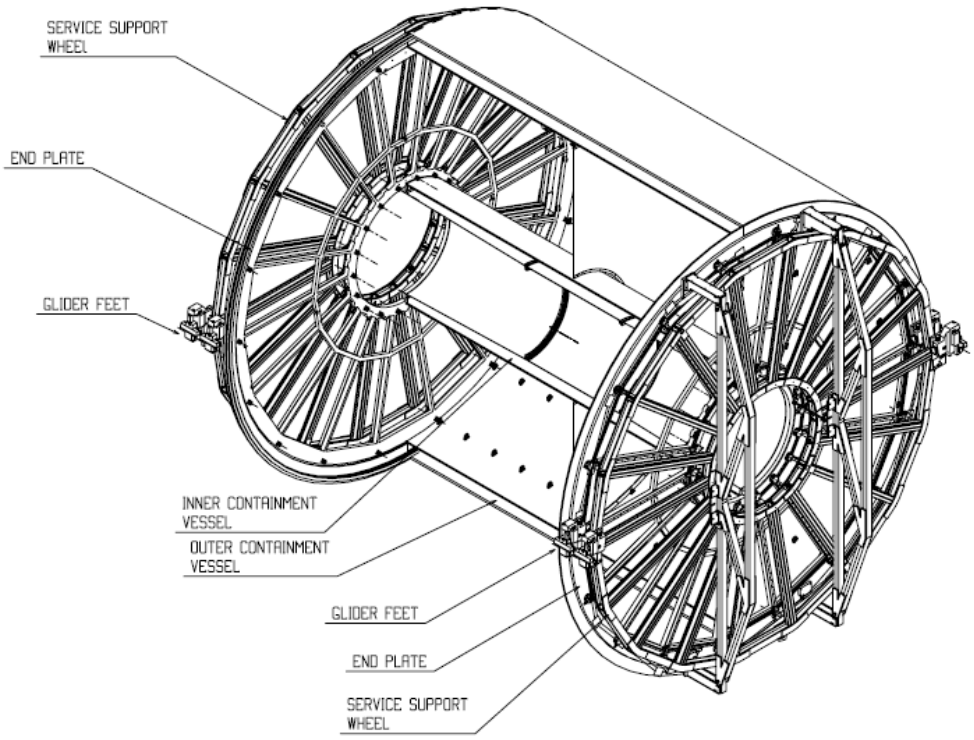

Figure 2.7: 3D view of the TPC.

radial dependence of the track density, the readout is segmented radially into two readout chambers. The detector layout is shown in Fig. 2.7.

The field cage is based on a design with a central high-voltage electrode and two opposite axial potential dividers which create a highly uniform electrostatic field in the common gas volume of about 400 V/cm, with a high voltage of 100 kV at the central electrode, which results in a maximum drift time of about 90 μs. The drift gas is optimised for drift speed, low diffusion, low radiation length and hence low multiple scattering, small space-charge effect, ageing, and stability properties.

TOF

The Time-Of-Flight (TOF) detector is a large area array that covers the central pseudo-rapidity region ($|\eta| < 0.9$) for particle identification through the measurement of the time of flight of tracks. It covers the intermediate momentum range, below about 2.5 GeV/c for pions and kaons, up to 4 GeV/c for protons, with a π/K and K/p separation better than 3σ. The TOF, coupled with the ITS and TPC for track and vertex reconstruction and for dE/dx measurements in the low-momentum range (up to about 1 GeV/c), will provide event-by-event identification of large samples of pions, kaons, and protons. In addition, at the inclusive level, identified kaons will allow invariant mass studies, in particular the detection of open heavy-flavoured states and vector-meson resonances such as the ϕ meson. Since a large area had to be covered, a gaseous detector was chosen, the Multi-gap Resistive-Plate Chamber (MRPC). The key aspect of these chambers is that the electric field is high and uniform over the full sensitive gaseous volume of the detector. Any ionisation produced by a traversing charged particle immediately starts a gas avalanche process which generates the observed signals on the pick-up electrodes. Unlike

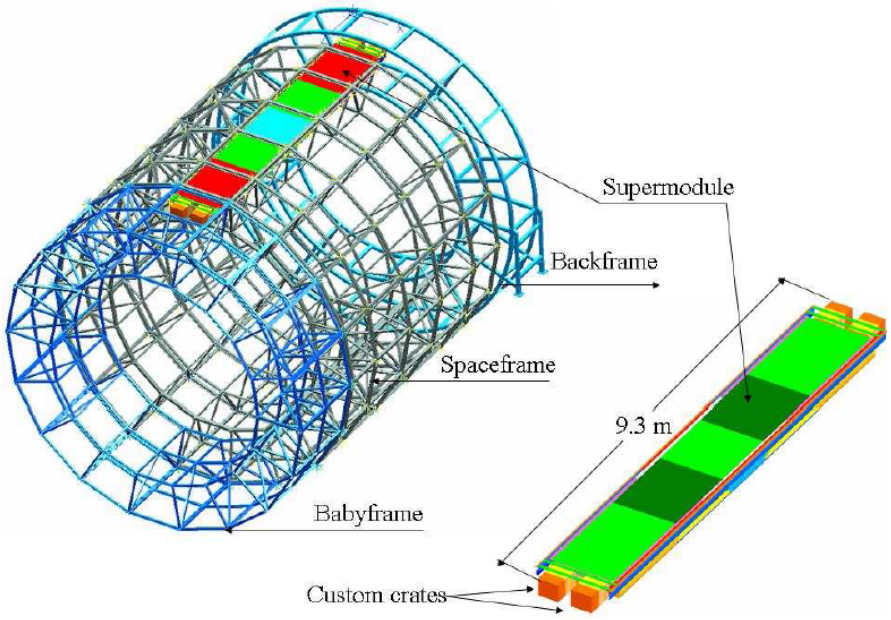

Figure 2.8: Schematic drawing of one TOF supermodule, consisting of 5 modules, in the ALICE spaceframe.

other types of gaseous detectors, there is no drift time associated with the movement of the electrons to a region of high electric field. Thus the time jitter of these devices is caused by the fluctuations in the growth of the avalanche. The final tests of several MRPC multicell strips from mass production confirmed that these devices indeed reach an intrinsic time resolution better than about 40 ps and an efficiency close to 100%. In Fig. 2.8 the location of one supermodule within the ALICE spaceframe is drawn.

V0

The V0 detector is a small angle detector consisting of two arrays of scintillator counters, called V0A and V0C (Fig. 2.9), which are installed on either side of the ALICE interaction point. This detector has several functions. It provides minimum-bias triggers for the central barrel detectors in pp and Pb–Pb collisions. These triggers are given by particles originating from initial collisions and from secondary interactions in the vacuum chamber elements. As the dependence between the number of registered particles on the V0 arrays and the number of primary emitted particles is monotone, the V0 serves as an indicator of the centrality of the collision via the multiplicity recorded in the event. Cuts on the number of fired counters and on the total charge can be applied to achieve rough centrality triggers. There are three such triggers, the multiplicity, semi-central and central triggers. In practice and during normal operation, both arrays are required (AND mode), but an OR mode can also be adopted. Finally, the V0 detector participates in the measurement of luminosity in pp collisions with a precision of about 10%. The V0A detector is located 340 cm from the vertex on the side opposite to the muon spectrometer whereas V0C is fixed to the front face of the hadronic absorber, 90 cm from the vertex. They cover the pseudo-rapidity ranges $2.8 < \eta < 5.1$ (V0A) and $-3.7 < \eta < -1.7$ (V0C) and are segmented into 32 individual counters each distributed in four rings.

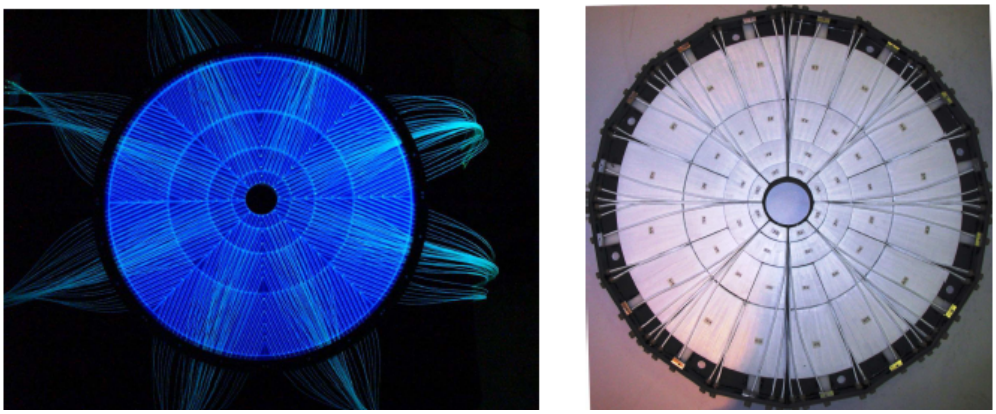

Figure 2.9: Front view of V0A (left) and V0C (right) arrays.

T0

The T0 detector consists of two arrays of Cherenkov counters, 12 counters per array. It was designed with the following objectives. First, to generate a start time (T0) for the TOF detector. This timing signal corresponds to the real time of the collision (plus a fixed time delay) and is independent of the position of the vertex. The required precision of this signal is about 50 ps (r.m.s.). Then, to measure the vertex position (with a precision $\pm$ 1.5 cm) for each interaction and to provide a L0 trigger when the position is within the preset values. This discriminates against beam-gas interactions. The T0 can also generate an early "wake-up" signal to the Transition Radiation Detector, described below, prior to the earliest trigger signals (L0). In addition, T0 provides redundancy to the V0 counters and can generate minimum bias (one or both arrays hit) and multiplicity triggers (semi-central and central).

2.3.2 Other detectors

Central barrel

The other detectors in the central barrel are the TRD, the HMPID, the PHOS and the EMCal.

The Transition Radiation Detector (TRD) has the aim of providing electron identification in the central barrel for momenta above 1 GeV/c. Below this momentum electrons can be identified via specific energy loss measurement in the TPC. Above 1 GeV/c transition radiation (TR) from electrons passing a radiator can be exploited in concert with the specific energy loss in a suitable gas mixture to obtain the necessary pion rejection capability. Exploiting the excellent impact parameter resolution of the ITS it is possible to reconstruct open charm and open beauty in semi-leptonic decays. The TRD was designed to derive a fast trigger for charged particles with high momentum. It is part of the Level 1 trigger and can significantly enhance the recorded Υ-yields, high-p_{t} J/ψ, the high-mass part of the dilepton continuum as well as jets. The TRD has 4π azimuthal coverage and pseudorapidity coverage $|\eta| < 0.84$.

The High-Momentum Particle Identification Detector (HMPID), is dedicated to inclusive measurements of identified hadrons at $p_{\mathrm{t}} > 1$ GeV/c. The aim is to enhance the PID capability of ALICE by enabling identification of charged hadrons beyond the momentum interval attainable through energy-loss (in ITS and TPC) and time-of-flight measurements (with TOF). The detector was optimised to extend the useful range for

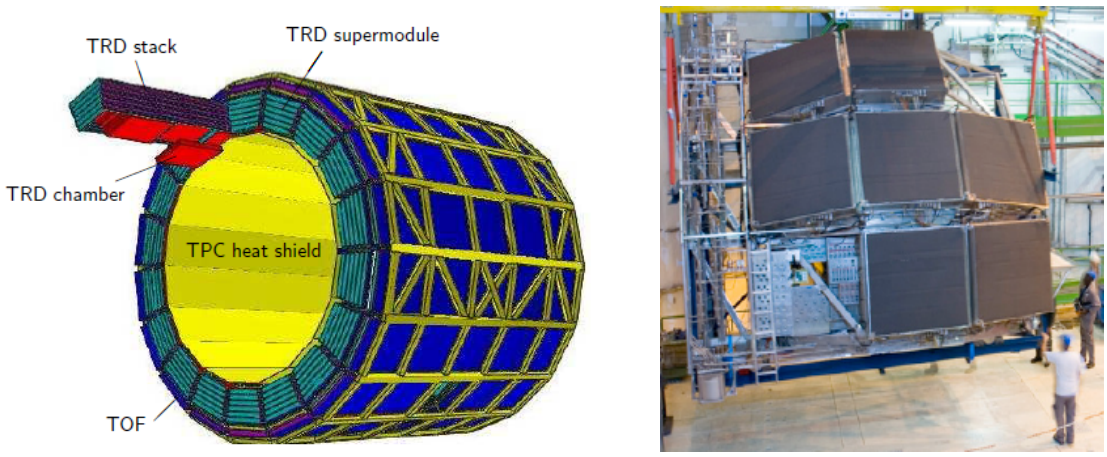

Figure 2.10: Left panel: Schematic drawing of the TRD layout in the ALICE space frame. Right panel: Photo of the HMPID mounted on the cradle.

π/K and K/p discrimination, on a track-by-track basis, up to 3 GeV/c and 5 GeV/c, respectively. The HMPID was designed as a single-arm array with an acceptance of 5% of the central barrel phase space. In addition the identification of light nuclei and anti-nuclei (d, t, ^{3}He, α) can also be performed with the HMPID. The working principle is the proximity-focusing Ring Imaging Cherenkov (RICH) counters.

The PHOton Spectrometer (PHOS) is a high-resolution electromagnetic spectrometer covering a limited acceptance domain at central rapidity. The main physics objectives are the test of thermal and dynamical properties of the initial phase of the collision extracted from low-p_{t} direct photon measurements and the study of jet quenching through the measurement of high-p_{t} π^0 and γ-jet correlations. Direct photons are discriminated against decay photons either through shower shape analysis at high p_{t} or through invariant mass analysis at low p_{t}. The identification of photons requires high discrimination power against charged hadrons, neutrons and anti-neutrons. The high-energy resolution and granularity are provided by using dense scintillator material (lead-tungstate, $PbWO_4$) of 20 X_0 with high photo-electron yield. The two-photon invariant mass resolution at the π^0 peak is 3.5%.

The construction of a large ElectroMagnetic Calorimeter (EMCal) began in 2008 with the aim to enable ALICE to explore in detail the physics of jet quenching (interaction of energetic partons with dense matter) over the large kinematic range accessible in heavy-ion collisions at the LHC. The EMCal is a large Pb-scintillator sampling calorimeter with cylindrical geometry, located at a radius of $\sim$ 4.5 metres from the beam line. It covers $|\eta| \leq 0.7$ and $\Delta\phi = 107°$ and it is positioned approximately opposite in azimuth to the PHOS. It provides a fast and efficient trigger (L0, L1) for hard jets, photons and electrons. The EMCal also measures the neutral energy component of jets, enabling full jet reconstruction in all collision systems and excellent sensitivity to the full range of jet-quenching effects expected at the LHC in Pb–Pb collisions.

At forward rapidity

The Muon spectrometer is located in the pseudorapity region $-4 < \eta < -2.5$. This detector is able to measure the complete spectrum of heavy-quark vector mesons resonances (J/ψ, ψ', Υ, ...) as well as the ϕ meson in the $\mu^+\mu^-$ decay. The spectrometer consists of the following components: a passive front absorber to stop hadrons and photons from

Figure 2.11: Left panel: Crystal detector unit of the PHOS detector. Right panel: Prototype of EMCal module.

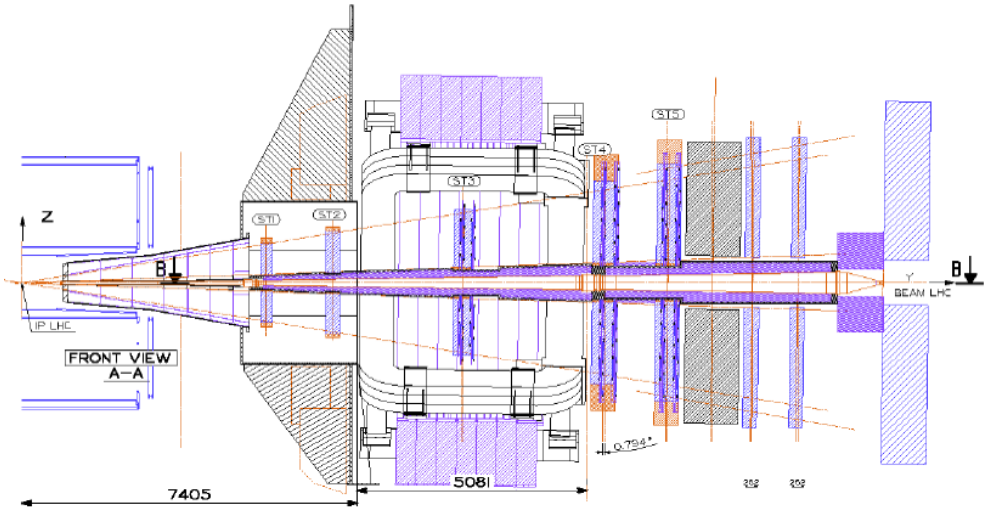

Figure 2.12: Muon spectrometer longitudinal section.

the interaction vertex; a high-granularity tracking system of 10 detection planes; a large dipole magnet; a passive muon-filter wall, followed by four planes of trigger chambers; an inner beam shield to protect the chambers from primary and secondary particles produced at large rapidities. The muon spectrometer relies on the V0 detector as a fast interaction trigger. A High-Level Trigger (HLT) for dimuons reduces, by a factor four to five, the need in bandwidth and data storage. The tracking chambers were designed to achieve a spatial resolution of about 100 μm, necessary for an invariant-mass resolution of the order of 100 MeV/c^2 at the Υ mass. The technology chosen is the Cathode Pad Chambers and the chamber thickness corresponds to about 0.03 X_0. In order to reduce the background from π and K decaying in low-p_{t} muons at the trigger level a position-sensitive trigger detector with space resolution better than 1 cm is required. This resolution is achieved by Resistive Plate Chambers (RPCs) operated in streamer mode. The trigger system consists of four RPC planes arranged in two stations, placed behind the muon filter.

A set of Zero-Degree Calorimeters (ZDC) measures the spectator nucleons in the collision. The number of participant nucleons is the observable most directly related to

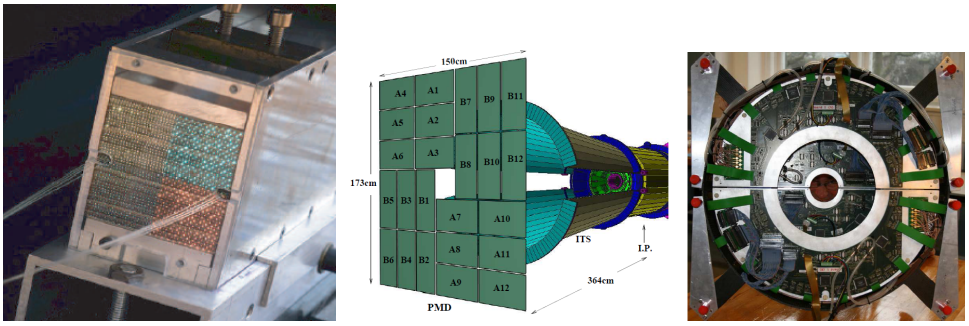

Figure 2.13: Left panel: Front face of the neutron calorimeter. Central panel: The position and layout in ALICE of the PMD detector with respect to the ITS. Right panel: Assembled FMD3 detector.

the geometry of nucleus-nucleus collisions. It can be estimated by measuring the energy carried in the forward direction (at 0° relative to the beam direction) by non-interacting (spectator) nucleons. The centrality information provided by the ZDC, with its impact parameter resolution of $\sim$ 1 fm, is also used for triggering at Level 1 (L1). Finally, the ZDC being also a position-sensitive detector, can give an estimate of the reaction plane in nuclear collisions. Two sets of hadronic ZDCs, made of quartz fibres sampling calorimeters, are located at 116 m on either side of the interaction point. In addition, two small electromagnetic calorimeters (ZEM) of a very dense W-alloy are placed on both sides of the beam pipe, opposite to the muon arm.

The multiplicity and spatial (η - ϕ) distribution of photons in the forward pseudo-rapidity region of $2.3 < \eta < 3.7$ are measured by the Photon Multiplicity Detector (PMD). These measurements also provide estimations of transverse electromagnetic energy and the reaction plane on an event-by-event basis. The measurement of photon multiplicity gives important information in terms of limiting fragmentation, order of phase transition, the equation of state of matter and the formation of disoriented chiral condensates. The sensitive element of the detector consists of large arrays of gas proportional counters in a honeycomb cellular structure.

The main functionality of the Forward Multiplicity Detector (FMD) is to provide charged-particle multiplicity information in the pseudo-rapidity range $-3.4 < \eta < -1.7$ and $1.7 < \eta < 5.0$. Overlap regions between the FMD silicon rings and the ITS inner pixel layer provide redundancy between subdetectors and ensures continuous coverage for a distribution of vertices along the z-axis. Additionally, high radial detector segmentation allows for the study of multiplicity fluctuations on an event-by-event basis while azimuthal segmentation allows for the determination of the reaction plane for each event and the analysis of flow within the FMD's pseudo-rapidity coverage. The system readout time (> 1.2 μs) does not allow the FMD to serve as a multiplicity trigger and, therefore, provides only offline analysis information. Each of the three FMD ring consists of 10 (inner) or 20 (outer) silicon sensors.

2.4 Processing of the raw data

2.4.1 Offline framework, simulation and reconstruction

A schematic diagram of the ALICE offline framework, *AliRoot* [91], is shown in Fig. 2.14. Its implementation is based on Object-Oriented techniques for programming and, as a supporting framework, on the *ROOT* system [92], complemented by the *AliEn* system

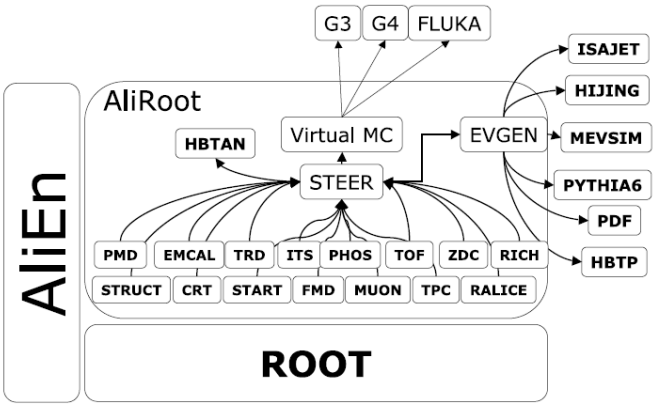

Figure 2.14: Schematic view of the AliRoot framwork.

[93] which gives access to the computing Grid [94]. These fundamental technical choices result in one single framework, entirely written in C++, with some external programs (hidden to the users) still in FORTRAN. The AliRoot framework is used for simulation, alignment, calibration, reconstruction, visualisation and analysis of the experimental data.

Event simulation is performed through events generators, like PYTHIA [75] and HIJING [95]. All the information about the generated particles (e.g. type, momentum, parent particles and production process, decay products) is organised in a kinematic tree stored in a file. The particle transport in the detector is recorded as *hits*. The detector shape is modelled with ROOT geometrical tools, as much realistically as possible, down to the level of all mechanical structures and single electronic components. Particle transport codes like GEANT3 [96], GEANT4 [97, 98] and FLUKA [99], by interfacing with the geometry, can reproduce the particle interactions with the material. For each hit the corresponding digital output of the detector is stored as a *"summable" digit* taking into account the detector response function. The possible noise is taken into account moving from summable digit to *digit*. Finally the digits are converted to the simulated *raw data*, with the specific hardware format of the detector.

The raw data, representing the response of the detector, are the starting point of the reconstruction process, which is identical for both simulated and real events.

Typically the detectors perform a local reconstruction, or *clusterisation*, to better estimate the position of the crossing particle and to reduce the effect of random noise. Then the interaction primary vertex is estimated, followed by the real tracking exploiting the Kalman filter procedure, and by the PID. Finally the secondary vertices are reconstructed. All these steps will be explained in more detail below. The final output of the reconstruction is stored in the ESD (Event Summary Data), where all the useful information on the event is recorded. At the analysis level, a lighter and easy to handle object is created: the AOD (Analysis Object Data), a condensed version of the ESD containing only the information needed to the end user analysis. More specific and condensed versions of AODs can be produced *ad hoc* for different analyses. In Fig. 2.15, the steps of the simulation that lead to the raw data as well as the parallel path with real data are schematically represented together with the common reconstruction flow.

The analysis framework is organized in *scheduled* and *end-user* analysis. Scheduled analysis is performed in a way that sometimes is indicated as "freight train". ALICE generic analysis framework attaches a number of official (at the level of the collaboration) algorithms (the *"coaches"*) and "carries" them through the data. The advantage is that

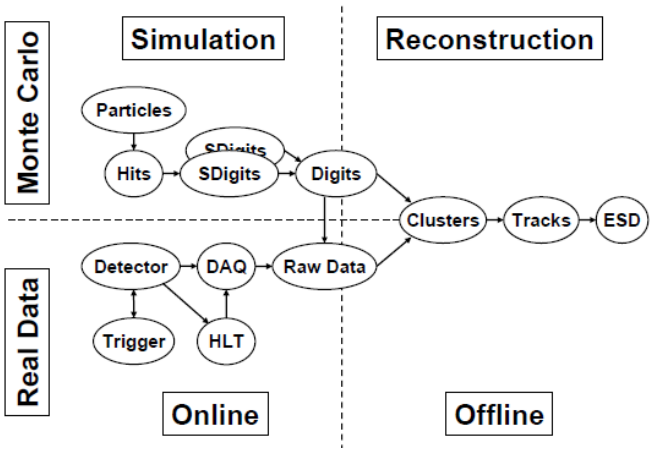

Figure 2.15: Schematic view of the reconstruction framework.

each event is read only once and the different algorithms are applied to it. End-user analysis comprises all the activities performed by users in the framework of a specific physics analysis activity.

2.4.2 Primary vertex determination

The reconstruction of the primary vertex is based on the information provided by the Silicon Pixel Detectors (SPD), the two innermost layers of the ITS. Pairs of reconstructed points in the two layers (called *tracklets*), close in azimuthal angle in the transverse plane, are selected. Then from their z-coordinates the z-position of the primary vertex is estimated using a linear extrapolation. Finally a similar procedure is performed in the transverse plane. Here, due to the bending in the magnetic field, the linear extrapolation is a somewhat crude approximation; however, thanks to the short distances from the interaction point, the x- and y-coordinates of the primary vertex are determined with a sufficient precision to be used as constraints in the first tracking pass. This estimate of the primary vertex position is then used to correct the measurement of the z-coordinate, for effects due to an off-axis position of the interaction point in the transverse plane. The resolution on the position of the primary vertex depends on the track multiplicity, i.e. on the charged-particle density. For heavy-ion charged-particle densities the resolution on the vertex position is at the 10 μm level, and for the average pp event ($\mathrm{d}N_{\mathrm{ch}}/\mathrm{d}\eta$ = 6-7) at the 150 μm level.

This measurement of the primary vertex position is used as an input for the tracking. After track reconstruction, the position of the primary vertex is recalculated using the measured track parameters.

In Fig. 2.16, left panel, the σ of the vertex distribution measured in pp collisions at 7 TeV by the SPD (empty markers) and after the tracking (filled markers) is shown as a function of the charged multiplicity for the x- and y-coordinate in circle and triangle, respectively. The asymptotic limit of the fit to the σ measured with tracks is an estimation of the size of the luminous region. The fitting function, reported in the figure, includes also a resolution term, proportional to $1/\sqrt{n_{tracklets}}$.

Fig. 2.16, right panel, shows the vertex resolution in Pb–Pb collisions at $\sqrt{s_{NN}}$ = 2.76 TeV as a function of half of the tracklet multiplicity of the event. The x-coordinate of the vertex is indicated by circles, the z-coordinate by triangles. The resolution of the vertexer is obtained dividing the tracks of the event into two random sub-sample and

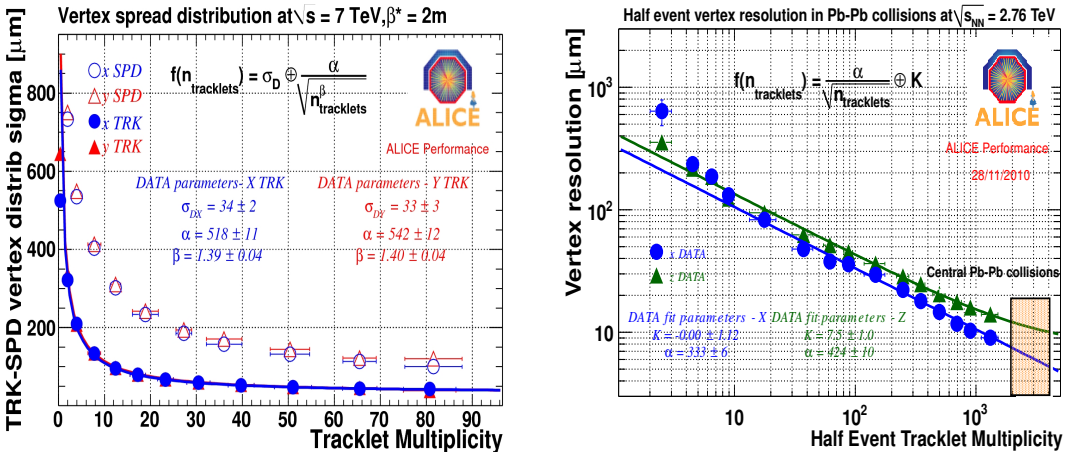

Figure 2.16: Left panel: Resolution on the primary vertex position determined using reconstructed tracks (closed markers) and SPD tracklets (open markers) in the x (circle) and y (triangle) directions, as a function of charged-particle multiplicity for pp data at $\sqrt{s} = 7$ TeV. Right panel: Vertex resolution in Pb–Pb collisions at $\sqrt{s_{NN}} = 2.76$ TeV as a function of half of the tracklet multiplicity of the event in the x- (circle) and z-direction (triangle). The orange box represents the vertex resolution for the multiplicities measured in 0-5% central events extrapolated from the fit.

reconstructing the vertex in each of them. The difference between the two vertices is the measure of the resolution as a function of half of the tracklet multiplicity. The orange box in the figure represents the vertex resolution for the multiplicities measured in 0-5% central events extrapolated from the fit.

2.4.3 Track reconstruction

The basic method employed for track finding and fitting is the *Kalman filter* as introduced to this field by P. Billoir [100–103]. This method depends critically on the determination, for each track, of a set of initial seed values for the track parameters and their covariance matrix. This seeding is done using the space points reconstructed in the TPC. The space-point positions are calculated from the centre of gravity of the two-dimensional clusters (in the pad-row and time directions). At high particle densities, due to the large occupancy, a more sophisticated cluster unfolding, which takes into account the cluster structure, is used. The seeding is done twice: the first time assuming that the track originated from the primary vertex and the second assuming that the track originated elsewhere (decay, secondary interaction, etc.).

The space points are combined starting from a few outermost pad rows using, in the first pass, the primary vertex position as a constraint. The procedure is repeated several times, choosing a set of pad rows closer and closer to the centre of the TPC. A track takes shape from each seed, pad row by pad row, inside the TPC. The Kalman filter essentially consists of the following steps:

1. the state vector of the track parameters and their covariance matrix are propagated to the next pad row,

2. a noise term (representing the information loss due to stochastic processes like multiple scattering and energy loss fluctuations) is added to the inverted covariance

matrix (which represents the information matrix of the track parameters at that point),

3. if the filter finds, in the new pad row, a space point compatible with the track prolongation, this measurement is added and the track parameters are updated to the covariance matrix, increasing the information.

The seeding is repeated a second time, without the primary vertex constraint proceeding again as outlined above. The track-finding efficiency after this stage, normalized to the number of tracks which are potentially findable (i.e. without taking into account decays in flight, detector acceptances, etc.), is nearly 100%.

After this step, the tracks are propagated to the outer layers of the ITS starting with the highest-momentum tracks in order to make the most precise (i.e. less ambiguous) track-space point assignments first. For highly ionizing tracks in the TPC, this knowledge is used in the ITS tracking for energy loss corrections and multiple scattering noise estimates. Tracks found in the TPC as primaries are followed by the Kalman filter in two independent passes, first imposing the primary vertex position as a constraint, and then without this condition. Both sets of track parameters are stored for further analysis. The tracks found during the second TPC pass (i.e. without vertex constraint) are followed in the ITS only without imposing the primary vertex constraint. Whenever more than one space-point candidate is found within the search window around the prolongation of a track (a half-width of four standard deviations is typically used), all possible assignments are used as different hypotheses and are followed independently towards the innermost ITS layer. In this way each TPC track can have several candidate paths throughout the ITS. A decision is made only at the end, based on the sum of the χ^2 along the track-candidates' path in the ITS. Optionally, layer skipping and cluster sharing between tracks are allowed.

When the ITS tracking is completed, the Kalman filter is applied again in the reversed order following the track from the inner ITS layers outwards. Starting with much more precise track parameters than during the first step, improperly assigned points (outliers) can be eliminated.

The procedure then continues following the tracks beyond the TPC, assigning space points in the TRD, and matching the tracks with hits in the TOF, minimum-ionizing clusters in the HMPID and space points in the CPV (Charged-Particle Veto detector), located in front of the PHOS.

Finally, the Kalman filter is reversed one last time refitting all tracks from the outside inwards, in order to obtain the values of the track parameters at, or nearby, the primary vertex. Optionally, it is possible to proceed with an additional track-finding step using only points from the ITS, after having removed all the ITS space points already assigned to tracks. This is useful for finding tracks that have not been seeded in the TPC because they went through a non-sensitive area (e.g. in between the readout chambers). The best relative momentum precision, limited by multiple scattering to about 0.7%, is achieved for low-momentum tracks with p_{t} of about 500 MeV/c.

The track parameters obtained both with and without the primary vertex constraint are stored for all tracks, in order to allow for the subsequent analysis of short-lived particle decays (such as charm and beauty decays) taking place very close to the primary vertex.

Tracking performance

The main performance parameter relevant for heavy-flavour analyses is the resolution of the impact-parameter (the distance between the primary vertex and the track prolon-

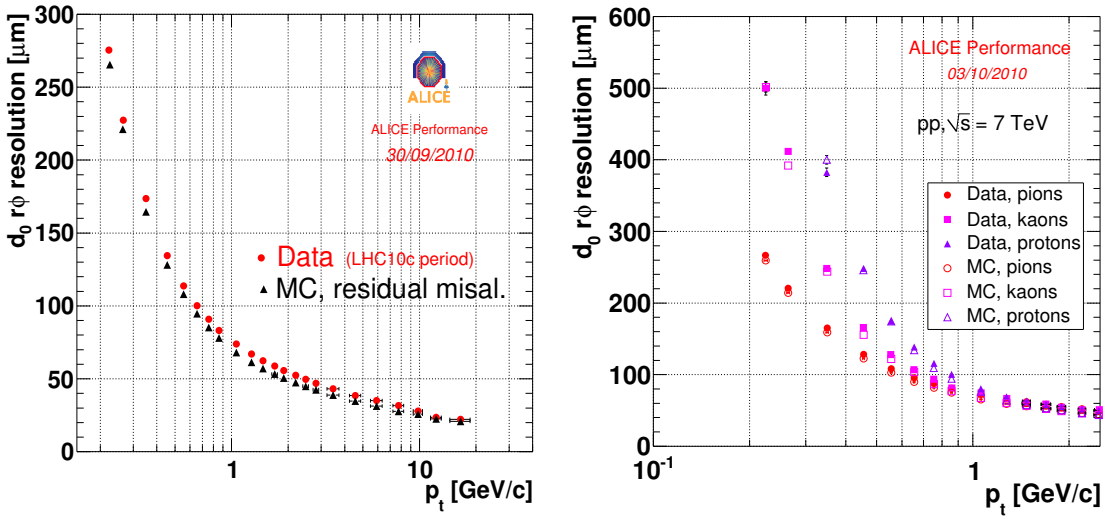

(a) Charged tracks: data in red square, Monte Carlo simulations in black triangle.

(b) Pion (red circle), kaon (magenta square), and proton (violet triangle). Data are closed and Monte Carlo open markers.

Figure 2.17: Resolution on the impact parameter in the transverse plane ($r\phi$) for pp collisions at $\sqrt{s} = 7$ TeV.

gation to the point of closest approach to the primary vertex). This resolution depends both on the precision of the primary-vertex-position determination and on the precision of the determination of the track-parameters. In Fig. 2.17 the impact-parameter resolution in the transverse direction ($r\phi$) is shown as a function of p_{t}, in pp collisions at 7 TeV compared to Monte Carlo simulations. In Fig. 2.17(a), the impact parameter resolution is determined for all charged tracks, while, in Fig. 2.17(b), the particle identification form ITS at low-p_{t} is used to separate the contribution of different species. The resolutions for Pb–Pb collisions at 2.76 TeV are shown in Fig. 2.18.

Figure 2.19, left panel, shows the TPC-ITS prolongation efficiency in pp collisions, for data (closed markers) and Monte Carlo (open markers) and for two choices of requests on ITS hits. The efficiency is constant as a function of p_{t}, compatible with the Monte Carlo expectations, and close to 1 with the loosest request of ITS hits. In the right panel, the ratio between the TPC-ITS prolongation efficiency in central over peripheral Pb–Pb collisions is shown, as a function of p_{t}, for data (red circle) and Monte Carlo (black triangle). The efficiency increases at low p_{t} for central events due to the presence of more fake tracks with respect to peripheral events.

The achieved p_{t} resolution in Pb–Pb collisions for tracks reconstructed with TPC and ITS is shown in Fig. 2.20, where the worsening of the resolution at low p_{t} is dominated by the multiple scattering.

2.4.4 Secondary-vertex finding

Vertices from strange particle decays are searched for at the reconstruction level. Only secondary tracks, i.e. tracks which have a large enough impact parameter, are used for this purpose. The distance of closest approach (dca) of pairs of opposite-sign secondary tracks is calculated. If this distance is below some predetermined value and the point of the closest approach is located before the first measured points on both tracks, the pair

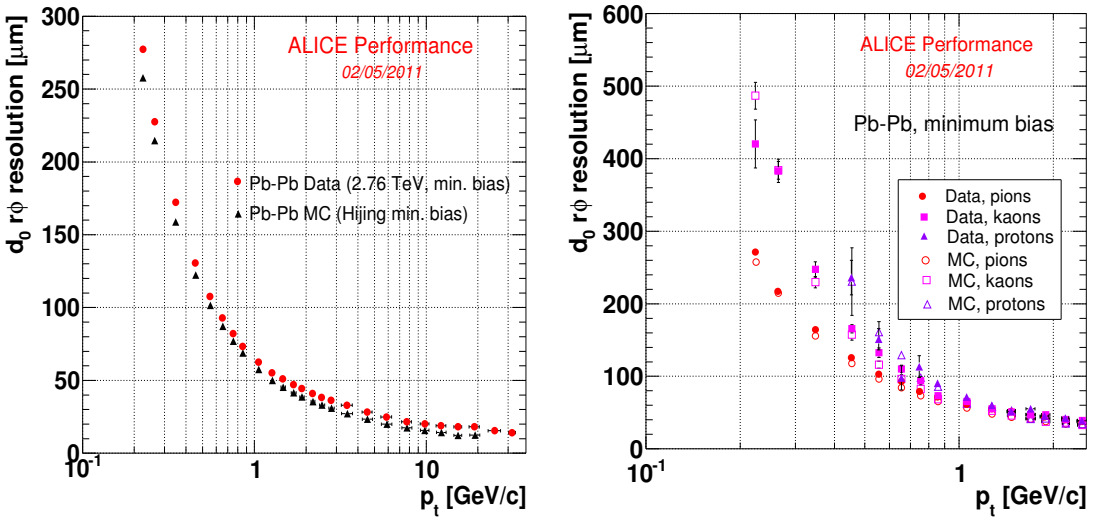

(a) Charged tracks: data in red square, Monte Carlo simulations in black triangle.

(b) Pion (red circle), kaon (magenta square), and proton (violet triangle). Data are closed and Monte Carlo open markers.

Figure 2.18: Resolution on the impact parameter in the transverse plane ($r\phi$) for Pb–Pb collisions at $\sqrt{s_{NN}} = 2.76$ TeV.

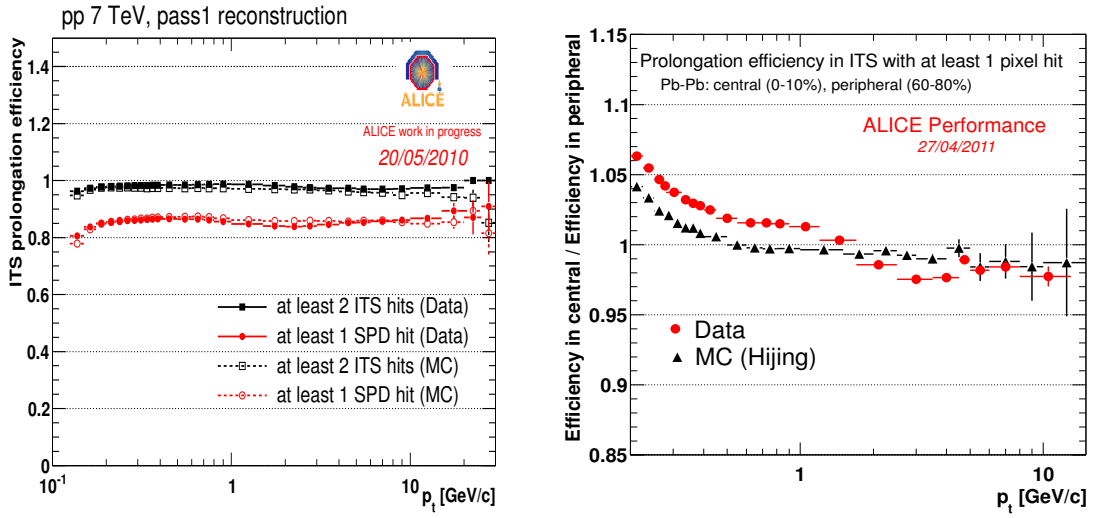

Figure 2.19: Left panel: TPC-ITS prolongation efficiency for pp data at $\sqrt{s} = 7$ TeV, pass 1 reconstruction (closed markers) and Monte Carlo simulation (open markers) as a function of p_{t}. Squares and circles markers correspond to the request of at least 2 hits in the ITS or 1 hit in the SPD, respectively. Right panel: Ratio of the TPC-ITS prolongation efficiency in central (0-10%) over peripheral (60-80%) events for Pb–Pb data at $\sqrt{s_{NN}} = 2.76$ TeV (red circle) and HIJING Monte Carlo simulations (black triangle) as a function of p_{t}. At least 1 pixel hit in the ITS requested.

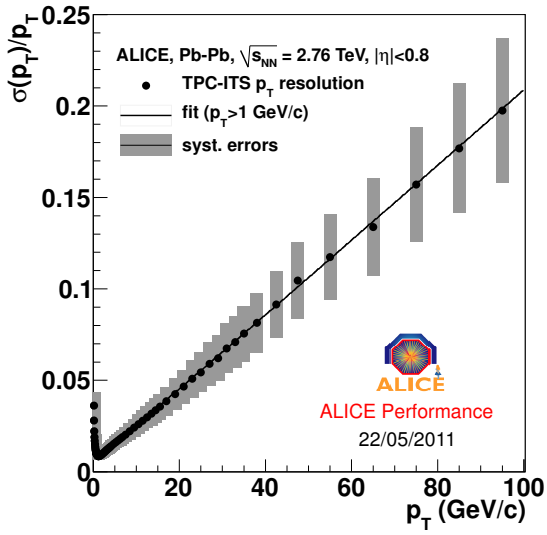

Figure 2.20: Right panel: p_{t} resolution as a function of p_{t} in Pb–Pb collisions at $\sqrt{s_{NN}}$ = 2.76 TeV.

becomes a candidate for a secondary decay vertex. Additional cuts are then imposed in the subsequent analysis phase.

At the reconstruction level, the decays in flight within the TPC fiducial volume are searched for by combining a primary track disappearing before the end of the TPC, with a secondary track of the same sign. The track pair has to be closely matched in space and to have correct space ordering of the last measured point on the primary track and the first measured point on the secondary track.

No attempt to reconstruct secondary vertices from decays of heavy-flavour particles is made at the reconstruction stage. Such decays are only dealt with at the analysis level.

2.4.5 Particle identification performance

Particle identification is a crucial tool for ALICE in the heavy-ion physics, due to the high combinatorial background to deal with. Most of the sub-detectors provide PID information, allowing for the identification of K, π, p, electrons, and γ in various range of momentum, according to the specific detector characteristics.

In this sections the focus will be mainly on the detectors used in the analyses presented in Chapters 4 and 5, namely TPC and TOF, with the addition of some highlights from ITS PID and high-momentum PID, not used in the analyses described in this thesis. The main interest for the D meson related analyses is the identification of the K which enter in the D meson hadronic decay channels and allow to reject a large amount of background, mainly at low p_{t}.

The TOF detector exploits the characteristic time-of-flight of the particles to distinguish them. Its PID power extends to the intermediate momenta, above 300 MeV/c and below about 2 GeV/c for kaons and $\sim$ 4 GeV/c for protons. In Fig. 2.21 an example of the TOF PID performance is shown for pp (left panel) and Pb–Pb (right panel) collisions. In the left panel, the measured TOF particle β is shown as a function of the momentum divided by the charge of the particle. The bands of pion, kaon, proton, and deuteron are nicely distinguishable for momenta lower than 1.5 GeV/c for π/K and lower than $\sim$ 3 GeV/c for K/p. In the right panel the distribution of the difference

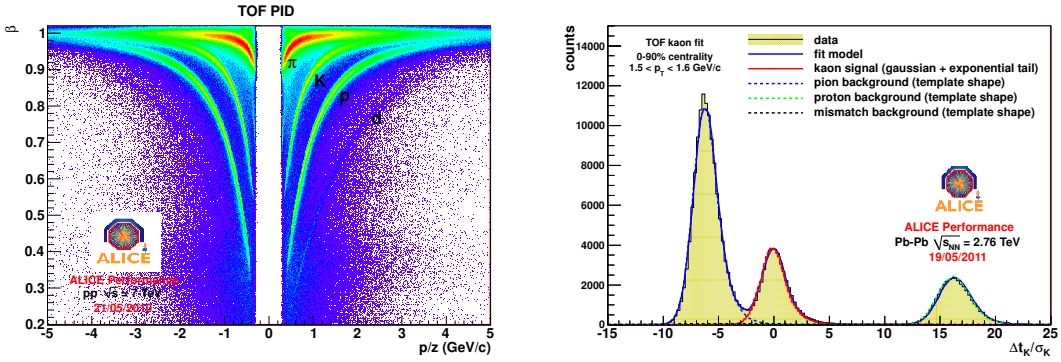

Figure 2.21: Left panel: TOF measured particle beta vs. signed momentum in pp collisions at $\sqrt{s} = 7$ TeV. Right panel: TOF kaon fit in Pb–Pb 0-90% central collisions at $\sqrt{s_{NN}} = 2.76$ TeV in $1.5 < p_{\mathrm{t}} < 1.6$ GeV/c. The shaded area represents data, the lines are described in the legend.

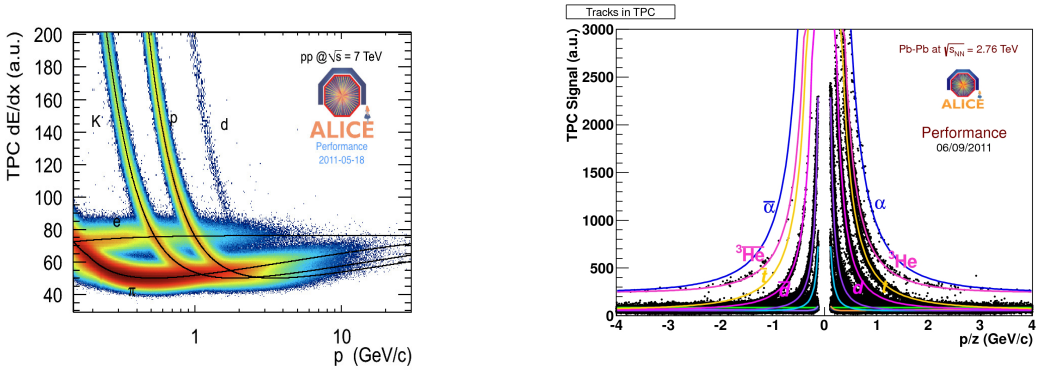

Figure 2.22: Left panel: $\mathrm{d}E/\mathrm{d}x$ as a function of momentum measured by the TPC in pp collisions at $\sqrt{s} = 7$ TeV. Right panel: TPC signal as a function of signed momentum in Pb–Pb collisions at $\sqrt{s_{NN}} = 2.76$ TeV. In both figures, the Bethe-Bloch lines for various particle species are superimposed.

between the measured and the expected time for kaon normalized to the resolution is fitted with the expected functional forms for kaons (red Gaussian with exponential tails around zero in the figure), pions (at negative times), and protons (positive times). In the range $1.5 < p_{\mathrm{t}} < 1.6$ GeV/c used in the pictures, the contribution of the different particles is clearly separated.

The TPC detector can measure the energy deposit by the particles per unit length ($\mathrm{d}E/\mathrm{d}x$) and extract the PID information comparing the $\mathrm{d}E/\mathrm{d}x$ signal to the expected Bethe Bloch parametrization. The momentum range covered is below 800 MeV/c for kaons and below ~ 1.2 GeV/c for protons. Electrons can be identified applying a preliminary selection on TOF signal in order to reject hadrons.

In Fig. 2.22, left panel, the $\mathrm{d}E/\mathrm{d}x$ measured by the TPC is shown as a function of momentum in pp collisions. The lines are the Bethe Bloch parametrizations for kaon, proton, electron, and pion. In the right panel of Fig. 2.22, the TPC signal in Pb–Pb collisions is shown as a function of momentum divided by the charge. Besides pions, electrons, kaons, and protons, deuteron, tritium, ^{3}He, and α particles are detected together with their anti-particles.

Finally, in Fig. 2.23 an example of the possible extension of the PID power at low- and high-momenta is shown. In the left panel, the $\mathrm{d}E/\mathrm{d}x$ from the ITS as standalone

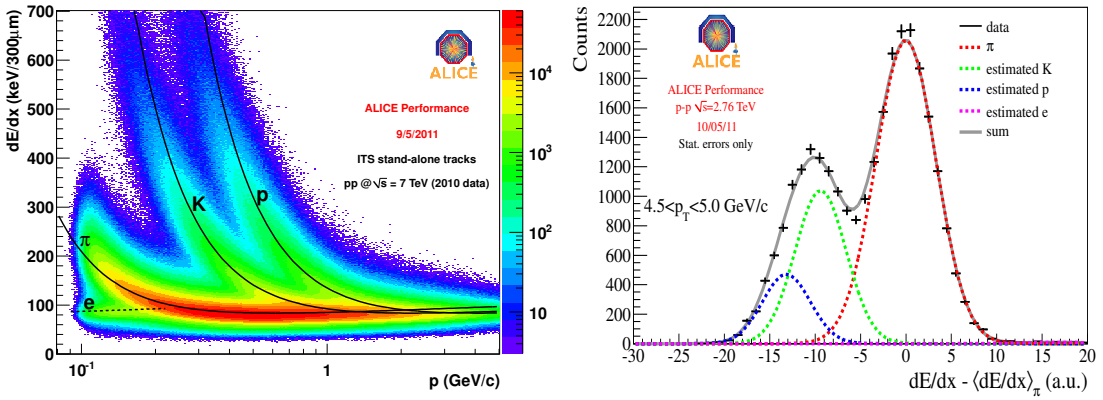

Figure 2.23: Left panel: $\mathrm{d}E/\mathrm{d}x$ as a function of momentum from ITS stand alone tracks in pp collisions at $\sqrt{s} = 7$ TeV. Right panel: $\mathrm{d}E/\mathrm{d}x$ measurement for $4 < p_{\mathrm{t}} < 5$ GeV/c in pp collisions at $\sqrt{s} = 2.76$ TeV.

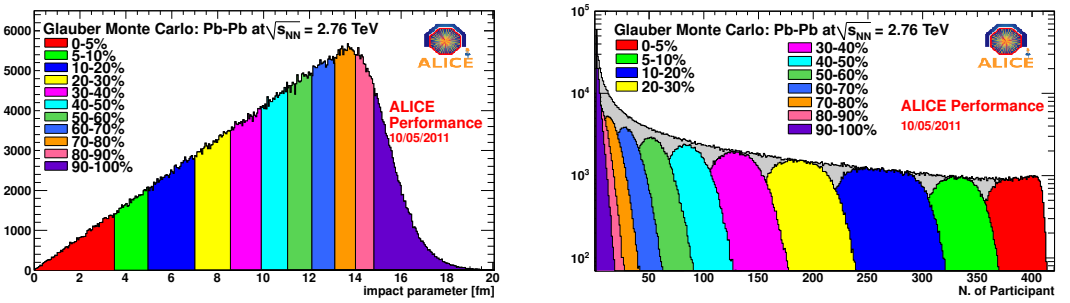

Figure 2.24: Variables related to the collision centrality calculated with a Glauber model. Left panel: Impact parameter (b). Right panel: Number of participants (N_{part}).

detector is shown as a function of momentum in pp collisions at 7 TeV. The accessible momentum goes down to ~ 100 MeV/c.

In the right panel the possibility of identification of high-p_{t} pions (~ 4.5 GeV/c in the figure) via $\mathrm{d}E/\mathrm{d}x$ measurement exploiting its relativistic rise is shown.

2.5 Centrality determination

The centrality measurement in Pb–Pb collisions is crucial for all analyses. In the ALICE experiment, different detectors are able to perform a centrality measurement hence the information is redundant and allows for important cross-checks.

The basic assumption is that the measured multiplicity is directly related to the impact parameter of the interaction and to the number of participating nucleons (N_{part}) which are determined by the collision geometry. In Fig. 2.24 the impact parameter (left) and the number of participants (right) obtained from a Glauber Model [6] Monte Carlo are correlated to the percentiles of the total cross section.

Hadronic processes are described in a simple geometrical picture by the Glauber Model, which assumes straight-line nucleon trajectories and nucleons-nucleons cross section independent of the number of collisions the nucleons have undergone before. The nuclear density profile is given by a Wood-Saxon distribution. As far as the case of Pb–Pb collisions analysed by ALICE is concerned, a spherical nucleus with a radius

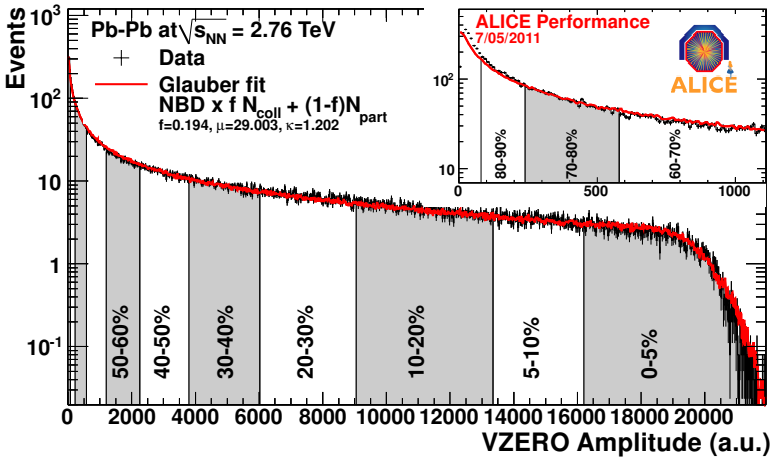

Figure 2.25: Multiplicity distribution measured via the V0A+V0C amplitude. The Glauber model fit is shown with a red line.

of 6.62 fm and a skin depth of 0.546 fm, is considered. The values are based on data from low energy electron-nucleus scattering experiments [104][3]. A hard-sphere exclusion distance of 0.4 fm between nucleons is employed. Nuclear collisions are modelled by randomly displacing the two colliding nuclei in the transverse plane. Nucleons from each nucleus are assumed to collide if the transverse distance between them is less than the distance corresponding to the inelastic nucleon-nucleon cross section. This is estimated to be 64 ± 5 mb at $\sqrt{s} = 2.76$ TeV according to interpolations of data at different centre-of-mass energies [105] and to direct measurements at LHC [106].

The measurable observables for the centrality determination are the charged-track multiplicity at mid-rapidity (related to $N_{\rm part}$) or the multiplicity observed in the ZDC due to the spectator nucleons. The multiplicity distributions from each detector have a typical shape. For instance in Fig. 2.25, the sum of the V0 scintillators amplitude is shown. The red line is the fit with the Glauber Model calculation. Some centrality classes that can be defined are indicated with alternate white and grey shadows.

Another way to determine the centrality is to measure the energy deposit of the spectator nucleons in the Zero Degree Calorimeter (ZDC). This in principle provides directly the number of participants, however the nuclear fragmentation breaks the simple relation in the measured variables. The ZDC therefore needs to be correlated to another detector, in this case the electromagnetic calorimeter ZEM. In Fig. 2.26, left panel, the ZDC energy is shown versus the ZEM amplitude and the lines correspond to the centrality percentiles indicated in the plot. Since the ZDC is far from the interaction point and therefore rather independent on the vertex, this centrality measurement is particularly suited for the analysis that does not require any vertex cut, and it gives good results for central collisions, where the ZDC signal is well correlated with the number of spectators.

In Fig. 2.26, right panel, the resolution on the centrality determination is measured as a function of centrality percentile for different methods. The resolution depends on the rapidity coverage of the detector used, hence, when scaled by the square root of the $N_{\rm ch}$ measured in that detector, all the results line up together. The resolution ranges from 0.5% in central to 2% in peripheral collisions.

[3]Since the Woods-Saxon parameters for ^{208}Pb are not available, the values for ^{207}Pb were used. Note that the Bessel-Fourier coefficients for the two nuclei are similar.

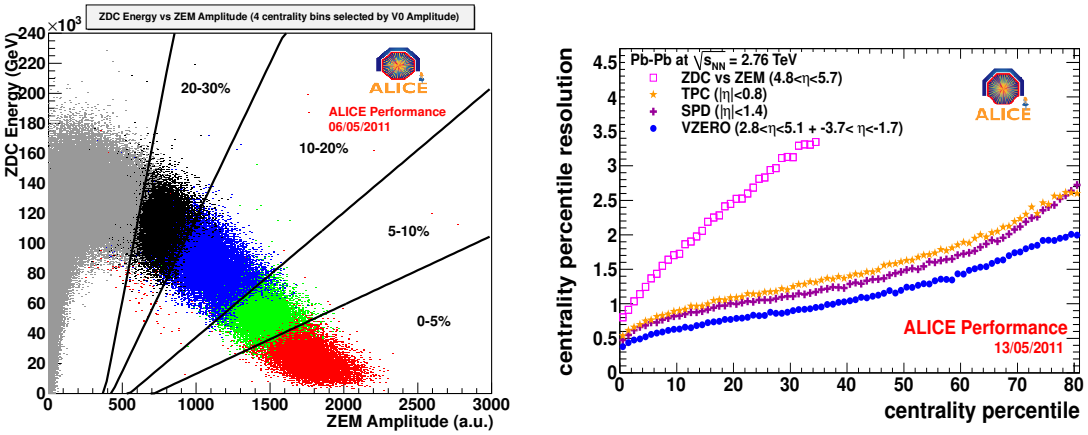

Figure 2.26: Left panel: ZDC energy versus ZEM amplitude. Each bin contains the mean centrality percentile obtained by V0 amplitude. The lines represent a fit to the 5%, 10%, 20% and 30% centrality bins. Right panel: Resolution on the centrality determination with different estimators (cf. legend).

2.6 Data taking conditions

After a technical problems at the first LHC start-up in 2008, a recovery action was taken and the machine was ready to accelerate protons and ions from November 2009. pp collisions at $\sqrt{s}$ = 900 GeV, 2.36 TeV, 2.76 TeV, and 7 TeV and Pb–Pb collisions at $\sqrt{s_{NN}}$ = 2.76 TeV were delivered, allowing a smooth data taking to all the experiments. After the first period of LHC low luminosity, the beams crossing at the interaction point 2, where ALICE is located, were defocused in order to maintain an instantaneous luminosity of $\sim 10^{29}$ cm^{-2}s^{-2} and as low as possible pile-up, while for the other experiments the luminosity was pushed to 10^{31} - 10^{32} cm^{-2}s^{-2}.

2.6.1 Data acquisition and processing

The main difference between ALICE and the other LHC experiments is that ALICE is interested to minimum-bias collisions to study low-p_{t} and bulk properties, while the other experiments aim at rare events and need very stringent triggers to reduce the huge background of QCD processes. To give an idea of the size of the cross sections involved, in Fig. 2.27, left panel, the cross section of different processes as a function of the centre-of-mass energy is shown, spanning more than 16 orders of magnitude. The interesting ones (e.g. Higgs boson production) are of the order of 10^{-2} nb, to be compared to the total inelastic cross section of 10^{8} nb. Of the 40 MHz collisions delivered by LHC only 100 Hz can be registered on tape and must be selected among the interesting events. The goal is then to use the trigger to reject all the background and collect as much interesting data as possible, keeping the detector and the triggers as efficient as possible.

The problems ALICE encounters are completely different. The luminosity is not as high as for ATLAS and CMS, but, due to the types of detectors used, most of them giving 3D spatial coordinates and energy loss information, and to the granularity required during Pb–Pb runs, the data-size produced is particularly high. The situation is sketched in Fig. 2.27, right panel, where past and present experiments' correlation between level 1 trigger rate and event size is shown.

As already mentioned when talking about the ALICE analysis framework (Section

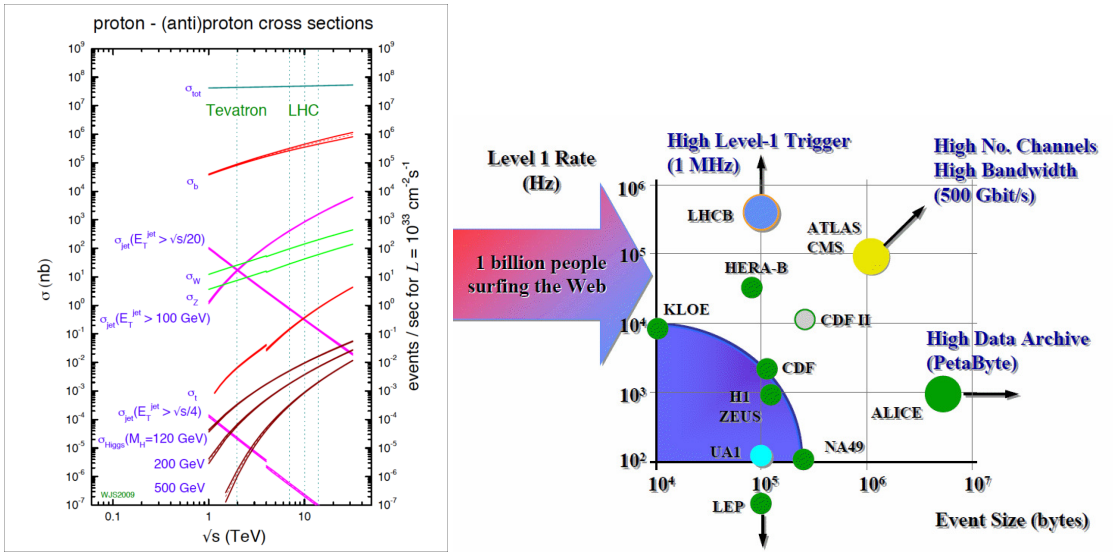

Figure 2.27: Left panel: pp cross section for different processes as a function of the centre of mass energy. The scale on the right indicates the number of events/sec expected with a luminosity of 10^{34} cm^{-2}s^{-2}. Right panel: Sketch of the relation between the level 1 trigger (L1) rate and the event size for different experiments.

2.4.1), the huge amount of data collected by the experiments is distributed world wide through the GRID [94], a network created to store and analyse data in a distributed way. Data are recorded on magnetic tapes in the so-called Tier-0 computing centre. Large regional computing centres, called Tier-1, share with CERN the roles of a safe storage of the data on high reliably storage media and to perform the bulk of the organised processing of the data. Smaller centres, called Tier-2, are logically clustered around the Tier-1's. The main difference between the two kind of centres is the availability of high-reliability mass-storage media at Tier-1's. Tier-2's use the closest Tier-1 to store the data that they produce. The major role of Tier-2's is simulation and end-user analysis. All the members of the Collaboration have access to the data once they are provided with a valid certificate to access the Grid.

In Fig. 2.28, left panel, the data recorded by ALICE between April and October 2010 (pp collisions) with different triggers, namely minimum bias (INT1 B), muon trigger (MUS1 B) and high multiplicity trigger (SH1 B) are shown as a function of time. The transition to LHC high luminosity period is visible in the muon trigger (very last group of points). In the right panel, the integrated luminosity versus time, delivered in the period from March to September 2011 by LHC as recorded from the four experiments, is shown. The 4 fb^{-1} recorded from ATLAS and CMS and the reach of 1 fb^{-1} by LHCb are remarkable (ALICE is not visible, since its integrated luminosity is 3 order of magnitude lower).

2.6.2 pp sample collected in 2010

During the first year of pp collisions in 2010, ALICE collected mainly minimum-bias triggered events. Other triggers were used, for instance high multiplicity and muon triggers, which will not be discussed here.

The minimum-bias trigger conditions are a logical OR between:

- at least one hit in either of the V0 counters,

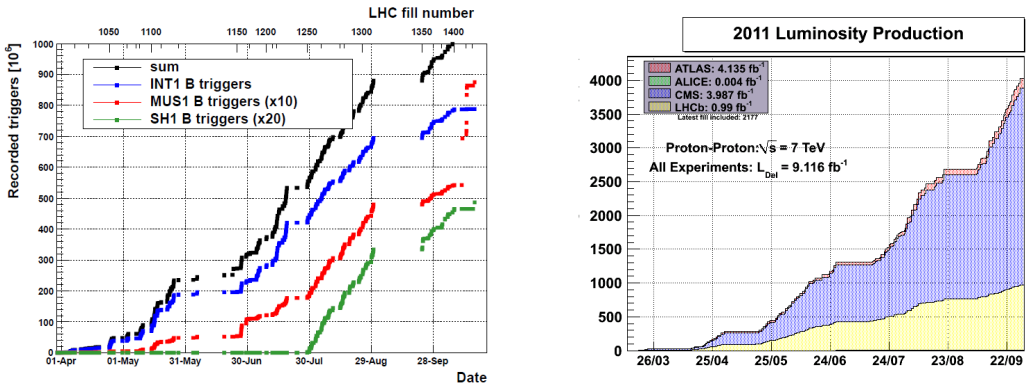

Figure 2.28: Left panel: Minimum bias (blue) and triggered (muon in red and high multiplicity in green) data in ALICE as a function of time (year 2010) and LHC fill number. The total number of events recorded in black. Right panel: Luminosity recorder by ATLAS (red), CMS (blue), LHCb (yellow), and ALICE (green, not visible) in the period from March to September 2011.

- one hit in the SPD ($|\eta| < 2$),

in coincidence with the arrival of proton bunches from both directions. This trigger was estimated to be sensitive to about 87% of the pp inelastic cross section [106]. It was verified on Monte Carlo simulations based on PYTHIA (with Perugia-0 tuning [77]) that the minimum-bias trigger is 100% efficient for D mesons with $p_{\rm t} > 1$ GeV/c and $|y| < 0.5$. Contamination from beam-induced background was rejected offline using the timing information from the V0 and the correlation between the number of hits and tracklets in the SPD detector. The instantaneous luminosity in the ALICE experiment was limited to 0.6-1.2$\times10^{29}$ cm^{-2}s^{-1} by displacing the beams in the transverse plane by 3.8 times the r.m.s of their transverse profile. In this way, the interaction probability per bunch crossing was kept in the range 0.04-0.08, with probability of collision pile-up below 4% per triggered event. The luminous region was measured with high precision from the distribution of the interaction vertices reconstructed from the charged particles tracked in the ALICE central barrel detectors, yielding $\sigma_x^{luminous} \approx \sigma_y^{luminous} \approx$ 35- 50 μm in the transverse plane and $\sigma_z^{luminous} \approx$ 4-6 cm along the beam direction (the quoted ranges are due to the variations of the beam conditions during the data taking).

The data sample used for the analysis presented in Chapter 4 consists of 314$\times10^6$ minimum-bias events including only those with interaction vertex in the range $|z| < 10$ cm. The corresponding integrated luminosity collected during the 2010 LHC run with pp collisions at $\sqrt{s} = 7$ TeV is $L_{\rm int} = 5$ nb^{-1}.

2.6.3 Pb–Pb sample collected in 2010

The trigger configuration used during the first run of Pb–Pb collisions, in November 2010, is minimum-bias, with gradually tighter conditions during the data taking. Two of the following conditions first and then the last two conditions were required:

- two pixel chips hit in the outer layer of the SPD,
- a signal in the V0-A,
- a signal in the V0-C.

The bunch intensity was typically 10^7 lead ions per bunch and each beam had 4 colliding bunches. The estimated luminosity was $\sim 10^{24}$ cm^{-2}s^{-1}, producing collisions with a minimum-bias trigger at a rate of 100 Hz.

A removal of background events was carried out offline using the V0 timing information and the requirement of two tracks in the central detector. Only the events with a vertex found in $|z| < 10$ cm were used to ensure a uniform acceptance in the central rapidity region. The luminous region had a r.m.s. width of about 6 cm in the longitudinal direction and 50-60 μm in the transverse direction, which was stable during the entire data taking period.

A sample of 17×10^6 Pb–Pb collisions passed the selection and were used for the analysis presented in Chapter 5. The centrality was estimated using the V0 detector and the class selected for the measurement ranges between 30 and 50%. Applying the centrality selection, the data sample reduces to 3×10^6 events.

Chapter 3

D meson analysis tools

3.1 D meson analysis strategy

This chapter is devoted to the description of some technical aspects of the D meson analysis, developed during this thesis work.

The measurement of D^0 meson production was performed by reconstructing the decay mode $D^0 \to K^-\pi^+$. The D^0 meson has a proper decay length of $\sim$ 123 μm, its decay secondary vertex is therefore typically displaced by a few hundred μm from the primary vertex of the pp interaction. The analysis strategy for the extraction of the D^0 signal from the large combinatorial background due to uncorrelated tracks is based on the reconstruction and selection of secondary vertex topologies that have significant separation from the primary vertex. The identification of the charged kaons in the TPC and TOF detectors provides additional background rejection in the low-momentum region. Finally, an invariant mass analysis was used to extract the signal yield.

The first important item discussed in the following is the quality assurance check (QA), which aims at spotting possible problems in the data to be analysed. Those checks are crucial for the physics results to be robust. On top of the checks carried out at the reconstruction level, some additional tools specific for the D mesons analysis were developed. These will be described in Section 3.2. The results obtained on the data sample used for the analyses of Chapters 4 and 5 will be also shown.

The second aspect that will be treated is related to the D meson signal extraction. In Section 3.3 the fitting procedure used for the signal extraction from an invariant mass histogram will be described and its validation with simulations will be shown.

3.2 Quality assurance (QA) for D meson analysis

The data quality assurance is performed at different levels. On-line, the Data Quality Monitor (DQM) tools, allow to perform checks on the status of the detector during the data taking using the raw data, for example by verifying that the busy time, the data size, and the reliability of the detector response are under control. Later, at the reconstruction level, a further set of checks is performed on the reconstructed tracks using the information stored in the ESD to ensure that the performance is as expected. A third level of checks, specific for each analysis, can be done. In the case treated here, the verification is particularly important because it tests first of all if the AOD production worked smoothly. Finally, it checks whether the quantities interesting for the analysis are properly reproduced in the simulated samples to be used for the corrections.

The monitored observables are:

- the distribution of ITS hits per track;
- the p_{t} and impact parameter d_0 distributions of so-called "good tracks", required to pass through all the steps of the track reconstruction (cf. Section 2.4.3), to have $p_{\mathrm{t}} > 0.3$ GeV/c, and at least one cluster reconstructed in the SPD;
- the track multiplicity distribution;
- the vertex position distribution;
- the particle identification with TOF and TPC.

In the case of Pb–Pb data also the following quantities are considered:

- the multiplicity distribution in 10% centrality percentiles;
- the centrality percentile distributions as a function of time.

Starting from 2011 most of those quantities are studied as a function of the trigger configuration, but this is not discussed here since in 2010 data only minimum-bias trigger was used for the analyses of D mesons.

The benchmark to compare with should be a Monte Carlo simulation with the same conditions as the data sample. In practice, this was not always possible and most of the times the comparison was carried out with another data sample, already checked to be reliable and expected to have the same features as the data under study.

The data used for D meson analysis in pp collisions include 4 so-called "periods", namely `LHC10b`, `LHC10c`, `LHC10d`, and `LHC10e`. The final analysis and the checks shown in this chapter were performed with the following AOD productions of the *pass2* reconstruction step:

- AOD038 for `LHC10b` and `LHC10c`, ROOT version `v5-28-00a`, AliRoot version `v4-21-17b-AN`
- AOD057 for `LHC10d` and `LHC10e`, ROOT version `v5-28-00-1`, AliRoot version `v4-21-26-AN-1`.

The data sample for the flow analysis in Pb–Pb was referred to as `LHC10h`. Also in this case the *pass2* reconstruction step was used and the AOD production:

- AOD049, ROOT version `v5-28-00c`, AliRoot version `v4-21-21-AN`.

In Section 3.2.1 and 3.2.3 the QA studies for pp and Pb–Pb data, respectively, will be described.

3.2.1 QA on pp 2010 data

The quality check figures reported in the following refer to the `LHC10d` period, if not otherwise specified, but the performance was checked to be the same in all periods.

Tracking quality

The tracking quality is verified starting from the performance of the ITS, which provides the impact parameter resolution.

The performed checks are shown in Fig. 3.1. Fig. 3.1(a) shows the number of tracks with a hit in a specific ITS layer. The bottom panel of Fig. 3.1 reports the performance of the ITS as a standalone detector, showing the distribution of number of clusters in the

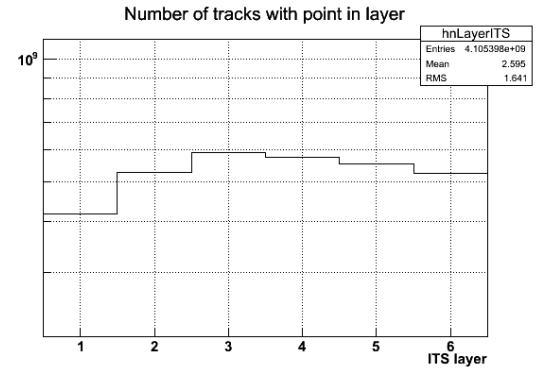

(a) Distribution of number of tracks with a hit in a specific ITS layer.

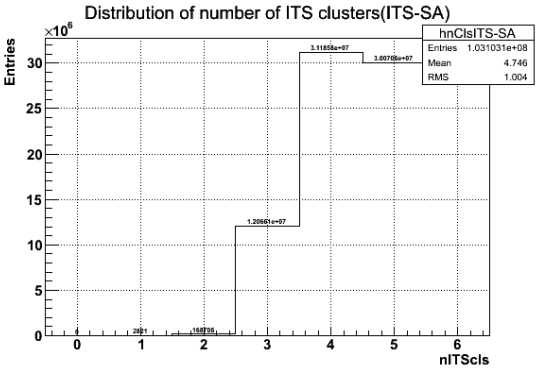

(b) Number of clusters in the ITS as standalone tracker.

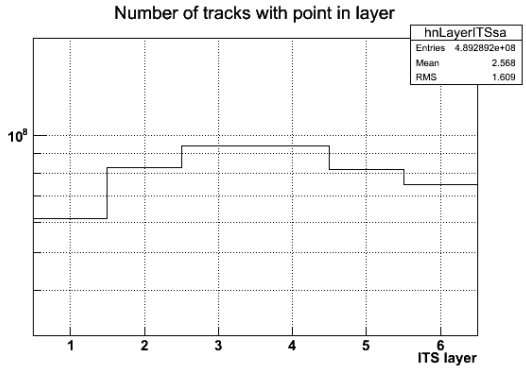

(c) Distribution of number of tracks with a hit in a specific ITS layer, with ITS as standalone tracker.

Figure 3.1: Quality assurance results for the ITS tracking performance in pp collisions.

ITS (3.1(b)) and the number of tracks with a hit in a specific layer of the ITS (3.1(c)). These checks are meant to spot possible inefficiencies in some of the layers and the results do not present any unexpected behaviour.

The quality of the sample is further verified by investigating the track multiplicity and the p_{t} distributions. In Fig. 3.2 top panel the distribution of the event multiplicity given by the number of tracks and the distribution of number of tracklets are shown.

Fig. 3.2(c) shows the distribution of *good* tracks, namely those satisfying the following requirements:

- at least 1 cluster in the SPD;
- $p_{\mathrm{t}} > 0.3$ GeV/c;
- flags `ITSrefit` and `TPCrefit` true, i.e. the refitting of the track in the inward direction was successful.

In Fig. 3.2(d) their p_{t} distribution is shown.

All the checks gave a stable performance within the different periods analysed.

3.2.2 PID quality

The PID strategy for the D^0 (D^+, D^{*+}, and D_s^+) analyses is aimed at identifying the kaon among the candidate decay tracks. This allows for the rejection of a large amount

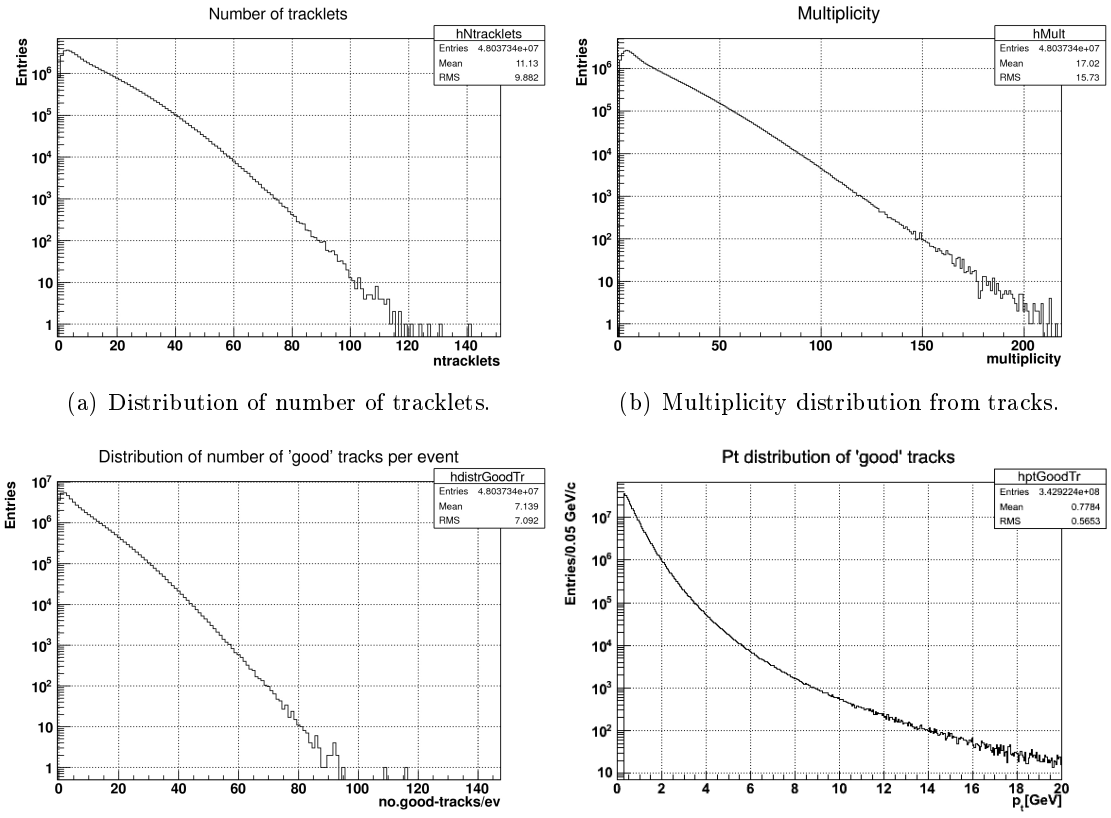

(a) Distribution of number of tracklets.

(b) Multiplicity distribution from tracks.

(c) Distribution of 'good' tracks.

(d) Transverse momentum distribution of 'good' tracks.

Figure 3.2: Quality assurance for the multiplicity and p_{t} distributions in pp collisions.

of background, mostly at low p_{t}. In pp collisions, the PID is helpful but not mandatory, while in Pb–Pb it is crucial to achieve the signal significance.

The detectors involved are TPC and TOF. As already mentioned in the description of the detectors and their performance in Section 2.3.1 and 2.4.5, the TOF exploits the time-of-flight of the particles and the TPC their energy loss in the gas volume. The PID information is given by two possible strategies: the *"$n\sigma$"* and the *Bayesian* approaches. The former, used in the following, consists in applying a selection $\pm n\sigma$, where σ is the width of the Gaussian signal shape at fixed momentum, around the expected signal (time or energy) for the considered species. The Bayesian approach requires to estimate an a priori probability for each species to calculate the PID weight for the considered specie j (where $j = \pi$, K, p...) by means of the Bayes' formula. The $n\sigma$ approach was adopted for the first analyses since its outcome is less hypothesis-dependent. With both approaches the answer from more detectors can be combined to improve the results.

In Fig. 3.3, the arrival time measured by TOF with respect to the expected arrival time for kaon is shown as a function of momentum. The expected time depends on the particle mass, on its momentum, and on the length covered. The band at zero (kaons) can be separated from protons (upper band) up to about 2-2.5 GeV/c and from pions (lower band) up to 1.5 GeV/c.

The time measured by TOF (T_{TOF}) has to be referred to the time zero (T_0) of the collision. The T_0 is provided either by a specific detector, the T0, or by the TOF itself, with a special procedure described below.

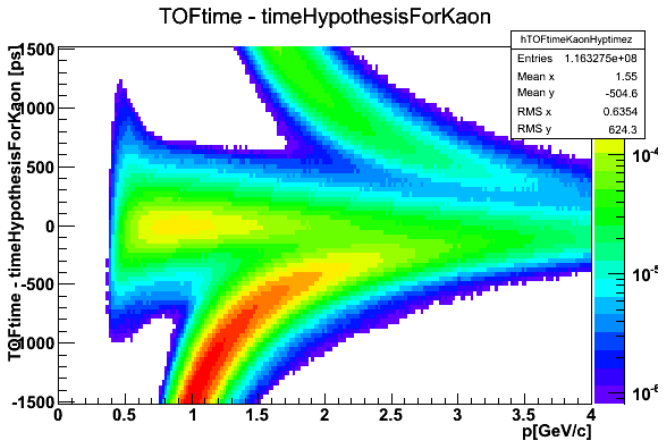

Figure 3.3: Time from TOF with respect to the expected time for kaon as a function of momentum. The figure refers to pp collisions.

The $T_0^{\rm TOF}$ is estimated starting from the N tracks reaching TOF with momentum $0.5 < p < 3$ GeV/c. All the combinations of mass hypotheses are considered and the T_0 is calculated, for each hypothesis, as:

$$T_0^j = \frac{1}{N} \times \sum_i^N (T_{\rm TOF}^i - T_{\rm Exp}^j), \tag{3.1}$$

where $T_{\rm Exp}^j$ is the expected time for each specie and i runs over the N tracks. In practise, N is taken $\lesssim 6$ in order to limit the number of possible combinations, which can explode in Pb–Pb collisions. From each set of 6 tracks a $T_0^{\rm TOF}$ is extracted, choosing that with the minimum χ^2, and the average is computed to obtain the final $T_0^{\rm TOF}$.

In the case both $T_0^{\rm T0}$ and $T_0^{\rm TOF}$ are available, T_0 is estimated as their weighted average, otherwise the available one is used. If none is present $T_0^{\rm FILL}$, the average T_0 of the run calculated on-line and offline during the calibration, is taken.

The final $T_{\rm TOF}^{\rm PID}$ resolution is obtained as the sum in quadrature of the resolution of the best estimation of T_0 and the resolution of $T_{\rm TOF}$. The former depends on the method used to determine T_0 and the latter on the $p_{\rm t}$ resolution of the track and on the matching with the TPC.

In Fig. 3.4 the resolution obtained for kaons is shown for each period. The "peaks" are due to the events in which the estimation of the T_0 with $T_0^{\rm T0}$ and/or $T_0^{\rm TOF}$ was not possible. In this case a comparison among the periods is important and the final PID performance must be checked.

In Fig. 3.5 the distribution of the number of σ around the expected time for kaon is shown as function of momentum and for each period. The points are the mean value and the σ of a Gaussian fit performed on each momentum slice. The lines correspond to the expected average (black line at zero) and to $\sigma = 1$ (red line). Kaons are selected with a cut at $\pm 3\sigma$ on this distribution in the momentum range $p < 1.5$ GeV/c. The strategy applied is conservative and fully efficient for the selection of $\rm D^0$ mesons (see Section 4.1.3). From a careful comparison of `LHC10d` with respect to the others, the separation of kaons from pions in `LHC10d` is slightly worse, but still good enough to apply a "3σ cut" selection.

The TPC signal as a function of momentum is shown in Fig. 3.6. The thin almost vertical bands are, from left to right, pions, kaons, and protons which then cross each

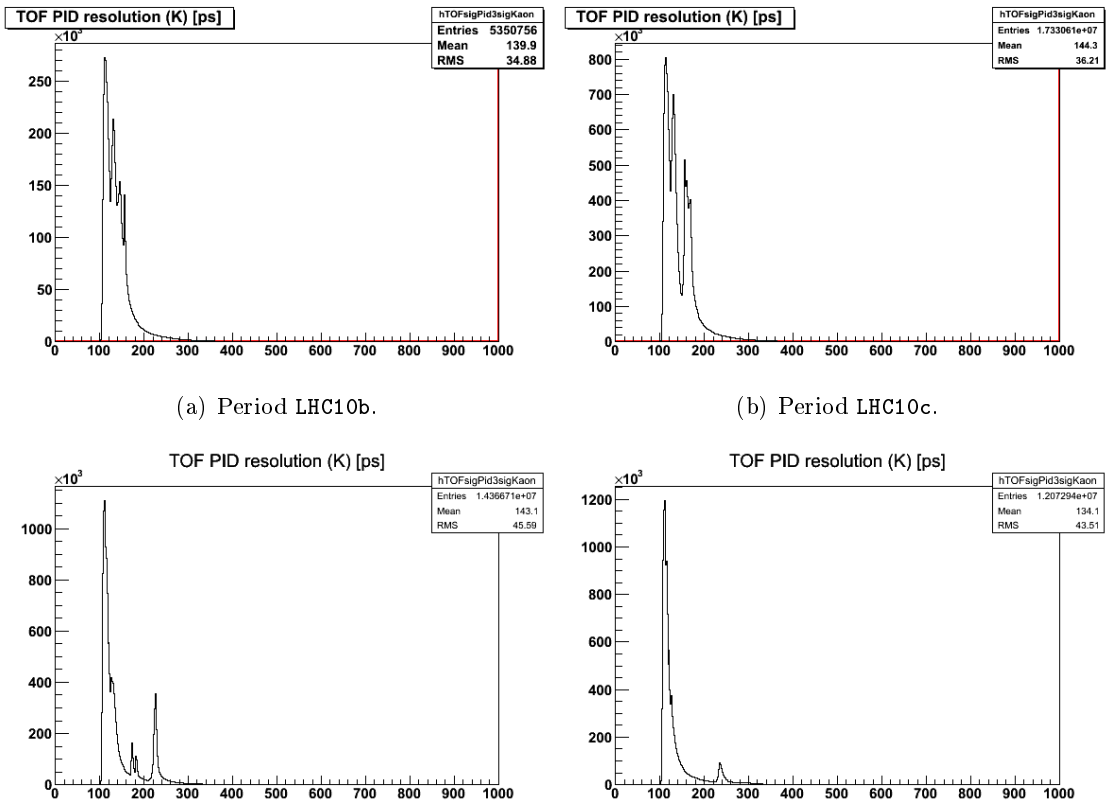

(a) Period `LHC10b`.

(b) Period `LHC10c`.

(c) Period `LHC10d`.

(d) Period `LHC10e`.

Figure 3.4: PID resolution for kaon with TOF in pp collisions.

other in a wide horizontal band. The pion will deviate again at higher momentum (not visible in the figure). The electrons are also visible as another horizontal but more round shape above. The ionization energy loss of a charged particle interacting with a material is known from the Bethe Bloch formula and shown in Fig. 3.7. By relating the signal from the TPC and the corresponding Bethe Bloch parametrization, it is possible to proceed to the identification.

In Fig. 3.8 the $n\sigma$ distribution as a function of momentum is shown for pions, kaons, and protons. Three ranges of momentum with a different $n\sigma$ selection for both kaon and pion identification were used. Below 0.6 GeV/c $n = 2$, between 0.6 and 0.8 GeV/c $n = 1$. Above 0.8 GeV/c the TPC PID was not used.

The TPC PID performance was found to be stable in the four periods.

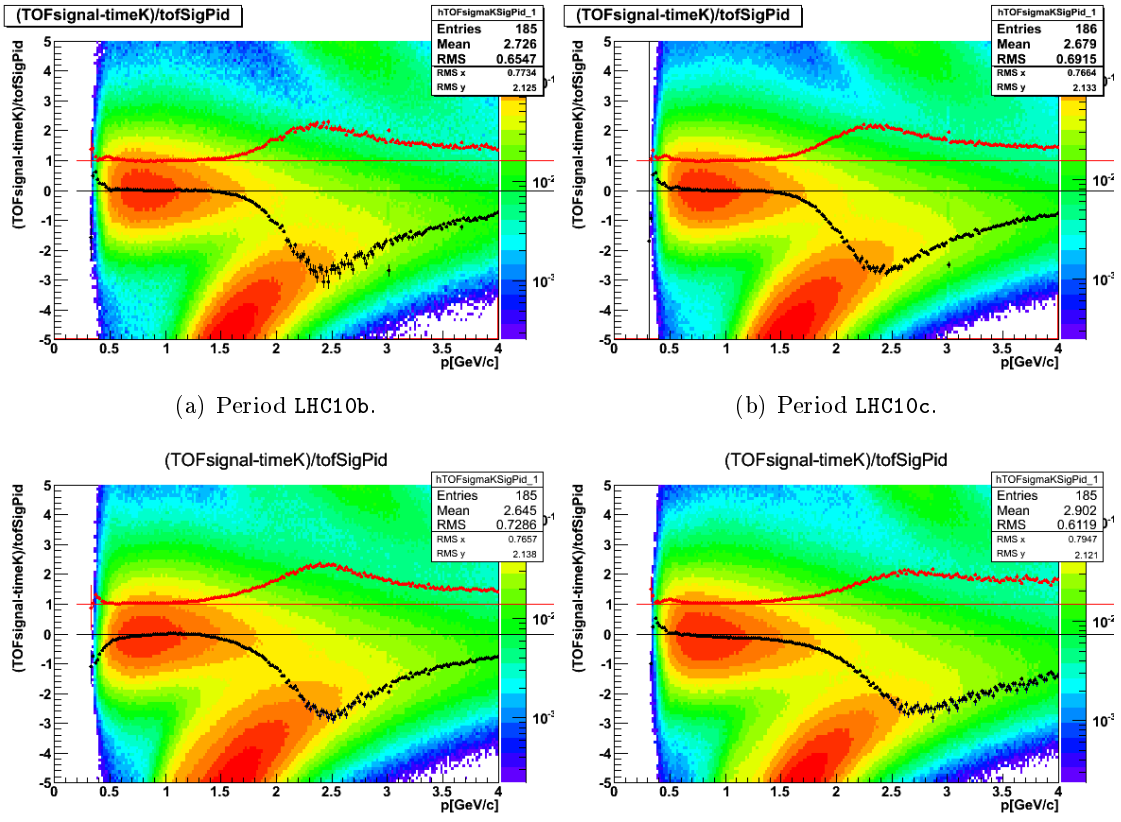

(a) Period LHC10b. (b) Period LHC10c.

(c) Period LHC10d. (d) Period LHC10e.

Figure 3.5: TOF time with respect to the expected time for kaon normalized by the resolution (number of σ). The points are the mean value and σ of a Gaussian fit performed on each momentum slice. The lines correspond to the expected average (black line at zero) and to $\sigma = 1$ (red line). The figures refer to pp collisions.

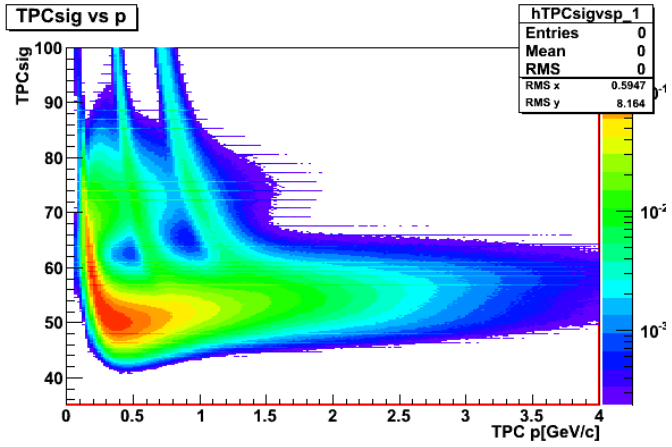

Figure 3.6: TPC signal as a function of momentum. The signal is proportional to the energy loss of the particle in the TPC. The figure refers to pp collisions.

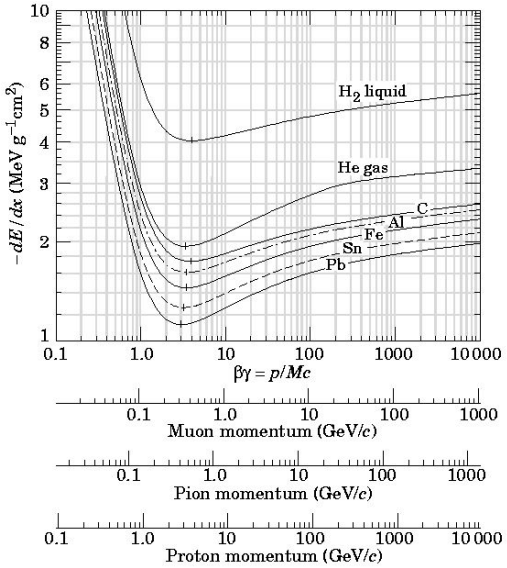

Figure 3.7: Energy loss in different materials and for different particles (x-axes) [105].

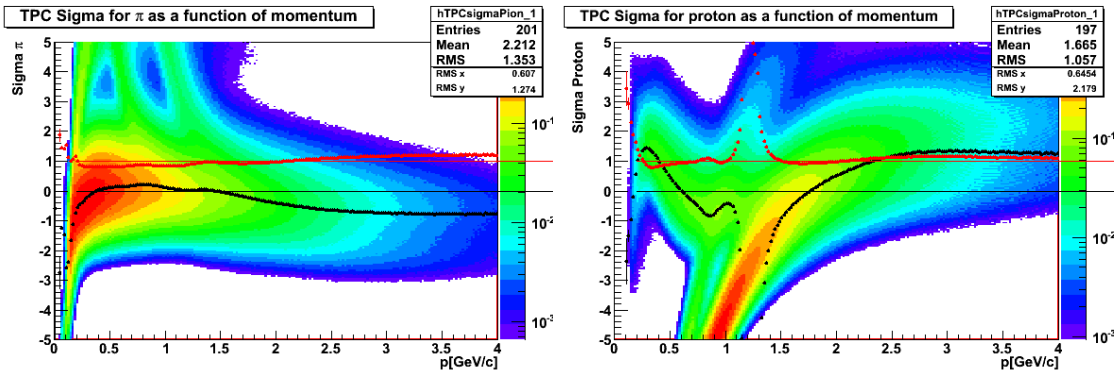

(a) Pion.

(b) Kaon.

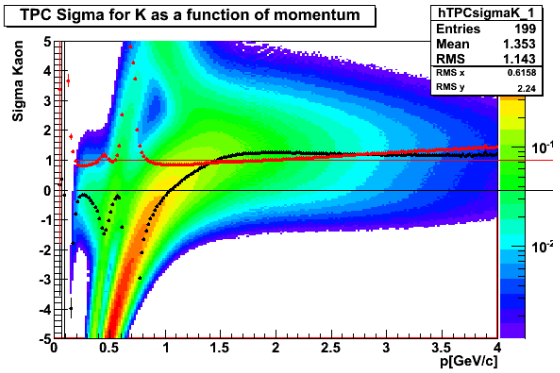

(c) Proton.

Figure 3.8: Number of σ for identification with TPC in pp collisions.

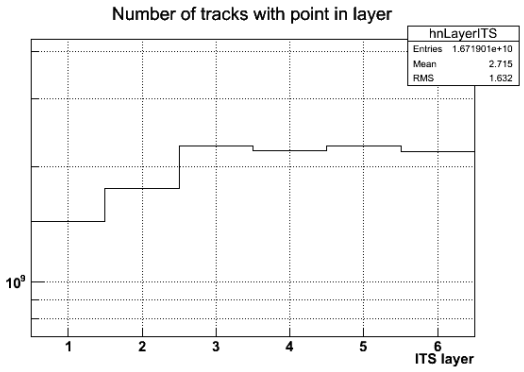

Figure 3.9: Distribution of number of tracks with a hit in a specific ITS layer (Pb–Pb collisions).

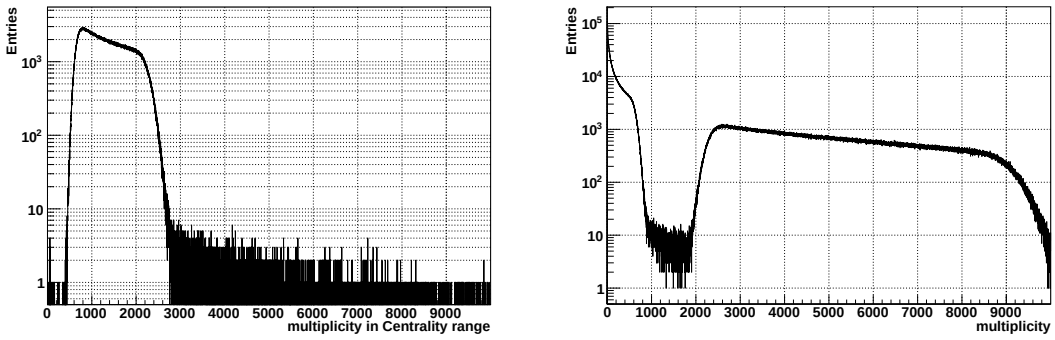

(a) In 30-50%.

(b) Out of 30-50%.

Figure 3.10: Multiplicity distribution in two centrality classes in Pb–Pb collisions.

3.2.3 QA in Pb–Pb 2010 data

In the following paragraphs, the same QA observables as in Section 3.2.1 will be studied for the case of Pb–Pb collisions. At the end of this section other checks specific of nucleus-nucleus collisions, concerning centrality, will be shown.

Tracking quality

The performance of the ITS detector does not differ substantially from the pp case. In Fig. 3.9 the number of tracks with a hit in a ITS layer for the ITS+TPC tracks is reported.

The track multiplicity distribution is shown in two centrality classes: 30-50% in Fig. 3.10(a) and elsewhere in Fig. 3.10(b). The centrality is determined through the V0 detector. The difference with pp data is remarkable (cf. Fig. 3.2(b)): in pp collisions the highest multiplicity measured was about 200, in central Pb–Pb collision more than 10000 tracks can be observed.

PID quality

In Fig. 3.11 the TOF time with respect to kaon time and the TPC signal are shown for the Pb–Pb case. The observed performance improved with respect to pp collisions as far as TOF is concerned. The $\mathrm{d}E/\mathrm{d}x$, instead, by the highest multiplicity is negatively

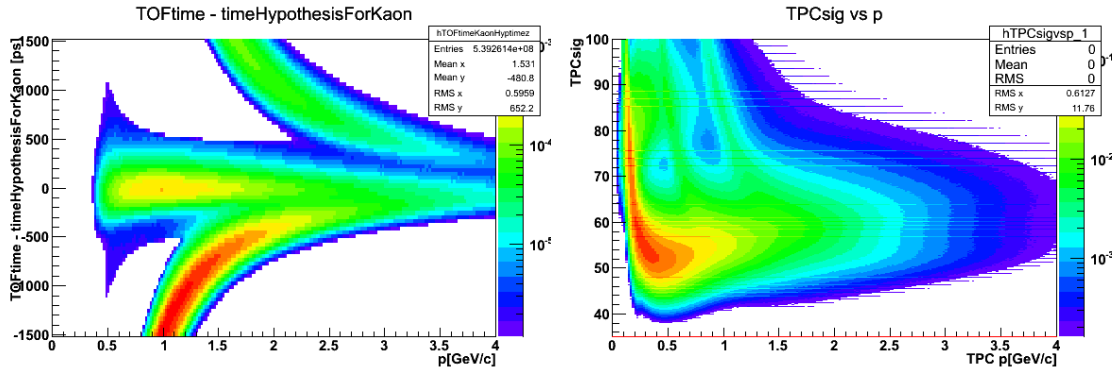

Figure 3.11: Left panel: Time from TOF with respect to the expected time for kaon as a function of momentum. Right panel: TPC signal as a function of momentum. The signal is proportional to the energy loss of the particle in the TPC. Both figures refer to Pb–Pb collisions.

affected.

The improved performance of TOF is related to the better resolution with respect to pp as shown in Fig. 3.12 for pion, kaon and proton. The reason of the improvement is partly due to a better resolution of the T0 detector in the `LHC10h` period. In addition, the T_0 measured by TOF is also more precise because more tracks are available. Therefore the peaks at higher times present in pp (Fig. 3.4) disappear.

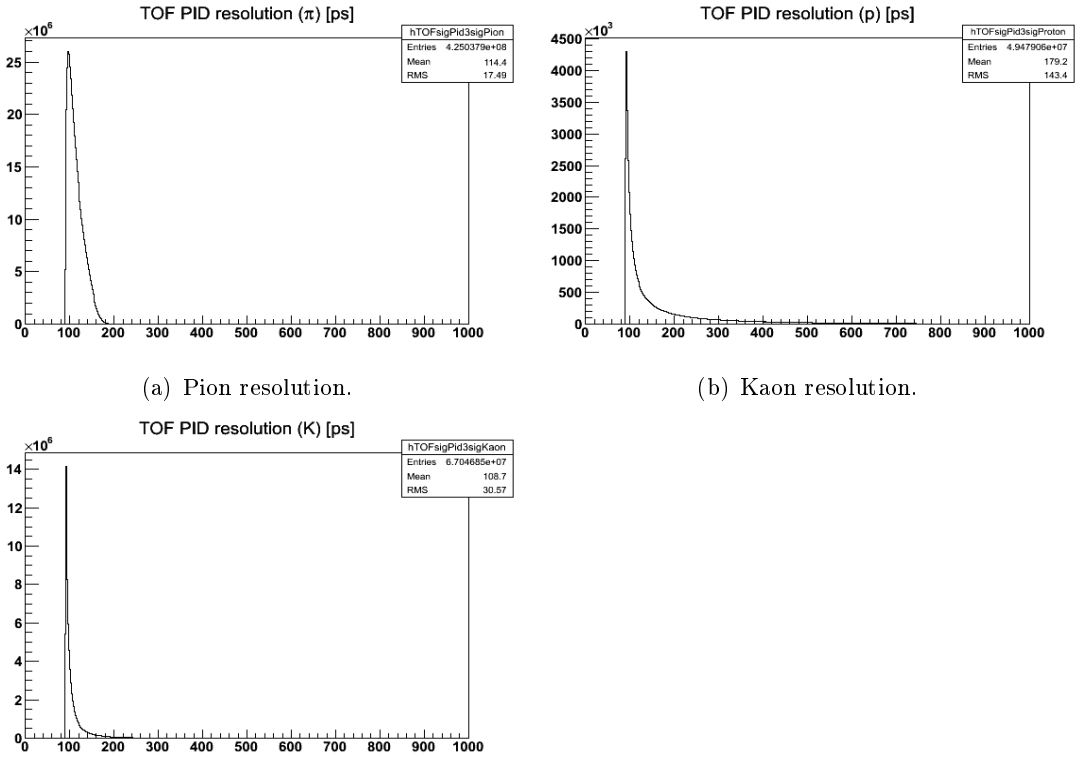

(a) Pion resolution.

(b) Kaon resolution.

(c) Proton resolution.

Figure 3.12: TOF resolution in Pb–Pb collisions.

In Fig. 3.13 the number of sigma for TOF as a function of momentum for pion, kaon, and proton are reported. As already mentioned, the separation achieved for kaons

extends to higher momentum (up to 1.4 GeV/c). The PID strategy uses a selection at 3σ for $p < 2$ GeV/c.

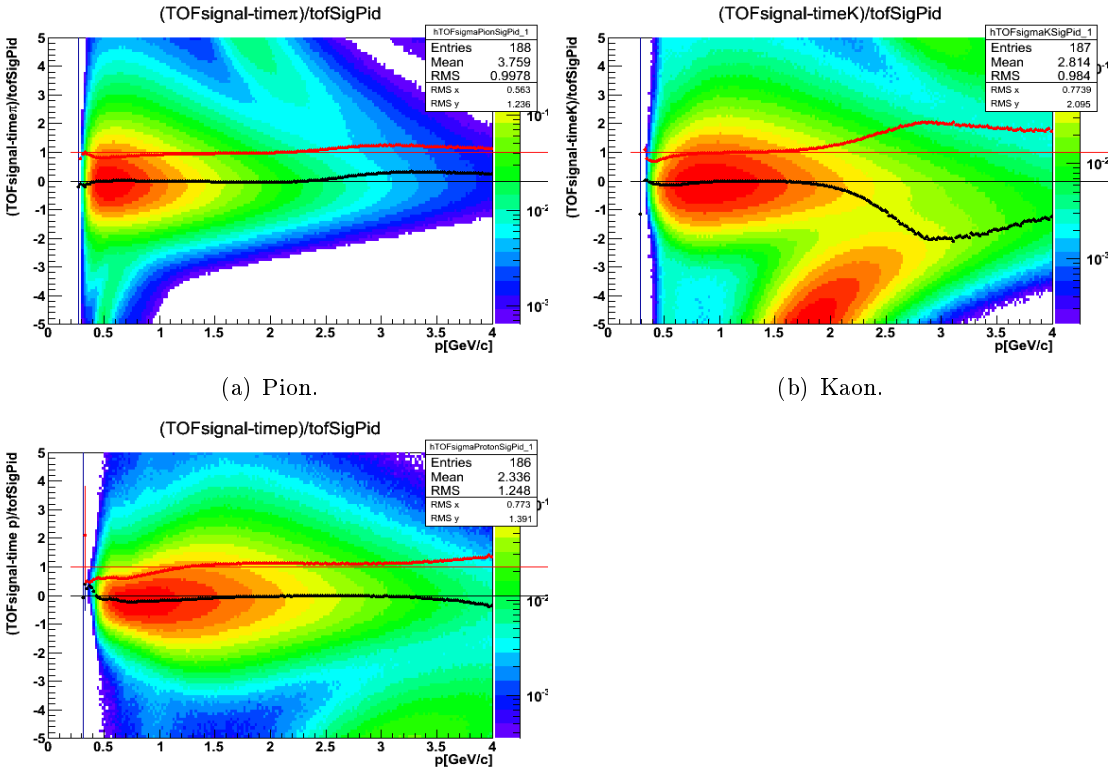

(a) Pion.

(b) Kaon.

(c) Proton.

Figure 3.13: Number of σ for TOF in Pb–Pb collisions.

In Fig. 3.14, the $n\sigma$ distribution for pion, kaon, and proton hypothesis with the TPC is shown. For Pb–Pb collisions the PID strategy is the same as for pp collisions: the identification of kaon and pion with a selection to 2σ for 0.6 GeV/c, 1σ between 0.6 and 0.8 GeV/c, and no selection above 0.8 GeV/c.

Centrality estimation quality

The QA of the centrality estimation is crucial for the Pb–Pb analyses. Fig. 3.15 shows the correlation between centrality percentile, measured from the V0 signal amplitude using a Glauber model fit, and multiplicity of charged tracks. The entries at centrality < 0 are events with no centrality information, while those at centrality > 100 are events with exactly 100% centrality which fill the bin 100-110 of the histograms but belong indeed to the bin 90-100. The events in the bin -10-0 and the outliers at low multiplicity in central events, or at high multiplicity in peripheral events, indicate that in those cases the centrality can be problematic, but their amount is negligible.

Another check is shown in Fig. 3.16. The fraction of events in the centrality class 0-20% (20-80%) with respect to the total in 0-80% in shown as a function of run in Fig. 3.16(a) (3.16(b)). The centrality is estimated with the V0 detector (full square) and with the TPC tracks (empty circle). The results are compatible and the distributions are flat as a function of time within the statistical errors, which are related to the statistics of each run. The ratio, as expected, is ~ 0.25 / ~ 0.75 for 0-20%/20-80%.

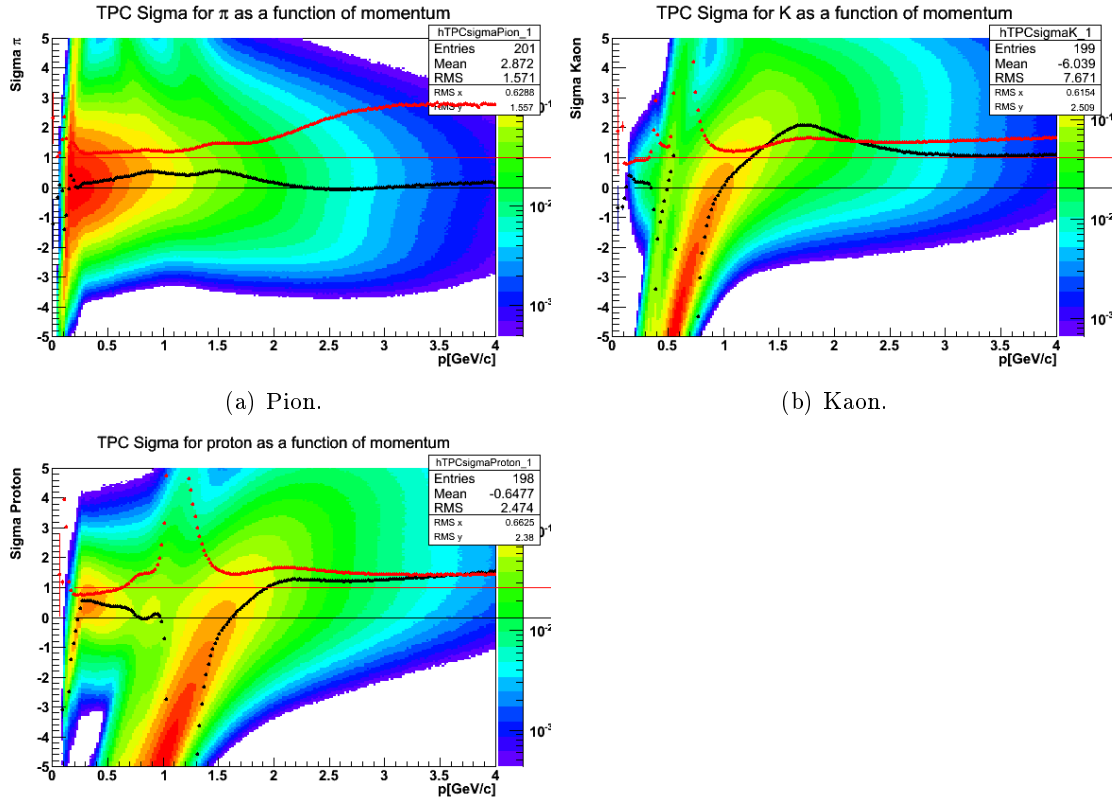

(a) Pion.

(b) Kaon.

(c) Proton.

Figure 3.14: Number of σ for identification with TPC in Pb–Pb collisions.

3.3 D meson invariant mass fit

The invariant mass distribution can be considered as the sum of a Gaussian distribution representing the D meson signal plus a background distribution that can be approximated with polynomial or exponential functions depending to the p_{t} interval. The signal yield can be determined as the difference between the histogram, or the total fit function, and the background function. This paragraph describe the fitting procedure that was used for all the analyses that involve D mesons [107].

The fit is performed in two steps using the Minuit [108] package. First, the sidebands of the invariant mass histogram, where no signal is present, are fit with the chosen background function. Then, the total fit is performed using as a starting point the information about the background obtained from the first step.

Three possible background shapes are foreseen. In all parametrizations, `par[0]` represents the background integral.

i) **Exponential:** $A \cdot e^{Bx}$
where, calling $x_{\mathrm{min/max}}$ the mass range limits:

$$\begin{aligned} A =& \texttt{par[0]} \cdot \texttt{par[1]} / \left(e^{\texttt{par[1]} x_{\mathrm{max}}} - e^{\texttt{par[1]} x_{\mathrm{min}}} \right) \\ B =& \texttt{par[1]} \end{aligned} \tag{3.2}$$

ii) **Linear:** $A + Bx$

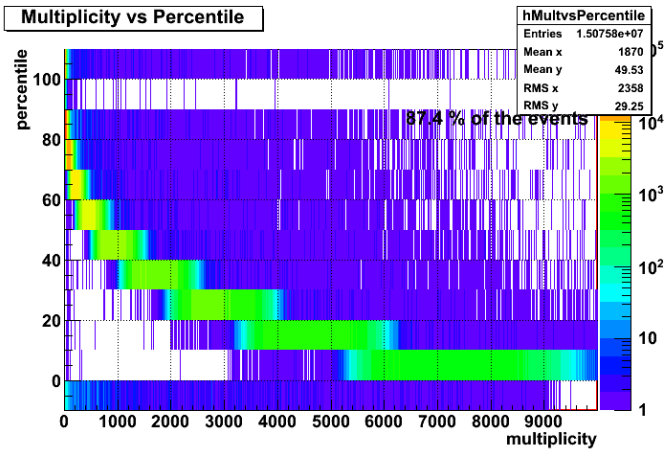

Figure 3.15: Centrality percentile versus multiplicity.

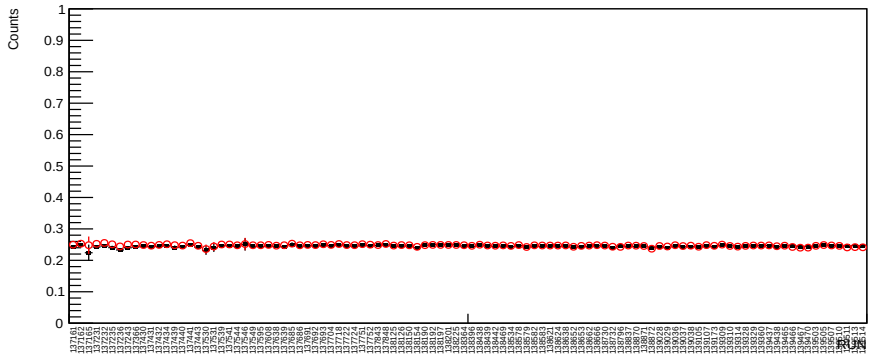

(a) 0-20% centrality class.

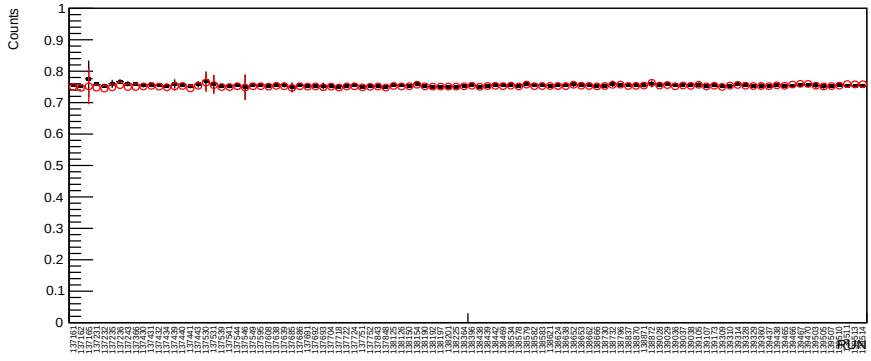

(b) 20-80% centrality class.

Figure 3.16: Events in a central and in a semi-peripheral centrality class normalized by the number of events in 0-80%. Centrality estimated with V0 detector (full square) and with TPC tracks (open circle).

where:

$$\begin{aligned} A =& \texttt{par}[0] / \left(x_{\max} - x_{\min}\right) - \frac{1}{2} \cdot \texttt{par}[1] \left(x_{\max} + x_{\min}\right) \\ B =& \texttt{par}[1] \end{aligned} \tag{3.3}$$

iii) **2nd order polynomial:** $A + Bx + Cx^2$,
where

$$\begin{aligned} A =& \texttt{par}[0] / \left(x_{\max} - x_{\min}\right) - \frac{1}{2} \cdot \texttt{par}[1] \left(x_{\max} + x_{\min}\right) \\ & - \frac{1}{3} \cdot \texttt{par}[2] \left(x_{\max}^3 - x_{\min}^3\right) / \left(x_{\max} - x_{\min}\right) \\ B =& \texttt{par}[1] \\ C =& \texttt{par}[2] \end{aligned} \tag{3.4}$$

The signal shape is a Gaussian with the following normalization:

$$f(S) = \frac{\texttt{par}'[0]}{\sqrt{2\pi}\,\texttt{par}'[2]} \cdot e^{-\frac{\left(x - \texttt{par}'[1]\right)^2}{2\,\texttt{par}'[2]^2}}, \tag{3.5}$$

where $\texttt{par}'[0]$ is the signal integral and it is initialized to the total integral of the histogram minus the background integral $\texttt{par}[0]$ found from the first step; $\texttt{par}'[1]$ and $\texttt{par}'[2]$ the mean value and σ of the Gaussian, respectively, can be initialized by the user.

3.3.1 Performance

The fitter was tested using "fake" invariant mass histograms randomly generated using a Gaussian plus an exponential (G+E) function smeared with a Poissonian bin by bin. The parameters of the functions that generate the test histograms were extracted from previous simulations [109] in order, for instance, to have a steeper and higher background at low p_{t}, a broader mass peak at higher p_{t}, and the expected quantity of signal and background per event. In Fig. 3.17 an example of invariant mass histogram used for testing is shown. The solid blue line is the result of the fit of the histogram including signal and background contributions, while the solid red line shows the background contribution only. Finally, the dot-dashed grey line is the result of the fit of the background in the side-band regions.

The effect of using the three background shapes was studied by performing the fit and comparing the results with the input. One thousand histograms and fits were averaged for each p_{t} bin (15 bins from 0 to 14 GeV/c), in order to validate the fit procedure in different conditions.

In order to verify the reliability of the statistical error on the signal integral obtained from the fit, the relative error was calculated using different methods and the results were compared for the whole statistics of test histograms.

The relative statistical error on the signal was estimated with the methods listed below:

1. **Residuals**: the σ of the residuals, defined as the difference between $\texttt{par}'[0]$ and the true integral, is normalized by the true integral itself;

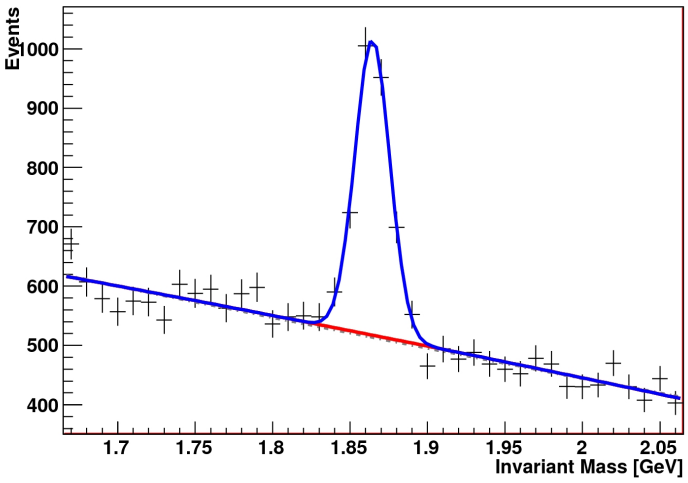

Figure 3.17: Test invariant mass histogram produced by the superimposition of a Gaussian and an exponential function both smeared with a Poissonian distribution. The solid lines represent the fit to the background (red) and to the signal+background (blue), while the dot-dashed (gray) line is the first step fit performed on the side-bands.

2. **Inverse of the significance (H or F)**: the significance, defined as $\frac{S}{\sqrt{S+B}}$, where S and B are signal and background in a $\pm 3\sigma$ range around the mean value, respectively, represents the inverse of the relative error. S and B can be extracted either from the histogram itself, using the inputs chosen to produce it (H), or from the fit parameters (F);

3. **Error on the fit parameter**: the error returned by the fit for the parameter that represents the signal integral, `par'[0]`, normalized by the parameter itself, is considered as relative error.

In Fig. 3.18 the relative errors determined with the methods listed above are shown as a function of p_{t} for the case of exponential generation of the background and for the three fit background functions: exponential (3.18(a)), linear (3.18(b)) and 2$^{\mathrm{nd}}$ order polynomial (3.18(c)). The true relative statistical error on the signal yield is given by the residuals (method 1), or, equivalently, by the inverse of the significance, calculated using the true S and B (method 2 H). As shown in the figure, they are very close. The best estimate of the relative statistical error, i.e. the closest to the true value, is obtained as the inverse of the significance, calculated using S and B from the fit (method 2 F), while the error on the fit parameter (method 3) deviates from the true error at high p_{t}.

The comparison between the error obtained with method 2 F and with method 3 was performed also on the pp data of Chapter 4.

In order to evaluate the reliability of the signal estimation using the different functional shapes the deviation of the resulting signal integral (I_S^{fit}) is compared to the input value (I_S^{true}) as:

$$(I_S^{\mathrm{fit}} - I_S^{\mathrm{true}})/I_S^{\mathrm{true}} \tag{3.6}$$

Figure 3.19, left panel, shows eq. (3.6) as a function of p_{t} for the three types of background fit functions. The error bars indicated come from are the σ of the distributions obtained from all the simulated test histograms divided by the corresponding signal integral. At

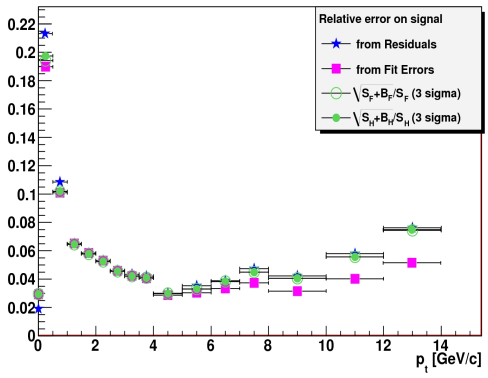

(a) Gaussian+Exponential histogram with Gaussian+Exponential fit

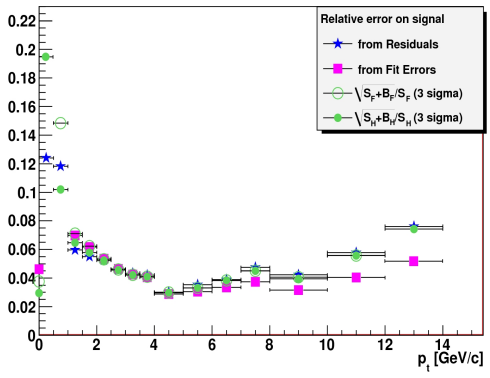

(b) Gaussian+Exponential histogram with Gaussian+Linear fit

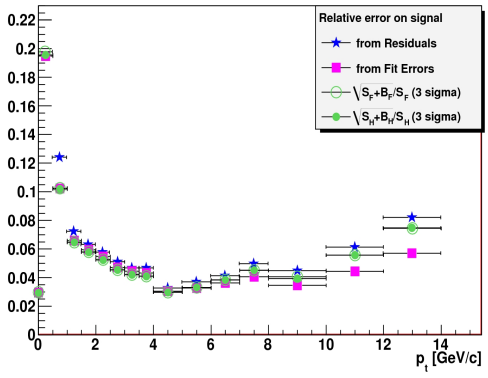

(c) Gaussian+Exponential histogram with Gaussian+Polynomial fit

Figure 3.18: Relative error on signal integral found from fit compared with other three estimators (see text) as a function of p_t: Residuals (blue stars), Error on the fit parameter (pink squares) and Inverse of the significance (green circles) from histogram (open) and from fit (full).

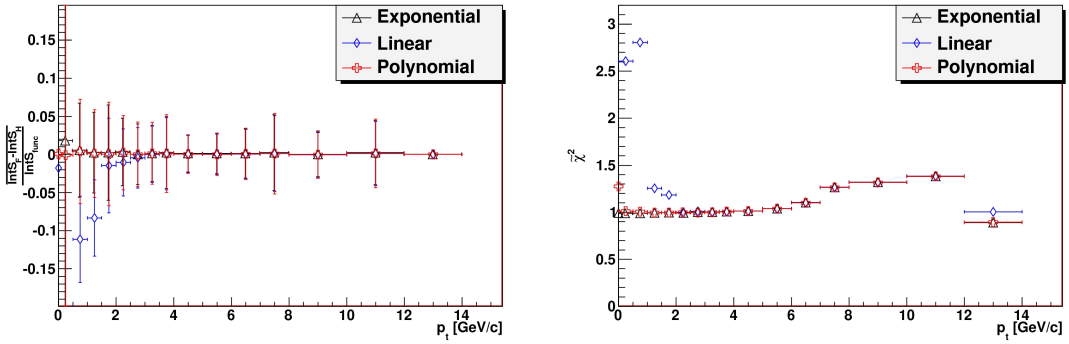

Figure 3.19: Left panel: Mean value of residuals $(I_S^{\rm fit} - I_S^{\rm true})/I_S^{\rm true}$ as a function of $p_{\rm t}$. The error bars represent the widths of the residual distributions normalized by the corresponding signal integral. Right panel: Reduced χ^2 as a function of $p_{\rm t}$.

low $p_{\rm t}$, the linear fit underestimates the signal integral by about 10% at $p_{\rm t} < 1.5$ GeV/c and by 1-2% at $p_{\rm t} \sim 2$ GeV/c, while the exponential and polynomial fits do not bias the extracted signal yield. The fact that the linear fit is not adequate at low $p_{\rm t}$ is confirmed by the large value of the reduced χ^2 obtained from the fit (Fig. 3.19, right panel). This suggests that the linear fit gives a good description of the background shape only at relatively high $p_{\rm t}$ (> 3 GeV/c).

Chapter 4

D^0 meson production cross section in pp collisions

The measurement of the production of hadrons containing heavy quarks in pp collisions at LHC energies provides a way to test quantum chromodynamics (QCD) calculations, based on the factorization approach as described in Section 1.3.1.

In this chapter the analysis strategy for the D^0 case is described and the factors contributing to the differential cross section in eq. (4.1) below are extracted. The D^+, D^{*+} [1], and D_s meson cross sections were also measured by ALICE and they will be shown in Section 4.3.

The D^0 meson has a mass $m^{D^0} = 1864.83 \pm 0.14$ MeV and a $c\tau = 122.9$ μm [105]. It can decay hadronically or semi-leptonically. For this analysis the decay channel $D^0 \to K^-\pi^+$ with a branching ratio (BR) of $(3.89 \pm 0.05)\%$ [105] will be considered.

The expression of the cross section for a hard process of eq. (1.12) in practice becomes:

$$\left.\frac{d\sigma^{D^0}}{dp_t}\right|_{|y|<0.5} = \frac{1}{2}\frac{1}{\Delta y \Delta p_t}\frac{f_{\text{prompt}}(p_t)\cdot N^{\text{raw}\,D^0}(p_t)\Big|_{|y|<y_{\text{fid}}}}{(Acc\times\varepsilon)_{\text{prompt}}(p_t)\cdot \text{BR}\cdot L_{\text{int}}} \tag{4.1}$$

where Δy $(= 2y_{\text{fid}})$ is the width of the rapidity coverage, the factor $1/2$ accounts for the fact that the measured yields include particles and anti-particles, while the cross sections are given for particles only.
L_{int} is the integrated luminosity computed as $L_{\text{int}} = N_{\text{pp,MB}}/\sigma_{\text{pp,MB}}$, where $N_{\text{pp,MB}}$ and $\sigma_{\text{pp,MB}}$ are the number and the cross section of pp collisions passing the minimum-bias trigger condition defined in Section 2.6.2. The $\sigma_{\text{pp,MB}}$ value, 62.5 ± 2.1 mb, was derived from a measurement using a van der Meer scan [110].

In Section 4.1 the other terms of eq. (4.1) are described. The D^0 raw yield, $N^{\text{raw}\,D^0}(p_t)$, in Sections 4.1.1, 4.1.2, 4.1.3, and 4.1.4; the correction factors giving the fraction of D^0 from charm $f_{\text{prompt}}(p_t)$ (a big fraction of the total measured D^0 comes from the decay of the B mesons) and the acceptance times efficiency, $(Acc \times \varepsilon)$, in Section 4.1.5. In Section 4.1.6 the systematic uncertainties are addressed and finally in Section 4.2 the results are shown and compared to fixed-order-next-to-leading-log (FONLL) [45] and Global Mass - Variable Flavour Number Scheme (GM-VFNS) [111] calculations.

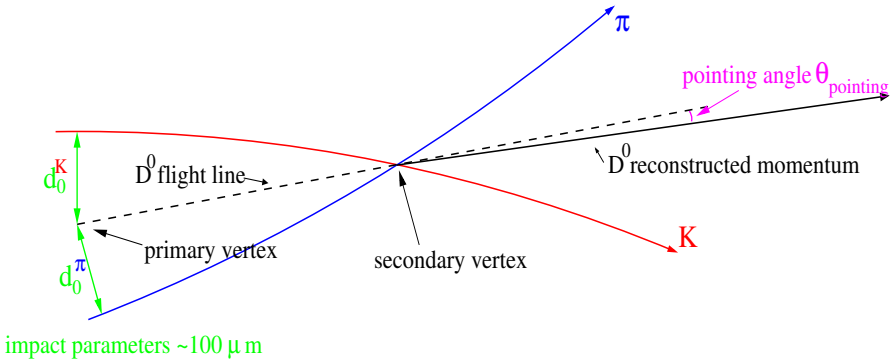

Figure 4.1: $D^0 \to K^-\pi^+$ decay.

4.1 Introduction to the analysis strategy

The data used in this analysis are a minimum bias sample (cf. Section 2.6.2) collected during the 2010 LHC run[1], for a total of 314×10^6 minimum bias events corresponding to an integrated luminosity of 5 nb^{-1}.

The analysis flow foresees a first selection of the "good" events, then the pairing of opposite sign tracks to form the D^0 *candidates*. Afterwards, the candidates are selected according to quality and topological cuts and particle identification. The candidates left undergo an invariant mass analysis that provides the raw signal in bins of p_t. The following step is the correction for efficiency and feed-down to get the corrected yield as a function of p_t. Finally a normalization according to eq. (4.1) is required to obtain the cross section. For all the steps a study of the systematic uncertainties was performed and each contribution was added in quadrature.

4.1.1 Event and candidate selection

The selection of the "good" events for this analysis, namely those with the optimal condition for recovering the information needed at the analysis level, is done by requiring that a primary vertex with $|z| < 10$ cm is reconstructed with tracks (cf. Section 2.4.2 for vertex reconstruction). The candidate pairs are matched using tracks having $|\eta| < 0.8$, $p_t > 0.4$ GeV/c, at least 70 associated space points and $\chi^2/\text{ndf} < 2$ in the TPC, at least one hit in either the two layers of the SPD, and to be refitted inwards from TPC to ITS.

4.1.2 Topological cuts

The huge amount of combinatorial pairs which passes the track selection hide the tiny D^0 signal. Further selections, exploiting the decay topology of the D^0 mesons which distinguish them from the background, have to be applied. In Fig. 4.1, a sketch of the $D^0 \to K^-\pi^+$ decay vertex is depicted. To be noticed, as features of the decay topology, the distance between the prolongation of the secondary tracks and the primary vertex (*impact parameter* d_0), which is not compatible with zero, and the small angle between the reconstructed momentum and the flight line of the D^0. From those and other features, some variables are defined to spotlight the signal. Their detailed description is given below.

Two kinds of variables are used to enhance the signal-to-background ratio: single track variables and pair variables. Single track selection is based on a lower cut on the

[1] In four so-called periods, namely LHCb, c, d, and e.

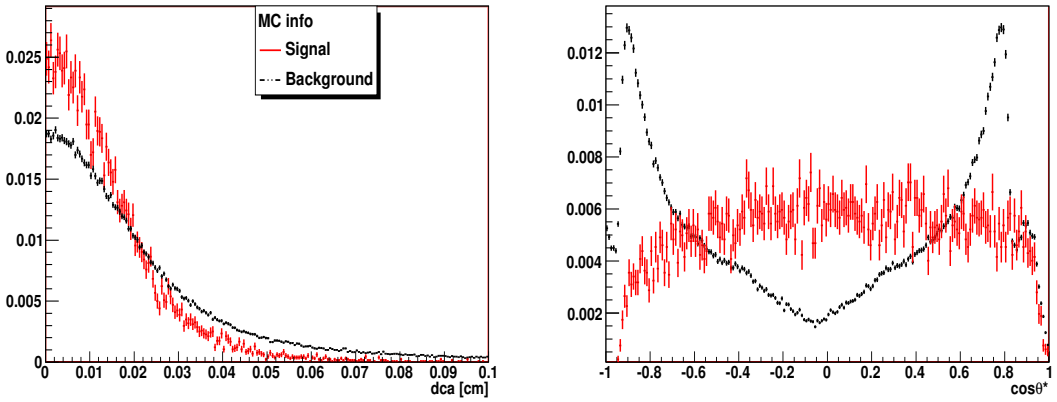

Figure 4.2: Comparison of *dca* (left) and $\cos\theta^*$ (right) distributions for signal (dotted red) and background (dashed black) from Monte Carlo simulations in the $p_{\rm t}$ range $2 < p_{\rm t} < 3$ GeV/c.

transverse momentum and a window on the track impact parameter with respect to the reconstructed primary vertex. The lower impact parameter cut rejects part of the background from primary tracks, while the upper cut rejects part of the background from secondaries coming from decays far from the primary vertex (mainly of strange hadrons) or particle interactions in the material.

The pair variables are more peculiar of the decay type and are also more powerful in the rejection of background. The *distance of closest approach* (*dca*) between the two tracks is the length of the segment minimizing the distance between the two track helices. For tracks coming from a common point, like a decay vertex or the primary vertex of interaction, the observed *dca* is determined by the detector spatial resolution on the track position, the ideal *dca* being zero. The distinction between signal and background is based on the shape of the distribution, more peaked towards zero for the signal with respect to background pairs, as it is shown in Fig. 4.2 left panel where the signal (red) and the background (black) *dca* distributions are superimposed (normalized to the same integral).

The $\rm D^0$ *decay angle* θ^*, defined as the angle between the kaon momentum in the $\rm D^0$ rest frame and the boost direction, is essentially flat, due to the isotropic decay direction in the $\rm D^0$ rest frame (see red points in Fig. 4.2 right panel), while the background distribution peaks at $|cos\theta^*| = 1$ (black points). Note that the depletion at $|\cos\theta^*| \approx 1$ is related to the cuts applied in the candidate reconstruction ($p_{\rm t} > 0.4$ GeV/c) and to detector effects: if the particles are emitted parallel to the $\rm D^0$ momentum, one of the two is boosted at very low momenta and can go out of the geometrical acceptance. An interesting feature is that this variable must be computed for the two possible mass hypotheses of the candidate ($\rm K^-\pi^+$ or $\rm K^+\pi^-$) allowing to distinguish between $\rm D^0$ and $\overline{\rm D}^0$ in case one of the two does not pass the selection.

The *pointing angle* $\theta_{\rm pointing}$, defined as the angle between the $\rm D^0$ flight line and the sum of the momenta of the two daughter tracks, is peaked at 1 for signal, while almost no correlation is present for the background, formed by random associations of tracks (Fig. 4.3, left panel).

The typical *impact parameters* (d_0) for a pion and a kaon track coming from a $\rm D^0$ decay is of the order of ~ 100 μm and have opposite signs. Ideally, their product would be negative. Due to detector resolution the observed distribution shows both positive and negative values, but it is strongly asymmetric with respect to zero. For background

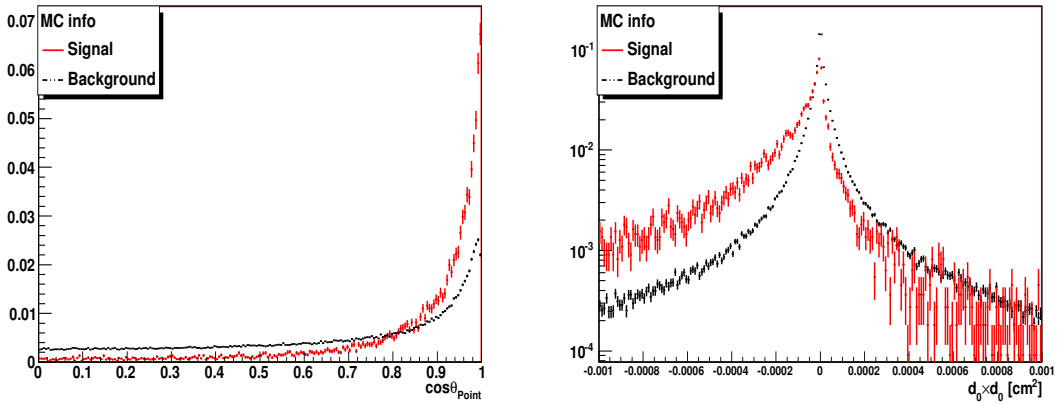

Figure 4.3: Comparison of $\cos\theta_{\rm pointing}$ (left) and $d_0^{\rm K} \times d_0^{\pi}$ (right) distributions for signal (dotted red lines) and background (dashed black lines) from Monte Carlo simulations in the $p_{\rm t}$ range $2 < p_{\rm t} < 3$ GeV/c.

Table 4.1: Cuts variables to increment the D^0 signal-to-background ratio.

Variable	Description
$p_{\rm t}$	Lower cut on transverse momentum
d_0	Window on the impact parameter with respect to primary vertex
d_0/δ	Lower cut on the impact parameter normalized to its error
dca	Upper cut on distance of closest approach with respect to primary vertex
$\cos\theta^*$	Upper cut on the cosine of the angle between the kaon momentum in the D^0 rest frame and the boost direction
$d_0^{\rm K} \times d_0^{\pi}$	Upper cut on the product of impact parameters of the daughter tracks
$\cos\theta_{\rm pointing}$	Lower cut on the cosine of the angle between the D^0 flight line and the sum of the daughter track momenta
Decay length	Lower cut on the distance from primary and secondary vertex
Decay length/δ	Lower cut on the decay length normalized to its error

pairs, composed mainly of randomly associated primary tracks with opposite charges, the distribution is symmetric (Fig. 4.3, right panel).

The *decay length*, namely the distance between the primary and the secondary vertex, is larger for signal than for background, since the latter is mainly composed by primary tracks and the separation of reconstructed secondary vertex from the primary vertex is determined only by the finite spatial tracking resolution. The decay length normalized by its error is also useful to the signal selection. A drawback of this selection is that the D^0 mesons from beauty decays are preferably selected, hence a balance between background rejection and acceptable fraction of feed-down D^0 mesons has to be found. A summary of the cut variables described above is presented in Table 4.1.

The selection cut values are tuned using a semi-automatic procedure of maximization of the significance, defined as $\frac{S}{\sqrt{S+B}}$, controlled by an empirical optimization based on the evaluation of the efficiency of each variable in the discrimination of the signal. The cuts are the final result of several Monte Carlo studies (see for instance [112]) and they

Table 4.2: Candidates identification schema. The first raw and first column indicate the possible outcome of the PID for the negative and positive track respectively. In the table the subscript "compat" stands for "compatible" and the dash (-) indicate that no conclusion can be drawn, but both imply that both mass hypothesis must be considered. A decision can be taken only in case of "$D^0/\overline{D}^0$" or "discard $D^0/\overline{D}^0$".

daugh −/+	π_{is}	K_{is}	π_{compat}	K_{compat}	$\pi_{is\ not}$	$K_{is\ not}$
π_{is}	discard	D^0	$D^0{}_{compat}$	$D^0{}_{compat}$	discard $\overline{D}^0$	discard D^0
K_{is}	$\overline{D}^0$	discard	$\overline{D}^0{}_{compat}$	$\overline{D}^0{}_{compat}$	discard $\overline{D}^0$	discard D^0
π_{compat}	$\overline{D}^0{}_{compat}$	$D^0{}_{compat}$	-	$D^0{}_{compat}$	discard $\overline{D}^0$	discard D^0
K_{compat}	$\overline{D}^0{}_{compat}$	$D^0{}_{compat}$	$\overline{D}^0{}_{compat}$	-	discard $\overline{D}^0$	discard D^0
$\pi_{is\ not}$	$\overline{D}^0{}_{compat}$	discard	$\overline{D}^0{}_{compat}$	discard D^0	discard	discard D^0
$K_{is\ not}$	discard	$D^0{}_{compat}$	discard $\overline{D}^0$	$D^0{}_{compat}$	discard $\overline{D}^0$	discard

have been studied again on a part of 2010 LHC data sample.

4.1.3 Particle identification

Additional background rejection, that will become more important in Pb–Pb collisions, is achieved by using particle identification. For the $D^0 \to K^-\pi^+$ channel the strategy consists in identifying the kaon and rejecting all candidates which are of the type $\pi\pi$, KK, or contain protons or electrons. The approach is conservative and aimed at reducing the combinatorial background without losing signal.

This is achieved by combining the information of two detectors, TOF and TPC, exploiting the different momentum reach they provide. The detectors were described in Section 2.3.1 and their performance was shown in Sections 2.4.5 and 3.2.2. The PID strategy for the single track was also explained in Section 3.2.2, while this section will focus on the PID strategy for D^0 candidates.

The identification is based on the combination of the response of both detectors: given for example the *kaon hypothesis*, +1 is assigned if the particle is identified as kaon, −1 if it is identified ad non-kaon, and 0 if it is not identified. This is done consulting both detectors and their exit codes are summed. The decoded answer will be: "it is a kaon" if +2, "it is not a kaon" if −2, "it is compatible with a kaon" if ±1 or 0. The same applies for the π. The selection of the candidates D^0 or $\overline{D}^0$ is a combination of the answers for both daughters as tabulate in Table 4.2. In summary, when the negative (positive) daughter is identified as non-π or non-K the $\overline{D}^0$ (D^0) or D^0 ($\overline{D}^0$) hypothesis, respectively, is discarded. When the positive daughter is identified as a K (π) and the negative one as a π (K) the candidate is identified as a $\overline{D}^0$ (D^0).

4.1.4 Signal extraction

The candidates surviving both cut and PID selections are used to fill an invariant mass histogram corresponding to a defined p_t interval. The signal peak is visible in nine p_t bins, from 1 to 16 GeV/c as shown in Fig. 4.4 and the spectra can be fitted with a Gaussian+exponential function (for details about the fitting procedure refer to Section 3.3).

The signal is extracted by subtracting the background below the red dashed line in Fig. 4.4 from the total fit (blue solid line) in a 3σ range around the mean value (both

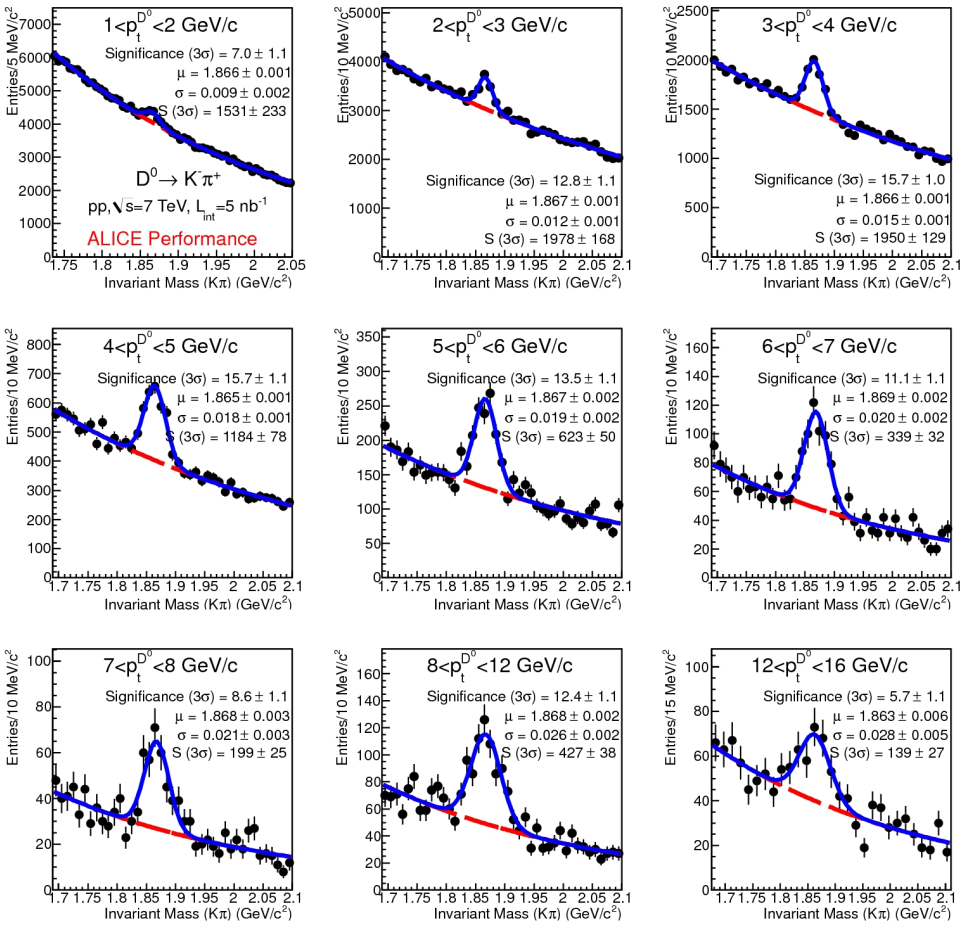

Figure 4.4: Invariant mass spectra in nine p_{t} bins fitted with a Gaussian + exponential function.

σ and mean extracted from the fit). The raw yields are shown in Table 4.3 for each p_{t} interval. The error on signal given by the fit was compared to the error calculated as the inverse of the significance, as mentioned in Section 3.3.1. They were found to be in agreement within the statistical uncertainty on the inverse of the significance.

4.1.5 Corrections and normalization

The efficiency correction, which was determined using detailed Monte Carlo simulations, accounts for primary vertex and track reconstruction, as well as for the single track, topological cut, and particle identification selections. The luminous region distribution and the conditions of all the ALICE detectors in terms of active channels, gain, noise level, and alignment, and their evolution with time during the 2010 LHC run, were included in the simulations. pp collisions were simulated using the PYTHIA 6.4.21 event generator [75] with Perugia-0 tuning [113]. Only events containing D mesons were transported through the apparatus and reconstructed.

In order to be confident with the efficiencies measured with Monte Carlo, the capability in reproducing the cut variables measured with data must be verified. In Fig. 4.5 the distribution of the $\cos\theta_{\mathrm{pointing}}$ (left) and the $d_0^{\mathrm{K}} \times d_0^{\pi}$ (right) for data (blue stars) and Monte Carlo (red crosses) are shown. Only single track selections are applied, hence the

Table 4.3: Raw signal from invariant mass fit in 3σ as a function of $p_{\rm t}$ with statistical errors.

$p_{\rm t}$ range (GeV/c)	raw yield±stat
1-2	1531±233
2-3	1978±168
3-4	1950±129
4-5	1184±78
5-6	623±50
6-7	339±32
7-8	199 ± 25
8-12	427±38
12-16	139± 27

candidates selected are mostly background. The comparison shows that the agreement between data and Monte Carlo is good.

The Monte Carlo sample used for the efficiency determination is enriched in signal. A $c\bar{c}$ pair is injected in each event and the D mesons forced to decay in the interesting hadronic channels. The efficiency was extracted separately for prompt D mesons and D mesons from B meson decays. The extracted $\rm D^0$ signal includes prompt $\rm D^0$, coming from charm quarks, and a significant amount of feed-down $\rm D^0$, coming from the decay of B mesons. It is therefore necessary to subtract the beauty contribution to get the correct final cross section.

Fig. 4.6 shows, as a function of transverse momentum, the $\rm D^0$ meson acceptance times efficiency ($Acc \times \varepsilon$) with $|y| < y_{\rm fid}$, where $y_{\rm fid}$ varies from 0.5 at low $p_{\rm t}$ to 0.8 at high $p_{\rm t}$, region where the $\rm D^0$ rapidity distribution has been checked to be uniform (within 1%). At low $p_{\rm t}$, the efficiency is of the order of 1% or less, while, for large $p_{\rm t}$, it increases and flattens at about 10-20%. The efficiency without particle identification selection, shown for comparison, is the same as that with particle identification, indicating that this selection is essentially fully efficient for the signal. The efficiency for $\rm D^0$ mesons from B meson decays, also shown for comparison, is larger by about a factor of two. This behaviour is due to the fact that feed-down $\rm D^0$ mesons decay further from the primary vertex, because of the large B decay length, hence the secondary candidates are favoured by the cut selection.

The fraction of prompt $\rm D^0$ mesons ($f_{\rm prompt}$) is estimated relying on the FONLL pQCD calculation [45], which well describes beauty production at Tevatron [114] and LHC [115, 116], and on the efficiency of secondary $\rm D^0$, as:

$$f_{\rm prompt} = 1 - \left(N^{\rm D^0,\overline{D}^0 \,from\, B\, raw} / N^{\rm D^0,\overline{D}^0 raw} \right) \tag{4.2}$$

with

$$N^{\rm D^0,\overline{D}^0 \,from\, B\, raw}(p_{\rm t})\Big|_{|y|<y_{acc}} = \left.\frac{{\rm d}\sigma^{\rm D^0,\overline{D}^0 from\, B}_{\rm FONLL}}{{\rm dp_t}}\right|_{|y|<0.5} \cdot \Delta y \Delta p_{\rm t} ({\rm Acc} \times \varepsilon)_{\rm feed\text{-}down} {\rm BR} \cdot {\rm L_{int}}. \tag{4.3}$$

The resulting prompt fraction is shown in the red lines in Fig. 4.7, left panel. It ranges between 75% and 90%, depending on the $p_{\rm t}$ interval, these values being determined also by the different efficiencies for prompt and feed-down $\rm D^0$ mesons. The systematic

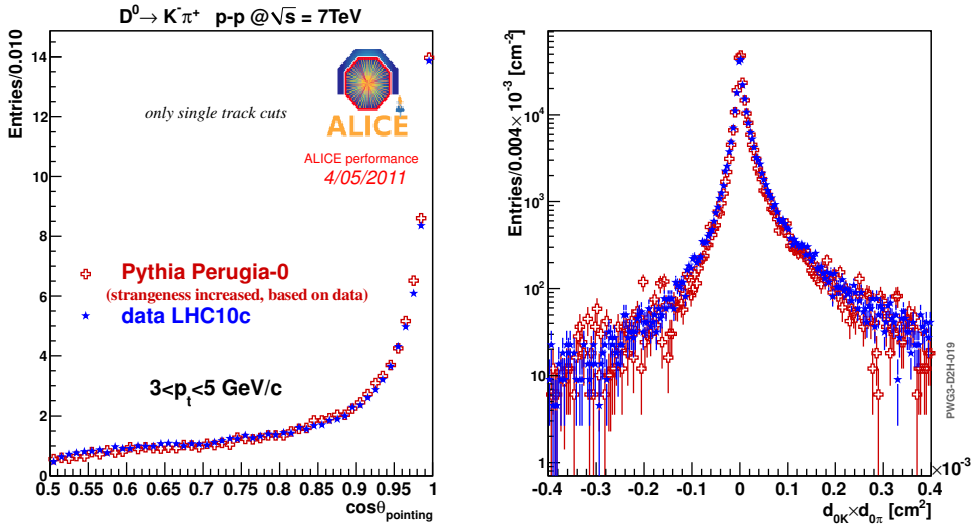

Figure 4.5: Comparison of $\cos\theta_{\rm pointing}$ (left) and $d_0^{\rm K} \times d_0^{\pi}$ (right) distributions for data (blue stars) and PYTHIA simulations (red crosses) with single track cuts only and $3 < p_{\rm t} < 5$ GeV/c.

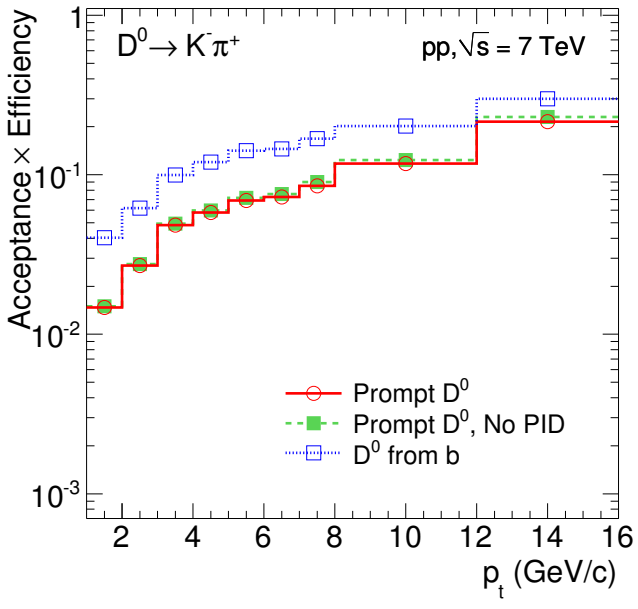

Figure 4.6: D^0 efficiency times acceptance as a function of $p_{\rm t}$. Empty circles refer to prompt D^0, full squares to prompt D^0 without PID selection, and empty squares to secondary D^0.

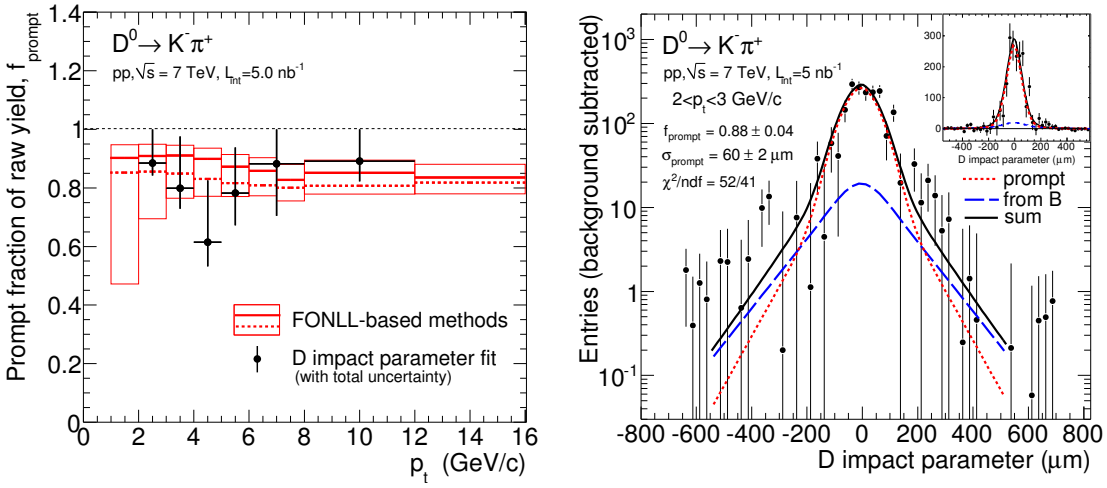

Figure 4.7: Left panel: Fraction of prompt D^0 mesons as a function of p_t as measured from FONLL calculation [45] (red empty boxes) and with the data-driven method (black points). Right panel: D^0 impact parameter exploited by the data-driven estimation of $f_{\rm prompt}$. The different dashed lines are the contributions from prompt and secondary D^0, the solid is the total fit. The inset is the same plot in linear scale. From [1].

uncertainty is estimated considering the uncertainty on the FONLL bottom production cross section, as well as an alternative way of using the FONLL calculation (see below). The former contribution was obtained by varying the b quark mass and the factorization and renormalization scales as suggested in, e.g., [117]. The alternative method consists in computing the prompt fraction using the FONLL cross sections for prompt and feed-down D mesons and their respective Monte Carlo efficiencies:

$$f_{\rm prompt} = \left(1 + \frac{(Acc \times \varepsilon)_{\rm feed-down}}{(Acc \times \varepsilon)_{\rm prompt}} \cdot \frac{\frac{{\rm d}\sigma^{\rm D^0\ from\ B}_{\rm FONLL}}{{\rm d}p_{\rm t}}}{\frac{{\rm d}\sigma^{\rm D^0}_{\rm FONLL}}{{\rm d}p_{\rm t}}} \right)^{-1} \tag{4.4}$$

The resulting prompt fraction is shown by the dashed horizontal lines in Fig. 4.7 (left panel). The full envelope of the uncertainty bands from the two methods, which is shown by the boxes in the figure, was taken as a systematic uncertainty.

The experimental measurement of $f_{\rm prompt}$ is also possible. CDF developed a method which exploits the different shape of the impact parameter distribution for prompt and feed-down D mesons [49]. As it is sketched in Fig. 4.8 the secondary D^0 mesons, and hence their daughters, are more displaced from the primary vertex with respect to the prompt, because of the decay length of the B mesons. The feasibility of this analysis in ALICE was studied with Monte Carlo simulations [118]. Applying the CDF method on the data sample used for this analysis the statistical uncertainties are larger than those from the MC-based methods, as shown in Fig. 4.7, left panel (markers). Also, the data-driven method is not reliable in the lowest and the highest p_t bins. So far, the data-driven method was used as a cross-check for the FONLL-based method. In short, the method relies on the following relation:

$$F_{d_0} = f_{\rm prompt} F_{\rm det}(d_0) + (1 - f_{\rm prompt}) \int F_{\rm B}(x) F_{\rm det}(d_0 - x) {\rm d}x, \tag{4.5}$$

where F_{d_0} is the impact parameter distribution of the reconstructed D^0 mesons, $f_{\rm prompt}$

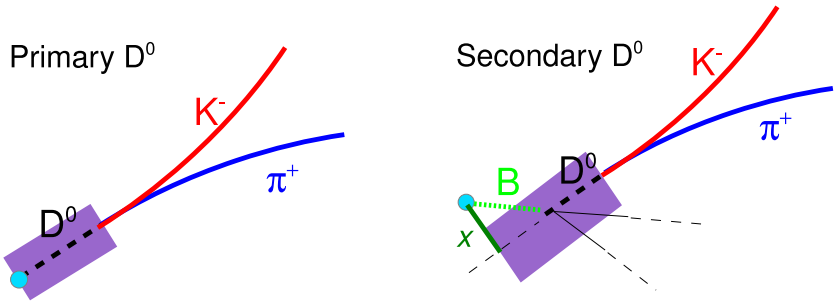

Figure 4.8: Sketch of prompt (left panel) and feed-down (right panel) D^0 mesons decay. The rectangle represents the resolution on the impact parameter due to the detector performance and the dashed black line the D^0 flight line (decay length). In the right panel the green thin dashed line is the B meson flight line and the green solid line (x) the impact parameter of the secondary D^0 meson.

is the fraction of D^0 from charm to be determined, $F_{\rm det}$ is the detector impact parameter resolution (assumed to be equal for primary and secondary D^0), and $F_{\rm B}$ is the true impact parameter distribution for secondary D^0 mesons. The impact parameter distribution of D^0 mesons is obtained from that measured for candidates with invariant mass in $M_{\rm D^0}\pm 2\sigma$ after subtracting the background contribution estimated from the candidates in the side-bands. The resolution term ($F_{\rm det}$) is parametrized by a Gaussian plus an exponential tail, as already done by CDF, and the true impact parameter distribution for secondary D^0, $F_{\rm B}$, can be described by a double exponential function.

Equation (4.5) is used to fit the impact parameter distribution of the selected D^0 candidates with $f_{\rm prompt}$ and the width of the Gaussian as free parameters. In Fig. 4.7, right panel, the impact parameter distribution fitted with eq. (4.5) (solid black line) is shown and the charm and beauty components are superimposed in dotted blue and dashed red lines respectively in the $p_{\rm t}$ range from 2 to 3 GeV/c.

4.1.6 Systematic uncertainties

Several sources of systematic uncertainties were considered, namely those affecting the signal extraction from the invariant mass spectra and all the correction factors applied to obtain the $p_{\rm t}$-differential cross sections. A summary of the estimated relative systematic errors is given in Table 4.4.

The systematic uncertainty on the yield extraction from the invariant mass spectra was determined by repeating the fit, in each $p_{\rm t}$ interval, in a different mass range, with a different function (a polynomial) to describe the background (not shown), and a method based on bin counting. The linear fit function for the background fit was not used for the estimation of the systematic uncertainty since, as in was shown in Section 3.3.1, it can bias the signal extraction, in particular at low $p_{\rm t}$. The bin counting method determines the yield by counting the entries of the invariant mass histogram in a fixed range of mass (60 MeV in this case), after the subtraction of the background fit. The result is

Table 4.4: Summary of relative systematic errors for D^0 cross section.

	Low p_t	High p_t
Yield extraction	20%	10%
Tracking efficiency	8%	
Cut efficiency	10%	10%
PID efficiency	5%	3%
MC p_t shape	3%	1%
Feed-down from B	$^{+5}_{-45}$ %	$^{+8}_{-10}$ %
Branching ratio	1.3%	
Normalization	3.5%	

shown in the left panel of Fig. 4.9 where the two series of points are the signal extracted with two estimations of the background: the red stars ("Bin Counting 2" in the plot) corresponds to using the fit of the side bands and the blue triangles ("Bin Counting 1") the final background fit. The relative difference with respect to the signal extracted with the standard procedure (S_{fit} in the axis label) shows that the results are in agreement. The discrepancy at high p_t is expected since the interval used for bin counting is fixed, while the signal width increases at high p_t. The final systematic uncertainty for the signal extraction is estimated to 20% at low p_t and 10% at high p_t.

The systematic uncertainty on the tracking efficiency includes the effects arising from track finding in the TPC, from track propagation from the TPC to the ITS, and from track quality selection. It was estimated from the comparison of data and simulation and from the variation of the track selection and it amounts to 8%. A systematic effect can arise due to different features in data and simulation for the variables used to select the signal D^0 meson candidates. The distributions of these variables were compared for candidates passing loose topological cuts, i.e. essentially for background candidates, and found to be well described in the simulation (Fig. 4.5).

The systematic effect due to residual differences between data and simulation was quantified by repeating the analysis procedure with different sets of cuts. In Fig. 4.9, right panel, the ratio between the resulting corrected yield extracted with three sets of cuts and the corrected yield obtained with the standard cuts is reported as a function of p_t. In the first and in the last bin, the difference in the case of looser and tighter selection, respectively, is due to the fact that the signal becomes too poor. From the spread of this ratio a systematic uncertainty was estimated to be at the level of 10%.

The systematic uncertainty induced by particle identification selection was studied by extracting the signal with and without the PID. In Fig. 4.10, left panel, the ratio of the yield in the two cases is shown. The signal extraction becomes delicate in some cases (e.g. the first bin), but this should not be considered in the evaluation of the systematic uncertainty. The PID efficiency was evaluated as well in data and simulation by repeating the analysis without applying this selection or with more stringent ($2\,\sigma$ compatibility instead of $3\,\sigma$) selection. The systematic uncertainty accounted for the PID was finally estimated to 5% at low p_t and 3% at high p_t.

Furthermore, the p_t-differential yields of particles and anti-particles were extracted separately. The ratio is shown in Fig. 4.10, right panel. Also in this case, the reduction of the statistics by a factor 2 has a negative effect on the signal extraction in the low- and high-p_t bins, but the yield extracted are compatible and no systematic uncertainty was assigned.

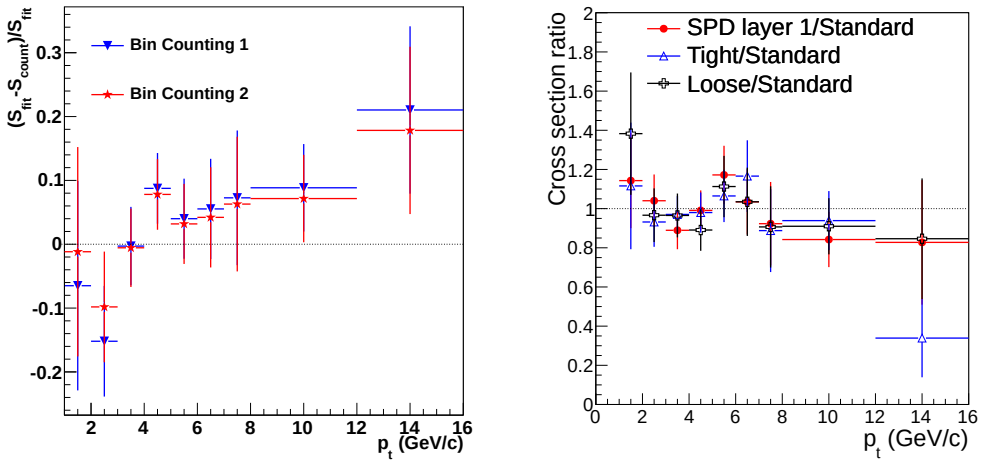

Figure 4.9: Left panel: Effect on the raw yield using different methods of signal extraction. See text for detail. Right panel: Ratio of the corrected yield extracted with three different sets of cuts with respect to the standard cuts.

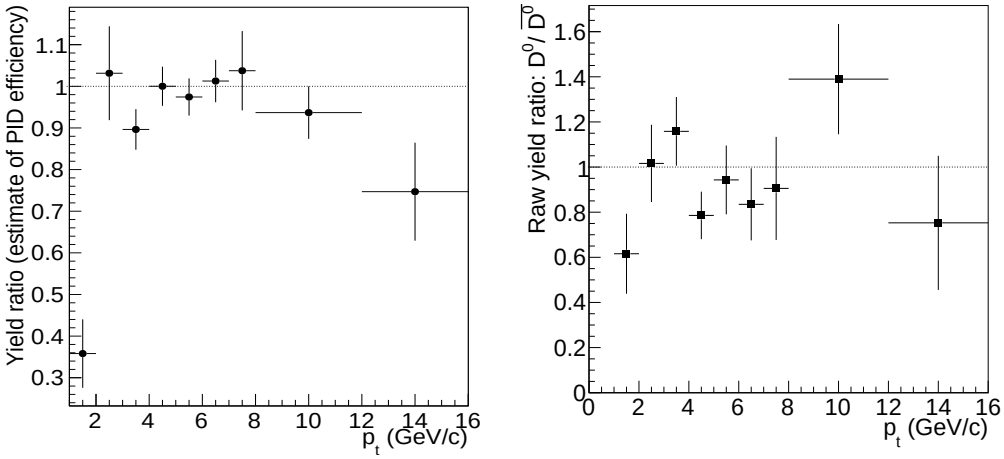

Figure 4.10: Left panel: Ratio of the raw yield obtained with PID and w/o PID. Right panel: Ratio of the signal extracted for D^0 and $\overline{D}^0$.

The correct description of the evolution of the experimental conditions with time was verified by analysing separately sub-samples of data collected with different detector configurations and also different orientation of the magnetic field. The results were found to be compatible within statistical errors.

The effect of the shape of the simulated D mesons spectrum within our p_t intervals was estimated from the relative difference in the Monte Carlo efficiencies obtained with the p_t shapes from PYTHIA [75] with Perugia-0 tune [113] and from the FONLL pQCD calculation [45]. In Fig. 4.11 the ratio of the efficiency from FONLL over the efficiency from PYTHIA for the case of the D^+ meson is reported. These two models predict a significantly different slope at high p_t, which however results in a systematic effect on the D^0 meson selection efficiency below 3%.

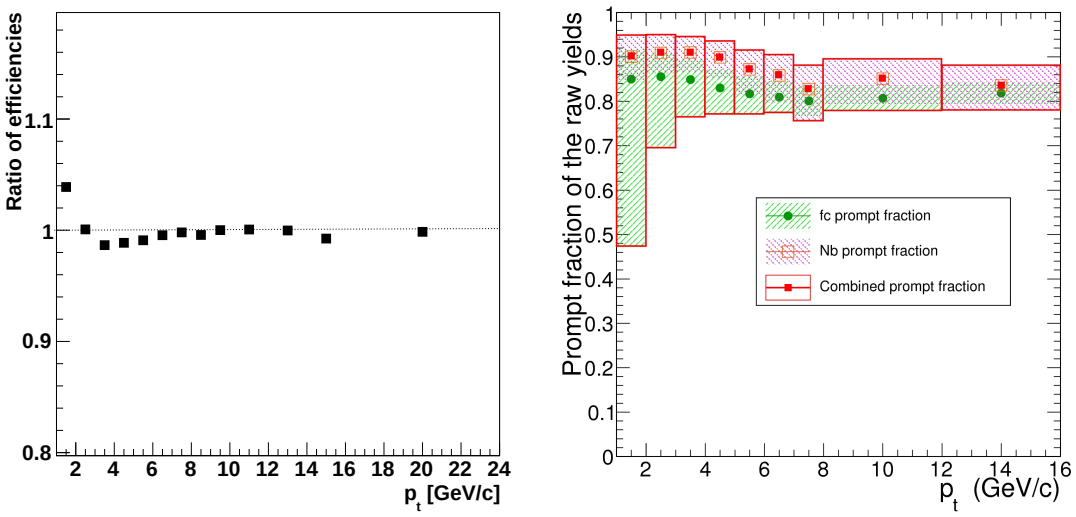

Figure 4.11: Left panel: Ratio of efficiencies for prompt D^+ from FONLL over PYTHIA as a function of p_t. Right panel: Fraction of prompt charm calculated with the f_c method (green circle) and with the N_b method (empty red square). The combined prompt fraction and the total systematic uncertainties are indicated by full red square and red box.

The contribution to the systematics from the feed-down subtraction was described in section 4.1.5. The left panel of Fig. 4.12 shows the fraction of prompt D^0 obtained with the two methods based on FONLL predictions and their systematic uncertainties. One method determines the yield of secondary D^0 (N_b) as in eq. (4.2) and it is used as central value. The other method calculate the fraction of prompt D^0 (f_c) using the cross sections from FONLL and the efficiencies for prompt and feed-down from Monte Carlo simulations according to eq. (4.4). The envelope of the systematic uncertainties from the two methods is used as systematic uncertainty for the central value, used to correct the final cross section.

Finally, the systematic error on the branching ratios [105] and the 3.5% uncertainty on the minimum-bias pp cross section were considered. The integrated luminosity was computed as $L_{int} = N_{pp,MB}/\sigma_{pp,MB}$, where $N_{pp,MB}$ and $\sigma_{pp,MB}$ are the number and the cross section of pp collisions passing the minimum-bias trigger condition defined in section 2.4.1. The $\sigma_{pp,MB}$ value, 62.5 ± 2.1 mb, was obtained relative to the cross section of collisions that give signals in both sides of the V0 scintillator detector ($\sigma_{V0\text{-}AND}$), measured with the van der Meer technique [110]. The relative factor, $\sigma_{pp,V0\text{-}AND}/\sigma_{pp,MB} \approx 0.87$, was found to be stable within 2% over the analysed data sample, as shown if Fig. 4.12.

4.2 Results

The p_t-differential cross sections for prompt D^0, obtained from the yields extracted by fitting the invariant mass spectra and corrected with the procedure described in the previous sections, is shown in Fig. 4.13. The error bars represent the statistical error, while the systematic errors, described in section 4.1.6, are plotted as rectangle areas around the data points. The numerical values are reported in Table 4.5 together with their statistical and systematic uncertainties. The measured D^0 meson production cross sections are compared with two theoretical predictions, namely FONLL [45]

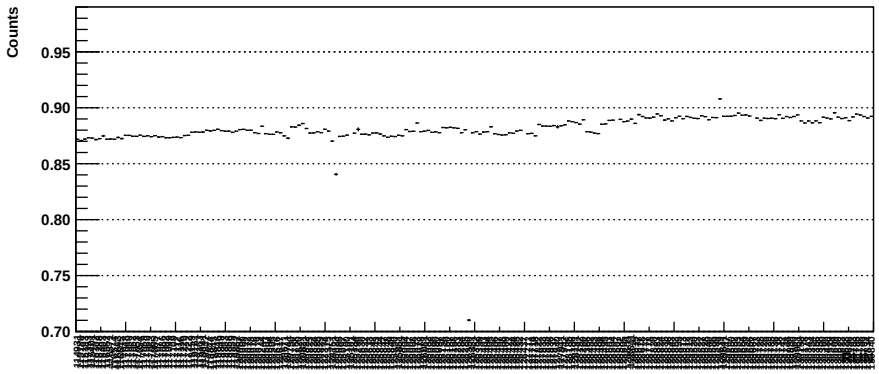

Figure 4.12: Ratio of events with a signal in both V0 scintillators over the events triggered as CINT1B (minimum-bias trigger as defined in Section 2.6.2) as function of run number.

and GM-VFNS [111]. Both calculations use CTEQ6.6 parton distribution functions (PDF) [119] and vary the factorization and renormalization scales, $\mu_{\rm F}$ and $\mu_{\rm R}$, independently in the ranges $0.5 < \mu_{\rm F}/m_{\rm T} < 2$, $0.5 < \mu_{\rm R}/m_{\rm T} < 2$, with the constraint $0.5 < \mu_{\rm F}/\mu_{\rm R} < 2$, where $m_{\rm T} = \sqrt{p_{\rm t}^2 + m_c^2}$. The charm quark mass is varied in FONLL within $1.3 < m_c < 1.7$ GeV/c^2. In Fig. 4.13 bottom panel the ratio between the measured cross section and the models is shown. Our measurement of D^0 at LHC energies are reproduced by both models within their theoretical uncertainties. The FONLL central value lies systematically below the data, while that of the GM-VFNS predictions lies above the data. With a reach down to $p_{\rm t} = 1$ GeV/c, this measurement probes the gluon distribution in the x range of a few 10^{-4}. Within the current uncertainties of the experimental measurement and of the theoretical predictions, it is not possible to draw conclusions about saturation effects.

Table 4.5: Production cross section in $|y| < 0.5$ for prompt D^0 in pp collisions at $\sqrt{s} = 7$ TeV, in transverse momentum intervals. The normalization systematic error of 3.5% is not included in the systematic errors reported in the table.

$p_{\rm t}$ interval (GeV/c)	$\mathrm{d}\sigma/\mathrm{d}p_{\rm t}\|_{\|y\|<0.5}$ $\pm$ *stat* $\pm$ *syst* (μb/GeV/c)
1-2	$180 \pm 30^{+48}_{-98}$
2-3	$115 \pm 11^{+20}_{-33}$
3-4	$59.7 \pm 4.3^{+8.5}_{-12.6}$
4-5	$29.1 \pm 2.1^{+4.2}_{-5.8}$
5-6	$12.5 \pm 1.1^{+1.8}_{-2.3}$
6-7	$6.37 \pm 0.70^{+0.94}_{-1.08}$
7-8	$3.07 \pm 0.47^{+0.50}_{-0.53}$
8-12	$1.23 \pm 0.13^{+0.19}_{-0.21}$
12-16	$0.215 \pm 0.050^{+0.037}_{-0.038}$

4.3 Other measurements of heavy-flavour production at mid-rapidity in pp collisions at 7 TeV

ALICE heavy-flavour programme in pp collisions is mainly devoted to test pQCD calculations at unprecedented centre-of-mass-energies and to serve as reference for Pb–Pb

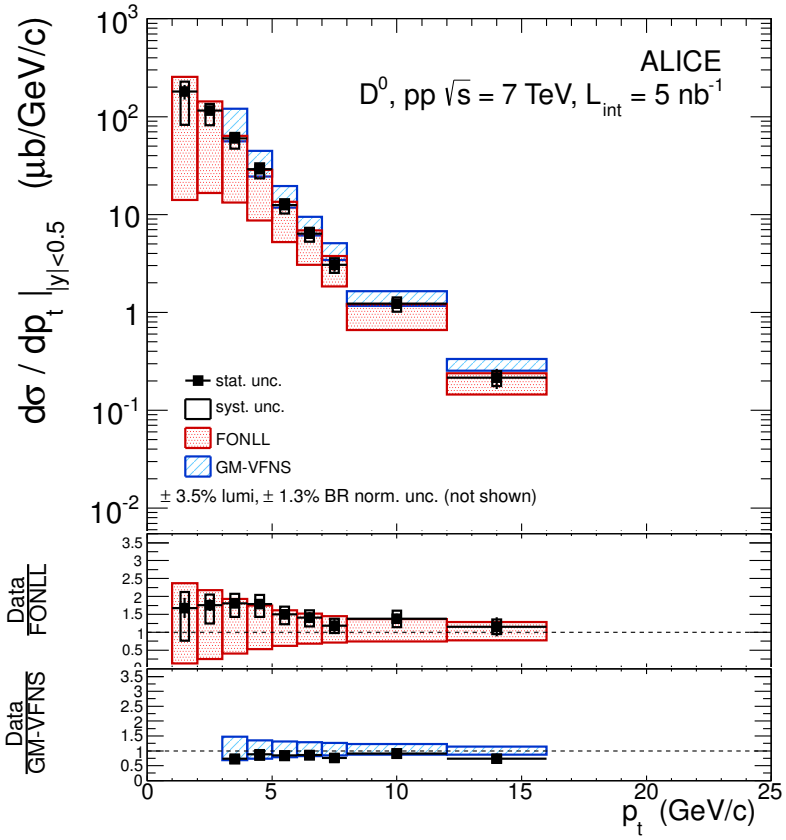

Figure 4.13: p_{t}-differential cross section for prompt D^0 in pp collisions at $\sqrt{s} = 7$ TeV compared with FONLL [45] and GM-VFNS [111] theoretical predictions.

measurements. The ALICE detector is well suited to perform exclusive charm and beauty measurements thanks to its vertex detector and tracking precision down to low p_{t}.

In this chapter the measurement of the D^0 meson cross section in the decay channel $\mathrm{D}^0 \to \mathrm{K}^-\pi^+$ was described. Similar analyses were performed to extract the cross section of D^{*+}, D^+ and D_s^+. The results are presented in Fig. 4.14 and they are compared to FONLL [45] and GM-VFNS [111] calculations, as it was done also for the D^0. While the FONLL calculation tends to underestimate the data, GM-VFNS tends to overestimates them, but both calculations are compatible with data.

The total charm cross section was measured by ALICE extrapolating the D^0, D^{*+}, and D^+ cross sections to $p_{\mathrm{t}} = 0$ and full rapidity using the FONLL calculation [120]. In Fig. 4.15 the total charm cross section measured by ALICE, together with the results from ATLAS [121], LHCb, and previous measurements, is shown as a function of the centre of mass energy. The LHC charm cross section measurements are consistent and compatible with MNR next-to-leading-order calculation [122], within uncertainties.

ALICE is able to measure heavy quarks also via their decay in electrons. The preliminary results available are described in the following.

The inclusive electron spectrum is obtained from the electron identification provided by the $\mathrm{d}E/\mathrm{d}x$ measurement in the TPC and the hadron rejection from TOF. Further extension of the p_{t} range is achieved with the TRD in the final results.

The background is subtracted from the inclusive electron spectrum via a Monte

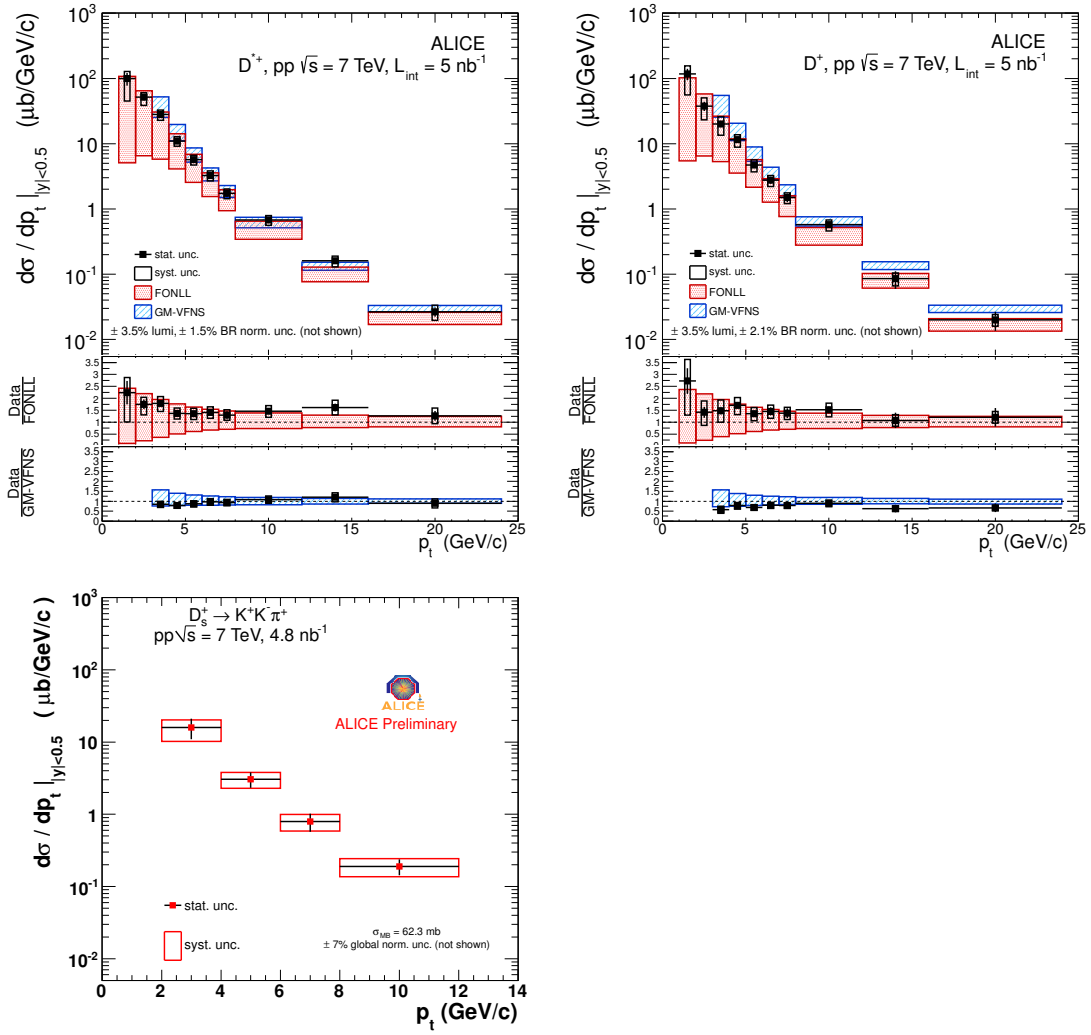

Figure 4.14: D^{*+} (top left), D^+ (top right) and D_s^+ (bottom) p_t-differential cross section from ALICE. D^{*+} and D^+ (from [1]) are also compared to models (FONLL [45] and GM-VFNS [111]) and the ratios between data and models are reported in the two lower panels.

Carlo data-tuned cocktail. The cocktail includes: (a) photonic background from Dalitz decays of light neutral mesons and photon conversions; (b) non-photonic background from $K^0_L \to e^{\mp}\pi^{\pm}\nu_e$ (K_{e3}), dielectron decays of light vector mesons, and heavy quarkonia (J/ψ, Υ). The photonic contribution is simulated using as input the π^0 spectrum measured by ALICE and the m_T scaling for heavier vector mesons (η, ρ, ω, η', ϕ). The contribution from J/ψ and Υ is parametrized from ALICE [123] and CMS [124] measurements, respectively.

In Fig. 4.16, left panel, the cocktail-subtracted electron spectrum in shown compared to the FONLL calculation for charm+beauty. The data lie between the central value and the upper limit of the theoretical uncertainty. The other set of points in Fig. 4.16, left panel, is obtained using the D^0 and D^+ cross sections measured by ALICE to calculate the transverse momentum spectrum of electrons decaying from charm. The charm-electron cross section is then compared to the appropriate FONLL calculation. Also in this case, the charm cross sections are at the upper edge of the FONLL predictions.

The electrons from beauty decay can be separated in ALICE applying a selection on

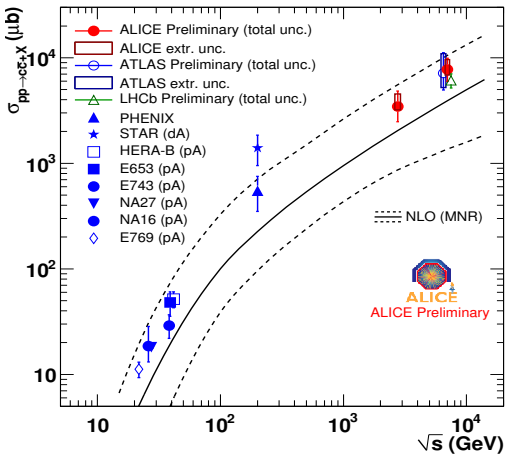

Figure 4.15: Total charm cross section as a function of $\sqrt{s}$.

the impact parameter. The electrons from beauty have an average impact parameter $d_0 \approx 500$ μm and a hard momentum spectrum. A high-purity beauty sample can be obtained with an impact parameter cut to reject misidentified hadrons, electrons from Dalitz decays, γ conversions, and charm meson decays. The remaining electrons from charm decays are estimated via measured D meson cross sections. The electrons from Dalitz decays and γ conversions left are subtracted via measured π^0 meson cross section. The resulting beauty cross section is shown in Fig. 4.16, right panel, compared to the subtraction between the cross section for charm+beauty and the cross section from charm showed in Fig. 4.16, left panel. Also the FONLL calculation for beauty is reported. Data and model are in agreement within uncertainties.

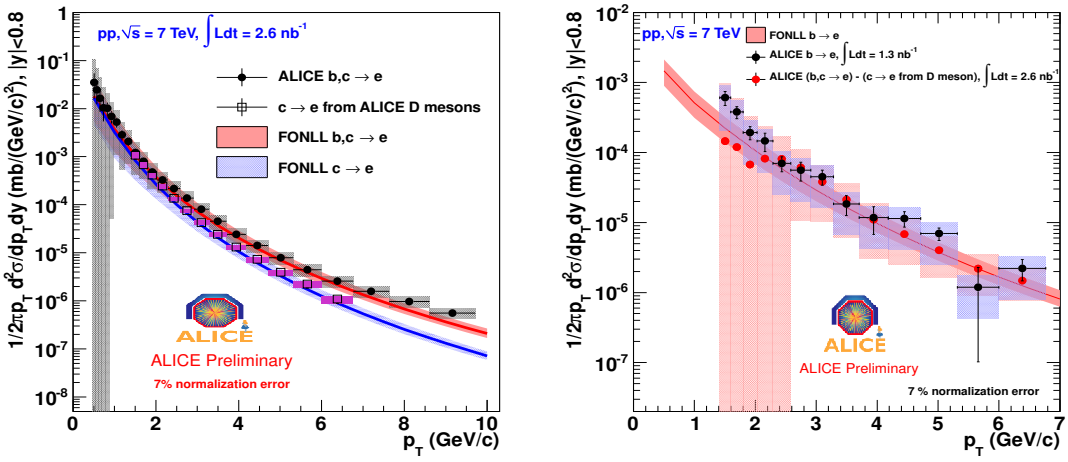

Figure 4.16: Left panel: Heavy-flavour electron cross section (full circle), compared to FONLL calculation for c+b $\to e$ (upper red band). Charm electron cross section from D meson measurement (empty rectangle) compared to FONLL calculation for c $\to e$ (lower blue band). Right panel: Beauty cross section from impact parameter cut based method (black circle) and difference of inclusive minus charm only cross sections (red circle) compared to FONLL b $\to e$.

According to the presented results, FONLL calculation better reproduces beauty than charm, even if both are compatible with the prediction in the quoted uncertainties.

Chapter 5

D^0 meson elliptic flow in Pb–Pb collisions

5.1 Introduction to the analysis methods and data sample

Different approaches to perform the elliptic flow measurement are possible, all of them having advantages and drawbacks, and a physics conclusions can be drawn only comparing the results from different methods and being aware of what each measurement is exactly probing. In Section 1.2.5 and 1.3.5 the present knowledge on flow and on heavy flavour flow in heavy ion collisions at different energies via the measurements performed by RHIC experiments and ALICE at the LHC was described. In this Chapter the focus will be on heavy-flavour elliptic flow measurements in the channel $D^0 \to K^-\pi^+$, which is the first preliminary result concerning flow obtained by ALICE in the heavy flavour domain. Further measurements with other D mesons and with heavy-flavour-electrons are ongoing. The outcome of different measurements can possibly answer the question whether heavy quarks flow like light quarks.

The first measurement of the D^0 v_2 was performed with three event plane based methods and a 2-particle cumulant method. Ideally, the event plane methods are not the best option, because they are sensitive to non-flow effects, to event-by-event fluctuations, and to the azimuthal acceptance of the detector. The multi-particle cumulants automatically cancel or reduce those contributions, especially increasing the number of correlated particles, and they allow for acceptance corrections. The statistics available from the 2010 Pb run at LHC allowed for only a 2-particle correlation measurement on top of the event plane methods, which intrinsically require less statistics.

The data sample consists in 3×10^6 minimum-bias events in the centrality class 30-50%. The data taking and trigger conditions were described in Section 2.6.3. The centrality measurement is performed with the V0 detector, described in Section 2.5.

The centrality class of 30-50% was chosen as a good compromise between having enough D^0 candidates and, at the same time, probing a region in which elliptic flow may be large. According to the measured charged track v_2 as a function of centrality (Fig. 5.1), flow does not vary too much in the region chosen, where it reaches its maximum.

The first step of the analysis, common to all methods, is the selection of the D^0 candidates, which follows the same strategy described in Sections 4.1.1-4.1.4, with a few variations needed to adapt to the particular Pb–Pb environment, as it will be shown in Section 5.2.

Section 5.3 will be devoted to the description of the tools for the determination of the event plane and to the three methods used, while in Section 5.4 the measurement

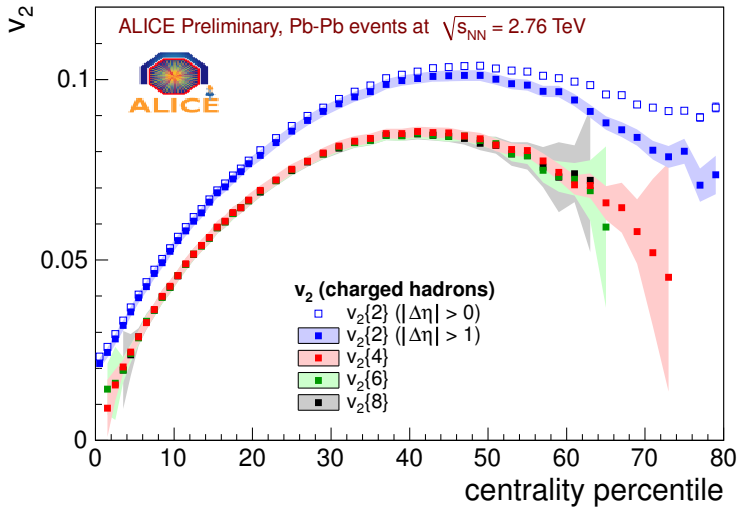

Figure 5.1: Elliptic flow of charged tracks as a function of centrality measured with multi-particle Q-cumulants [125] by the ALICE experiment.

with the 2-particle cumulant method will be described. In Section 5.5 the systematic uncertainties will be addressed and, finally, in Section 5.6 the results will be presented.

5.2 Signal extraction

The signal extraction follows the same procedure as for the pp analysis (refer to Sections 4.1.1-4.1.4). In this section, some Pb–Pb specific details will be discussed.

The heavy-ion environment is particularly critical because of the high track multiplicity of the events and, therefore, the high combinatorial background. The particle identification becomes mandatory, the topological cuts have to be tightened, or more powerful ones have to be found. As an example, in Fig. 5.2 the invariant mass distributions for $p_{\rm t} > 2$ GeV/c in Pb–Pb collisions 0-20% central with and without PID are shown. In both cases the same topological cuts are applied, while PID is used only in the right panel figure, where the significance improves by more than 30%, the background is reduced of a factor ~ 2.7, and the signal is unchanged within errors.

The selection conditions of Table 4.1 (pp) were updated in Table 5.1 for Pb–Pb signal extraction: among the variable listed, those in italics are specific for the Pb–Pb case, while the others are as in pp. In particular, two cuts on $\cos\theta_{\rm pointing}$ and decay length in the transverse plane were added because very effective in suppressing combinatorial background. In Fig. 5.3 the signal selection potential is visible by looking at the difference between the signal distribution in solid red lines and the background distribution in dashed blue lines, obtained from Monte Carlo simulations (HIJING Pb–Pb minimum bias plus signal from pp PYTHIA) and normalized to the same integral.

In Table 5.2 the cut values used for the Pb–Pb analysis are listed.

5.3 Event plane methods

The determination of the event plane in ALICE can be performed using either the tracks reconstructed in the TPC, which has a uniform azimuthal coverage in the central rapidity region, or the V0 detectors, located at forward ($2.8 < \eta < 5.1$) and backward

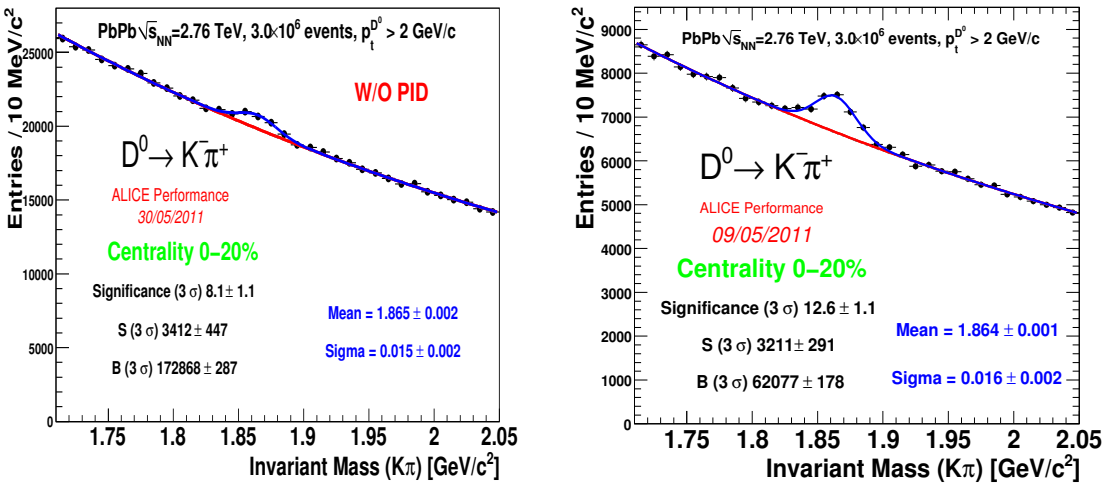

Figure 5.2: D^0 invariant mass distribution in the range $p_t > 2$ GeV/c for central (0-20%) collisions. Left panel: only topological cuts applied. Right panel: Topological cuts and particle identification (TPC+TOF) are applied.

Table 5.1: Selection variables to increment the D^0 signal-to-background ratio in Pb–Pb analyses.

Variable	Description
p_t	Lower cut on transverse momentum
d_0	Window on the impact parameter with respect to primary vertex
d_0/δ	Lower cut on the impact parameter normalized to its error
dca	Upper cut on distance of closest approach with respect to primary vertex
$\cos\theta^*$	Upper cut on the cosine of the angle between the kaon momentum in the D^0 rest frame and the boost direction
$d_0^K \times d_0^\pi$	Upper cut on the product of impact parameters of the daughter tracks
$\cos\theta_{\rm pointing}$	Lower cut on the cosine of the angle between the D^0 flight line and the sum of the daughter tracks momenta
$\lvert\cos\theta_{\rm pointingXY}\rvert$	*Lower cut on the absolute value of the cosine of* $\theta_{\rm pointing}$ *in the transverse plane*
Decay length	Lower cut on the distance from primary and secondary vertex
Decay length/δ	Lower cut on the decay length normalized to its error
Decay length XY/δ	*Lower cut on the decay length in the transverse plane normalized to its error*

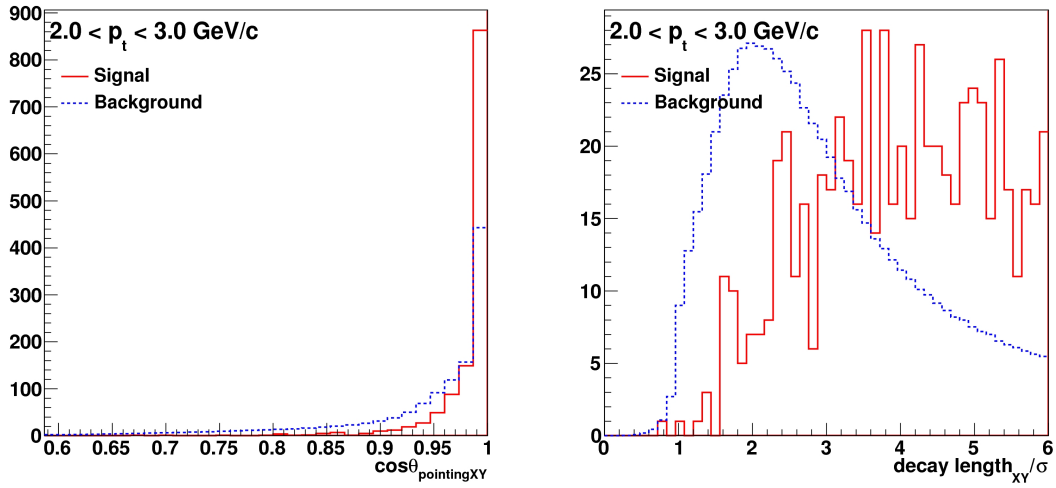

Figure 5.3: $\cos\theta_{\mathrm{pointingXY}}$ (left) and normalized decay length in XY (right) for signal (solid red) and background (dashed blue) from Monte Carlo simulations (HIJING Pb–Pb minimum bias plus signal from pp PYTHIA simulations).

Table 5.2: Selection cuts used in the Pb–Pb analysis.

p_{t}[GeV/c] bin	$\cos\theta^*$	dca [cm]	$d_0^K \times d_0^\pi$ [cm^2]	$\cos\theta_{\mathrm{pointing}}$
$2 < p_{\mathrm{t}} < 3$	< 0.8	< 0.025	< -0.00026	> 0.9
$3 < p_{\mathrm{t}} < 4$	< 0.8	< 0.025	< -0.00015	> 0.85
$4 < p_{\mathrm{t}} < 5$	< 0.8	< 0.025	< -0.00015	> 0.85
$5 < p_{\mathrm{t}} < 6$	< 0.8	< 0.025	< -0.0001	> 0.85
$6 < p_{\mathrm{t}} < 8$	$< 1.$	< 0.025	< -0.0001	> 0.8
$8 < p_{\mathrm{t}} < 12$	$< 1.$	< 0.025	< -0.0001	> 0.8
decl [cm]	$> \mathrm{Min}(p_{\mathrm{t}}\times 0.0066+0.01, 0.06)$			

p_{t} independent cuts:

$\lvert d_0^{K,\pi}\rvert$ [cm]	< 0.1
$p_{\mathrm{t}}^{K,\pi}$ [GeV/c]	> 0.8
$\lvert d_0/\delta d_0\rvert$	> 0.5
decl/δdecl	$> 1.$
$\lvert\cos\theta_{\mathrm{pointingXY}}\rvert$	> 0.998
declXY/δdeclXY	$> 5.$

pseudorapidity ($-3.7 < \eta < -1.7$). For this analysis, the TPC tracks were used, while the event plane with the V0 detectors requires further calibration procedure that is currently being validated.

For each harmonic n, the event plane angle ψ_n is measured through the Q-vector, which is a weighted sum of the azimuthal angle (ϕ) of all tracks but those coming from the D^0 candidate under exam, in order to remove autocorrelation [126].

In formulas:

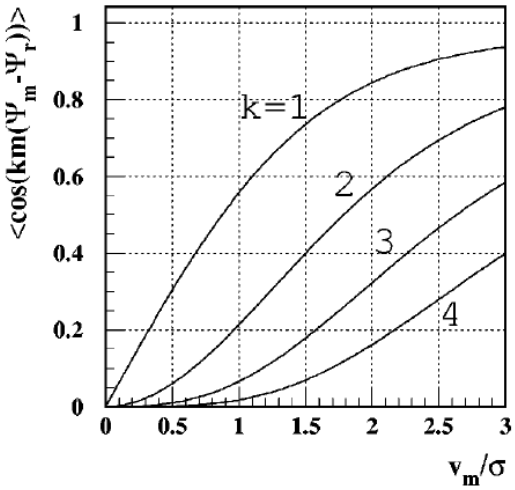

Figure 5.4: The event plane resolution for the n-th ($n = km$, according the the conventions of eq. (5.2) harmonic of the particle distribution with respect to the m-th harmonic plane, as a function of χ_m (figure taken from [127]).

$$Q_n = \begin{pmatrix} \sum_{i=0}^{N} w_i \cos n\phi_i \\ \sum_{i=0}^{N} w_i \sin n\phi_i \end{pmatrix} \qquad \psi_n = \frac{1}{n} \tan^{-1}\left(\frac{Q_{n,y}}{Q_{n,x}}\right) \tag{5.1}$$

The event plane angle ψ_n is an approximation of the reaction plane angle (Ψ_{RP}), i.e. the true reaction plane formed by the impact parameter of the two colliding nuclei and the beam direction. Due to the finite number of detected particles, the resolution in angle is limited and can be estimated for each harmonic considered. The measured v_n^{obs} must be divided by the resolution term to obtain the real v_n.

The resolution can be expressed as [127]:

$$\langle \cos km\,(\psi_m - \Psi_{\mathrm{RP}})\rangle = \sqrt{\frac{\pi}{8}}\chi_m \cdot \mathrm{e}^{-\chi_m^2/4} \cdot I_{(k-1)/2}(\chi_m^2/4) + I_{(k+1)/2}(\chi_m^2/4) \tag{5.2}$$

where $\chi_m = v_n\sqrt{2N}$ (N is the multiplicity) and I_ν the Bessel function of order ν, as drawn in Fig. 5.4. The mean cosine values are less than one, thus the correction always increases the flow coefficients.

The resolution can be measured from data using two sub-events, provided that they have the same multiplicity and they cover equal (or specular) rapidity region in order to expect the flow to be the same in both sub-events. The first condition grants that the resolution of the two sub-events is the same. If no other correlation is present except for those due to flow, or it is negligible, the following relations hold:

$$\left\langle \cos n\left(\psi_m^A - \psi_m^B\right)\right\rangle = \left\langle \cos n\left(\psi_m^A - \Psi_{\mathrm{RP}}\right)\right\rangle \times \left\langle \cos n\left(\psi_m^B - \Psi_{\mathrm{RP}}\right)\right\rangle, \tag{5.3}$$

$$\left\langle \cos n\left(\psi_m^A - \Psi_{\mathrm{RP}}\right)\right\rangle = \sqrt{\langle \cos n\,(\psi_m^A - \psi_m^B)\rangle}. \tag{5.4}$$

Hence the sub-event resolution can be measured from data by applying eq. (5.4).

Then, inverting eq. (5.2), $\chi_m^{\mathrm{sub-event}}$ can be retrieved giving the sub-event resolution as an input. Graphically, it means that considering on the y-axis of Fig. 5.4 the value obtained from eq. (5.4) the corresponding x-axis value gives $\chi_m^{\mathrm{sub-event}}$ (in the case treated

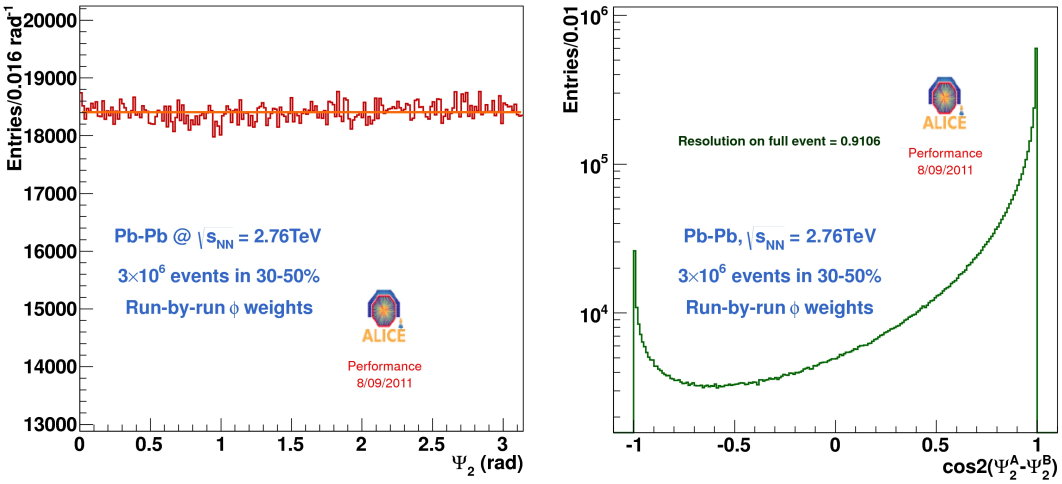

Figure 5.5: Left panel: event plane determined from TPC tracks with ϕ-weights and autocorrelation removed in the centrality class 30-50%. Right panel: distribution of the $\langle \cos 2\left(\psi_2^{\mathrm{A}} - \psi_2^{\mathrm{B}}\right)\rangle$ with $\psi_2^{\mathrm{A,B}}$ the second order event plane angle for the random sub-events A and B.

the function labelled with $k = 1$ is considered). The variable $\chi_m^{\mathrm{full-event}}$ is then obtained as

$$\chi_m^{\mathrm{full-event}} = \sqrt{2}\chi_m^{\mathrm{sub-event}} \tag{5.5}$$

being $N^{\mathrm{sub-event}} = \frac{1}{2}N^{\mathrm{full-event}}$ and $v_n^{\mathrm{sub-event}} = v_n^{\mathrm{full-event}}$, according to the assumptions made. All the ingredients needed to compute the resolution of the full event with eq. (5.2) are available.

In order to reduce non-flow effects, a pseudorapidity gap should be introduced between the "signal" particle and the "bulk" particles used for the event plane determination, but this is not yet included in the analysis described here.

The event plane is obtained in $|\eta| < 0.8$ with TPC tracks constrained to the SPD primary vertex, passing the following quality criteria:

- at least 70 clusters in the TPC;
- a χ^2/n.d.f < 2;
- a distance of closest approach to the primary vertex < 3.2 cm in z and 2.4 cm in x, y;
- a p_{t} between 0.15 and 20 GeV/c.

The aim at rejecting low quality and secondary tracks, not coming from the primary vertex. The weights used were determined as a function of time from the ϕ angle distribution. In Fig. 5.5, left panel, the event plane angle distribution obtained in the centrality class 30-50%, is shown. It is flat with deviations below 2%. Fig. 5.5, right panel, shows the distribution of $\langle \cos 2\left(\psi_2^{\mathrm{A}} - \psi_2^{\mathrm{B}}\right)\rangle$, where A and B are randomly defined sub-events. The resolution of the full event, i.e. the factor that divide the observed v_2, is estimated to be 0.91 for this centrality class.

In the following paragraphs the three methods used to extract the D^0 v_2 are described in detail. Namely:

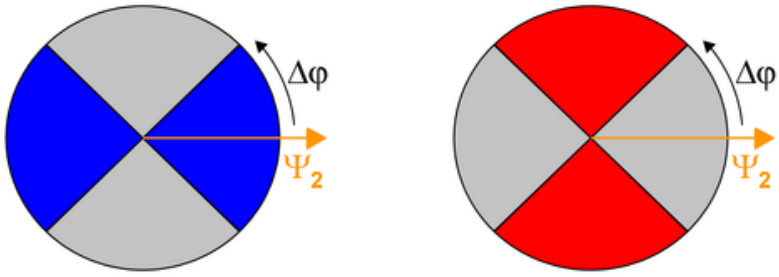

(a) In-plane. (b) Out-of-plane.

Figure 5.6: Intervals in $\Delta\phi$ used for the method of the fit of the invariant mass (Section 5.3.1).

1. fit to invariant mass in two $\Delta\phi$ bins (Section 5.3.1),
2. subtraction of the side bands (Section 5.3.2),
3. fit of v_2 vs mass (Section 5.3.3).

5.3.1 Fit to the invariant mass in two $\Delta\phi$ intervals

The first method measures directly the v_2 of the signal, after extracting it with an invariant mass analysis, hence it does not rely on any assumption on the background flow, at variance with the other methods described in the following. The D^0 candidates are grouped into three bins of p_t and two bins of $\Delta\phi = \phi - \psi_2$, where ϕ is the azimuthal angle of the D^0 candidate and ψ_2 is the event plane angle (autocorrelation is subtracted). The $\Delta\phi$ bins are chosen to be in the "in-plane" and "out-of-plane" directions defined respectively as (see Fig. 5.6):

$$\Phi_\mathrm{IN} = \left(\left[-\frac{\pi}{4}, \frac{\pi}{4}\right) \bigcup \left[\frac{3}{4}\pi, \frac{5}{4}\pi\right)\right) \tag{5.6}$$

$$\Phi_\mathrm{OUT} = \left(\left[\frac{\pi}{4}, \frac{3}{4}\pi\right) \bigcup \left[\frac{5}{4}\pi, \frac{7}{4}\pi\right)\right) \tag{5.7}$$

A mathematical expression of the yield in-plane (N_IN) and out-of-plane (N_OUT) is obtained by integrating the Fourier expansion truncated at the second order (hence assuming the higher harmonic are negligible) in Φ_IN and Φ_OUT:

$$N_\mathrm{IN,OUT} = \int_{\Phi_\mathrm{IN,OUT}} \frac{\mathrm{d}N}{\mathrm{d}\Delta\phi} = \int_{\Phi_\mathrm{IN,OUT}} \left[N_0(v_1 + v_2 \cos 2\Delta\phi)\right]. \tag{5.8}$$

The v_2 is thus related to the signal yield extracted from the fit to the invariant mass distribution through the following formula:

$$v_2^\mathrm{obs} = \frac{\pi}{4} \frac{N_\mathrm{IN} - N_\mathrm{OUT}}{N_\mathrm{IN} + N_\mathrm{OUT}}. \tag{5.9}$$

It was checked that the contribution from other harmonics is negligible using a Monte Carlo. The result is shown in Fig. 5.7.

In principle, more (at least six) $\Delta\phi$ bins can be used to obtain the signal distribution as a function of $\Delta\phi$ and v_2 can be obtained from a fit with a truncated Fourier expansion,

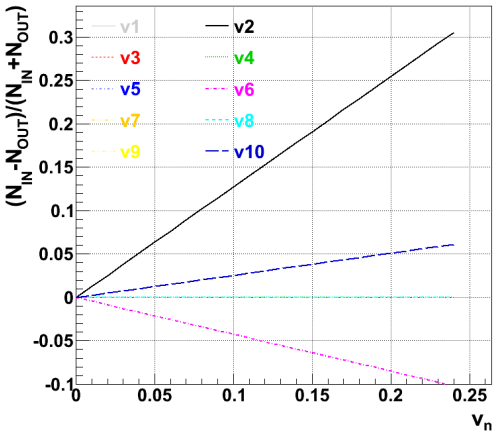

Figure 5.7: Method of the fit to the invariant mass distributions in $\Delta\phi$ intervals: contribution to the right side of the formula (5.9), as far as the harmonics from 1 to 10 are considered, it is dominated by v_2.

Table 5.3: Method of fit to the invariant mass in $\Delta\phi$ intervals: v_2 after correcting for the event plane resolution.

p_t (GeV/c)	v_2±stat.
2-5	0.14±0.07
5-8	0.04±0.09
8-12	0.13±0.14

but the limited statistics available did not allow to have enough bins, even integrating over p_t.

In each $\Delta\phi$ and p_t bin, the signal is extracted by performing a Gaussian plus exponential fit to the invariant mass distributions and subtracting the exponential background from the total fit (refer to Section 3.3 for more details on the fit). In Fig. 5.8 the invariant mass distributions and the fits are shown for three p_t intervals in the two $\Delta\phi$ regions, while in Fig. 5.9 the signal extracted and the corresponding significance in-plane (black) and out-of-plane (red) are drawn as a function of p_t. Since the 3σ range, where the signal is extracted, must be the same in-plane and out-of-plane to have a fair comparison, the value of σ is fixed to the σ obtained from the fit of the $\Delta\phi$-integrated invariant mass distribution for each p_t region. This also allows for a more stable performance in case of low significance.

5.3.2 2D methods: side band subtraction

The "2D methods", described here and in the following section, are based on the 2D distribution of $\cos 2\Delta\phi$ *vs the invariant mass* of the candidate, where $\Delta\phi$ is defined, as in Section 5.3.1, by $\phi - \psi_2$. Also in this case, the analysis is performed in intervals of p_t. In Fig. 5.10, left panel, an example of the 2D histogram in the p_t bin from 2 to 5 GeV/c is shown. The advantage of the "2D methods" is that a further splitting in $\Delta\phi$ is not needed. v_2 is then measured through projections on one of the axes, as it will be described below.

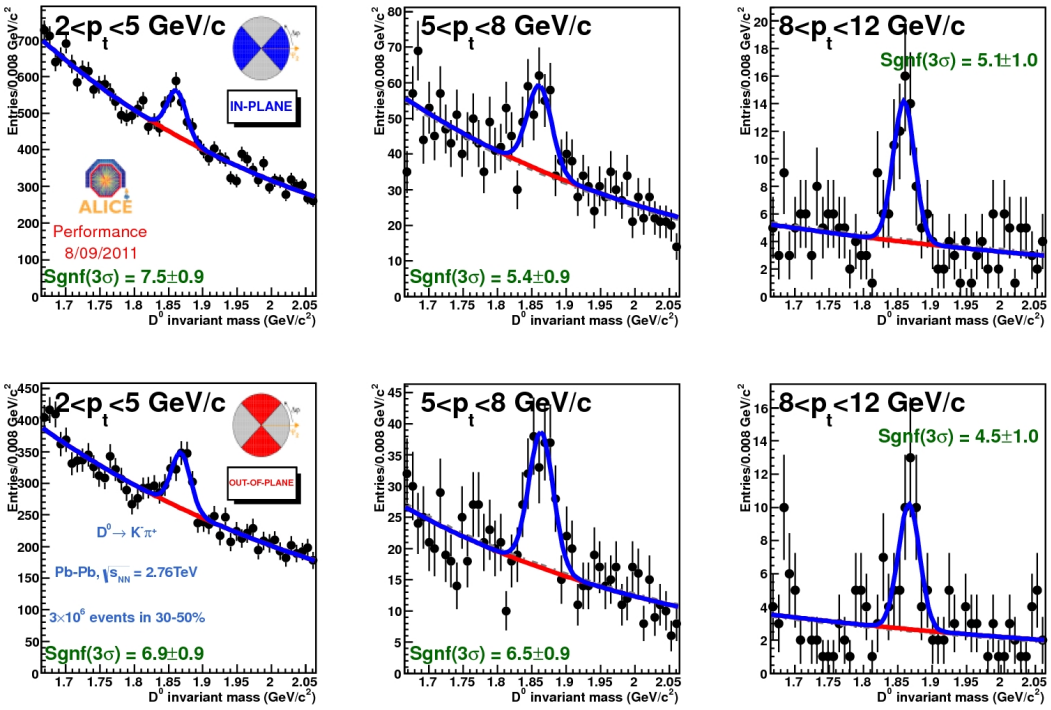

Figure 5.8: Method of the fit to the invariant mass distributions in $\Delta\phi$ intervals: D^0 invariant mass histograms for p_t from 2 to 5 (left), 5 to 8 (middle) and 8 to 12 (right) GeV/c in-plane (top) and out-of-plane (bottom).

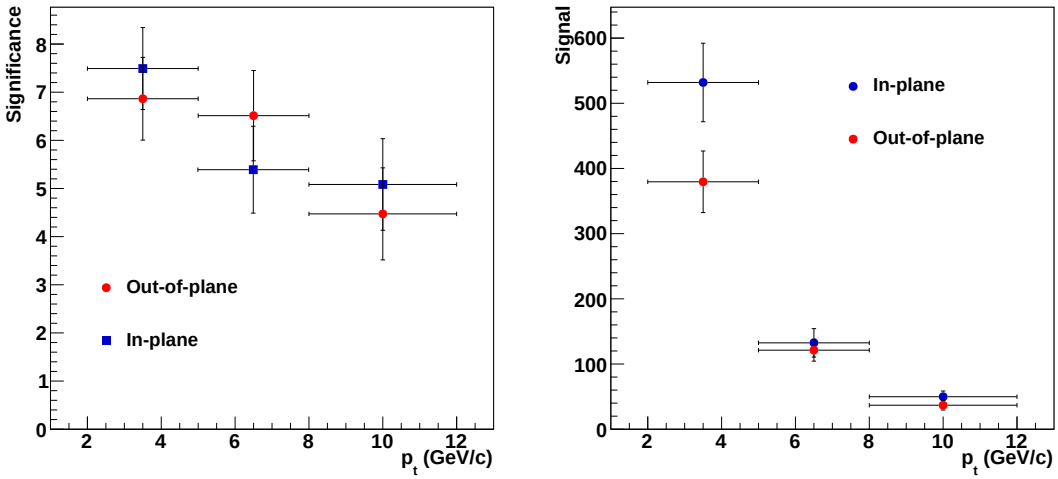

Figure 5.9: Method of the fit to the invariant mass distributions in $\Delta\phi$ intervals: significance (left panel) and signal (right panel) extracted in a 3σ range around the mass peak from the mass fit as a function of p_t in-plane (blue square) and out-of-plane (red circle).

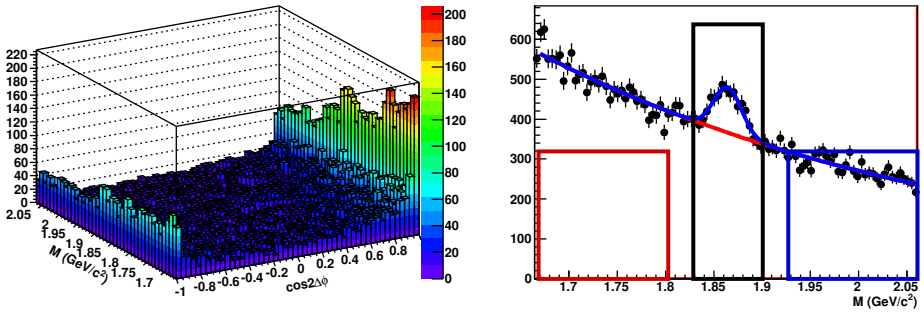

Figure 5.10: "2D Methods". Left panel: 2D histogram of $\cos 2\Delta\phi$ vs mass in $2 < p_t < 5$ GeV/c. Right panel: projection of the 2D histogram on the y-axis. The Gaussian + exponential fit and the invariant mass regions considered in the text are shown.

Table 5.4: Method of the side band subtraction: v_2 after correcting for the event plane resolution.

p_t (GeV/c)	v_2±stat.
2-5	0.167±0.072
5-8	0.115±0.072
8-12	0.137±0.098

In this Section the method of the side band subtraction is explained. Projections with respect to the $\cos 2\Delta\phi$, the x-axis in the left panel of Fig. 5.10, are done in three ranges of mass, as illustrated in Fig. 5.10, right panel. The width of the bands is: $\pm 2.5\sigma$ around the nominal D^0 mass, for the peak region, and $\pm 4.5\sigma$ away from the D^0 mass up to about $\pm 7\sigma$, and symmetric with respect to it for the side bands.

The histograms of the $\cos 2\Delta\phi$ distribution in the side bands and their average are normalized by the factor $f_{\text{left/right}}$ to be rescaled to the signal region:

$$f_{\text{left}} = \frac{\int_{\text{S region}} b(M)}{\int_{\text{SBleft}} b(M)} \qquad f_{\text{right}} = \frac{\int_{\text{S region}} b(M)}{\int_{\text{SBright}} b(M)} \tag{5.10}$$

where $b(M)$ is the fitting function for the background and the integrals are over the left (right) side band (SBleft(right)) and over the signal region (S region) defined in Fig. 5.10, right panel. The resulting projections are shown in Fig. 5.11, left panel, for the three p_t bins. The distribution of $\cos 2\Delta\phi$ for the signal is obtained by subtracting the average distribution of the side bands from the distribution in the signal region. This is shown in the right panel of Fig. 5.11, per each p_t interval. v_2^{obs} is obtained as $\langle \cos 2\Delta\phi \rangle$ and reported in the text boxes in the figures of Fig. 5.11, right panel. v_2^{obs}, corrected for the resolution, is summarized in Table 5.4.

5.3.3 2D methods: fit of v_2 vs mass

The distribution of $v_2^{\text{obs}} = \langle \cos 2\Delta\phi \rangle$ as a function of mass is obtained from the projection of the 2D histograms (left panel of Fig. 5.10) on the y-axis, the mass, as shown in the right panel of Fig. 5.12, for three p_t intervals. Given the fact that the elliptic flow is additive, v_2^{obs} in each invariant mass range is determined by the sum of v_2^{obs} for signal

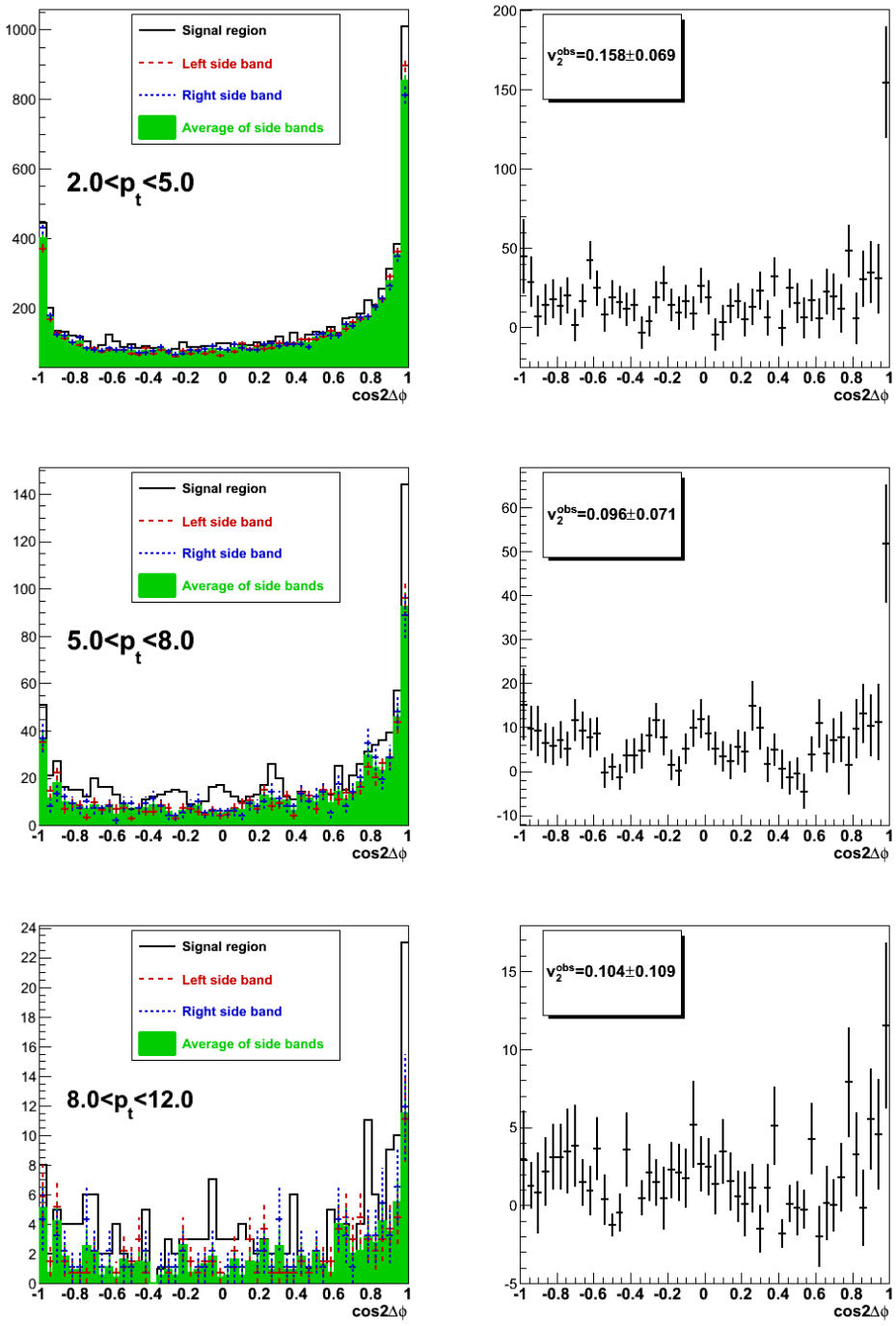

Figure 5.11: Method of the side band subtraction. Left panels: $\cos 2\Delta\phi$ distributions for peak region (solid black), left-hand (red dashed), right-hand (blue short dashed) side bands, and average of the bands (green area) in $2 < p_{\rm t} < 5$ GeV/c (top), $5 < p_{\rm t} < 8$ GeV/c (middle), and $8 < p_{\rm t} < 12$ GeV/c (bottom). Right panels: subtraction of the $\cos 2\Delta\phi$ averaged among the two side bands from the distribution in the peak region in the same $p_{\rm t}$ bins as in the left panels. In the boxes the resulting $v_2^{\rm obs}$ computed as $\langle \cos 2\Delta\phi \rangle$ and uncorrected for the event plane resolution is reported.

Table 5.5: Method of the fit to v_2 vs mass: v_2 after correcting for the event plane resolution.

p_t (GeV/c)	v_2±stat.
2-5	0.14±0.06
5-8	0.07±0.07
8-12	0.09±0.09

(S) and v_2^{obs} for background (B). The histograms of Fig. 5.12, right panel, are thus fitted with the following function:

$$\frac{B}{S+B} \cdot v_2^{bkg}(M) + \frac{S}{S+B} \cdot v_2^{sig} \tag{5.11}$$

where $v_2^{bkg}(M)$ and v_2^{sig} are given by:

$$v_2^{bkg}(M) = p_0 M + p_1 \quad \text{and} \quad v_2^{sig} = p_2 \tag{5.12}$$

being p_0, p_1, p_2 the free parameters of the fit, and M the mass. The fraction of signal ($\frac{B}{S+B}$) and background ($\frac{S}{S+B}$) with respect to the total number of candidates as a function of mass, which enter in function (5.11), are obtained from the fit to the invariant mass spectra and shown in Fig. 5.12, left panel. The resulting v_2 corrected for the resolution factor is reported in Table 5.5 for the three p_t intervals.

5.4 Q-Cumulants method

As described in Appendix A the measurement of v_n using multi-particle correlations eliminates order by order non-flow correlations [128, 129]. The cumulant expansion of multi-particle azimuthal correlations (*Q-cumulants* or *direct cumulants*) is not affected by higher order flow contribution differently from other [128, 130] multi-particle correlation methods. The correction for detector non-uniform acceptance, also possible with the other multi-particle methods, is more effective and can be performed in a single pass over data.

The 2-particle correlation methods [129, 131] are more or less equivalent to the event plane methods. The latter correlates two sub-events and the former sums the correlations between two particles. The two-particle correlation methods can be used when the non-flow contribution is small, but in general this is not negligible. Some sources of non-flow are well known and can become harmless after appropriate cuts in the phase space, but there is no systematic way to separate the effects of flow from other effects, at the level of two particle correlations.

As already mentioned, the limited statistics of the first Pb–Pb run at the LHC did not allow to go further than 2-particle correlations. The results that will be presented are still important as a check of the measurement stability and to validate the multi-particle correlation method using reconstructed candidates as input instead of identified tracks.

The 2-particle Q-cumulants [125] are related to the elliptic flow as:

$$\mathrm{QC}\{2\} \equiv v_2\{2\} = \langle \cos 2(\phi_1 - \phi_2) \rangle = \left\langle e^{in(\phi_1 - \phi_2)} \right\rangle = \langle v_2^2 \rangle + \delta_2, \tag{5.13}$$

where v_2 is the part due to anisotropic flow and δ_2 represents the so-called non-flow contribution, that comes from correlations not related to the initial geometry. In our analysis, the contribution from non-flow is not subtracted.

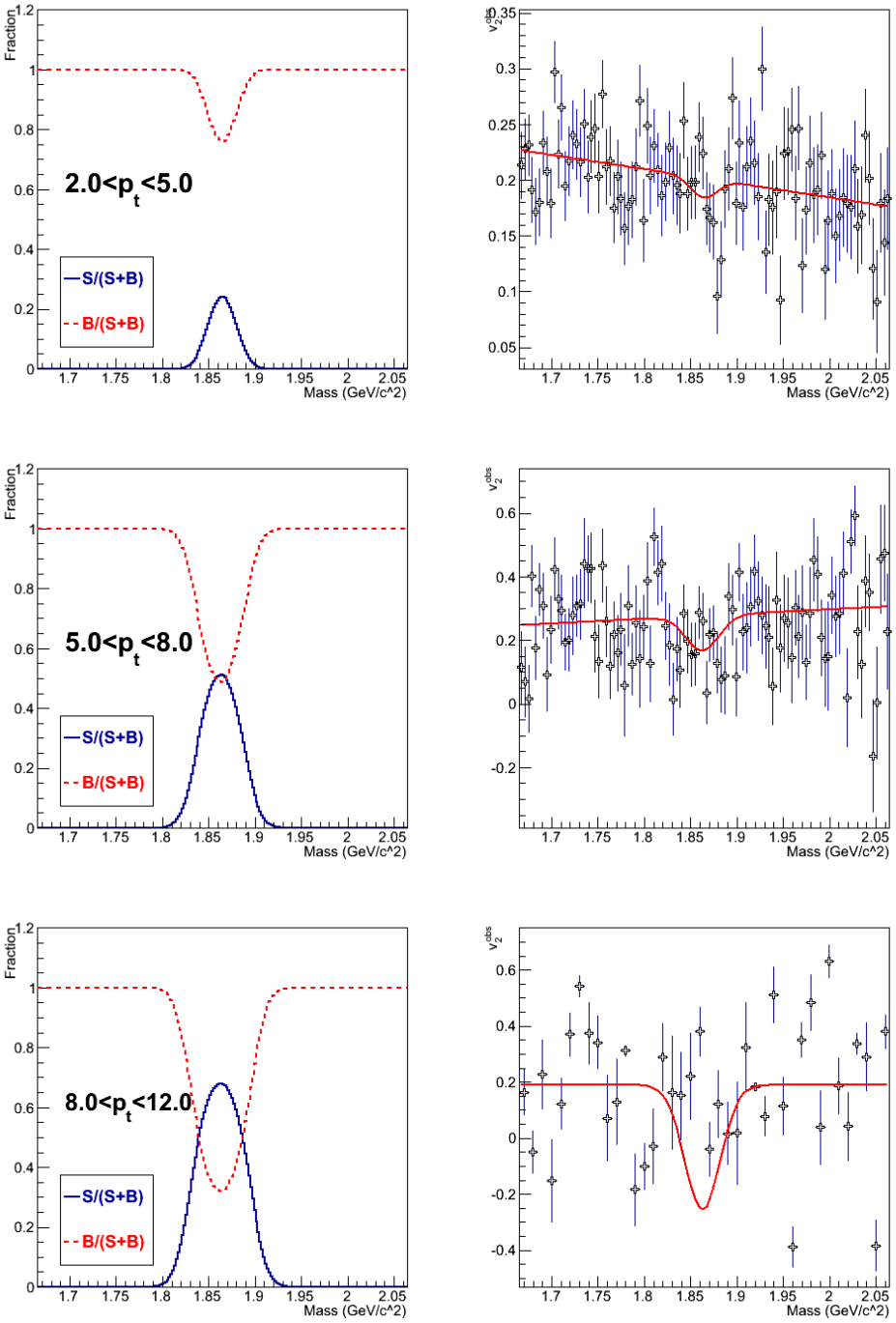

Figure 5.12: Method of fit of v_2 vs mass. Left panels: Fraction of signal and background over the total number of candidates as a function of mass obtained from the fit of the invariant mass histogram. Right panel: $v_2^{\mathrm{obs}} = \langle \cos 2\Delta\phi \rangle$ as a function of mass obtained from projections of the 2D histogram of Fig. 5.10, left panel. Top raw: $2 < p_{\mathrm{t}} < 5$ GeV/c. Middle raw: $5 < p_{\mathrm{t}} < 8$ GeV/c. Bottom raw: $8 < p_{\mathrm{t}} < 12$ GeV/c.

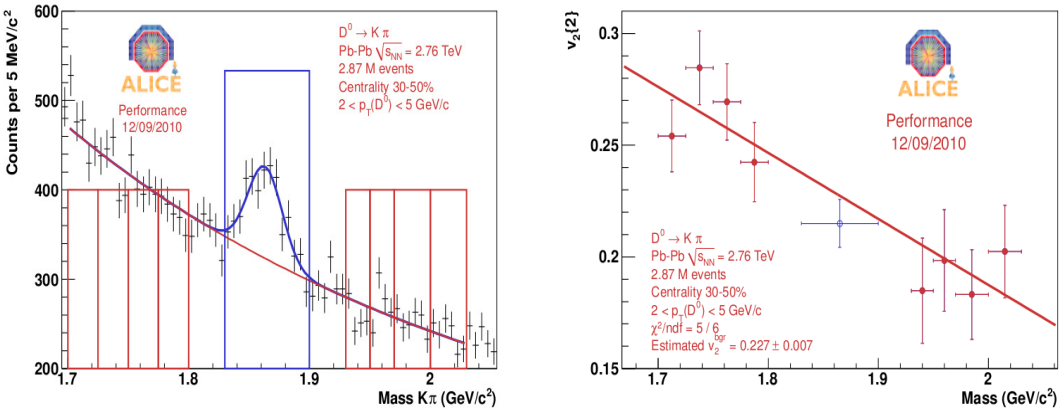

Figure 5.13: Left panel: Invariant mass spectrum with boxes indicating the mass ranges considered in the side bands and in the signal region. The fit is also shown. Right panel: $v_2\{2\}$ as a function of mass and a linear fit to interpolate the side bands points. The $p_{\rm t}$ ranges from 2 to 5 GeV/c.

Table 5.6: Results from 2-particle cumulants.

$p_{\rm t}$ (GeV/c)	v_2±stat.
2-5	0.62 ± 0.09
5-8	-0.070 ± 0.114
8-12	0.25 ± 0.14

The first step of the analysis is the selection of the candidates, performed by applying track selection, topological cuts, and PID, as for the previous methods. Then, $v_2\{2\}$ is measured for different mass regions as shown in Fig. 5.13, in particular $v_2^{\rm peak}$ in the D^0 mass range and $v_2^{\rm bkg}$ in the side bands. The v_2 of the signal ($v_2^{\rm sgn}$) is obtained as:

$$v_2^{\rm sgn} = \frac{S+B}{S} v_2^{\rm peak} - \frac{B}{S} v_2^{\rm bkg}. \tag{5.14}$$

The subtraction of the contribution from background is the most delicate part because it is based on the assumption that $v_2^{\rm bkg}$ is linear with mass. This appears to be the case, as it is qualitatively visible from the linear fit in Fig. 5.13, right panel, but also an interpolation with a parabola is possible (see Section 5.5). The linear function was used because it is the simplest good (χ^2/n.d.f. = 5/6 for the fit shown) approximation of the data. Another delicate point is the balance between high signal purity and the accuracy in the measurement of the background $v_2\{2\}$ in the mass side bands. In fact, in order to have a reliable extrapolation to the signal region, it is important to have as many points as possible in the side bands. In order to split the side bands in more bins and to perform a more robust linear fit, the background statistics should be high enough. On the other hand this prevents from having the highest possible purity in the signal region. For this reason, the cut variation is an important tool to study the systematic uncertainty for this method.

In Table 5.6 the obtained v_2 values are reported for the three $p_{\rm t}$ intervals.

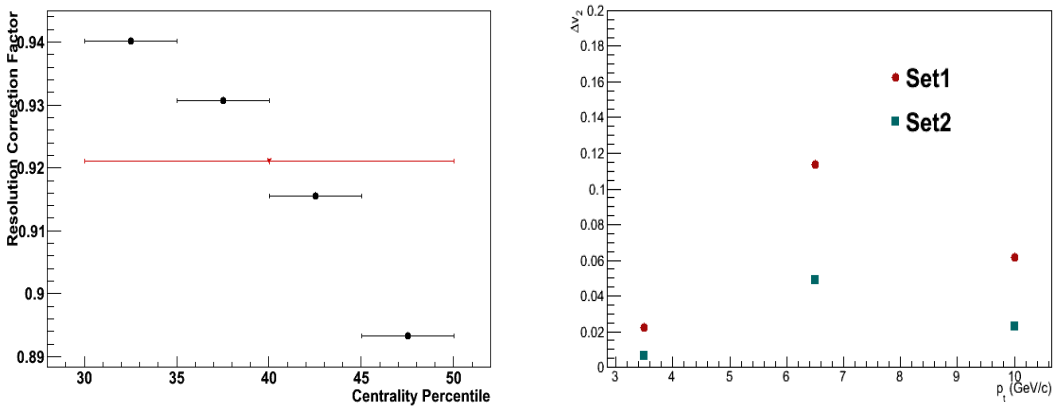

Figure 5.14: Left panel: Event plane resolution correction factor in 5% centrality bins (black circles) and in 20% centrality bin (red star) 30-50%. The systematic uncertainty is evaluated to be 2.5%, that is half of the total spread. Right panel: Difference in the v_2 extracted varying set of cuts with respect to the v_2 extracted with the standard set of cuts reported in Table 5.2.

5.5 Systematic uncertainties

The common sources of systematic uncertainties in the event plane based methods come from:

- the cut stability,
- the variation of the event plane resolution within the wide centrality bin 30-50%,
- and the validation of the method used comparing the results obtained with charged tracks with another independent event plane based analysis performed in ALICE.

The contribution due to the event plane resolution is small and it is estimated to be of about 2.5%, corresponding to half of the spread of the event plane resolution correction factors in 5% centrality ranges shown in Fig. 5.14, left panel, where the correction factor in 30-50% is also drawn.

The variation of the cuts has a strong influence on the results. One of the reasons is the limited statistics available which does not allow for large variation of the cuts. Another reason, as it was mentioned before, is peculiar of the 2D methods and the cumulants method. They rely on the hypothesis made for the background v_2 shape, hence the cuts should not reject much background allowing for a poorer statistical significance on the signal. It has to be noticed, however, that if the statistics was high enough, the significance would not be degraded too much by a loose selection. The variation of the selection cuts gives a systematic uncertainty on v_2 of about 20% at low p_{t} and up to a factor 3 at mid-p_{t}, as it is shown is Fig. 5.14, right panel, for the $2\Delta\phi$ bins method.

5.5.1 Method of fit to the invariant mass distribution in $\Delta\phi$ intervals

When comparing the v_2 of charged tracks measured with our $2\Delta\phi$ bins method to another analysis performed in ALICE, labelled in the following as *ALICE-PWG2*, we find a discrepancy, as shown in Fig. 5.15 where the v_2 of charged tracks measured with our method, with the ALICE-PWG2 event plane method, and with the scalar product method are compared. The systematic uncertainty was quantified in absolute values on v_2: 0.004 for

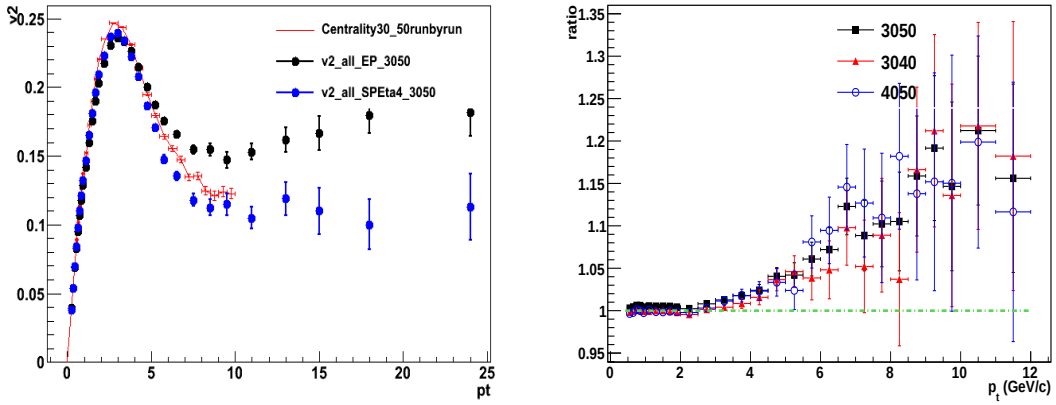

Figure 5.15: Left panel: v_2 of charged tracks measured with the method of the $2\Delta\phi$ bins (red points and lines) and the ALICE-PWG2 procedures: Event Plane method (black circles) and Scalar Product with an η gap of 0.4 (blue circles). The centrality class considered is 30-50%. Right panel: Ratio of the red and black points of the left figure (black squares) and the corresponding ratios in the centrality classes 30-40% (red triangle) and 40-50% (blue circles).

Table 5.7: Systematic uncertainties evaluated for the method of the fit to the invariant mass in 2 $\Delta\phi$ bins.

Source	p_t range (GeV/c)		
	2-5	5-8	8-12
Signal extraction	0.02	0.02	negligible
Cut variation	0.02	0.11	0.06
Event plane resolution	5%		
Comparison with ALICE-PWG2 method	0.004	0.01	0.03

$2 < p_t < 5$ GeV/c, 0.01 for $5 < p_t < 8$ GeV/c, and 0.03 for $8 < p_t < 12$ GeV/c. Possible explanations of this effect are the intrinsically different contributions from non-flow correlations and a different selection of the centrality class. The former is due to the $\Delta\phi$ binning, which is not present in the ALICE-PWG2 analysis, where $\Delta\phi$ is measured track-by-track and not using a wide bin. The latter comes from the fact that in the ALICE-PWG2 method a cross check with the centrality estimated with TPC tracks is done and the event is rejected if the response differs by more than 5%, while in our method this request is not applied.

For the $2\Delta\phi$ bins method a study on the systematic uncertainty on signal extraction was done by varying the range of fitting, the input value for the mean and the sigma of the Gaussian, and by using a bin counting method consisting in counting the entries of the invariant mass histogram in the signal region ($m^{D^0} \pm 50$ MeV) and subtracting the background fit function in the same mass interval. The systematic uncertainty was estimated to be less than 20%.

5.5.2 Side band subtraction method

The systematic uncertainty on the method of the side band subtraction was estimated by repeating the analysis with different sets of parameters, as listed below:

- the width of the invariant mass region of the signal was varied from 2 to 3 σ,
- the separation of the side bands was varied from 4 to 6 σ,
- the bin size of the $\cos 2\Delta\phi$ projected histogram was varied by a factor 20,
- the background under the signal was estimated with the left or right side band only, instead of the average of the two.

The results of $v_2^{\rm obs}$ as a function of the parameters listed above are shown in Fig. 5.16. The full spread, about 0.03-0.06 large in absolute value, is assigned as systematic error on the elliptic flow determination and it is represented by the grey shaded boxes around the empty triangles in Fig. 5.18, right panel.

5.5.3 Fit of v_2 vs mass

Similarly, the method of the fit of v_2 versus mass is repeated changing the following quantities to check the result stability:

- the width of the invariant mass bins was varied by a factor 10,
- the value of signal yield entering into the $S/(S+B)$ and $B/(S+B)$ terms in the fit function was varied by $\pm 1\sigma$ around the value extracted from the fit to the mass spectrum,
- the fit to the $v_2^{\rm obs}$ of candidates as a function of the invariant mass was repeated assuming a flat (instead of linear) $v_2^{\rm obs}$ of the background.

In Fig. 5.17 the results of these studies are shown: the full spread used as systematic uncertainty is of 0.03-0.05 in absolute value of v_2.

In the left panel of Fig. 5.18, the different contributions to the systematic uncertainty for the method of the $\Delta\phi$ intervals are summarized and the statistical errors are reported as well. In the right panel, the results for the three event plane methods are compared. They are in agreement within statistical uncertainties, hence no further systematics was added to the central point, which will be shown and commented in Section 5.6.

5.5.4 Q cumulant method

Two sources of systematic uncertainties were taken into account for the QC{2} method: the cut variation and the fitting function for the interpolation of the background v_2 to the signal region in the mass distribution.

The first source was studied by repeating the v_2 extraction with two sets of cuts that provide different purities. The comparison of the results gives a spread between 35% and a factor 2 depending on $p_{\rm t}$.

As mentioned in Section 5.4, the data in the side band region can be fitted with a line, but the statistical errors are large enough to allow for other parametrizations. A quadratic polynomial was used as well and the systematic uncertainty extracted amounts to 70-100%.

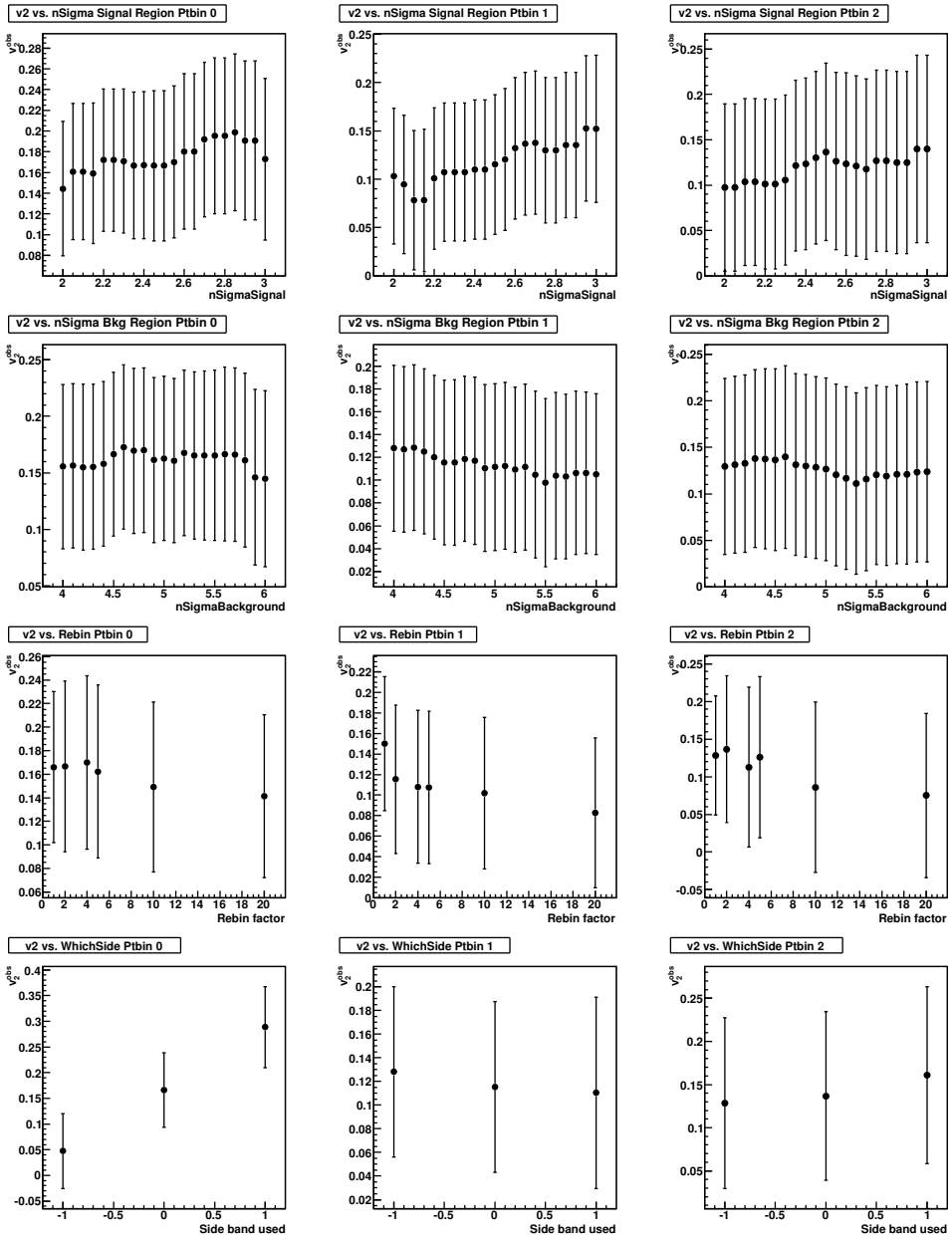

Figure 5.16: Systematic uncertainties on $v_2^{\rm obs}$ for the side band subtraction method. Top row: variation of $n\sigma$ in the width of the peak region. Second raw: variation of $n\sigma$ separation of the side bands. Third row: variation of bin size. Forth row: effect using only left (-1) or right (1) side band instead if the average (0) for background subtraction. Left column: $2 < p_{\rm t} < 5$ GeV/c. Central column: $5 < p_{\rm t} < 8$ GeV/c. Right column: $8 < p_{\rm t} < 12$ GeV/c.

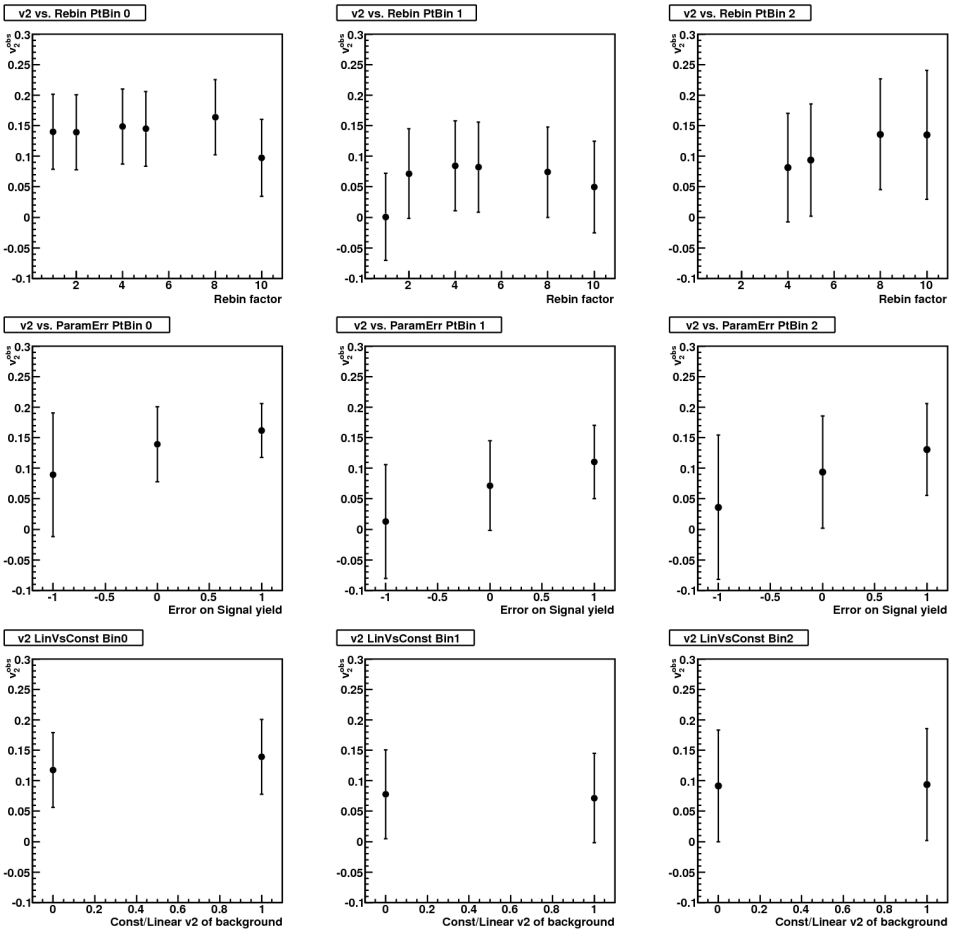

Figure 5.17: Systematic uncertainties on the method of the fit of v_2^{obs} versus mass. Top raw: variation of invariant mass bin size. Middle raw: effect of varying the signal yield in the fitting function by $+1$ and -1 times its statistical error. Bottom row: effect of using constant (0) vs linear (1) parameterization for the v_2 of the background vs invariant mass. Left column: $2 < p_{\mathrm{t}} < 5$ GeV/c. Central column: $5 < p_{\mathrm{t}} < 8$ GeV/c. Right column: $8 < p_{\mathrm{t}} < 12$ GeV/c.

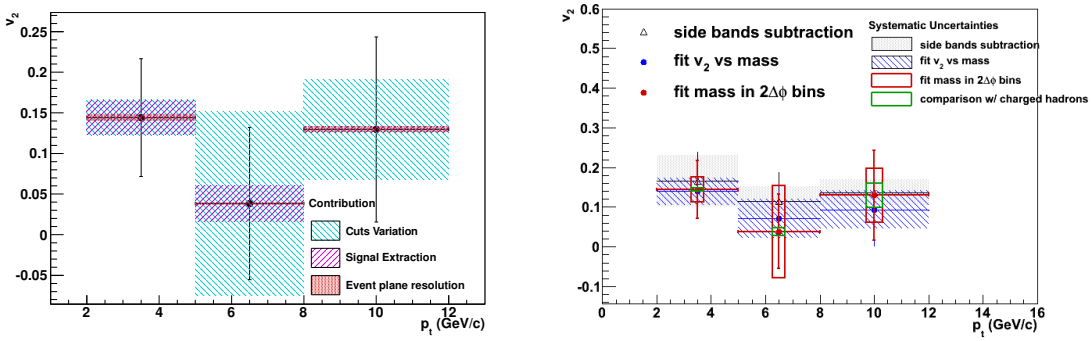

Figure 5.18: v_2 with the method of $\Delta\phi$ intervals with statistical and systematic uncertainties in the left panel. Comparison of the three event plane based methods in the right panel. In the legend the different contributions are listed. Note that the systematic in green is included also in the red boxes.

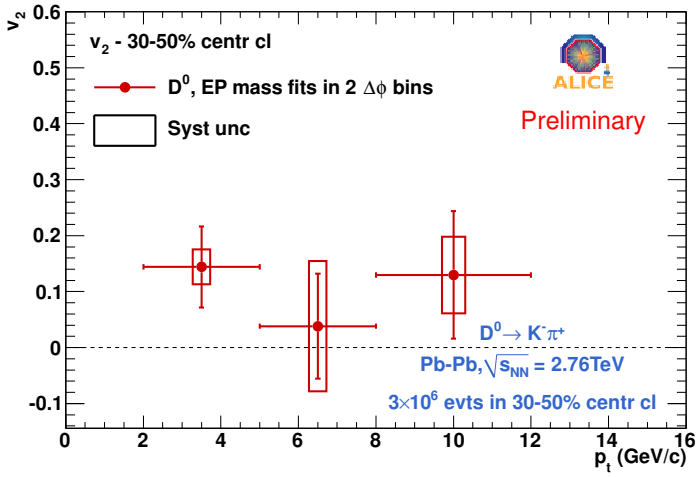

Figure 5.19: D^0 v_2 with the method of $\Delta\phi$ intervals as a function of p_t in the centrality class 30-50%. Boxes are total systematic uncertainties.

5.6 Results

The first measurement of inclusive D^0 v_2 with three different event plane methods and 2-particle Q-cumulants was described. No further corrections for non-flow correlation and feed-down subtraction were applied so far, even if both contributions are known to be seizable.

In Fig. 5.19 the v_2 measured in $2 < p_t < 12$ GeV/c with the method of $\Delta\phi$ intervals is shown. It was chosen among the event plane results because it does not require any assumption on the v_2 of the background. The "2D methods" in principle need less statistics because they do not split in $\Delta\phi$, but the sensitivity on the estimation of the background flow is critical at high p_t because of the low background statistics.

The figure also gives a hint for a D^0 v_2 greater than zero, however within 1.8σ only.

The same figure is reported in Fig. 5.20 compared with the result of the QC{2} method. Also in this case, the subtraction of the background contribution suffers the same difficulties as in the "2D methods", leading to bigger statistical uncertainties.

The comparison of all the results available for the bin $2 < p_t < 5$ GeV/c is displayed in Fig. 5.21 and shows a good compatibility among all measurements, but confirms that the statistics is at the limit for this measurement.

In Fig. 5.22 the comparison between the D^0 v_2 and the charged tracks v_2, measured by ALICE [80], in the centrality class 30-50%, is shown.

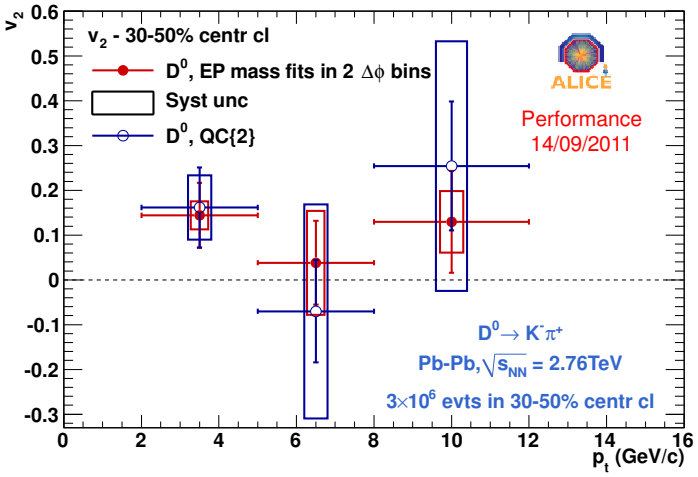

Figure 5.20: Results shown in 5.19 (red closed points) compared to the QC{2} (blue open points) as a function of p_{t} in the centrality class 30-50%. Boxes are total systematic uncertainties.

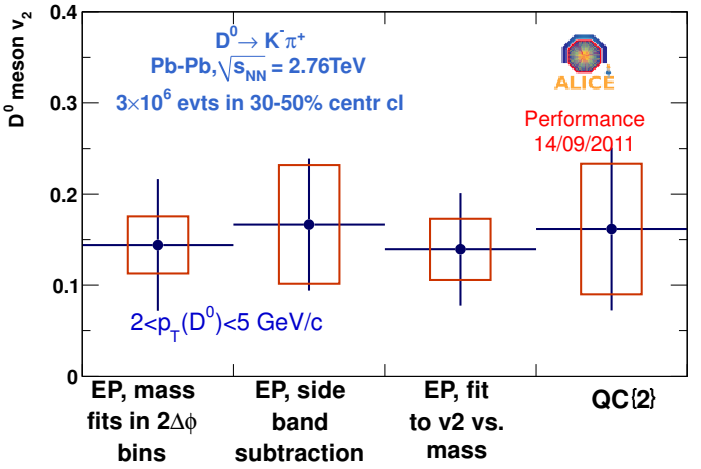

Figure 5.21: D^0 v_2 in $2 < p_{\mathrm{t}} < 5$ GeV/c measured with two intervals of $\Delta\phi$, side band subtraction, fit of v_2 vs mass and 2-particle cumulants.

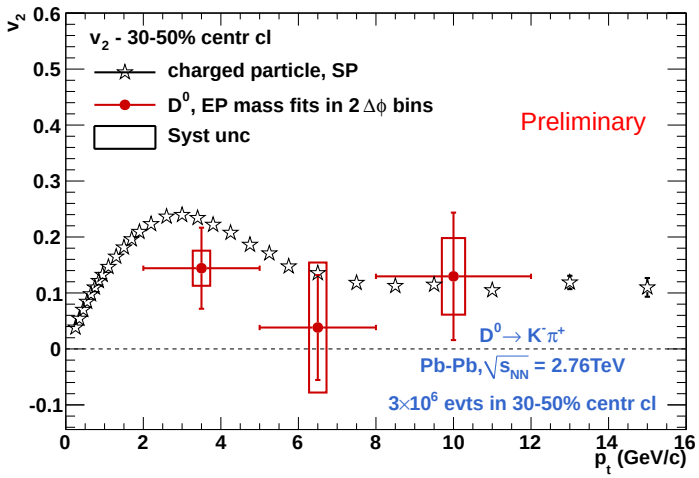

Figure 5.22: D^0 v_2 with the two $\Delta\phi$ bins method (circle) compared to charged tracks elliptic flow measured with the Scalar Product method [81] (star) as a function of $p_{\rm t}$ in the centrality class 30-50%.

Chapter 6

Conclusions

The ALICE experiment heavy-ion and proton-proton programmes are delivering many interesting results based in the data collected in 2010 and 2011.

Concerning the heavy-flavour physics, the analyses presented in this thesis added a contribution to the general picture.

As far as pp collisions are concerned, the D^0 meson production cross section was measured. The pQCD theoretical predictions are in agreement with the measurement. The FONLL calculation tends to underestimate the data, while GM-VFNS slightly overestimates them. The difference between the two models is in the way they treat the introduction of the heavy-quark masses. These results confirm what was obtained at lower-energies comparing to FONLL, but goes in the opposite direction with respect to what was observed at Tevatron comparing to GM-VFNS. This indicates that the energy dependence in this model is steeper than in data.

Furthermore, the measurements presented open new possibilities to test PDF dynamics, in the regime of parton fractional momentum below $x \sim 10^{-4}$ and squared momentum transfer down to $Q^2 \sim (4\text{GeV})^2$, where the onset of gluon PDF saturation effects has been conjectured [132]. Within the uncertainties of the data and of the theoretical predictions, the framework of factorized QCD calculations provides a reasonable description of the data points down to the lowest measured transverse momentum. However, accurate calculations incorporating saturation effects are needed in order to draw firm conclusions on their relevance for low-momentum charm production at LHC energies.

The D^0 cross section in pp collisions served also as a reference for the measurement of the D^0 suppression in Pb–Pb collisions [64].

The outlook for this measurement is to extend the high-p_{t} reach, using the 2011 LHC pp sample including EMCal trigger data. This would be desirable also to obtain a high-p_{t} reference for the study of D^0 production with 2011 Pb–Pb data. The low-p_{t} region is more difficult to be further extended, because the selection of the signal is complicated by the topology of D^0 candidates which is more similar to background candidates at low momentum.

In addition, it is foreseen to reduce the systematic uncertainties, for instance by measuring directly the B meson feed-down contribution.

The measurement of D^0 flow in Pb–Pb collisions is aimed at understanding the degree of thermalization of the medium. This is the first elliptic flow measurement of charmed hadrons. The previous measurement of heavy-flavour v_2, performed by PHENIX at RHIC with non-photonic electrons, gave an important contribution in testing the available models to describe both energy loss (R_{AA}) and flow. This new measurement is a starting

point to have a complete picture of heavy-flavour thermalization and interaction with the Quark-Gluon Plasma produced at LHC.

The precision of the measurement in presently limited by the statistical uncertainty. With the 2011 Pb–Pb data, the performance is expected to improve, reducing both statistical and systematic uncertainties, and the study of the p_{t} dependence will be refined and extended. This will allow for a better comparison with charged-particle elliptic flow and with models.

Other important improvements to be addressed are the subtraction of non-flow effects, for instance using methods such as multi-particle cumulants to measure elliptic flow, the dependence of v_2 on centrality, and the subtraction of the beauty feed-down contribution.

Appendices

Appendix A

Flow analysis tools

A.1 Azimuthal distribution

A characteristic consequence of collective flow in nucleus-nucleus collision is that the direction of the particles produced in a collision are correlated to the orientation of the impact parameter: that is to say, azimuthal distributions measured with respect to the impact parameter are not uniform. The observation of collective effects is not straightforward because the orientation of the impact parameter in not known *a priori*. It must be estimated event-by-event from particles produced in the collision, and these estimates are generally subject to large statistical fluctuations due to finite multiplicity. Azimuthal anisotropies are conveniently parametrized in terms of Fourier coefficients of the azimuthal distribution [19]: if there is no collective flow, the azimuthal distribution is uniform and its Fourier coefficients vanish. In general, each coefficient does not vanish event by event due to finite multiplicity fluctuations, but its average over many events vanishes. On the contrary, non zero value will be a signature of QGP. Anisotropic flow corresponding to (at least) the first two harmonics plays a very important role: the two coefficients have special names, "directed" and "elliptic" flow. The former comes from the fact that this flow has a direction, the latter is due to the fact that in polar coordinates the azimuthal distribution with non-zero second harmonic represents an ellipse. The third coefficient is expected to be non-zero for asymmetric nuclear collisions, due to the different sizes of the colliding nuclei, but also due to fluctuations in the distribution of the nucleons inside the nuclei.

A.2 Correlation with respect to the event plane

The use of Fourier expansion is suitable to study the anisotropic flow. The reaction plane must be estimated first. The estimated reaction plane is called "event plane". The Fourier coefficients in the expansion of the azimuthal distribution of particles with respect to the event plane are evaluated. The coefficients must be corrected up to what they would be relative to the real reaction plane, dividing the observed coefficient by the event plane resolution, which is estimated from the correlation of the planes of independent sub-events. If the detector does not have full azimuthal acceptance, this must be also corrected for. In the most general case, the triple differential distribution is considered. The dependence on particle emission angle with respect to the (true) reaction plane

(Ψ_{RP}) can be written as:

$$E\frac{\mathrm{d}^3N}{\mathrm{d}^3p} = \frac{1}{2\pi}\frac{\mathrm{d}^2N}{p_\mathrm{t}\mathrm{d}p_\mathrm{t}\mathrm{d}y}\left(1+\sum_{n=1}^{\infty}2v_n\cos\left[n(\phi-\Psi_{RP})\right]\right), \tag{A.1}$$

where the sine terms vanish due to the reflection symmetry with respect to the reaction plane. The reaction plane is estimated through the event plane (ψ_n) that can be determined for each harmonic on an event-by-event basis. Due to the finite multiplicity of the events the reaction plane is estimated with a given resolution and the Fourier coefficients, determined with respect to the event plane, must be corrected for.

The Fourier coefficients v_n can be determined by their definition and are usually called v_n^{obs} to distinguish those measured through the event plane from the true ones correlated to the reaction plane:

$$v_n^{\mathrm{obs}} = \langle\cos\left[n(\phi-\psi_n)\right]\rangle \tag{A.2}$$

For a given n the corresponding v_n can be evaluated using the reaction plane determined from any harmonic m, with $n \geq m$, if n is a multiple of m. The periodicity of the quantity $(\phi-\psi_m)$ is $2\pi/m$.

The event flow vector Q_n and the event plane angle ψ_n are linked by the following relations:

$$Q_n\cos\left(n\psi_n\right) = \quad X_n \quad = \sum_i w_i\cos\left(n\phi_i\right) \tag{A.3}$$

$$Q_n\sin\left(n\psi_n\right) = \quad Y_n \quad = \sum_i w_i\sin\left(n\phi_i\right) \tag{A.4}$$

$$\psi_n = \frac{1}{n}\tan^{-1}\left(\frac{Y_n}{X_n}\right) \quad = \quad \frac{1}{n}\tan^{-1}\frac{\sum_i w_i\sin\left(n\phi_i\right)}{\sum_i w_i\cos\left(n\phi_i\right)} \tag{A.5}$$

The sums go over the particle used in the event plane determination and the w_i are weights, usually optimized to make the reaction plane resolution the best as possible. It can be done by selecting the particles of one particular type, p_t, ϕ... The event plane ψ_n, determined for the n-th harmonic is in the range $0 \leq \psi_n < \frac{2\pi}{n}$. For the case $n = 2$, $0 \leq \psi_2 < \pi$.

A.2.1 Acceptance corrections

Biases due to the finite acceptance of the detector which causes the particles to be azimuthally anisotropic in the laboratory system can be removed by making the distribution of event planes isotropic in the laboratory. Some methods are listed below together with their advantages and disadvantages.

The simplest method is to *recentre* the distribution (X_n, Y_n) by subtracting the (X_n, Y_n) values averaged over all events. The main disadvantage of this method is that it does not remove higher harmonics from the resulting ψ_n distribution. If such harmonics are present, then a further flattening of the event plane distribution is required.

One of the most common method uses the *distribution of particles* themselves as measure of the acceptance. The inverse of the laboratory azimuthal distribution is used as weights. This method does not take into account the multiplicity fluctuations around the mean value.

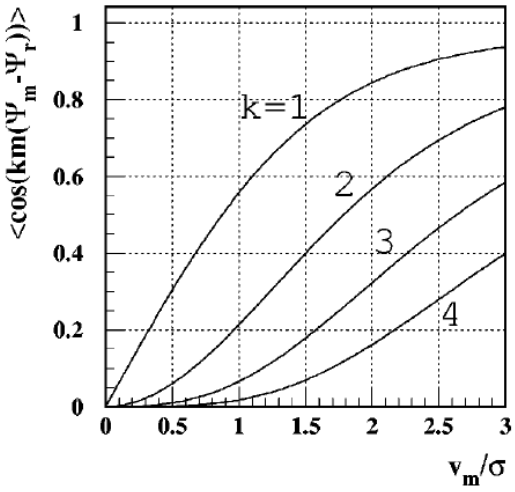

Figure A.1: The event plane resolution for the n-th ($n = km$, according the the conventions of eq. (A.6)) harmonic of the particle distribution with respect to the m-th harmonic plane, as a function of χ_m Figure taken from [127].

A third method considers *mixed events*. The correlations of the real events are divided by the correlations in the mixed events. This method suffers of the problem that using only one mixed event for each real event, the errors are $\sqrt{2}$ larger. Using n_{mix} mixed events for each real event, the errors decrease as $n_{mix}^{1/4}$.

A.2.2 Event plane resolution determination

For each harmonic n, the event plane angle ψ_n is measured through the Q-vector, which is a weighted sum of the azimuthal angle (ϕ) of all tracks but those coming from the D^0 candidate under exam, in order to remove autocorrelation [126]: eqs. (A.3), (A.4), and (A.5).

The event plane angle ψ_n is an approximation of the reaction plane angle (Ψ_{RP}), i.e. the true reaction plane formed by the impact parameter of the two colliding nuclei and the beam direction.

The resolution can be expressed by [127]:

$$\langle \cos km\,(\psi_m - \Psi_{RP})\rangle = \sqrt{\frac{\pi}{8}}\chi_m \cdot \mathrm{e}^{-\chi_m^2/4} \cdot I_{(k-1)/2}(\chi_m^2/4) + I_{(k+1)/2}(\chi_m^2/4) \qquad \text{(A.6)}$$

with $\chi_m = v_n\sqrt{2N}$, where N is the multiplicity, and I_ν the Bessel function of order ν, as plotted in Fig. A.1. The mean cosine values are less than one and thus the correction always increases the flow coefficients.

The resolution can be measured from data using two sub-events, provided that they have the same multiplicity and they cover equal (or specular) rapidity region in order to expect the flow to be the same in both sub-events. The first condition grants that the resolution of the two sub-events is the same. If no other correlation is present excepted those due to flow, or it is negligible, the following relations hold:

$$\left\langle \cos n\left(\psi_m^A - \psi_m^B\right)\right\rangle = \left\langle \cos n\left(\psi_m^A - \Psi_{RP}\right)\right\rangle \times \left\langle \cos n\left(\psi_m^B - \Psi_{RP}\right)\right\rangle, \qquad \text{(A.7)}$$

$$\left\langle \cos n\left(\psi_m^A - \Psi_{RP}\right)\right\rangle = \sqrt{\langle \cos n\,(\psi_m^A - \psi_m^B)\rangle}. \qquad \text{(A.8)}$$

Hence the sub-event resolution can be measured from data by applying eq. (A.8). Then, inverting eq. (A.6), the $\chi_m^{\mathrm{sub-event}}$ can be retrieved giving the sub-event resolution as an input. Graphically, it means that considering on the y-axis of Fig. A.1 the value obtained from eq. (A.8), the corresponding x-axis value gives $\chi_m^{\mathrm{sub-event}}$ (in the case treated the function labelled with $k = 1$ is considered). The variable $\chi_m^{\mathrm{full-event}}$ is then obtained as

$$\chi_m^{\mathrm{full-event}} = \sqrt{2}\chi_m^{\mathrm{sub-event}} \tag{A.9}$$

being $N^{\mathrm{sub-event}} = \frac{1}{2}N^{\mathrm{full-event}}$ and $v_n^{\mathrm{sub-event}} = v_n^{\mathrm{full-event}}$, according to the assumptions made. All the ingredients needed to compute the resolution of the full event with eq. (A.6) are available.
In case of low resolution, where the curves in Fig A.1 are linear, the full event resolution reduces to:

$$\langle \cos km \left(\psi_m - \Psi_{RP}\right)\rangle = \sqrt{2}\left\langle \cos n \left(\psi_m^A - \Psi_{RP}\right)\right\rangle . \tag{A.10}$$

Correlations among particles, which are not due to flow, are called *non-flow* effects. In order to reduce non-flow effects, a possible way out is to separate in (pseudo)rapidity the "signal" particle from the "bulk" particles used for the event plane determination. In this case, or when the sub-events are not "equal", then at least three sub-events are needed to determine the event plane resolution for each of them. For example, the resolution of the first sub-event is determined as:

$$\left\langle \cos n \left(\psi_m^A - \Psi_{RP}\right)\right\rangle = \sqrt{\frac{\left\langle \cos n \left(\psi_m^A - \psi_m^B\right)\right\rangle \left\langle \cos n \left(\psi_m^A - \psi_m^C\right)\right\rangle}{\left\langle \cos n \left(\psi_m^B - \psi_m^C\right)\right\rangle}} \tag{A.11}$$

Possible sources of such correlations are global constraints on the system, like energy and momentum conservation, and particle decays in which the decay products populate both sub-events and are not negligible *a priori*.

A.3 Multiparticle azimuthal correlation

In this section a different strategy for measuring the Fourier coefficients v_n (eq. (A.2)), overcoming the problem of the determination of the reaction plane angle, namely the analysis of multi-particle azimuthal correlations, is presented. The method presented has the advantage of removing the non-flow correlations in both integrated and differential flow. Originally (e.g. [128]) the method had the disadvantage of being affected from the other harmonics, if they are larger. For instance, the interference could hinder the measurement of directed flow when elliptic flow was larger. This problem was solved with an improvement in the azimuthal correlations, not using the flow vector **Q**, but new generating functions.

A.3.1 Integrated flow

Called ϕ_j, with $j = 1, \ldots, M$ the azimuthal angles of the particles seen in an event with multiplicity M, measured with respect to a fixed direction in the detector, the multi-particle azimuthal correlation is of the form

$$\langle \exp\left[in\left(\phi_1 + \ldots \phi_k - \phi_{k+1} - \ldots - \phi_{k+l}\right)\right]\rangle \tag{A.12}$$

where n is the harmonic under study and the brackets indicate an average performed in two steps: first the average on the possible combinations of $k + l$ particles detected in

the same event; then, the average on the events.
Correlations between $k+l$ particles can be decomposed into a sum of terms involving correlations between smaller number of particles. For instance, the two-particle azimuthal correlation $\left\langle e^{in(\phi_1-\phi_2)}\right\rangle$ can be written as:

$$\left\langle e^{in(\phi_1-\phi_2)}\right\rangle = \left\langle e^{in\phi_1}\right\rangle\left\langle e^{in\phi_2}\right\rangle + \left\langle\left\langle e^{in(\phi_1-\phi_2)}\right\rangle\right\rangle, \tag{A.13}$$

where $\left\langle\left\langle e^{in(\phi_1-\phi_2)}\right\rangle\right\rangle$ is by definition the second-order cumulant. To understand the physical meaning of this quantity, consider first a "perfect" detector, i.e. with isotropic acceptance in azimuth. The average $\left\langle e^{in\phi_j}\right\rangle$ vanishes by symmetry (ϕ_j is measured with respect to a fixed reference in the laboratory, not with respect to the reaction plane). The first term in the right hand side of eq. (A.13) vanishes and the cumulant reduces to the measured two-particle correlation.

In the case of a realistic detector, with non-uniform acceptance, the first term in the right hand side of eq. (A.13) may not vanish, but the cumulant vanishes if ϕ_1 and ϕ_2 are uncorrelated. Thus the cumulant $\left\langle\left\langle e^{in(\phi_1-\phi_2)}\right\rangle\right\rangle$ isolates the physical correlation, and disentangle from trivial detector effects. There are several physical contributions to the correlation $\left\langle\left\langle e^{in(\phi_1-\phi_2)}\right\rangle\right\rangle$ which separate into flow and non-flow (or direct) correlations. The direct correlations scale with the multiplicity M as $1/M$, as can be understood when considering correlation between the decay products of a resonance. For instance considering the ρ meson decays into two pion, momentum conservation induces an angular correlation of order unity between the decay pions; besides, the probability that two arbitrary pions seen in the detector result from the same ρ decay scales with the total number of pions as $1/M$. When the source is not isotropic, flow, which is by definition a correlation between emitted particles and the reaction plane, generates azimuthal correlations between any two outgoing particles and gives contribution v_n^2, as it will be shown later, to the second-order cumulant. One can use the second-order cumulant if this contribution dominates over the non-flow contribution, i.e. $v_n \gg 1/\sqrt{M}$.

The construction of higher order cumulants, allow to separate flow and non-flow correlations. The four-particle azimuthal correlation, for a perfect detector is defined as

$$\begin{aligned}\langle\exp\left[in\left(\phi_1+\phi_2-\phi_3-\phi_4\right)\right]\rangle \;=\; &\left\langle e^{in(\phi_1-\phi_3)}\right\rangle\left\langle e^{in(\phi_2-\phi_4)}\right\rangle + \\ &\left\langle e^{in(\phi_1-\phi_4)}\right\rangle\left\langle e^{in(\phi_2-\phi_3)}\right\rangle + \\ &\langle\langle\exp\left[in\left(\phi_1+\phi_2-\phi_3-\phi_4\right)\right]\rangle\rangle\,.\end{aligned} \tag{A.14}$$

If particles are correlated pairwise, there are two possible combination leading to a non-vanishing value for the left-hand side: either (1,3) and (2,4), or (1,4) and (2,3) (the first two terms in the right-hand side). The remaining term is by definition the fourth-order cumulant and it is thus insensitive to two-particle non-flow correlations. It may still be influenced by higher-order non-flow correlations (for instance a resonance decaying into four particles), but their contribution is small, scaling as $1/M^3$, while the measured correlation $\langle\exp\left[in\left(\phi_1+\phi_2-\phi_3-\phi_4\right)\right]\rangle$ is generally larger, of order $1/M^2$. Flow yields a contribution $-v_n^4$ to the cumulant, therefore the cumulant is dominated by the flow as soon as $v_n \gg 1/M^{3/4}$, improving the stronger constraint of $v_n \gg 1/\sqrt{M}$ of the two-particles correlation.

Eq. (A.14) hold for a perfect detector. The corresponding expression in case of a real detector, which eliminates both detector effects and non-flow correlation, is more complicated and can be obtained with *generating functions*, which enable to construct

cumulants of arbitrary order for arbitrary detector. The cumulants can be expressed in terms of the generating functions of the multi-particle correlation. The coefficients of the expansion of the generating function of the cumulants are the cumulants. Only the diagonal terms are interesting, because related to flow and they are denoted by [129]

$$c_n\{2k\} \equiv \left\langle\left\langle e^{in(\phi_1+\ldots+\phi_k-\phi_{k+1}-\phi_{2k})}\right\rangle\right\rangle. \tag{A.15}$$

In practice the simplest way to extract $c_n\{2k\}$ is to tabulate the generating function and then compute numerically the coefficients of its power-series expansion using interpolation formulas (refer again to [129] for details). This means that approximations enter the determination of cumulants and therefore can bias the result.

The contribution of flow to the cumulants is summarized in the following list, for the first 3 orders:

- $v_n\{2\}^2 = c_n\{2\}$
- $v_n\{4\}^4 = -c_n\{4\}$
- $v_n\{6\}^6 = c_n\{6\}/4.$

The proof, both for perfect and real detector, can be found in [129]. In the same reference, a description of the magnitude of the statistical and systematic uncertainties is presented.

Differential flow

The differential flow is the measurement of flow in a narrower phase space window. The particles of interest (POI) are correlated to the other particles (reference particles, RP), used to determine the integrated flow. The differential flow of the POI is measured by correlating its azimuthal angle with the RP azimuths. To avoid autocorrelation, the POI must be different from the RP, or it must be subtracted from the correlation. As in the case of integrated flow, cumulants of different orders yield different estimates of the differential flow. The details of the determination of the generating functions, the relations between cumulants and flow harmonics, and the errors are treated in [129].

A.3.2 Q-cumulants

This method [125] is not biased by interference between various harmonics, interpolating formulas, and all detector effects can be disentangled from the flow estimate. Since cumulants are calculated without any approximation and directly from the data the procedure is referred to with the name of *direct cumulants* or *Q-cumulants* because they are expressed analytically in terms of different harmonic Q-vectors.

Flow fluctuations are an important part of an anisotropic flow study. They are believed to be determined mostly by initial geometry fluctuations of the system created in the collision. An important consequence of this is that flow develops relative to the so-called *participants plane(s)* instead of the reaction plane determined by the direction of the impact parameter. The Q-cumulants method is not influenced by how exactly the anisotropic flow is being developed.

The method consists in calculating the *reference flow*, first. The reference flow is the average flow in a momentum window and it is used to calculate the differential flow afterwards.

In the expression of the multi-particle correlations, mixed harmonics correlations are needed for any multi-particle correlation with order higher than 2. The explicit

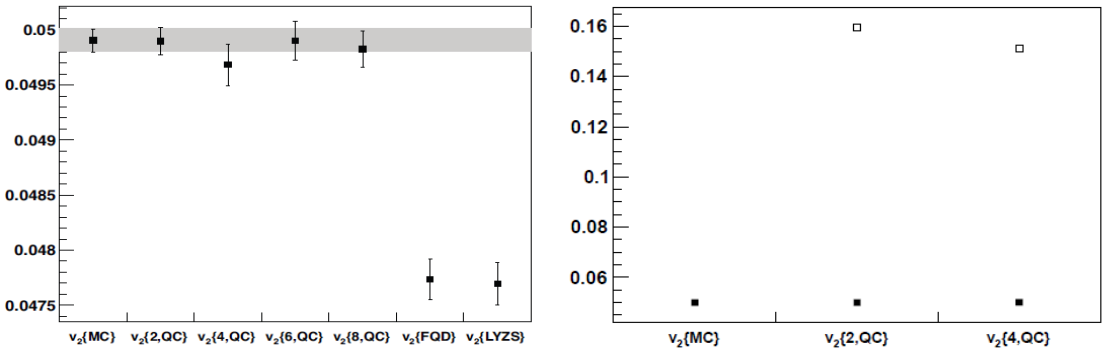

Figure A.2: Left panel: Elliptic flow extracted by different methods for 10^5 simulated events with multiplicity $M = 500$, $v_2 = 0.05$ and $v_4 = 0.1$. Right panel: Elliptic flow extracted accounting (closed markers) or not (open markers) for acceptance effects. Figures from [125].

dependence of the multi-particle correlation on different harmonics of the Q-vector is crucial to disentangle the interference between harmonics and eliminates the bias which affected the previous methods.

Weights can be applied in order to minimize the errors in the final result and corrections for non-uniform acceptance can be also applied.

In order to compute the differential flow, particles are divided into *reference flow particle (RFP)* and/or *particle of interest (POI)*. The flow analysis is performed in two steps: first the reference flow is computed only with the RFP, then the differential flow is estimated with POI with respect to the reference flow obtained in the first step.

The different terms to obtain the differential flow are not discussed here (cf. [125]), but some examples of simulation results to compare with other methods and among different cumulant orders are reported.

Figure A.2, left panel, shows the results from simulation of events with anisotropic flow present in two harmonics, the second and the forth. $v_2\{\text{MC}\}$ represents the Monte Carlo estimate, which is obtained using the known reaction plane. The other results in the figure do not use this information. The estimates from fitting of the Q-distribution method ($v_2\{\text{FQD}\}$) and the Lee-Yang Zero's Sum method ($v_2\{\text{LYZS}\}$) show a clear bias from the forth harmonic. Results obtained with direct cumulants of different orders ($v_2\{k, \text{QC}\}$) are unaffected by v_4 interference.

The results of a simulation with a detector with "holes" in the acceptance are shown in Fig. A.2, right panel. The elliptic flow extracted with (closed markers) and without (open markers) the equations that are valid for non-uniform detector acceptance is shown. Clearly, comparing to $v_2\{\text{MC}\}$, the estimate without correction is biased.

Bibliography

[1] K. Aamodt, "Measurement of charm production at central rapidity in proton–proton collisions at $\sqrt{s} = 7$ TeV," *accepted by Eur. Phys. J. C*, 2011.

[2] C. Alcock, "The Astrophysics and Cosmology of Quark-Gluon Plasma, in Quark-Gluon Plasma," *Springer-Verlag*, 1990.

[3] M. G. Alford, "QCD at high density / temperature," *Nucl. Phys. Proc. Suppl.*, vol. 117, no. 65, 2003.

[4] A. Chodos, R. L. Jaffe, K. Johnson, C. B. Thorn, and V. F. Weisskopf, "New extended model of hadrons," *Phys. Rev. D*, vol. 9, pp. 3471–3495, Jun 1974.

[5] J. D. Bjorken *Phys. Rev. D*, vol. 27, no. 140, 1983.

[6] R. J. Glauber, *Lectures in Theoretical Physics*, vol. I. Interscience, New York, 1958.

[7] F. Karsch *Nucl. Phys.*, vol. A698, no. 199c, 2002.

[8] F. Karsch, "Lattice QCD at high temperature and density," *Lect. Notes Phys.*, vol. 583, pp. 209–249, 2002.

[9] B. I. Abelev, "Systematic measurements of identified particle spectra in pp, d+Au, and Au + Au collisions at the STAR detector," *Phys. Rev. C*, vol. 79, no. 034909, 2009.

[10] C. Shen, U. Heinz, P. Huovinen, and H. Song, "Radial and elliptic flow in Pb + Pb collisions at energies available at the CERN Large Hadron Collider from viscous hydrodynamics," *Phys. Rev. C*, vol. 84, p. 044903, Oct 2011.

[11] R. C. Hwa and K. Kajantie *Phys. Rev. D*, vol. 32, p. 1109, 1985.

[12] B. B. Back, "Centrality dependence of the charged particle multiplicity near midrapidity in Au + Au collisions at $\sqrt{s_{\mathrm{NN}}} = 130$ and 200 GeV," *Phys. Rev. C*, vol. 65, p. 061901, Jun 2002.

[13] C. Adler, "Centrality Dependence of High-p_T Hadron Suppression in Au + Au Collisions at $\sqrt{s_{NN}} = 130$ GeV," *Phys. Rev. Lett.*, vol. 89, p. 202301, Oct 2002.

[14] P. Huovinen, "Hydrodynamical description of collective flow." arXiv:nucl-th/0305064, 2003.

[15] D. Teaney, J. Lauret, and E. V. Shuryak, "Flow at the SPS and RHIC as a Quark-Gluon Plasma Signature," *Phys. Rev. Lett.*, vol. 86, pp. 4783–4786, May 2001.

[16] S. A. Bass and A. Dumitru, "Dynamics of hot bulk qcd matter: From the quark-gluon plasma to hadronic freeze-out," *Phys. Rev. C*, vol. 61, p. 064909, May 2000.

[17] F. Cooper and G. Frye *Phys. Rev. D*, vol. 10, no. 186, 1974.

[18] J.-Y. Ollitrault, "Anisotropy as a signature of transverse collective flow," *Phys. Rev. D*, vol. 46, no. 229, pp. 229–245, 1992.

[19] S. A. Voloshin and Y. Zhang, "Flow Study in Relativistic Nuclear Collisions by Fourier Expansion of Azimuthal Particle Distributions," 1994.

[20] K. H. Ackermann, "Elliptic Flow in Au+Au Collisions at $\sqrt{s_{NN}} = 130$ GeV," *Phys. Rev. Lett.*, vol. 86, pp. 402–407, Jan 2001.

[21] A. Adare, "Scaling Properties of Azimuthal Anisotropy in Au + Au and Cu + Cu Collisions at $\sqrt{s_{\rm NN}} = 200$ GeV," *Phys. Rev. Lett.*, vol. 98, p. 162301, Apr 2007.

[22] C. Adler, "Identified Particle Elliptic Flow in Au+Au Collisions at $\sqrt{s_{NN}} =$ 130GeV," *Phys. Rev. Lett.*, vol. 87, p. 182301, Oct 2001.

[23] R. Snellings, "Anisotropic flow from RHIC to LHC," *Eur. Phys. J. C*, vol. 49, pp. 87–90, 2007.

[24] P. Huovinen, P. Kolb, U. Heinz, P. Ruuskanen, and S. Voloshin, "Radial and Elliptic Flow at RHIC: Further Predictions," *Phys. Lett. B*, vol. 503, no. 58, 2001.

[25] J. Adams, "Particle-Type Dependence of Azimuthal Anisotropy and Nuclear Modification of Particle Production in Au+Au Collisions at $\sqrt{s_{NN}} = 200$ GeV," *Phys. Rev. Lett.*, vol. 92, p. 052302, Feb 2004.

[26] S. A. Voloshin, "Anisotropic flow," *Nucl.Phys. A*, vol. 715, pp. 379–388, 2003.

[27] D. Molnár and S. A. Voloshin, "Elliptic Flow at Large Transverse Momenta from Quark Coalescence," *Phys. Rev. Lett.*, vol. 91, p. 092301, Aug 2003.

[28] P. F. Kolb, J. Sollfrank, and U. Heinz, "Anisotropic transverse flow and the quark-hadron phase transition," *Phys. Rev. C*, vol. 62, p. 054909, Oct 2000.

[29] D. Teaney, "Effect of shear viscosity on spectra, elliptic flow, and Hanbury Brown–Twiss radii," *Phys. Rev. C*, vol. 68, p. 034913, Sep 2003.

[30] U. Heinz, "Viscous relativistic hydrodynamics," 2005.

[31] T. Hirano, U. W. Heinz, D. Kharzeev, R. Lacey, and Y. Nara, "Elliptic Flow from a Hybrid CGC, Full 3D Hydro and Hadronic Cascade Model," *J.PHYS.G*, vol. 34, p. S879, 2007.

[32] T. Hirano and K. Tsuda, "Collective flow and two-pion correlations from a relativistic hydrodynamic model with early chemical freeze out," *arXiv:nucl-th/0205043v2*, 2002.

[33] T. Hirano, U. Heinz, D. Kharzeev, R. Lacey, and Y. Nara, "Elliptic Flow from a Hybrid CGC, Full 3D Hydro and Hadronic Cascade Model," *J. Phys. G: Nucl. Part. Phys.*, vol. 34, p. S879, 2007.

[34] Rafelski *Phys. Rep.*, vol. 88, no. 331, 1982.

[35] Koch, Müller, and Rafelski *Phys. Rep.*, vol. 142, no. 167, 1986.

[36] K.Fanebust and NA57, "Results on hyperon production from NA57," *J. Phys. G: Nucl. Part. Phys.*, vol. 28, no. 7, 2002.

[37] B. I. Abelev, "Enhanced strange baryon production in Au+Au collisions compared to p+p at $\sqrt{s_{NN}}$ = 200 GeV," *Phys. Rev. C*, vol. 77, no. 044908, 2008.

[38] T. Matsui and H. Satz *Phys. Lett. B*, vol. 178, no. 416, 1986.

[39] M.C. Abreu, "Evidence for deconfinement of quarks and gluons from the Jψ suppression pattern measured in Pb-Pb collisions at the CERN-SPS," *Phys. Lett. B*, vol. 477, pp. 28–36, 2000.

[40] N. Brambilla *et al.*, "Heavy quarkonium: progress, puzzles, and opportunities," 2011.

[41] P. Braun-Munzinger, J. Stachel, J. Wessels, and N. Xu, "Thermal and hadrochemical equilibration in nucleus-nucleus collisions at the sps," *Physics Letters B*, vol. 365, no. 1–4, pp. 1–6, 1996.

[42] S.S.Adler, "High-p_T charged hadron suppression in Au+Au collisions at $\sqrt{s_{NN}}$=200 GeV," *Phys. Rev. C*, vol. 69, no. 034910, 2004.

[43] J. Adams, "Evidence from d + Au Measurements for Final-State Suppression of High-p_T Hadrons in Au + Au Collisions at RHIC," *Phys. Rev. Lett.*, vol. 91, p. 072304, 2003.

[44] D. d'Enterria, "Jet Quenching," *Springer Verlag. Landolt-Boernstein*, vol. I, no. 23A, 2009.

[45] M. Cacciari, M. Greco, and P. Nason, "The p_T Spectrum in Heavy-Flavour Hadroproduction," *J. High Energy Phys.*, no. 007, p. 9805, 1998.

[46] H. Bethe and W. Heitler *Proc. Roy. Soc. Lond.*, vol. A 146, no. 83, 1934.

[47] A. B. Migdal *Phys. Rev.*, vol. 103, no. 1811, 1956.

[48] Y. L. Dokshitzer and D. E. Kharzeev, "Heavy quark colorimetry of QCD matter," *Phys. Lett.*, vol. B519, pp. 199–206, 2001.

[49] D. Acosta, "Measurement of Prompt Charm Meson Production Cross Sections in $p\bar{p}$ Collisions at $\sqrt{s}$ = 1.96 TeV," *Phys. Rev. Lett.*, vol. 91, no. 24, 2003.

[50] C. Chen, *A Measurement of the direct charm meson production cross-section at CDF II.* PhD thesis, Univerity of Pennsylvania, 2003.

[51] M. Cacciari and P. Nason, "Charm cross sections for the Tevatron Run II," *J. High Energy Phys.*, no. 0309, p. 006, 2003.

[52] B. Kniehl, G. Kramer, and B. Pötter, "Testing the universality of fragmentation functions," *Nuclear Physics B*, vol. 597, no. 1–3, pp. 337–369, 2001.

[53] A. Adare, "Measurement of High-p_T Single Electrons from Heavy-Flavor Decays in p+p Collisions at $\sqrt{s}$ = 200 GeV," *Phys. Rev. Lett.*, vol. 97, no. 252002, 2006.

[54] H. Agakishiev, "High p_T non-photonic electron production in p+p collisions at $\sqrt{s}$ = 200 GeV," *Phys. Rev. D*, vol. 83, no. 52006, 2011.

[55] M. M. Aggarwal, "Measurement of the Bottom Quark Contribution to Nonphotonic Electron Production in p+p Collisions at $\sqrt{s} = 200$ GeV," *Phys. Rev. Lett.*, vol. 105, no. 202301, 2010.

[56] N. Armesto, A. Dainese, C. A. Salgado, and U. A. Wiedemann, "Testing the color charge and mass dependence of parton energy loss with heavy-to-light ratios at bnl rhic and cern lhc," *Phys. Rev. D*, vol. 71, p. 054027, Mar 2005.

[57] J.Adams, "Transverse-Momentum and Collision-Energy Dependence of High-p_T Hadron Suppression in Au+Au Collisions at Ultrarelativistic Energies," *Phys. Rev. Lett.*, vol. 91, p. 172302, 2003.

[58] N. Armesto, M. Cacciari, A. Dainese, C. A. Salgado, and U. A. Wiedemann, "How sensitive are high- electron spectra at RHIC to heavy quark energy loss?," *Physics Letters B*, vol. 637, no. 6, pp. 362–366, 2006.

[59] H. van Hees, V. Greco, and R. Rapp, "Heavy-quark probes of the quark-gluon plasma and interpretation of recent data taken at the bnl relativistic heavy ion collider," *Phys. Rev. C*, vol. 73, p. 034913, Mar 2006.

[60] G. D. Moore and D. Teaney, "How much do heavy quarks thermalize in a heavy ion collision?," *Phys. Rev. C*, vol. 71, p. 064904, Jun 2005.

[61] A. Adare, "Energy Loss and Flow of Heavy Quarks in Au+Au Collisions at $\sqrt{s_{NN}} = 200$ GeV," *Phys. Rev. Lett.*, vol. 98, no. 172301, 2007.

[62] M. Djordjevic, M. Gyulassy, R. Vogt, and S. Wicks, "Influence of bottom quark jet quenching on single electron tomography of Au + Au," *Physics Letters B*, vol. 632, no. 1, pp. 81–86, 2006.

[63] S. Wicks, W. Horowitz, M. Djordjevic, and M. Gyulassy, "Elastic, inelastic, and path length fluctuations in jet tomography," *Nuclear Physics A*, vol. 784, no. 1–4, pp. 426–442, 2007.

[64] Quark Matter 2011 Proceedings, *D meson nuclear modification factors in Pb–Pb collisions at $\sqrt{s_{NN}}$ = 2.76 TeV, measured with the ALICE detector*, 2011.

[65] R. H. Brown and R. Twiss *Nature*, vol. 178, no. 1046, 1956.

[66] R. Q. Twiss *Philos. Mag.*, vol. 45, no. 663, 1945.

[67] K. Aamodt, "Two-pion Bose-Eistein correlations in central Pb-Pb collisions at $\sqrt{s_{NN}} = 2.76$ TeV," *Phys. Lett. B*, vol. 696, pp. 328–337, 2011.

[68] K. Aamodt, "Charged-Particle Multiplicity Density at Midrapidity in Central Pb-Pb Collisions at $\sqrt{s_{NN}} = 2.76$ TeV," *Phys. Rev. Lett.*, vol. 105, p. 252301, 2010.

[69] J. Albacete and A. Dumitru, "A model for gluon production in heavy-ion collisions at the LHC with rcBK unintegrated gluon densities,"

[70] K.Aamodt, "Centrality Dependence of the Charged-Particle Multiplicity Density at Midrapidity in Pb-Pb Collisions at $\sqrt{s_{NN}} = 2.76$ TeV," *Phys. Rev. Lett.*, vol. 106, no. 032301, 2011.

[71] J. Cleymans, K. Redlich, and E. Suhonen, "Canonical description of strangeness conservation and particle production," *Z. Phys. C*, no. 51, p. 137, 1991.

[72] A.Adare, "J/ψ suppression at forward rapidity in Au+Au collisions at $\sqrt{s_{NN}} = 200$ GeV," *Phys. Rev. C*, vol. 84, no. 5, p. 054912, 2011.

[73] R. Haegedorn *Riv. Nuovo Cimento*, vol. 6, no. 1, 1983.

[74] R. Engel, J. Ranft, and S. Roesler *Phys. Rev. D*, vol. 52, no. 1495, 1995.

[75] T. Sjöstrand, S. Mrenna, and P. Skands, "PYTHIA 6.4 physics and manual," *J. High Energy Phys.*, no. 05, p. 026, 2006.

[76] T. Sjöstrand and P. Skands *Eur. Phys. J. C*, vol. 39, no. 129, 2005.

[77] P. Skands, "Contribution to the 1st International Workshop on Multiple Partonic Interactions at the LHC, Perugia, Italy," October 2008.

[78] J. Otwinowski, "Charged Particle Production at Large Transverse Momentum in Pb−Pb Collisions at $\sqrt{s_{NN}} = 2.76$ TeV Measured with ALICE at the LHC," *J. Phys.*, vol. G38, p. 124112, 2011.

[79] K.Aamodt, "Suppression of charged particle production at large transverse momentum in central Pb–Pb collisions at $\sqrt{s_{NN}} = 2.76$ TeV," *Phys. Lett. B*, vol. 696, pp. 30–39, 2011.

[80] K.Aamodt, "Elliptic Flow of Charged Particles in Pb-Pb Collisions at $\sqrt{s_{NN}} = 2.76$ TeV," *Phys. Rev. Lett.*, vol. 105, no. 252302, 2010.

[81] C. Adler, "Elliptic flow from two- and four-particle correlations in Au+Au collisions at $\sqrt{s_{NN}} = 130$ GeV," *Phys. Rev. C*, vol. 66, no. 034904, 2002.

[82] J. Borburgh, J. Bosser, C. Carli, M. Chanel, V. Chohan, T. Fowler, B. Frammery, R. Garoby, S. Hancock, J. Hansen, J.-Y. Hemery, C. Hill, E. Mahner, M. Martini, S. Maury, D. Möhl, J. Royer, L. Sermeus, M. Silari, L. Soby, and G. Tranquille, "PS ion for LHC Design Report," *CERN/PS, PIL/LEIR Note 001*, 2002.

[83] G. Aad, "The ATLAS Experiment at the CERN Large Hadron Collider," *JINST*, vol. 2, no. 3, p. S08003, 2008.

[84] CMS Collaboration, "The CMS experiment at the CERN LHC," *JINST*, vol. 2, no. 3, p. S08004, 2008.

[85] "The LHCf experiment." http://hep.fi.infn.it/LHCf/.

[86] "The TOTEM experiment." http://totem.web.cern.ch/Totem/.

[87] K.Aamodt, "The ALICE experiment at the CERN LHC," *JINST*, vol. I, no. 3, p. S08002, 2008.

[88] F. Carminati, "ALICE: Physics Performance Report, Vol I," *J. Phys. G: Nucl. Part. Phys.*, vol. 2, no. 30, p. 1517, 2004.

[89] A. Rashevsky *et al.*, "Characteristics of the ALICE Silicon Drift Detector," *Nucl. Instrum. Meth. A*, no. 461, p. 133, 2001.

[90] ALICE Collaboration, "ALICE time projection chamber: Technical Design Report," *CERN-LHCC-2000-001*, 2000.

[91] "The ALICE experiment Offline project." http://aliweb.cern.ch/Offline/AliRoot/Manual.html.

[92] "An object-oriented data analysis framework." http://root.cern.ch.

[93] "ALICE Environment for Grid." http://alien2.cern.ch/.

[94] I. Foster and C. Kesselmann, "The grid: blueprint for a new computing infrastructure," *Morgan Kaufmann Publisher*, 1999.

[95] X.-N. Wang and M. Gyulassy, "hijing: A Monte Carlo model for multiple jet production in pp, pA, and AA collisions," *Phys. Rev. D*, vol. 44, pp. 3501–3516, Dec 1991.

[96] "Geant 3 (GEometry ANd Tracking)." http://wwwasdoc.web.cern.ch/wwwasdoc/geant/geantall.html.

[97] S. Agostinelli *et al.*, "Geant4 – a simulation toolkit," *Nuclear Instruments and Methods in Physics Research Section A: Accelerators, Spectrometers, Detectors and Associated Equipment*, vol. 506, no. 3, pp. 250–303, 2003.

[98] J. Allison *et al.*, "Geant4 developments and applications," *Nuclear Science, IEEE Transactions on*, vol. 53, pp. 270–278, feb. 2006.

[99] "FLUKA (FLUktuierende KAskade)." http://www.fluka.org/fluka.php?id=publications&mm2=3.

[100] P. Billoir, "Track fitting with multiple scattering: a new method," *Nucl. Instrum. Meth. A*, vol. A 225, p. 352, 1984.

[101] P. Billoir, "Track element merging strategy and vertex fitting in complex modular detectors," *Nucl. Instrum. Meth.*, vol. A 241, p. 115, 1985.

[102] R. Frühwirth, "Application of Kalman filtering to track and vertex fitting," *Nucl. Instrum. Meth.*, vol. A 262, p. 444, 1987.

[103] P. Billoir, "Progressive track recognition with a Kalman like fitting procedure," *Comput. Phys. Commun.*, vol. 57, p. 390, 1989.

[104] H. D. Vries, C. D. Jager, and C. D. Vries, "Nuclear charge-density-distribution parameters from elastic electron scattering," *Atomic Data and Nuclear Data Tables*, vol. 36, no. 3, pp. 495–536, 1987.

[105] K. Nakamura *et al.*, "The Review of Particle Physics," 2010.

[106] M. Gagliardi for the ALICE Collaboration, "Measurement of reference cross sections in pp and Pb–Pb collisions at the LHC in van der Meer scans with the ALICE detector," *arXiv:1109.5369v1 [hep-ex]*, 2011.

[107] C. Bianchin, A. Dainese, C. D. Giglio, A. Rossi, and C. Zampolli, "Preparation for the $D^0 \to K^-\pi^+$ analysis in pp collisions: yield measurement and correction for efficiency," 2011.

[108] F. James, "MINUIT Function Minimization and Error Analysis." http://wwwasdoc.web.cern.ch/wwwasdoc/minuit/minmain.html.

[109] A. Dainese, *Charm production and in-medium QCD energy loss in nucleus-nucleus collisions with ALICE. A performance study.* PhD thesis, Padova University, Italy, 2003.

[110] S. van der Meer, "Calibration of the effective beam height in the ISR/68/31," *ISR-PO/68-31*, 1968.

[111] B. Kniehl, "Recent developments in quarkonium and open flavour production calculations," *Phys. Rev. Lett.*, no. 96, p. 012001, 2006.

[112] B. Alessandro, "ALICE: Physics Performance Report, Vol II," *J. Phys. G: Nucl. Part. Phys.*, vol. 1, no. 32, p. 1295, 2006.

[113] P. Skands, "The "Perugia" Tunes," *FERMILAB-CONF-09-113-T*, 2009.

[114] M. L. Mangano, "The saga of bottom production in proton-antiproton collisions," 2004.

[115] R. Aaij, "Measurement of $\sigma(pp \to bbX)$ at $\sqrt{s} = 7$ TeV in the forward region," *Phys. Lett. B*, 2010.

[116] V. Khachatryan *Eur. Phys. J. C*, vol. 157, 2011.

[117] M. Cacciari, P. Nason, and R. Vogt, "To be added," *Phys. Rev. Lett.*, vol. 95, no. 122001, 2005.

[118] A. Rossi, *Charm production in proton-proton collisions at the LHC with the ALICE detector.* PhD thesis, XXII ciclo Univ Trieste, 2009.

[119] P. Nadolsky, H.-L. Lai, Q.-H. Cao, J. Huston, J. Pumplin, D. Stump, W.-K. Tung, and C.-P. Yuan, "Implications of CTEQ global analysis for collider observables," *Phys. Rev. D*, vol. 78, no. 013004, 2008.

[120] XIV International Conference on Hadron Spectroscopy (hadron2011), *Heavy-flavor production in pp and Pb–Pb collisions at LHC with ALICE*, 2011.

[121] "Measurement of D^* meson production cross sections in pp collisions at $\sqrt{s} = 7$ TeV with the ATLAS detector," 2011.

[122] M. L. Mangano, P. Nason, and G. Ridolfi, "Heavy-quark correlations in hadron collisions at next-to-leading order," *Nuclear Physics B*, vol. 373, no. 2, pp. 295–345, 1992.

[123] K. Aamodt, "Rapidity and transverse momentum dependence of inclusive production in pp collisions at 7 TeV," *Physics Letters B*, vol. 704, no. 5, pp. 442–455, 2011.

[124] V. Khachatryan, A. M. Sirunyan, and C. C. Tumasyan, "Upsilon production cross section in *pp* collisions at $\sqrt{s} = 7$ TeV," *Phys. Rev. D*, vol. 83, p. 112004, Jun 2011.

[125] A. Bilandzic, R. Snellings, and S. Voloshin, "Flow analysis with cumulants: Direct calculations," *Phys. Rev. C*, vol. 83, p. 044913, 2001.

[126] P. Danielewicz and G. Odyniec, "To be added," *Phys. Lett.*, vol. 157B, no. 146, 1985.

[127] A. M. Poskanzer and S. A. Voloshin, "Methods for analyzing anisotropic flow in relativistic nuclear collisions," *Phys.Rev.*, vol. C58, pp. 1671–1678, 1998.

[128] N. Borghini, P. M. Dinh, and J.-Y. Ollitrault, "A new method for measuring azimuthal distributions in nucleus-nucleus collisions," *Phys. Rev. C*, vol. 63, no. 054906, 2011.

[129] N. Borghini, P. M. Dinh, and J.-Y. Ollitrault, "Flow analysis from multiparticle azimuthal correlations," *Phys. Rev. C*, vol. 64, no. 054901, 2001.

[130] R. S. Bhalerao, N. Borghini, and J.-Y. Ollitrault, "Genuine collective flow from Lee-Yang zeroes," *Phys. Lett. B*, vol. 580, no. 157, 2004.

[131] S. Wang, Y. Z. Jiang, M. Liu, D. Keane, B. Beavis, S. Y. Chu, S. Y. Fung, M. Vient, C. Hartnack, and H. Stöcker, "Measurement of collective flow in heavy-ion collisions using particle-pair correlations," *Phys. Rev. C*, vol. 44, no. 3, 1991.

[132] S. Alekhin *et al.*, "HERA and the LHC," *arXiv:hep-ph/0601013*, vol. Part B, 2006.

List of Figures

List of Tables

Acknowledgements

Questo lavoro di tesi è stato possibile grazie all'incomparabile guida di A. Dainese e al supporto di tutto il gruppo di ALICE Padova, tra cui in particolare M. Lunardon, R. Turrisi, D. Caffarri e A. Rossi. Molte figure mi sono state gentilmente fornite dai colleghi di Padova e dal gruppo D2H-PWG3, tra cui G. Ortona, R. Bala, F.Prino, Z. Conesa del Valle. Ringrazio inoltre E. Benedetto per le preziose informazioni su LHC. Ringrazio G. Martínez García, P. Pillot e S. Masciocchi per il frequente e generoso aiuto e per la fiducia che mi hanno accordato e l'intera Collaborazione ALICE per le stimolanti esperienze che mi ha permesso di realizzare.